KONINKLIJK BELGISCH INSTITUUT VOOR NATUURWETENSCHAPPEN
OD NATUUR – BEHEERSEENHEID VAN HET MATEMATISCH MODEL

# MOnitoring en MOdellering van het cohesieve sedimenttransport en evaluatie van de effecten op het mariene ecosysteem ten gevolge van bagger- en stortoperatie (MOMO)


## Activiteitsrapport (1 januari - 30 juni 2019)

Michael Fettweis, Matthias Baeye, Frederic Francken, Nicky Jespers, Marc Knockaert, Giacomo Montereale-Gavazzi, Koen Parmentier, Dries Van den Eynde

MOMO/9/MF/201911/NL/AR/1

museum
Operational Directorate Natural Environment
OD Nature I OD Natuur I DO Nature

KBIN-OD Natuur - BMM
Vautierstraat 29
B–1000 Brussel
België

# Inhoudstafel



Photo's voorpagina: De deelnemers aan de maandelijkse bio-geochemische monitorings-campagnes met de RV Belgica tijdens het eerste semester van 2019: Joan Backers, Matthias Baeye, Matthew Becks, Chloë Demilde, Tjörven Ditillieu, Michael Fettweis, Frederic Francken, Camille Gaulier, Kyra Gesquiere, Kevin Hindryckx, Nicky Jespers, Bob Rumes, Tom Scholdis, Dimitri Van der Zande, Wim Vanhaverbeke,

# 1. Algemeen overzicht van de activiteiten

## 1.1. Voorwerp van deze opdracht

Het MOMO-project (monitoring en modellering van het cohesieve sedimenttransport en de evaluatie van de effecten op het mariene ecosysteem ten gevolge van bagger- en stortoperatie) maakt deel uit van de algemene en permanente verplichtingen van monitoring en evaluatie van de effecten van alle menselijke activiteiten op het mariene ecosysteem waaraan België gebonden is overeenkomstig het verdrag inzake de bescherming van het mariene milieu van de noordoostelijke Atlantische Oceaan (1992, OSPAR-Verdrag). De OSPAR Commissie heeft de objectieven van haar Joint Assessment and Monitoring Programme (JAMP) gedefinieerd tot 2021 met de publicatie van een holistisch "quality status report" van de Noordzee en waarvoor de federale overheid en de gewesten technische en wetenschappelijke bijdragen moeten afleveren ten laste van hun eigen middelen.

De menselijke activiteit die hier in het bijzonder wordt beoogd, is het storten in zee van baggerspecie waarvoor OSPAR een uitzondering heeft gemaakt op de algemene regel "alle stortingen in zee zijn verboden" (zie OSPAR-Verdrag, Bijlage II over de voorkoming en uitschakeling van verontreiniging door storting of verbranding). Het algemene doel van de opdracht is het bestuderen van de cohesieve sedimenten op het Belgisch Continentaal Plat (BCP) en dit met behulp van zowel numerieke modellen als het uitvoeren van metingen. De combinatie van monitoring en modellering zal gegevens kunnen aanleveren over de transportprocessen van deze fijne fractie en is daarom fundamenteel bij het beantwoorden van vragen over de samenstelling, de oorsprong en het verblijf ervan op het BCP, de veranderingen in de karakteristieken van dit sediment ten gevolge van de bagger- en stort-operaties, de effecten van de natuurlijke variabiliteit, de impact op het mariene ecosysteem in het bijzonder door de wijziging van habitats, de schatting van de netto input van gevaarlijke stoffen op het mariene milieu en de mogelijkheden om deze laatste twee te beperken.

Een samenvatting van de resultaten uit de vergunningsperioden 2017-2021 kan gevonden worden in het "Vooruitgangsrapport (juni 2019) over de effecten op het mariene milieu van baggerspeciestortingen" (Lauwaert et al. 2019) dat gepubliceerd werden conform art. 10 van het K.B. van 12 maart 2000 ter definiëring van de procedure voor machtiging van het storten in de Noordzee van bepaalde stoffen en materialen.

## 1.2. Algemene doelstellingen

Het onderzoek kadert in de algemene doelstellingen om de baggerwerken op het BCP en in de kusthavens te verminderen en om een gedetailleerd inzicht te verwerven van de fysische processen die plaatsvinden in het mariene kader waarbinnen deze baggerwerken worden uitgevoerd. Dit impliceert enerzijds beleidsondersteunend onderzoek naar de vermindering van de sedimentatie op de baggerplaatsen en het evalueren van alternatieve stortmethoden. Anderzijds is onderzoek naar knelpunten voor het plannen en schatten van de effecten van de baggerwerken vereist. Dit is specifiek gericht op het dynamische gedrag van slib in de waterkolom en op de bodem en zal uitgevoerd worden met behulp van modellen en in situ metingen. De specifieke acties die binnen dit onderzoek uitgevoerd worden om de algemene doelstellingen in te vullen zijn:

**1. Streven naar een efficiënter stortbeleid** door een optimalisatie van de stortlocaties.

**2. Continue monitoring van het fysisch-sedimentologische milieu** waarbinnen de baggerwerken worden uitgevoerd (Taak 1) en aanpassing van de monitoring aan de nog op te stellen targets voor het bereiken van de goede milieutoestand (GES), zoals gedefinieerd zal worden binnen MSFD;

**3. Uitbouw en optimalisatie van het numerieke modelinstrumentarium**, ter ondersteuning van het onderzoek (Taak 2.1).

## 1.3. Specifieke doelstellingen voor 2017-2021

Voor de vergunningsperiode 2017-2021 werden volgende taken voorzien:

1) In situ en remote sensing metingen en data-analyse

De monitoring van effecten van baggerspeciestortingen gebeurd met behulp van een vast meetstation in de nabijheid van MOW1, en met meetcampagnes met de RV Belgica (een 4-tal meetcampagnes voor het verzamelen van traject informatie, profielen en de calibratie van sensoren; en een 10-tal campagnes voor het onderhoud van het meetstation te MOW1). De geplande monitoring is gericht op het begrijpen van processen, zodoende dat de waargenomen variabiliteit en de effecten van baggerspeciestortingen in een correct kader geplaatst kunnen worden. Een belangrijk deel is daarom gericht op zowel het uitvoeren van de in situ metingen, het garanderen van kwalitatief hoogwaardige data en het archiveren, rapporteren en interpreteren ervan. Remote sensing data afkomstig van onder andere satellieten worden gebruikt om een ruimtelijk beeld te bekomen.

2) Uitbouw en optimalisatie van het modelinstrumentarium

Het tijdens de voorbije jaren verbeterde en aangepaste slibtransportmodel zal verder worden ontwikkeld. Dit zal parallel gebeuren met de nieuwe inzichten die voorvloeien uit de metingen en de procesgerichte interpretatie van de metingen.

3) Ondersteunend wetenschappelijke onderzoek

Monitoring gebaseerd op wetenschappelijke kennis is essentieel om de effecten van menselijke activiteiten (hier het storten van baggerspecie) te kunnen inschatten en beheren. Om te kunnen voldoen aan de door OSPAR opgelegde verplichtingen van monitoring en evaluatie van de effecten van menselijke activiteiten is het ontwikkelen van nieuwe monitorings- en modelleractiviteiten nodig. Dit houdt in dat onderzoek dat de actuele stand van de wetenschappelijke kennis weerspiegelt wordt uitgevoerd en dat de hieruit voortvloeiende nieuwe ontwikkelingen geïntegreerd zullen worden in zowel de verbetering van het modelinstrumentarium als voor het beter begrijpen van het fysisch milieu.

## 1.4. Onderzoek Januari 2019 – December 2021

Het onderzoek uitgevoerd tijdens de periode 2017-2018 werd gerapporteerd in Fettweis et al. (2017, 2018a, 2018b, 2019). Voor de periode 2019-2021 werd in overleg met de ambtelijke werkgroep baggeren een nieuw takenpakket opgesteld waarbij rekening gehouden werd met de aanbevelingen voor de minister ter ondersteuning van de ontwikkeling van een versterkt milieubeleid zoals geformuleerd in het “Syntheserapport over de effecten op het mariene milieu van baggerspeciestortingen (2016)” dat uitgevoerd werd conform art. 10 van het K.B. van 12 maart 2000 ter definiëring van de procedure voor machtiging van het storten in de Noordzee van bepaalde stoffen en materialen.

### Taak 1: In situ en remote sensing metingen en data-analyse

#### Taak 1.1 Langdurige metingen

Sinds eind 2009 worden er continue metingen uitgevoerd te MOW1 met behulp van een meetframe (tripode). Met dit frame worden stromingen, slibconcentratie, korrelgroottever-deling van het suspensiemateriaal, saliniteit, temperatuur, waterdiepte en zeebodem altimetrie gemeten. Om een continue tijdreeks te hebben, wordt gebruik gemaakt van 2 tripodes. Na ongeveer 1 maand wordt de verankerde tripode voor onderhoud aan wal gebracht en wordt de tweede op de meetlocatie verankerd. Op de meetdata wordt een kwaliteitsanalyse uitgevoerd, zodat de goede data onderscheiden kunnen worden van slechte of niet betrouwbare data.

#### Taak 1.2 Calibratie van sensoren tijdens in situ metingen

Tijdens 11 meetcampagnes per jaar met de R/V Belgica zullen een 13-uursmetingen uitgevoerd worden met doel het calibreren van optische of akoestische sensoren en het verzamelen van verticale profielen. De metingen zullen plaatsvinden in een drietal punten gelegen op het BCP (zie Taak 3.1). De optische metingen (Optical Backscatter Sensor) zullen gecalibreerd worden met de opgemeten hoeveelheid materie in suspensie (gravimetrische bepalingen na filtratie) om te komen tot massa concentraties. Naast de totale hoeveelheid

aan suspensiemateriaal (SPM) wordt ook de concentratie aan POC/PON, chlorofyl (Chl-a, Chl-b), phaeofytine (a, b) en Transparante Exopolimerische Partikels (TEP) bepaald. Stalen van suspensiemateriaal zullen genomen worden met de centrifuge om de samenstelling ervan te bepalen.

### Taak 1.3: Data archivering en rapportage

De meetdata worden gearchiveerd en er wordt een kwaliteitsanalyse uitgevoerd, zodat de goede data onderscheiden kunnen worden van slechte of niet betrouwbare data. Slechte data kunnen bv optreden doordat het instrument slecht heeft gewerkt en verkeerd werd ingesteld. Niet betrouwbare data zijn typisch geassocieerd met bv biofouling. De data en metadata worden gearchiveerd.

### Taak 1.4: Verwerking en interpretatie van metingen

De metingen vergaard tijdens de 13-uursmetingen aan boord van de Belgica en met de tripode worden verwerkt en geïnterpreteerd. Hiervoor werden in het verleden reeds heel wat procedures (software) toegepast of ontwikkeld, zoals de berekening van de bodemschuifspanning uit turbulentiemetingen, entropieanalyse op partikelgrootteverdelingen, de opsplitsing van multimodale partikelgrootteverdeling in een som van lognormale verdelingen, het groeperen van de data volgens getij, meteorologie, klimatologie en seizoenen. Deze methodes (zullen opgenomen worden) zijn opgenomen in de standaardverwerking van de data. De aldus verwerkte data dienen als basis voor het verder gebruik binnenin wetenschappelijke vragen (zie taak 2.2, 2.3 en 4.2, 4.4).

## Taak 2: Uitbouw en optimalisatie van het modelinstrumentarium

### Taak 2.1: Opstellen van een slibtransportmodel voor het BCP met Coherens V2

Ondertussen is de nieuwe implementatie van het Noordzeemodel (inclusief een submodel van de Belgische kustzone) gerealiseerd voor de hydrodynamica. In een volgende fase zal op basis van dit model het slibtransportmodel worden geïmplementeerd en gevalideerd. Verdere ontwikkelingen aan het model parallel met nieuwe inzichten die voorvloeien uit de metingen en de procesgerichte interpretatie van de metingen zullen worden geïmplementeerd in het model.

### Taak 2.2: Validatie van het slibtransportmodel voor het jaar 2013 (stortproef)

Een eerste toepassing van het model kan het jaar 2013 zijn, waarin de terreinproef voor alternatieve stortplaats alsook een intensieve monitoring plaatsvond. Deze laatste zal gebruikt worden voor de validatie van het model.

## Taak 3: Ondersteunend wetenschappelijk onderzoek

Monitoring gebaseerd op wetenschappelijke kennis is essentieel om de effecten van menselijke activiteiten (hier het storten van baggerspecie) te kunnen inschatten en beheren. Om te kunnen voldoen aan de door OSPAR opgelegde verplichtingen van monitoring en evaluatie van de effecten van menselijke activiteiten is een verdere implementatie van huidige en het ontwikkelen van nieuwe monitoringsactiviteiten nodig. Meer specifiek gericht op de activiteit 'storten van baggerspecie' worden hier – wat het fysische milieu betreft - turbiditeit, samenstelling van de zeebodem, bathymetrie en hydrografische condities beoogt. Deze taak speelt hierop in door de ontwikkeling en de implementatie van nieuwe tools die de actuele stand van de wetenschappelijke kennis weerspiegelen teneinde de mathematische modellen te optimaliseren en verfijnen.

### Taak 3.1: Intensieve bio-geo-chemische monitoring van het SPM in de overgangszone kust – offshore in 2019

Een sleutelelement in het functioneren van kustnabije ecosystemen is de aanwezigheid van biotische en abiotische partikels. Verticale en dus ook horizontale fluxen van particulair suspensiemateriaal (verder afgekort als SPM) worden bepaald door hun valsnelheid, die afhangt van de capaciteit van de deeltjes om te flocculeren. Flocculatie beïnvloed de grootte van de gesuspendeerde deeltjes en bepaald daardoor ook de depositie van het slib in onder andere havens en vaargeulen. Op zijn beurt wordt flocculatie gestuurd door turbulentie, SPM concentratie en de oppervlakte eigenschappen van de deeltjes, die van elektrochemische of

biologische oorsprong kunnen zijn.

SPM bestaat uit minerale deeltjes van fysicochemische (b.v. kleimineralen, kwarts, veldspaat) en biogene oorsprong (b.v. calciet, aragoniet, opaal), levend (bacteriën, fyto- en zoöplankton) en niet-levend organisch materiaal (b.v. fecale pellets, detritus, exopolymeren), en partikels van menselijke oorsprong (microplastiek). Het SPM kan door hydrofobe organische polluenten of metalen gecontamineerd zijn. De samenstelling en concentratie van het SPM inclusief de hydrofobe polluenten en de metalen verandert in functie van de tijd en de locatie. Deze variaties worden beïnvloed door de interacties tussen de fysische processen (getij, meteo, klimaat), biologische cycli (algenbloei), chemische processen (koolstofcyclus) en menselijke activiteiten (aanvoer van nutriënten en polluenten, bagger- en stortactiviteiten, offshore constructies). Het doel van deze taak is om een integrale monitoring uit te voeren in 2019 van de belangrijkste parameters die betrokken zijn bij de SPM-dynamica.

Een nieuw geïntegreerd monitoringsprogramma zal worden opgezet in vier stations (MOW1, W03, W05, W08), zie Figuur 1.1. Deze stations worden aanzien als zijnde representatief voor de belangrijkste gradiënten vanaf de kustzone (invloed van de Schelde) naar offshore (invloed van het Engels Kanaal) en zullen maandelijks bemonsterd worden. Gedurende 13 uur zullen om het uur waterstalen genomen worden aan de oppervlakte en bodem in stations MOW1, W05 en W08. De monitoring bevat alle parameters die nu reeds worden bepaald (maar niet noodzakelijk samen) op waterstalen (SPM, POC/PON, DOC/DON, Chl, TEP, nutriënten, pH) en met behulp van sensoren (CTD, OBS, ABS, LISST), en zullen aangevuld worden met Chl in sedimenten, de hydrofobe chemische polluenten (b.v. PAHs, PCBs) Verder wordt een monitoring voorzien van fysische parameters (ADCP/tripode) in de stations W05 en W08.

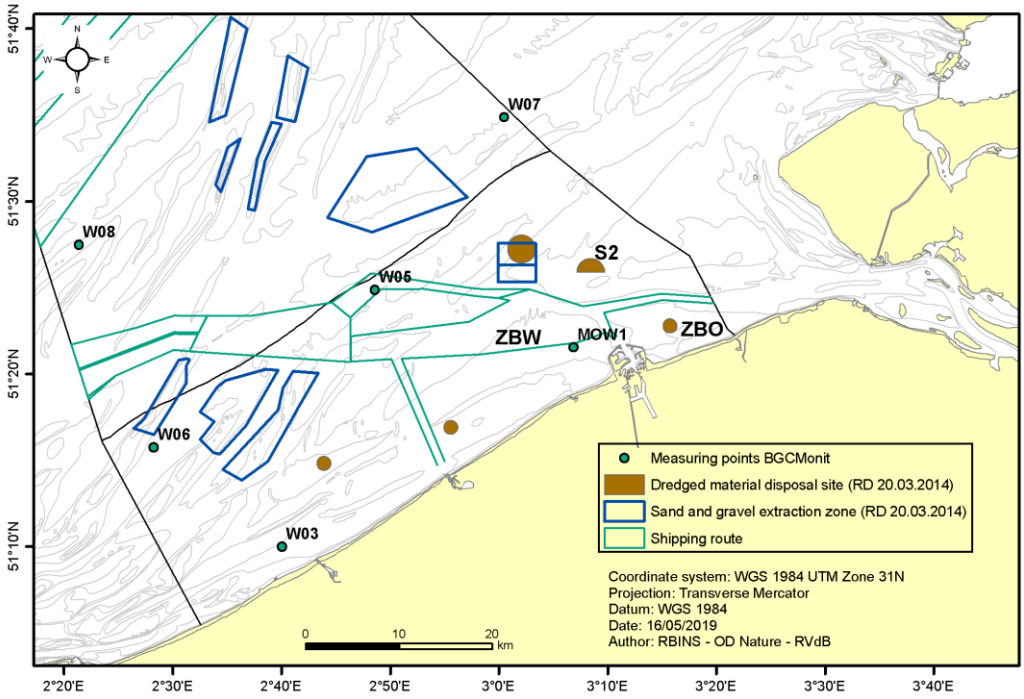


*Figuur 1.1: BGC-monitoringstations MOW1, W03, W05 en W08.*

Door de verschillende monitoringsactiviteiten van OD Natuur/BMM (MOMO, WFD, MSFD, OSPAR en satellietvalidatie) te combineren en de monitoringsfrequentie en stations aan te passen worden de inspanningen geoptimaliseerd, blijven de legale verplichtingen en validatieprotocollen verzekerd, komen state-of-the-art wetenschappelijke vragen aan bod en wordt een bevattelijk dataset bekomen die alle gemeten parameters met elkaar verbindt. Na een eerste jaar van intensieve monitoring in 2019 zal het staalname schema geëvalueerd worden voor alle parameters om aldus tot een kwalitatieve sprong in monitoringsstrategie te komen die tijdsgebonden veranderingen, invariante eigenschappen en ruimtelijke gradiënten kan identificeren. De belangrijkste wetenschappelijk vragen die aan de grondslag liggen van deze monitoring zijn:

1. Hoe variëren de fysische, biologisch en chemische parameters in de waterkolom tijdens een getijcyclus en tijdens de seizoenen.
2. Waarom is het kustgebied troebel en wat is hierbij de link met de cross-shore gradiënten in fysische, biologische en chemische parameters.
3. Hoe beïnvloedt de SPM-concentratie de algenbloei (lichtreductie) en vice versa (TEP-productie)? Hoe moet het modelinstrumentarium (flocculatiemodule) worden aangepast om deze seizoenaliteit te kunnen modelleren.
4. Wat is de variabiliteit van de concentratie aan chemische polluenten in het SPM? Hoe beïnvloed de variabiliteit in SPM-concentratie en samenstelling de variabiliteit van de chemische polluenten?
5. Verbetering van remote sensing producten (SPM, Chl) door in situ validatie.

Taak 3.2: Monitoring stortplaats ZBW

De concentratie en samenstelling van het suspensie- en bodemmateriaal zal gemonitoord worden in de nabijheid van de nieuwe stortplaats ZBW. Afhankelijk van de keuze van de stortplaats kan de langdurige meetlocatie MOW1 hiervoor in aanmerking komen of kan een andere locatie gekozen worden als de veiligheid van de meetapparatuur kan gegarandeerd worden. Details hiervan zullen op een vergadering van de technische werkgroep besproken worden.

Taak 3.3: Ondersteuning kader rond Passende Beoordeling van stortactiviteiten

Ondersteuning zal gegeven worden voor het opstellen van de passende beoordeling voor de vergunningsplichtige stortactiviteiten. Dit houdt in het meewerken aan een schriftelijk verslag waarin aan de hand van gemotiveerde argumenten uitgelegd wordt of de Europese natuurwaarden in het vogelrichtlijngebied nabij Zeebrugge al dan niet betekenisvol worden aangetast door het storten van baggerspecie in zee. Meer specifiek zal onderzoek worden uitgevoerd over de verstoring van het eetgedrag van zeevogels door de verhoging van de turbiditeit die gepaard gaat met de baggerspeciestortingen.

Taak 3.4: Trends in SPM concentratie

Om significante statistische trends te kunnen documenteren in SPM concentratie over de laatste decades, zijn kwalitatief hoogstaande metingen nodig die een lange tijdspanne omvatten en over een groot gebied verdeeld zijn. Deze data zijn helaas niet beschikbaar. Wat er wel beschikbaar is zijn de tripode metingen te MOW1 (vanaf 2005) en op andere locaties, de puntmetingen verzamelt met onderzoeksschepen in het Belgisch Deel van de Noordzee sinds ongeveer 1970 (cf. Belspo 4DEMON project) en satellietbeelden (vanaf 1997). De tripode data geven de temporele variabiliteit weer, maar zijn heel beperkt wat ruimtelijke spreiding betreft. De 4DEMON en satellietbeelden zijn beschikbaar over een lange periode en over een groot gebied, maar kunnen de temporele schaal niet oplossen. Om deze heterogene datasets samen te kunnen gebruiken, zal gekeken worden naar de statistische verschillen tussen de datasets en naar een manier om deze te combineren. Doel is om mogelijke trends in de SPM concentratie te identificeren en deze te linken aan natuurlijke veranderingen of aan menselijke activiteiten.

### Taak 4: Rapportage en outreach

Om de zes maanden zal er een activiteitenrapport worden opgesteld dat de onderzoeksresultaten beschrijft. Jaarlijks wordt er een 'factual data' rapport opgesteld van de verzamelde meetgegevens. De resultaten uit het onderzoek zullen tevens worden voorgesteld op workshops, conferenties en in de wetenschappelijke literatuur.

## 1.5. Gerapporteerde en uitgevoerde taken

Periode Januari 2019 – Juni 2019

Taak 1.1: De meetreeks te MOW1 werd verdergezet.

Taak 1.2: Calibratie van OBS sensoren werd uitgevoerd tijdens RV Begica campagnes 2019/01, 2019/03, 2019/07, 2019/11, 2019/14 en 2019/17.

Taak 2.1: Het 2 klassen population balance model van Lee at al. (2011) werd geïmplementeerd in Coherens V2 en gevalideerd met testcases, zie hoofdstuk 3 van dit rapport.

Taak 3.1: Intensieve bio-geochemische monitoring werd uitgevoerd te MOW1 (RV Belgica campagnes 2019/01, 2019/03, 2019/07, 2019/11, 2019/14, 2019/17), W03 RV Belgica campagnes 2019/03, 2019/11, 2019/14, 2019/17), W05 (2019/01, 2019/03, 2019/11, 2019/14, 2019/17) en W08 (2019/01, 2019/03, 2019/14, 2019/17).
De methode voor de TEP-analyse werd opgesteld en gevalideerd, zie hoofdstuk 2 van dit rapport.

## 1.6. Publicaties (januari 2019 – juni 2019)

Hieronder wordt een overzicht gegeven van publicaties met directe betrokkenheid van het KBIN waar resultaten en data uit het MOMO-project in werden gebruikt.


Activiteits-, Meet- en Syntheserapporten

Fettweis M, Baeye M, Francken F, Van den Eynde D. 2019. MOMO activiteitsrapport (1 januari – 30 juni 2019). BMM-rapport MOMO/9/MF/201911/NL/AR/1, 21pp + app.

Lauwaert B, Fettweis M, De Witte B, Van Hoei G, Timmermans S, Hermans L. 2019. Vooruitgangsrapport (juni 2019) over de effecten op het mariene milieu van baggerspeciestortingen (Vergunningsperiode 01/01/2017 – 31/12/2021). RBINS-ILVO-AMT-CD rapport. BL/2019/01, 28pp.

Backers J, Hindryckx K, Vanhaverbeke W. 2019. Rapport van de RV Belgica Meetcampagnes en Verankering van Meetsystemen MOMO – 2018. BMM-rapport BMM-MDO/2019-05/MOMO/2018, 169pp.

Conferenties/Workshops

Shen X, Toorman E, Fettweis M, Lee BJ. 2019. A population balance model for multi-class floc size distributions of cohesive sediments in Belgian coastal zones. EGU, 7-12 April, Vienna (Austria).

Fettweis M. 2019. Schwebstoff in Küstenmeeren – Flockige Fracht in ständigem Wandel: Gut zu sehen und doch schwer genau zu messen. Invited lecture at HZG Institute for Coastal Research, 31 January, Geesthacht (Germany).

Peer reviewed artikels

Fettweis M, Riethmüller R, Verney R, Becker M, Backers J, Baeye M, Chapalain M, Claeys S, Claus J, Cox T, Deloffre J, Depreiter D, Druine F, Flöser G, Grünler S, Jourdin F, Lafite R, Nauw J, Nechad B, Röttgers R, Sotollichio A, Vanhaverbeke W, Vereecken H. 2019. Uncertainties associated with in situ long-term observations of suspended particulate matter concentration using optical and acoustic sensors. Progress in Oceanography, 178, 102162. doi:10.1016/j.pocean.2019.102162

Montereale-Gavazzi G, Roche M, Degrendele K, Lurton X, Terseleer N, Baeye M, Francken F, Van Lancker V. 2019. Insight into short term tidal variability of multibeam backscatter from field experiments on different seafloor types. Geosciences 2019, 9, 34; doi:10.3390/geosciences9010034

Shen X, Toorman EA, Lee BJ, Fettweis M. 2019. Effects of aquatic biofilms on flocculation processes of cohesive sediments: A modeling approach. Journal of Geophysical Research, 124, 4098-4116. doi:10.10290/2018JC014493

Thesis, eindwerk

Demilde C. 2019. Analyse van transparante exopolymeerpartikels (TEP) optimaliseren en valideren. Bachelorproef, Bachelor in de Agro- en Biotechnologie, Afstudeerrichting Biotechnologie, VIVES Hogeschool, 66pp + bijlagen

# 2. Methodeontwikkeling en validatie TEP-analyse

Transparante exopolymeer partikels (TEPs) zijn een alomtegenwoordig bestanddeel van het organisch materiaal (OM) in aquatische milieus (Passow, 2002). Het zijn extrapolymere substanties (EPS) met een gel-achtige structuur en specifieke eigenschappen zoals transparantie, kleverigheid en flexibiliteit (Zhou et al., 1998; Passow, 2001; Passow, 2002; Mari & Robert, 2008). EPS zijn nano-gels van enkele nm groot, en maken deel uit van het opgeloste OM. EPSs zijn de voorlopers van TEPs. EPSs kunnen via abiotische en biotische processen gevormd worden. Een groot deel van de EPSs in natuurlijke omgevingen wordt door microalgen geproduceerd (Passow, 2001; Engel & Passow, 2001; Bar-Zeev et al., 2009). TEPs ontstaan door coagulatie en gelvorming van de draadvormige nano-gels (Passow, 2000).

TEPs zijn belangrijk omdat zij de vlokgrootte van het particulair suspensiemateriaal (SPM) kunnen veranderen en dus een invloed hebben op het transport van fijnkorrelige sedimenten. Het proces dat hierbij optreedt noemt men flocculatie. Flocculatie omvat zowel de processen van groei van de partikelgrootte als het opbreken ervan in kleinere bestanddelen ten gevolge van turbulentie in de waterkolom. Hierdoor wordt zowel de grootte als de valsnelheid van het suspensiemateriaal beïnvloed. Flocculatie zorgt ook ervoor dat biomassa en minerale deeltjes gecombineerd worden in grotere aggregaten met dikwijls een multimodale partikelgrootte-verdeling (PGV) en verschillende vloksterktes (Verney et al. 2009, Lee et al. 2012; Fettweis et al. 2014). Flocculatie hangt af van de aantrekkingskrachten die ingrijpen op de partikels. De microbiologische producten bestaan uit kleverige organische partikels (TEPs), die interageren met de minerale deeltjes en de eigenschappen van het SPM kunnen veranderen (Passow et al. 2001). In kustnabije zones is het SPM vooral samengesteld uit minerale partikel en de aanwezigheid van het organisch materiaal fungeert als een bijkomend bindingsmiddel (Hamm 2002; Fettweis et al. 2006; Maggi 2009; Bainbridge et al. 2012). Tijdens een algenbloei verhoogd de flocculatiecapaciteit (Chen et al. 2005; Fettweis et al., 2014; Fettweis & Baeye 2015; Lee et al. 2012, 2017; van der Lee 2000), wat verklaard wordt door de aanwezigheid van TEPs. Tot op heden werd er voor de Belgische kustzone nog niet bepaald hoe hoog de TEP-concentratie is en hoe deze varieert tijdens een jaar.

Een eerste kwantitatieve methode om TEPs te analyseren werd in 1993 voorgesteld door Aldredge et al. (1993), een meer praktische methode werd later ontwikkeld door Passow en Aldredge (1995). De Passow en Alldredge methode werd hierna nog tal van keren aangepast en alternatieve methoden werden ontwikkeld, met als doel de betrouwbaarheid, reproduceerbaarheid en eenvoudigheid te optimaliseren (zie Discart et al. 2015 voor een vergelijkend overzicht). Niettemin blijft het moeilijk om TEP nauwkeurig te kwantificeren. Deels is dit het gevolg van de eigenschappen van deze partikels. TEP is een soort microgel en de grootte en vorm van de deeltjes is sterk variabel als er lichte veranderingen optreden in de fysische en chemische parameters (Verdugo 2012). Anderzijds is dit te wijten aan de gebruikte methode. Discart et al. (2015) benadrukken dat niet enkel de verscheidenheid aan procedures in de verschillende methodes een effect heeft op de TEP-bepaling, maar ook de notie van wat TEPs zijn. Uit dit kort overzicht blijkt dus dat het heel belangrijk is om een gestandaardiseerde en gevalideerde procedure te hebben voor TEP-bepaling.

## 2.1. Methode

De methode die door ons wordt toegepast is gebaseerd op de Passow & Alldredge (1995) methode waarin TEPs gedefinieerd worden als deeltjes die op 0.4 µm polycarbonaat filter blijven liggen en die gekleurd kunnen worden met Alciaan Blauw (AB). TEP-concentraties kunnen niet rechtstreeks worden gemeten. Ze worden bepaald ten opzichte van oplossingen van een polysacharide met gekende concentraties, met name xanthangom (XG). De standaardoplossing XG moet gecalibreerd worden omdat AB-oplossingen niet stabiel zijn.

Een eerste methode die wij toegepast hebben voor het opstellen van een ijklijn, was gebaseerd op Claquin et al. (2008), maar er kon geen goede reproduceerbare resultaten voor de aanmaak van de standaardoplossing XG bekomen worden. Verschillende manieren (oplossen in water, oplossen in ethanol, ultrasoon bad, ultramixer) en combinaties ervan werden uitgetest voor de aanmaak van een standaardoplossing, zonder echter goede resultaten te bekomen.

Vervolgens werd contact opgenomen met de UGent waar eenzelfde analyse wordt

uitgebvoerd. Daar wordt voor de aanmaak van een ijklijn geen XG-standaardoplossing gebruikt, maar wordt de XG afgewogen en rechtstreeks gekleurd met Alciaan Blauw (AB) als stockoplossing. Deze methode is gebaseerd op Nosaka et al. (2017), het resultaate was succesvol (zie Tabel 2.1, Figuur 2.1). De vergelijking uit deze grafiek werd gebruikt om alle concentraties in dit verslag te bepalen. Er werd ook rekening gehouden met het volume zwavelzuur dat toegevoegd wordt om de kleuromslag te bekomen (6 ml).

*Tabel 2.1. Verdunningsreeks van XG gebonden aan Alciaan Blauw opgelost in 80% $H_2SO_4$.*

| Concentratie (µg/ml) | 5 | 10 | 25 | 50 | 100 | 150 | 250 |
|---|---|---|---|---|---|---|---|
| Absorbantie | 0,021 | 0,032 | 0,080 | 0,158 | 0,342 | 0,520 | 0,879 |

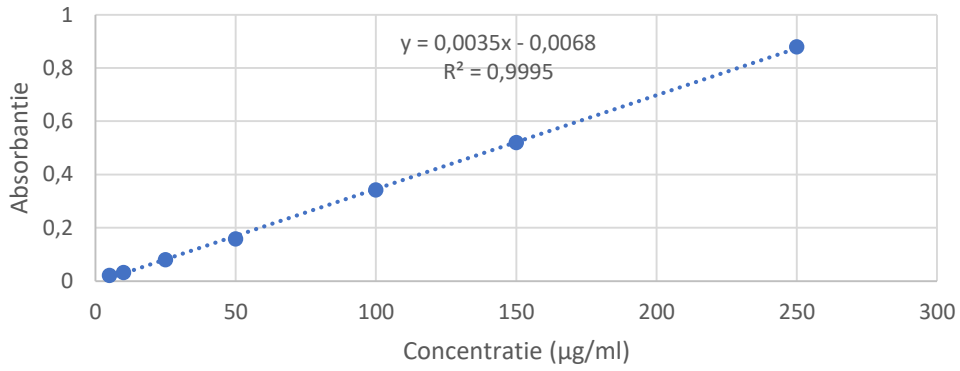


*Figuur 2.1: Absorbantie ijklijn en lineaire regressievergelijking voor een Alciaan Blauw stockoplossing.*

## 2.2. Validatie

### *2.2.1. Residuele standaardafwijking*

De residuele standaardafwijking wordt gebruikt om de afwijking tussen de standaarddeviatie van de werkelijke waarden en de theoretische waarden te beschrijven. Figuur 2.2 toont dat de experimenteel gemeten waarde en de berekende waarde willekeurig verdeeld zijn.

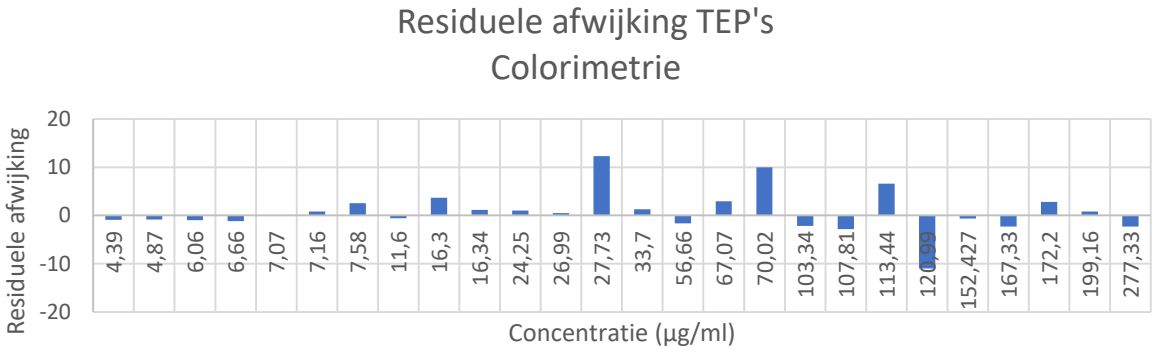


*Figuur 2.2: Residuele afwijking TEPs.*

### *2.2.2. Detectie- en bepalingsgrens*

De detectiegrens is bepaald door een oplossing met een lage concentratie (blanco= ultra puur water) in 8-voud te analyseren (onder reproduceerbaarheidscondities). Alle blanco's werden op één dag gefilterd en gekleurd met AB. Op verschillende tijdstippen werden de filters geanalyseerd. Van deze analyseresultaten is de standaarddeviatie bepaald (Tabel 2.2).

### *2.2.3. Herhaalbaarheid*

De herhaalbaarheid werd bepaald door een waterstaal van de haven van Oostende te analyseren. Dit werd gedaan onder herhaalbaarheidscondities in 8-voud en op dezelfde dag.

De waterstalen werden gefilterd, gekleurd en geanalyseerd op één dag (11/04/'19). Van deze analyseresultaten (Tabel 2.3) zijn het gemiddelde, standaarddeviatie en herhaalbaarheid berekend. De relatieve standaarddeviatie moet lager zijn dan 10% om een goede herhaal-baarheid aan te tonen. Dit werd vooraf vastgelegd. Er werd een relatieve standaarddeviatie bekomen van 8,5% (Tabel 2.3).

*Tabel 2.2: Waarden voor berekening bepalings- en detectiegrens. De blanco's werden gefilterd en gekleurd op 10/10/'19.*

| blanco | absorbantie | µg XG/ml | conc µg XG/ml |
|---|---|---|---|
| 11/04/'19 | 0,026 | 7,44 | 0,89 |
| 12/04/'19 | 0,024 | 6,86 | 0,82 |
| 15/04/'19 | 0,029 | 8,29 | 1,00 |
| 16/04/'19 | 0,029 | 8,29 | 1,00 |
| 17/04/'19 | 0,024 | 6,86 | 0,82 |
| 18/04/'19 | 0,026 | 7,44 | 0,89 |
| 19/04/'19 | 0,026 | 7,44 | 0,89 |
| 23/04/'19 | 0,025 | 7,15 | 0,86 |

| gem. (µg XG/ml) | SD (µg XG/ml) | RSD (%) | n |
|---|---|---|---|
| 0,90 | 0,07 | 7,49 | 8 |
| Detectiegrens: | | 3 x SD | 0,20 |
| Bepalingsgrens: | | 6 x SD | 0,40 |

*Tabel 2.3: Waarden voor berekening herhaalbaarheid.*

| | Absorbantie | *µg XG/ml | **conc µg XG/ml | *** conc – blanco (0.94 µg XG/ml) |
|---|---|---|---|---|
| 1 | 0.060 | 17,15 | 2,06 | 1,11 |
| 2 | 0.061 | 17,44 | 2,09 | 1,15 |
| 3 | 0.059 | 16,86 | 2,02 | 1,08 |
| 4 | 0.061 | 17,44 | 2,09 | 1,15 |
| 5 | 0.064 | 18,29 | 2,20 | 1,25 |
| 6 | 0.060 | 17,15 | 2,06 | 1,11 |
| 7 | 0.068 | 19,44 | 2,33 | 1,39 |
| 8 | 0.061 | 17,44 | 2,09 | 1,15 |

| gem. (µg XG/ml) | SD (µg XG/ml) | RSD (%) | n |
|---|---|---|---|
| 1,17 | 0,10 | 8,51 | 8 |

### *2.2.4. Reproduceerbaarheid*

De reproduceerbaarheid is bepaald door een waterstaal van de haven van Oostende te analyseren. Dit werd gedaan onder reproduceerbaarheidscondities in 8- voud. De waterstalen werden gefilterd en gekleurd op één dag en daarna op verschillende dagen geanalyseerd (Tabel 2.4). De relatieve standaarddeviatie moet lager zijn dan 20% om een goede reproduceerbaarheid aan te tonen. Dit werd vooraf vastgelegd. Er werd een relatieve standaarddeviatie bekomen van 16% (Tabel 2.4), de maximaal toegestane spreiding tussen 2 metingen van hetzelfde staal werd vastgelegd op 20%.

### *2.2.5. Terugvinding*

Testen werden uitgevoerd om de terugvinding te bepalen, hiervoor werden stalen gespiked met een gekende hoeveelheid XG en geanalyseerd zoals normale stalen maar hiervoor werden geen goede resultaten bekomen, bijkomende testen moeten uitgevoerd worden.

*Tabel 2.4: Waarden voor berekening reproduceerbaarheid.*

| Analyse op: | Absorbantie | *µg XG/ml | **conc µg XG/ml | *** conc - blanco |
|---|---|---|---|---|
| 11/04/'19 | 0.060 | 17,15 | 2,06 | 1,11 |
| 12/04/'19 | 0.071 | 20,29 | 2,44 | 1,49 |
| 15/04/'19 | 0.065 | 18,58 | 2,23 | 1,29 |
| 17/04/'19 | 0.062 | 17,72 | 2,13 | 1,18 |
| 18/04/'19 | 0.054 | 15,44 | 1,85 | 0,91 |
| 19/04/'19 | 0.065 | 18,58 | 2,23 | 1,29 |
| 23/04/'19 | 0.066 | 18,86 | 2,26 | 1,32 |
| 24/04/'19 | 0.056 | 16,01 | 1,92 | 0,98 |

| SD (µg XG/ml) | RSD (%) | n |
|---|---|---|
| 0,19 | 16,00 | 8 |

### *2.2.6. Robuustheid*

Om de robuustheid te bepalen werden achtereenvolgens blanco, waterstaal, blanco, waterstaal enzoverder gefiltreerd en geanalyseerd. De blanco's zijn ultrapuur water en de waterstalen zijn afkomstig van de haven van Oostende. De resultaten van de verschillende blanco's en waterstalen werden vergeleken met elkaar. Van deze analyseresultaten zijn het gemiddelde, standaarddeviatie en herhaalbaarheid berekend voor zowel blanco's als waterstalen. De relatieve standaarddeviatie voor de blanco's (ultrapuur water) bedraagt 5,57% (Tabel 2.5). De relatieve standaarddeviatie voor de waterstalen (haven Oostende) bedraagt 10,98% (Tabel 2.5). Deze relatieve standaarddeviaties zijn vergelijkbaar met de relatieve standaarddeviatie van herhaalbaarheid, nl 8.51% (Tabel 2.3).

*Tabel 2.5: Waarden robustheidsbepaling.*

| | Absorbantie | *µg XG/ml | **conc µg XG/ml | ***conc - blanco |
|---|---|---|---|---|
| Blanco | 0,04 | 11,15 | 1,34 | |
| Waterstaal | 0,10 | 28,58 | 3,43 | 2,09 |
| Blanco | 0,04 | 10,86 | 1,30 | |
| Waterstaal | 0,11 | 30,58 | 3,67 | 2,33 |
| Blanco | 0,04 | 10,01 | 1,20 | |
| Waterstaal | 0,12 | 32,86 | 3,94 | 2,61 |

| | gem. (µg XG/ml) | SD (µg XG/ml) | RSD (%) | n |
|---|---|---|---|---|
| Blanco: | 1,28 | 0,07 | 5,57 | 3 |
| Waterstaal | 2,34 | 0,26 | 10,98 | 3 |

## 2.3. Meetonzekerheid

De onzekerheid op de juistheid kan, afhankelijk van de beschikbare gegevens, op drie verschillende methoden berekend worden, met name via inter-laboratorium experimenten, via CRM's (= certificeert referentiemonster) of via spiking – terugvindbaarheid. Deze methoden kunnen hier niet toegepast worden omdat er geen geaccrediteerde inter-laboratorium experimenten mogelijk zijn voor TEP's. Er bestaan ook geen CRM's. De laatste methode is via spiking – terugvindbaarheid maar deze methode is onsuccesvol gebleken (zie paragraaf 2.2.5). Er werd daarom gekozen om de gecombineerde en de uitgebreide meetonzekerheid te bepalen.

De gecombineerde meetonzekerheid wordt berekend aan de hand van de volgende formule:

$$u_c = \sqrt{u_{bias}^2 + (ur_w)^2}$$

waarbij $u_c$ de gecombineerde meetonzekerheid is, $u_{bias}$ de onzekerheid op de juistheid en $ur_w$ de onzekerheid op de intra-laboratorium reproduceerbaarheid. De %bias (dit is het verschil tussen de gemeten waarde en de werkelijk waarde) werd berekend.

$$bias\% = \frac{\overline{x} - x_{ref}}{x_{ref}} 100$$

De bias werd berekend aan de hand van waarden die bekomen werden voor de parameter reproduceerbaarheid. Deze bedragen 2,39 %. Op basis van de %bias en de relatieve standaarddeviatie voor reproduceerbaarheid werd de gecombineerde meetonzekerheid bepaald. Er werd een gecombineerde meetonzekerheid bekomen van ±16 %.

$$U = 2u_c$$

waarin U de uitgebreide meetonzekerheid is. De uitgebreide meetonzekerheid is ±32%.

## 2.4. Besluit

De meetonzekerheid kon niet bepaald worden via; inter-laboratorium experimenten, CRM's, spiking – terugvindbaarheid. Daarom werd er gekozen om de gecombineerde meetonzekerheid te bepalen op basis van de bias% en de standaarddeviatie van de reproduceerbaarheid. Er werd een gecombineerde meetonzekerheid van +- 16% bekomen. Hieruit werd er een uitgebreide meetonzekerheid bekomen van ±32%.

Er is een foutmarge van ±32% op de waarden die bekomen werden. Dit is een geschatte waarden omdat de recovery niet bepaald kon worden.

Er werden stalen uitgewisseld tussen Ecochem (KBIN) en de UGent om zo zelf een inter-labo experiment op te zetten. De resultaten hiervan zijn nog niet beschikbaar.

# 3. Test cases voor het flocculatiemodel

Turbiditeit in de waterkolom is vooral bepaald door de aanwezigheid van suspended particulate matter (SPM). Het beter begrip van de sedimentdynamica en van de biochemische functies van het SPM is van groot belang, aangezien deze een belangrijke rol spelen in de functionering van pelagische en benthische ecosystemen, zowel in de kustzone als op het continentale plat (e.g. Maerz et al., 2016). De variatie van SPM concentratie in een gebied bepaalt mee de diepte van de euphotische laag (Capuzzo et al., 2015) en de diversiteit en de functionering van benthische gemeenschappen (Van Hoey et al., 2005). De bepaling en modellering van de SPM-concentratie is dan ook van groot belang.

Een belangrijk deel van de cohesieve partikels in de waterkolom bestaan uit vlokken, die in grootte, compositie en densiteit variëren in tijd en plaats (Eisma & Kalf 1987; Van Leussen 1994). SPM bestaat immers uit anorganisch en organische deeltjes, die interageren met de omgeving en grotere vlokken vormen onder de invloed van fysische, biologische en chemische factoren (Droppo 2001; Manning et al. 2006; Jago et al. 2007; Tan et al. 2012). Flocculatie bepaalt ook de valsnelheid van het materiaal in de waterkolom en dus de benedenwaartse flux en depositie van sedimenten (Winterwerp 1998). Een goed begrip en modellering van de valsnelheid en van de flocculatie is dan ook van groot belang.

## 3.1. Modellering

Voor het beheer van de bagger- en relocatie-activiteiten is de numerieke modellering van essentieel belang. Numerieke modellering laat toe om de processen goed te begrijpen en om tot een goed beheer te komen van de activiteiten, door het simuleren van verschillende scenario's. Tot nu toe vooral werd gebruik gemaakt van het twee-dimensionale mu-STM model (Fettweis & Van den Eynde 2003; 2006a). Een validatie van dit model werd uitgevoerd met behulp van langdurige tijdreeksen en satellietgegevens in Fettweis et al. (2007a, 2007b, 2007c, 2008b). Het model werd toegepast om de efficiëntie van een alternatieve stortplaats te Zeebrugge Oost te evalueren (zie Fettweis et al. 2009b; 2010a; 2011). Een semi-operationeel model voor de voorspelling van de dispersie van baggerspecie werd ontwikkeld op basis van dit mu-SEDIM model (Van den Eynde & Fettweis, 2006).

Recenter werd in het kader van het VLABEL project een sedimenttransportmodule en een morfologische module ontwikkeld voor het COHERENS software (Luyten 2015; Breugem et al. 2011). Dit model combineert zandtransport via bodemtransportformules met een advectie-dispersiemodel voor het transport van cohesief materiaal in de waterkolom. Bovendien is dit model een driedimensionaal model, zodat ook de verdeling van het materiaal over de waterkolom gemodelleerd kan worden.

## 3.2. Modellering van valsnelheid en flocculatie

Aangezien de valsnelheid een cruciale parameters is voor een goede modellering van de sedimentdynamica, werden in Fettweis et al. (2008a) verschillende modellen voor de berekening van de valsnelheid met elkaar vergeleken, gaande van een constante valsnelheid tot valsnelheden die afhankelijk zijn verschillende parameters, zoals de partikelgrootte en SPM concentratie, maar ook de schuifspanning, het getij, de fractale dimensie etc. (Dyer 1989; van Leussen 1994; Van der Lee 2000; Winterwerp 1998; Winterwerp et al. 2006). In deze modellen wordt inherent op een of andere manier rekening gehouden met de flocculatie van het SPM. Sommige modellen zijn eerder empirische, terwijl andere modellen de fysische processen beter beschrijven. Zoals Spearman & Robert (2002) vermelden, zijn deze laatsten niet noodzakelijk nauwkeuriger. De verschillende modellen kunnen redelijke grootte verschillen geven in resultaten. Uit de resultaten bleek dat de deze eenvoudige valsnelheidmodellen niet altijd een voldoende overeenkomst geven met de gemeten valsnelheid.

In Fettweis et al. (2009a) werd daarom een flocculatiemodel geïmplementeerd, dat gebaseerd is op Maggi (2005, 2009), en dat rekening houdt met biologische-fysische processen. Een 1D versie werd ontwikkeld en een 2D versie werd in het MU-STM model geïmplementeerd. Betere overeenkomsten werden bekomen tussen gemeten en gemodelleerde vlokgrotte, maar de calibratie van de parameterwaarden bleek niet eenvoudig. Fettweis et al. (2011) voerde een verder evaluatie van het Maggi-model uit,

tijdens verschillende omstandigheden, nadat het model was gecalibreerd voor rustige weersomstandigheden. De conclusie was dat door het in rekening te brengen van de invloed van golven de resultaten tijdens stormen sterk verbeterd konden worden. Recenter werd een automatische calibratie-procedure toegepast om de calibratie van het flocculatiemodel te verbeteren en de invloed van de verschillende factoren beter te bepalen (Fettweis et al. 2017; Chen et al. 2017). Ook hier bleek een verbetering van de modellering mogelijk door het inrekening brengen van de golven en het transport gedurende stormen. De resultaten bevestigden verder het belang van de sterkte van de vlokken, en van de seizoenale cyclus hiervan, op de grootte en de vorming van de vlokken.

Het Maggi-model maakt echter gebruik van unimodale vlokgrootteverdelingen, zodat de gemeten D50 niet altijd goed kan gemodelleerd worden. Fettweis et al. (2012a; 2012b) en Lee et al. (2012) toonden echter dat in de Belgische kustzone ook multimodale vlokgrootte-verdelingen kunnen worden waargenomen. Er werd dan ook aanbevolen een meer gesofistikeerd model toe te passen, dat multimodale verdelingen kan simuleren. Een goed compromis tussen een betere modellering van het flocculatieproces en een relatief eenvoudige en robuuste methode, met niet te veel calibratieparameters, dat ook in een driedimensionaal numeriek model kan geïmplementeerd worden, werd gevonden in een twee-klasse partikeldistributiemodel (TCPBE), dat gebruikt maakt van elementaire flocculi en van geaggregeerde vlokken (Lee et al., 2011; 2014). Een één-dimensionaal verticaal (1DV) TCPBE model, dat de Navier-Stokes vergelijking met een k-ε turbulentiemodel combineert met een sedimentmassabalansvergelijking, werd geïmplementeerd in het COHERENS model. Het model maakt gebruik van drie gemodelleerde variabelen, namelijk het aantal flocculi, het aantal vlokken en het aantal flocculi in de vlokken, wat de grootte van de vlokken beschrijft. Een advectie-diffusie vergelijking wordt opgelost voor elk van deze variabelen en een source-sink term beschrijft de aggregatie van flocculi tot vlokken en het opbreken van de vlokken tot flocculi. Een belangrijke parameter blijft de fractale dimensie die de vloksterkte beschrijft. Meer informatie is te vinden in Fettweis et al. (2013). Enkele eerste testen met dit model worden in hetzelfde rapport beschreven. Het model laat toe om op een meer systematische manier studies uit te voeren over de flocculatie van cohesieve sedimenten.

Recent werd de implementatie gecorrigeerd en gecontroleerd en werd een beschrijving van dit flocculatiemodel opgenomen in de officiële COHERENS V2 manual. In Appendix 1 is een beschrijving van dit model, zoals het in de gebruikershandleiding is opgenomen, weergegeven. Merk op dat het model op het ogenblik niet kan gebruikt worden in combinatie met bodemtransportmodel of met de morfologische module en dat het enkel in ééndimensionale (1DV) of driedimensionale mode kan gebruikt worden.

## 3.3. Test cases

Twee test cases werden ontwikkeld voor het testen van het flocculatiemodel. In het *flocvprof* testcase wordt het flocculatiemodel getest met een één-dimensionale simulatie met een diepte van 4.25 m en 20 verticale lagen. De invloed van verschillende parameters voor het flocculatiemodel worden onderzocht. In de testcase *flocest* wordt het flocculatiemodel toegepast op een estuarine configuratie.
De beschrijving en de resulaten van deze twee test cases worden gegeven in Appendix 2.

# 4. Variaties van de zeebodemsamenstelling in de Belgische kustzone

Om te kunnen verzekeren dat antropogene activiteiten, zoals bagger- en stortoperaties, uitgevoerd worden in overeenstemming met internationale overeenkomsten en gebeuren op een duurzame manier, is een goed begrip nodig van de complexe processen die zich in het benthische laag afspelen (Fettweis et al., 2011, 2016). Vroeger onderzoek heeft aangetoond dat onder bepaalde omstandigheden vloeibare sliblagen zich kunnen vormen ter hoogte van het meetstation MOW1 (Fettweis et al., 2010b). In een studie gebaseerd op de duale echosoundings van de RV Belgica werd het voorkomen van vloeibare sliblagen geanalyseerd in twee locaties, met name MOW1 en de haven van Zeebrugge (Nelson, 2015). Belangrijkste conclusies uit deze dataset zijn dat er een significant geografisch variatie optreedt in de dikte van de vloeibare sliblaag tussen beide locaties, dat het getij een grote invloed heeft op de dikte van de vloeibare sliblaag, dat de impact van doodtij-springtijcyclus vooral belangrijk is te MOW1 en dat de bij een negatieve Noord Atlantische Oscillatie index de vloeibare sliblaag dikker is. Een uitgebreide studie van de dikte van de vloeibare sliblagen in de haven van Zeebrugge gebaseerd op in situ en remote sensing data werd recent gepubliceerd (Vanlede et al., 2019).

Het gebruik van de Multibeam Backscatter Data (MBES) is een andere mogelijkheid om de zeebodem te karakteriseren. De sterkte van het teruggekaatste signaal hangt af van vele factoren, met name de samenstalling en geotechnische eigenschappen van de zeebodem-sedimenten, de frequentie van de sonar en de hoek warmme het geluidssignaal de bodem raakt. In Montereale-Gavazzi et al. (2019) worden drie experimenten besproken die de kortstondige variaties in de zeebodem backscatter te bestuderen. Eén van deze experimenten werd uitgevoerd in het station MOW1. In deze slibrijke locatie variëren de backscatter fluctuaties samen met de hooggeconcentreerde sliblagen. Een uitgebreide beschrijving van deze resultaten kan gevonden worden in Appendix 5. Conclusie uit dit onderzoek is dat deze techniek interessant kan zijn om veranderingen in sedimentsamenstelling ten gevolge van stortoperaties op te volgen. Een routinematige monitoring is op dit moment, gezien de vele wetenschappelijke uitdagingen die er nog zijn, heden nog niet mogelijk.

# 5. Referenties


Alldredge AL, Passow U, Logan BE. 1993. The abundance and significance of a class of large, transparent organic particles in the ocean. Deep-Sea Research 40, 1131–1140.

Bainbridge ZT, Wolanski E, Álvarez-Romero JG, Lewis SE, Brodie JE. 2012. Fine sediment and nutrient dynamics related to particle size and floc formation in a Burdekin River flood plume, Australia. Marine Pollution Bulletin 65, 236–248.

Bar-Zeev E, Berman-Frank I, Stambler N, Vázquez Domínguez E, Zohary T, Capuzzo E, Meeder E, Suggett D, Iluz D, Dishon G, Berman T. 2009. Transparent exopolymer particles (TEP) link phytoplankton and bacterial production in the Gulf of Aqaba. Aquatic Microbial Ecology 56, 217–225.

Breugem WA, Decrop B, Frederix K, Delecluyse K, van Holland G, Luyten P, Hyde P. 2011. Development of a sediment transport model in COHERENS. 5th Int. Conf. on Advanced Computational Methods in Engineering ACOMEN, Liège, Belgium, 14-17 November, 10pp.

Capuzzo E, Stephens D, Silva T, Barry J, Forster RM. 2015. Decrease in water clarity of the southern and central North Sea during the 20th century. Global Change Biology 21, 2206–2214

Chen MS, Wartel S, Temmerman S. 2005. Seasonal variation of floc characteristics on tidal flats, the Scheldt estuary. Hydrobiologia 540, 181–195.

Chen P, Yu JCS, Fettweis M. 2018. Modeling storm-influences suspended particulate matter flocculation using a tide-wave combined biomineral model. Water Enviromnent Research 90, 244-257.

Claquin P, Probert I, Lefebvre S, Veron B. 2008. Effects of temperature on photosynthetic parameters and TEP production in eight species of marine microalgae. Aquatic Microbial Ecology 51, 1-11.

Discart V, Bilad MR, Vankelecom IFJ. 2015. Critical evaluation of the determination methods for Transparent Exopolymer Particles, agents of membrane fouling. Critical Reviews in Environmental Science and Technology 45, 167-192.

Droppo IG. 2001. Rethinking what constitutes suspended sediment. Hydrological Processes 15, 1551-1564.

Dyer KR. 1989. Sediment processes in estuaries: future research requirements. Journal of Geophysical Research 94 (C10), 14327-14339.

Eisma D, Kalf J. 1987. Distribution, organic content and particle size of suspended matter in the North Sea. Netherlands Journal of Sea Research 21, 265-285.

Engel A, Passow U. 2001. Carbon and nitrogen content of transparent exopolymer particles (TEP) in relation to their Alcian blue adsorption. Marine Ecology Progress Series 219, 1–10.

Fettweis M, Van den Eynde D. 2003. The mud deposits and the high turbidity in the Belgian–Dutch coastal zone, southern bight of the North Sea. Continental Shelf Research 23, 669–691.

Fettweis M, Francken F, Pison V, Van den Eynde D. 2006. Suspended particulate matter dynamics and aggregate sizes in a high turbidity area. Marine Geology 235, 63–74.

Fettweis M, Nechad B, Van den Eynde D. 2007a. An estimate of the suspended particulate matter (SPM) transport in the southern North Sea using SeaWiFS images, in-situ measurements and numerical model results. Continental Shelf Research 27, 1568-1583.

Fettweis M, Van den Eynde D, Francken F. 2007b. Floc characteristics in a turbidity maximum: calibration of a sediment transport model of the southern North Sea. Intercoh, Brest, September 25-28.

Fettweis M, Van den Eynde D, Francken F. 2007c. Floc characteristics in a coastal turbidity maximum: calibration of a sediment transport model using in situ measurements. International Conference and 97th Annual Meeting of the Geologische Vereinigung, Bremen, October 1-5.

Fettweis M, Francken F, Van den Eynde D, 2008a. MOMO activiteitsrapport (1 april – 30 september 2007). BMM-rapport MOMO/3/MF/200801/NL/AR/3, 33pp + app.

Fettweis M, Van den Eynde D, Francken F, Nechad B. 2008b. MOMO activiteitsrapport (1 oktober 2007 – 31 maart 2008). BMM-rapport MOMO/3/MF/200805/NL/AR/4, 56pp.

Fettweis M, Van den Eynde D, Maggi F. 2009a. MOMO activiteitsrapport (1 april – 31 december 2008). BMM-rapport MOMO/4/MF/200904/NL/AR/1, 24pp + app.

Fettweis M, Van den Eynde D, Francken F, Van Lancker V. 2009b. MOMO activiteitsrapport (1 januari – 30 juni 2009). BMM-rapport MOMO/4/MF/200912/NL/AR/2, 34pp + app.
Fettweis M, Van den Eynde D, Francken F, Van Lancker V. 2010a. MOMO activiteitsrapport (1 juli – 31 december 2009. BMM-rapport MOMO/4/MF/201003/NL/AR/3, 38 pp + app.
Fettweis M, Francken F, Van den Eynde D, Verwaest T, Janssens J, Van Lancker V. 2010b. Storm influence on SPM concentrations in a coastal turbidity maximum area (southern North Sea) with high anthropogenic impact. Continental Shelf Research 30, 1417-1427.
Fettweis M, Baeye M, Francken F, Lauwaert B, Van den Eynde D, Van Lancker V, Martens C, Michielsen T. 2011. Monitoring the effects of disposal of fine sediments from maintenance dredging on suspended particulate matter concentration in the Belgian nearshore area (southern North Sea). Marine Pollution Bulletin 62, 258-269.
Fettweis M, Baeye M, Lee BJ, Chen P, Yu JCR. 2012a. Hydro-meteorological influences and multimodal suspended particle size distributions in the Belgian nearshore area (southern North Sea). Geo-Marine Letters 32, 123-137.
Fettweis M, Baeye M, Lee BJ, Francken F, Van den Eynde D, Van Lancker V. 2012b. MOMO activiteitsrapport (1 januari – 30 juni 2012). BMM-rapport MOMO/6/MF/201207/ NL/AR/1, 27 pp +app.
Fettweis M, Baeye M, Francken F, Lee BJ, Nechad B, Van den Eynde D, Van Lancker V. 2013. MOMO activiteitsrapport (1 juli – 31 december 2012). BMM-Rapport MOMO/6/MF/ 201301/NL/AR/2, 37pp +app.
Fettweis M, Baeye M, van der Zande D, van den Eynde D, Lee BJ. 2014. Seasonality of floc strength in the southern North Sea. Journal of Geophysical Research 119, 1911–1926
Fettweis M, Baeye M. 2015. Seasonal variation in concentration, size and settling velocity of muddy marine flocs in the benthic boundary layer. Journal of Geophysical Research 120, 5648–5667.
Fettweis M, Baeye M, Cardoso C, Dujardin A, Lauwaert B, Van den Eynde D, Van Hoestenberghe T, Vanlede J, Van Poucke L, Velez C, Martens C. 2016. The impact of disposal of fine grained sediments from maintenance dredging works on SPM concentration and fluid mud in and outside the harbor of Zeebrugge. Ocean Dynamics 66, 1497-1516.
Fettweis M, Baeye M, Francken F, Van den Eynde D, Chen P, Yu J. 2017. MOMO activiteitsrapport (1 januari – 30 juni 2017). BMM-rapport MOMO/8/MF/201708/ NL/AR/1, 32pp + app.
Fettweis M, Baeye M, Francken F, Van den Eynde D, Lee BJ. 2018a. MOMO activiteitsrapport (1 juli – 31 december 2018). BMM-rapport MOMO/8/MF/201801/NL/AR/2, 27pp + app.
Fettweis M, Baeye M, Francken F, Van den Eynde D. 2018b. MOMO activiteitsrapport (1 januari – 30 juni 2018). BMM-rapport MOMO/8/MF/201807/NL/AR/3, 61pp + app.
Fettweis M, Baeye M, Francken F, Van den Eynde D. 2019. MOMO activiteitsrapport (1 juli – 31 december 2019). BMM-rapport MOMO/8/MF/201906/NL/AR/4, 25pp + app.
Hamm CE. 2002. Interactive aggregation and sedimentation of diatoms and clay-sized lithogenic material. Limnology and Oceanography 47, 1790–1795.
Jago CF, Kennaway GM, Novarino G, Jones SE. 2007. Size and settling velocity of suspended flocs during a Phaeocystis bloom in the tidally stirred Irish Sea, NW European shelf. Marine Ecology Progress Series 345, 51-62.
Lauwaert B, Fettweis M, De Witte B, Van Hoei G, Timmermans S, Hermans L. 2019. Vooruitgangsrapport (juni 2019) over de effecten op het mariene milieu van baggerspeciestortingen (Vergunningsperiode 01/01/2017 – 31/12/2021). RBINS-ILVO-AMT-CD rapport. BL/2019/01, 28pp.
Lee BJ, Toorman E, Molz F, Wang J. 2011. A two-class population balance equation yielding bimodal flocculation of marine or estuarine sediments. Water Research 45, 2131–2145.
Lee BJ, Toorman E, Fettweis M. 2014. Multimodal particle size distributions of fine-grained sediments: mathematical modeling and field investigation. Ocean Dynamics 64, 429-441.
Lee BJ, Fettweis M, Toorman E, Molz F. 2012. Multimodality of a particle size distribution of cohesive suspended particulate matters in a coastal zone. Journal of Geophysical Research - Ocean 117, C03014.
Lee BJ, Hur J, Toorman EA. 2017. Seasonal variation in flocculation potential of river water: Roles of the organic matter pool. Water 9(5), 335.

Luyten P. (editor). 2015. Coherens, a couples hydrodynamical-ecological model for regional and shelf seas. User documentation. Version 2.7.1. RBINS-MUMM Report, Royal Belgian Institute of Natural Sciences 1790 pp.

Maerz J, Hofmeister R, van der Lee EM, Gräwe U, Riethmüller R, Wirtz KW. 2016. Maximum sinking velocities of suspended particulate matter in a coastal transition zone. Biogeosciences 13, 4863–4876.

Maggi F. 2005. Flocculation dynamics of cohesive sediment. PhD thesis, Technische Universiteit Delft, 154 pp.

Maggi F. 2009. Biological flocculation of suspended particles in nutrient-rich aqueous ecosystems, Journal of Hydrology 376, 116–125.

Manning AJ, Bass SJ, Dyer KR. 2006. Floc properties in the turbidity maximum of a mesotidal estuary during neap and spring tidal conditions. Marine Geology 235, 193–211.

Mari X, Robert M. 2008. Metal induced variations of TEP sticking properties in the southwestern lagoon of New Caledonia. Marine Chemistry 110, 98–108.

Montereale-Gavazzi G, Roche M, Degrendele K, Lurton X, Terseleer N, Baeye M, Francken F, Van Lancker V. 2019. Insight into short term tidal variability of multibeam backscatter from field experiments on different seafloor types. Geosciences 9, 34.

Nelson M. 2015 Soft sediment dynamics in a high-turbidity environment, Belgian coastal zone. Master Thesis, UGent, 42pp.

Nosaka Y, Yamashita Y, Suzuki K. 2017. Dynamics and origin of Transparent Exopolymer Particles in the Oyashio region of the Western Subarctic Pacific during the spring diatom bloom. Frontiers in Marine Science 4, 79.

Passow U, Alldredge AL. 1995. A dye-binding assay for the spectrophotometric measurement of transparent exopolymer particles. Limnology and Oceanography 40, 1326–1335.

Passow U. 2000. Formation of transparent exopolymer particles, TEP, from dissolved precursor material. Marine Ecology Progress Series 192, 1–11.

Passow U. 2001. The origin of transparent exopolymer particles (TEP) and their role in the sedimentation of particulate matter. Continental Shelf Research 21, 327–346.

Passow U. 2002. Transparent exopolymer particles (TEP) in aquatic environments. Progress in Oceanography 55, 287–333.

Shen X, Lee BJ, Fettweis M, Toorman E. 2018. A tri-modal flocculation model coupled with TELEMAC for estuarine muds both in the laboratory and in the field. Water Research, 145, 473-486.

Spearman JR and Roberts W. 2002. Comparison of flocculation models for applied sediment transport modelling. In: Fine sediment dynamics in the marine environment. (Winterwerp JC and Kranenburg C, eds.). Proceedings in Marine Science Nr 5., Elsevier, 277-293.

Tan XL, Zhang GP, Yi H, Reed AH, Furukawa Y. 2012. Characterization of particle size and settling velocity of cohesive sediments affected by a neutral exopolymer. International Journal of Sediment Research 27, 473-485.

Van den Eynde D, Fettweis M. 2006. Dumping of dredged material in sea: towards operational use of sediment transport models. International Hydrographic Conference 2006, Evolutions in Hydrography, 6-9 November 2006, Antwerp, Belgium.

van der Lee WTB. 2000. Temporal variation of floc size and settling velocity in the Dollard estuary. Continental Shelf Research, 20, 1495–1511.

Van Hoey G, Vincx M, Degraer S. 2005. Small- to large-scale geographical patterns within the macrobenthic Abra alba community. Estuarine, Coastal and Shelf Science 64, 751-763.

Vanlede J, Dujardin A, Fettweis M, Van Hoestenberghe T, Martens C. 2019. Mud dynamics in the port of Zeebrugge. Ocean Dynamics, 69, 1085-1099.

van Leussen W. 1994. Estuarine macroflocs and their role in fine-grained sediment transport. PhD thesis, University Utrecht, Utrecht. 488 pp.

Verdugo P. 2012. Marine microgels. Annual Review of Marine Science 4, 375–400.

Verney R, Lafite R, Brun-Cottan J-C. 2009. Flocculation potential of estuarine particles: The importance of environmental factors and of the spatial and seasonal variability of suspended particulate matter. Estuaries and Coasts 32, 678–693.

Winterwerp JC. 1998. A simple model for turbulence induced flocculation of cohesive sediment. Journal of Hydraulic Research 36, 309–326.

Winterwerp J, Manning AJ, Martens C, De Mulder T, Vanlede J. 2006. A heuristic formula for

turbulence-induced flocculation of cohesive sediment. Estuarine, Coastal and Shelf Science 68, 195-207.

Zhou J, Mopper K, Passow U. 1998. The role of surface-active carbohydrates in the formation of transparent exopolymer particles by bubble adsorption of seawater. Limnology and Oceanography 43, 1860–1871.

COLOPHON

Dit rapport werd voorbereid door de BMM in november 2019
Zijn referentiecode is .MOMO/9/MF/201911/NL/AR/1

De scheepstijd met de RV Belgica werd voorzien door BELSPO en KBIN-OD Natuur

Indien u vragen hebt of bijkomende copies van dit document wenst te verkrijgen, gelieve een e-mail te zenden naar mfettweis@naturalsciences.be, met vermelding van de referentie, of te schrijven naar:

Koninklijk Belgisch Instituut voor Natuurwetenschappen
OD Natuur – BMM
t.a.v. Michael Fettweis
Vautierstraat 10
B–1000 Brussel
België
Tel: +32 2 627 41 83



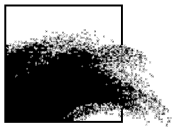

# APPENDIX 1

# Beschrijving van het Two-Class Population Balance Model in Coherens

3: TVD scheme. Default.

iopt_sed_ws_lim Disables/enables the limitation of the settling velocity for shallow waters.

0: Disabled. Default.

1: Enabled.

## 6.8 Flocculation model

In the multi-fraction sediment transport model, presented in the previous sections, the sediment particles are distributed among different size classes, each having its own diameter, mass, fall velocity, critical shear stress. The size distributions are considered as independent of each other. If the flocculation model is used instead, larger size particles (flocs) are formed from smaller size particles (flocculi) by aggregation. The opposite effect is the breakage of larger size particles into smaller ones. Diameter, mass and fall velocity are now defined as function of the number of flocculi within flocs, presented in the model as a volume concentration. The flocculation model, adopted in COHERENS, is the two-class bimodal population balance model, described in Lee *et al.* (2011, 2014).

The following remarks should be given concerning the use of the flocculation module with the other sediment modules:

- The flocculation and the multi-fraction model cannot be activated both within the same simulation.
- The morphology can only be activated in connection with the multi-fraction model. A morphological module coupled with the flocculation model, is not available in the current version of COHERENS.
- The flocculation model can only be used in 1-D water column or 3-D mode.

### 6.8.1 Flocculation transport model

The model contains three state variables: the number concentrations of flocculi $N_P$, flocs $N_F$ and flocculi bound in flocs $N_T$. They are calculated by solving the transport equations

$$\frac{1}{h_3}\frac{\partial}{\partial t}\left(h_3 N_P\right) + \mathcal{A}_{h1}(u, N_P) + \mathcal{A}_{h2}(v, N_P) + \mathcal{A}_v(\omega - w_{sP}, N_P) =$$

$$\mathcal{D}_{sv}(N_P) + \mathcal{D}_{sh1}(N_P) + \mathcal{D}_{sh2}(N_P) + A_P + B_P \tag{6.120a}$$

$$\frac{1}{h_3}\frac{\partial}{\partial t}(h_3 N_F) + \mathcal{A}_{h1}(u, N_F) + \mathcal{A}_{h2}(v, N_F) + \mathcal{A}_v(\omega - w_{sF}, N_F) =$$
$$\mathcal{D}_{sv}(N_F) + \mathcal{D}_{sh1}(N_F) + \mathcal{D}_{sh2}(N_F) + A_F + B_F \tag{6.120b}$$

$$\frac{1}{h_3}\frac{\partial}{\partial t}(h_3 N_T) + \mathcal{A}_{h1}(u, N_T) + \mathcal{A}_{h2}(v, N_T) + \mathcal{A}_v(\omega - w_{sF}, N_T) =$$
$$\mathcal{D}_{sv}(N_T) + \mathcal{D}_{sh1}(N_T) + \mathcal{D}_{sh2}(N_T) + A_T + B_T \tag{6.120c}$$

where the advective and diffusive operators are defined in Section 4.2.1.2, $N_C = N_T/N_F$ is the number of flocculi within flocs. Its value is limited by $N_{cmin} \leq N_C \leq N_{max}$ to prevent numerical instabilities. Contrary to the multi-fraction sediment model, the vertical diffusion coefficient is the same as the one used for $T$ and $S$.

The last two terms on the right hand side of (6.120a) and (6.120b) are source/sink terms due to respectively aggegration and breakage and are given by

$$A_P + B_P = -\frac{1}{2}\alpha\beta_{PP}\frac{N_P^2 N_C}{N_C - 1} - \alpha\beta_{PF} N_P N_F + f a_F N_C N_F \tag{6.121a}$$

$$A_F + B_F = \frac{1}{2}\alpha\beta_{PP}\frac{N_P^2}{N_C - 1} - \frac{1}{2}\alpha\beta_{FF} N_F^2 + a_F N_F \tag{6.121b}$$

$$A_T + B_T = -(A_P + B_P) \tag{6.121c}$$

where $f$ is the fraction of flocculi generated by floc breakage, $\alpha$ the collision efficiency factor and $\beta_{ij}$ the collision frequency function between size classes $i$ and $j$ (where the indices the $i$ and $j$ are equal to either $P$ for flocculi or $F$ for flocs) and $a_F$ the breakage kinetic factor. The collision function can be written as the sum of three collision factors, representing respectively the collision frequency due to Brownian motion, fluid shear and differential settling

$$\beta_{ij} = \beta_{BR,ij} + \beta_{SH,ij} + \beta_{DS,ij} \tag{6.122}$$

which are defined by

$$\beta_{BR,ij} = \frac{2k_B T_k}{3\rho\nu}\Big(\frac{1}{d_i} + \frac{1}{d_j}\Big)\Big(d_i + d_j\Big) \tag{6.123a}$$

$$\beta_{SH,ij} = \frac{1}{6}(d_i + d_j)^3 G \tag{6.123b}$$

$$\beta_{DS,ij} = 2\pi d_i^2 |w_{si} - w_{sj}| \tag{6.123c}$$

where $k_B$ is Boltzmann's constant, $T_k$ the water temperature in degrees K, $d_P$ the diameter of the flocculi, $d_F$ the floc diameter, defined below, and

$G = \sqrt{\varepsilon/\nu}$ the turbulent shear. The factor $a_i$ represents the rate of braking and is given by

$$a_i = E_b G\Big(\frac{d_i - d_p}{d_p}\Big)^p \Big(\frac{\rho\nu G}{F_y/d_i^2}\Big)^q \tag{6.124}$$

where $E_b$ is the breakage efficiency factor and $F_y$ the yield strength of flocs in Pa.

Open boundary conditions for the three transport variables are obtained by selecting one of the formulations given in Section 4.11.3.1. The most common method is either a zero-gradient condition (default) or the specification of an external profile.

The vertical boundary conditions at the surface are the same as for the multi-fraction model (zero advective and diffusive flux). At the bottom, deposition is given by (6.88). Erosion rate for flocculi is determined by the Partheniades formula (6.87), whereas erosion is set to zero for flocs since it is assumed that the binding of the microflocs inside flocs is broken once the flocs reach the sea bed.

### 6.8.2 Floc properties

The floc diameter and density are determined from fractal theory taking account of floc packing and shaping

$$d_F = N_C^{1/n_f} d_P \tag{6.125}$$

$$\rho_F = \rho_w + (\rho_P - \rho_w)\big(\frac{d_P}{d_F}\big)^{3-n_f} \tag{6.126}$$

where $n_f$ is the fractal dimension of flocs (between 1.7 and 2.3).

The fall velocity for flocculi is obtained from Stokes's formula (see equation (6.40))

$$w_{sP} = \frac{(s_P - 1)g d_P^2}{18\nu} \tag{6.127}$$

with $s_P = \rho_P/\rho_w$. The settling velocity for flocs is determined from a modified Stokes formula

$$w_{sF} = \frac{(s_P - 1)g}{18\nu} \frac{d_P^{3-n_f} d_F^{n_f-1}}{1 + 0.15 Re_F^{0.687}} \tag{6.128}$$

where $Re_F = w_{sF} d_F/\nu$ is the particle Reynolds number for flocs. Note that, since $w_{sF}$ appears both on the left and right side of (6.128), the equation should, in principle be solved by iteration. In the COHERENS code, this is avoided by taking the value from the previous time step in the definition of

$Re_F$. Effects of hindered settling can optionally by taken into account by multiplying (6.127)–(6.128) with a factor $f_{hs}$ for hindered settling, defined by (6.44). In the current implementation of the flocculation model, only the Richardson & Zaki (1954) formulation is allowed.

Once the number densities are calculated from the transport equations (6.120a)–(6.120c) the volume, total and mass concentrations become:

$$c_P = \frac{\pi}{6} N_P d_P^3 , \quad c_F = \frac{\pi}{6} d_P^3 N_c^{3/nf} \tag{6.129a}$$

$$c_t = c_P + c_F \tag{6.129b}$$

$$c_{mP} = \rho_P c_P \quad c_{mF} = \rho_F c_F \tag{6.129c}$$

**Switches**

The following switches are available:

iopt_kinvisc — Selects type of kinematic viscosity.

- 0: User-selected uniform value. Default.
- 1: From the ITTC (1978) equation.

iopt_sed — The flocculation model is activitated by setting this switch to 2.

iopt_sed_bstres_cr — Selects the formulation for the critical bottom shear stress.

- 1: User-defined value for each fraction. Default.
- 2: Brownlie (1981) as given by (6.30).
- 3: Soulsby & Whitehouse (1997) as given by (6.31).
- 4: Constant value for the critical Shield parameter from Wu *et al.* (2000).

iopt_sed_dens_grad — Disables/enables the inclusion of sediment stratification in the formulations for the bouyancy frequency and baroclinic pressure gradient.

- 0: Disabled. Default.
- 1: Enabled.

iopt_sed_hidexp — Selects the type of model for hiding and exposure.

- 0: Disabled. Default.
- 1: Wu *et al.* (2000) as given by (6.36).

2: Ashida & Michiue (1972) as given by (6.37).

iopt_sed_rough Selects formulation for the skin bottom roughness length.

0: Same value as the form roughness.

1: User-defined spatially uniform value.

2: As the sum of grain roughness, ripple roughness (selected by iopt_sed_rough_rip) and bedload roughness (selected by iopt_sed_rough_btr). Default.

iopt_sed_rough_btr Selects type of model for the bedload roughness length.

0: Disabled. Default.

1: Grant & Madsen (1982).

2: Wiberg & Rubin (1989).

3: Nielsen (1992).

iopt_sed_rough_rip Selects type of wave ripple model.

0: Disabled. Default.

1: Wiberg & Harris (1994).

2: Li *et al.* (1996).

3: Soulsby & Whitehouse (2005).

4: Goldstein *et al.* (2013).

iopt_sed_slope Selects the type of slope factor.

0: Disabled. Default.

1: Enabled using (6.38).

iopt_sed_vadv Selects the type of vertical advection scheme for settling in case of 1-D simulations.

0: Vertical settling disabled.

1: Upwind scheme.

2: Central scheme.

3: TVD scheme. Default.

iopt_sed_ws_hindset Formulation for hindered settling.

0: Hindered settling disabled

1: Richardson & Zaki (1954) equation (6.44)

iopt_sed_ws_lim — Disables/enables the limitation of the settling velocity for shallow waters.

0: Disabled. Default.

1: Enabled.

# APPENDIX 2

# Beschrijving van de test cases voor het TCPBE flocculatiemodel in Coherens

*Table 10.14: Values of parameters used in the flocculation module for the **flocprof** experiments.*

| experiment | $\alpha_{agg}$ | $E_b$ | $n_f$ | $\rho_p$ (kg/m$^3$) | breakage fraction $f$ |
|---|---|---|---|---|---|
| ***A*** | 0.1 | 0.0001 | 2.0 | 1800.0 | 0.1 |
| ***B*** | 0.05 | 0.0001 | 2.0 | 1800.0 | 0.1 |
| ***C*** | 0.15 | 0.0001 | 2.0 | 1800.0 | 0.1 |
| ***D*** | 0.1 | 0.00025 | 2.0 | 1800.0 | 0.1 |
| ***E*** | 0.1 | 0.00007 | 2.0 | 1800.0 | 0.1 |
| ***F*** | 0.1 | 0.0001 | 1.9 | 1800.0 | 0.1 |
| ***G*** | 0.1 | 0.0001 | 2.1 | 1800.0 | 0.1 |
| ***H*** | 0.1 | 0.0001 | 2.0 | 1600.0 | 0.1 |
| ***I*** | 0.1 | 0.0001 | 2.0 | 1400.0 | 0.1 |
| ***J*** | 0.1 | 0.0001 | 2.0 | 1800.0 | 0.0 |
| ***K*** | 0.1 | 0.0001 | 2.0 | 1800.0 | 0.3 |

## 10.8 *flocvprof*

### 10.8.1 Description

The flocculation model is tested by considering 1-D simulations within a water column with a depth of 4.25 m and 20 vertical levels. A spinup period of 1 day is considered without sediment. Afterwards, the flocculation module is activated and the simulation continues for another 3 days. Following Lee et al. different experiments are performed using each different values for the parameters of the flocculation model. Details are given in Table 10.14.
The following output parameters are defined

| | |
|---|---|
| umean | Depth-mean current [m/s]. |
| ubot | Bottom current [m/s]. |
| usur | Surface current [m/s]. |
| bstres | Bottom shear stress [Pa]. |
| floc_P_mean | Vertical mean concentration of flocculi [kg/m$^3$]. |
| floc_F_mean | Vertical mean concentration of flocs [kg/m$^3$]. |
| floc_dia_mean | Vertical mean diameter of flocs [$\mu$m]. |
| floc_dens_mean | Vertical mean density of flocs [kg/m$^3$]. |
| floc_ws_mean | Vertical mean fall velocity of flocs [m/s]. |
| floc_P_bot | Bottom concentration of flocculi [kg/m$^3$]. |
| floc_F_bot | Bottom concentration of flocs [kg/m$^3$]. |

| | |
|---|---|
| floc_dia_bot | Floc diameter at the bottom [$\mu$m]. |
| floc_dens_bot | Floc density at the bottom [kg/m$^3$]. |
| floc_ws_bot | Fall velocity of flocs at the bottom [m]. |
| floc_P_sur | Surface concentration of flocculi [kg/m$^3$]. |
| floc_F_sur | Surface concentration of flocs [kg/m$^3$]. |
| floc_dia_sur | Floc diameter at the surface [$\mu$m]. |
| floc_dens_sur | Floc density at the surface [kg/m$^3$]. |
| floc_ws_sur | Fall velocity of flocs at the suface [m/s]. |

### 10.8.2 Log files

This section contains the COHERENS *log* files reporting errors (*errlog*) and warnings (*warlog*) encountered while running the test case.
An *errlog* contains the list of critical errors encountered causing the simulation to stop. It is created by COHERENS at the beginning of the simulation and deleted in case of successful completion. An empty *errlog* also indicates that something went wrong.
A *warlog* contains a list of changes in setup variables and switches automatically performed by COHERENS during initialisation and warnings for "suspect" model settings.
Errlogs of reference version:

```
no errlog/warlog file
```

Errlogs of new version:

```
no errlog/warlog file
```

Warlogs of reference version:

```
flocvprof0A.warlog
flocvprof0B.warlog
flocvprof0C.warlog
flocvprof0D.warlog
flocvprof0E.warlog
flocvprof0F.warlog
flocvprof0G.warlog
flocvprof0H.warlog
flocvprof0I.warlog
```

```
flocvprof0J.warlog
flocvprof0K.warlog
flocvprof1A.warlog
flocvprof1B.warlog
flocvprof1C.warlog
flocvprof1D.warlog
flocvprof1E.warlog
flocvprof1F.warlog
flocvprof1G.warlog
flocvprof1H.warlog
flocvprof1I.warlog
flocvprof1J.warlog
flocvprof1K.warlog
```

Warlogs of new version:

```
flocvprof0A.warlog
flocvprof0B.warlog
flocvprof0C.warlog
flocvprof0D.warlog
flocvprof0E.warlog
flocvprof0F.warlog
flocvprof0G.warlog
flocvprof0H.warlog
flocvprof0I.warlog
flocvprof0J.warlog
flocvprof0K.warlog
flocvprof1A.warlog
flocvprof1B.warlog
flocvprof1C.warlog
flocvprof1D.warlog
flocvprof1E.warlog
```

flocvprof1F.warlog

flocvprof1G.warlog

flocvprof1H.warlog

flocvprof1I.warlog

flocvprof1J.warlog

flocvprof1K.warlog

### 10.8.3 Comparison graphs

The following figures are plotted for each of the eleven experiments in the ***flocvprof*** test (each containing the data of the reference version and of the new version):

- Time series (hours) of the bottom shear stress bstres (Pa).
- Time series (hours) of the vertical mean concentration of flocculi floc_P_mean ($kg/m^3$).
- Time series (hours) of the vertical mean concentration of flocs floc_F_mean ($kg/m^3$).
- Time series (hours) of the vertical mean of the floc diameter floc_dia_mean (m).
- Time series (hours) of the vertical mean of the floc density floc_dens_mean ($kg/m^3$).
- Time series (hours) of the vertical mean of the floc fall velocity floc_ws_mean (m/s).
- Time series (hours) of the bottom concentration of flocculi floc_P_bot ($kg/m^3$).
- Time series (hours) of the bottom concentration of flocs floc_F_bot ($kg/m^3$).
- Time series (hours) of the bottom floc diameter floc_dia_bot (m).
- Time series (hours) of the bottom floc density floc_dens_bot ($kg/m^3$).
- Time series (hours) of the bottom floc fall velocity floc_ws_bot (m/s).

- Time series (hours) of the surface concentration of flocculi floc_P_sur ($kg/m^3$).
- Time series (hours) of the surface concentration of flocs floc_F_sur ($kg/m^3$).
- Time series (hours) of the surface floc diameter floc_dia_sur (m).
- Time series (hours) of the surface floc density floc_dens_sur ($kg/m^3$).
- Time series (hours) of the surface floc fall velocity floc_ws_sur (m/s).
- Vertical profile of the current (m/s) at the end of the simulation.
- Vertical profile of the flocculi concentration ($kg/m^3$) at the end of the simulation.
- Vertical profile of the floc concentration ($kg/m^3$) at the end of the simulation.
- Vertical profile of the floc diameter (m) at the end of the simulation.
- Vertical profile of the floc density ($kg/m^3$) at the end of the simulation.
- Vertical profile of the floc fall velocity (m/s) at the end of the simulation.

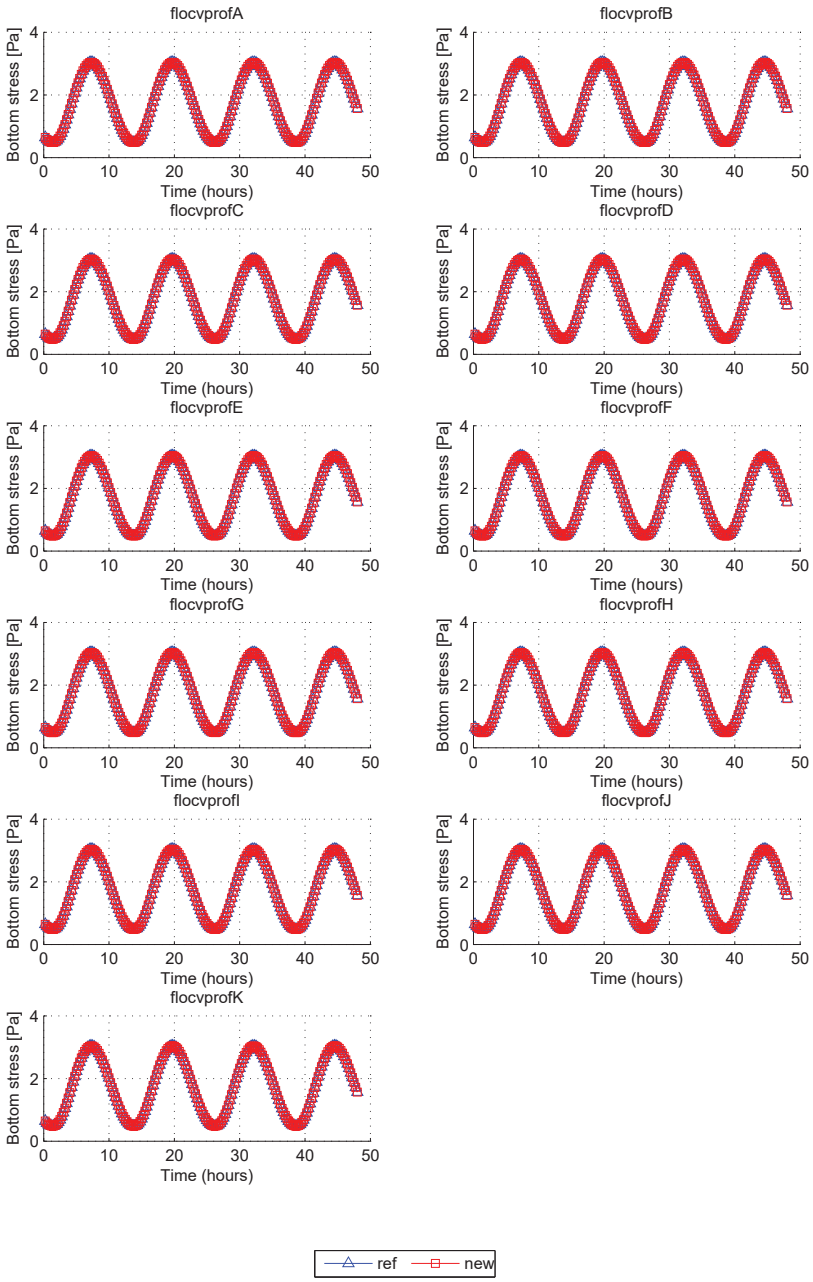


*Figure 10.61:* ***flocvprof****: Time series (hours) of the bottom shear stress* bstres *(Pa).*

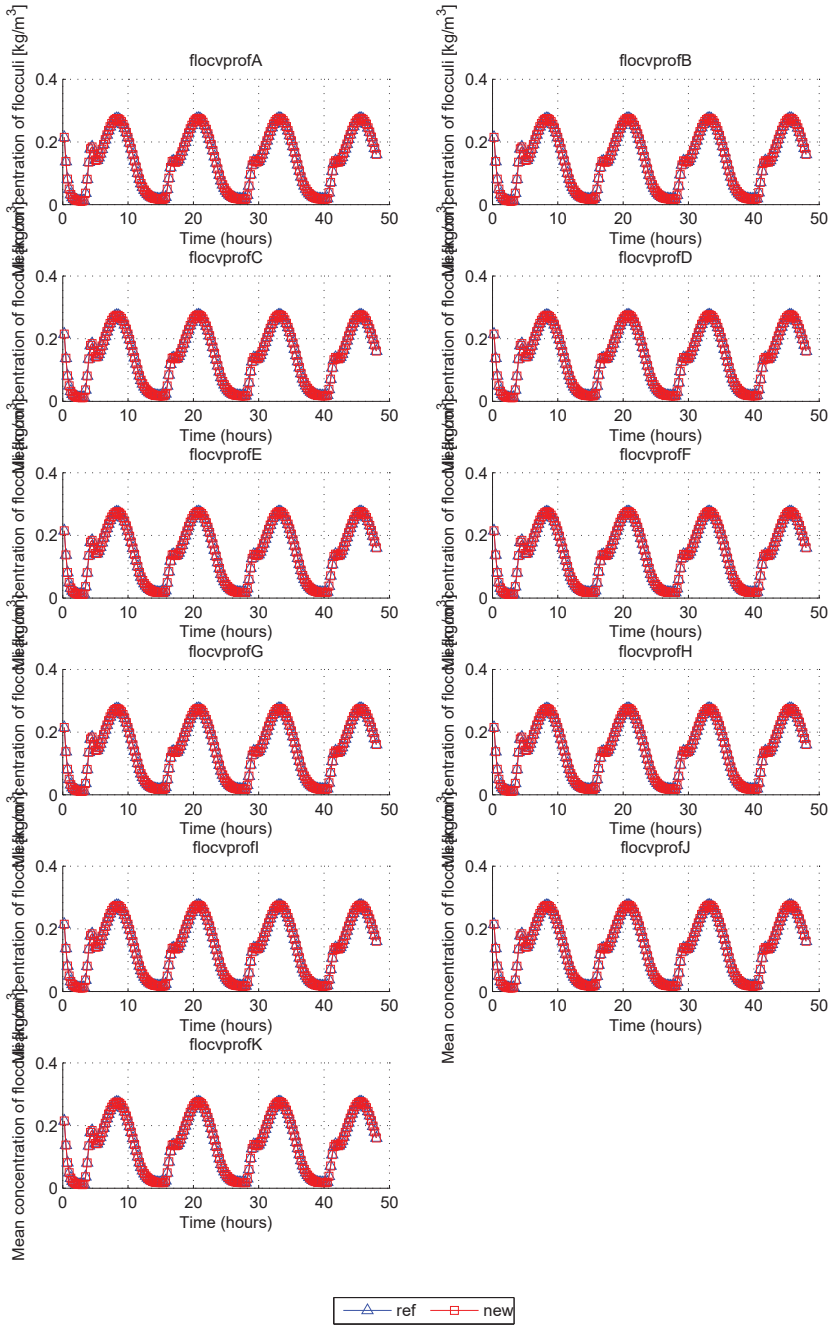


*Figure 10.62:* ***flocvprof****: Time series (hours) of the vertical mean concentration of flocculi* floc_P_mean *(Pa).*

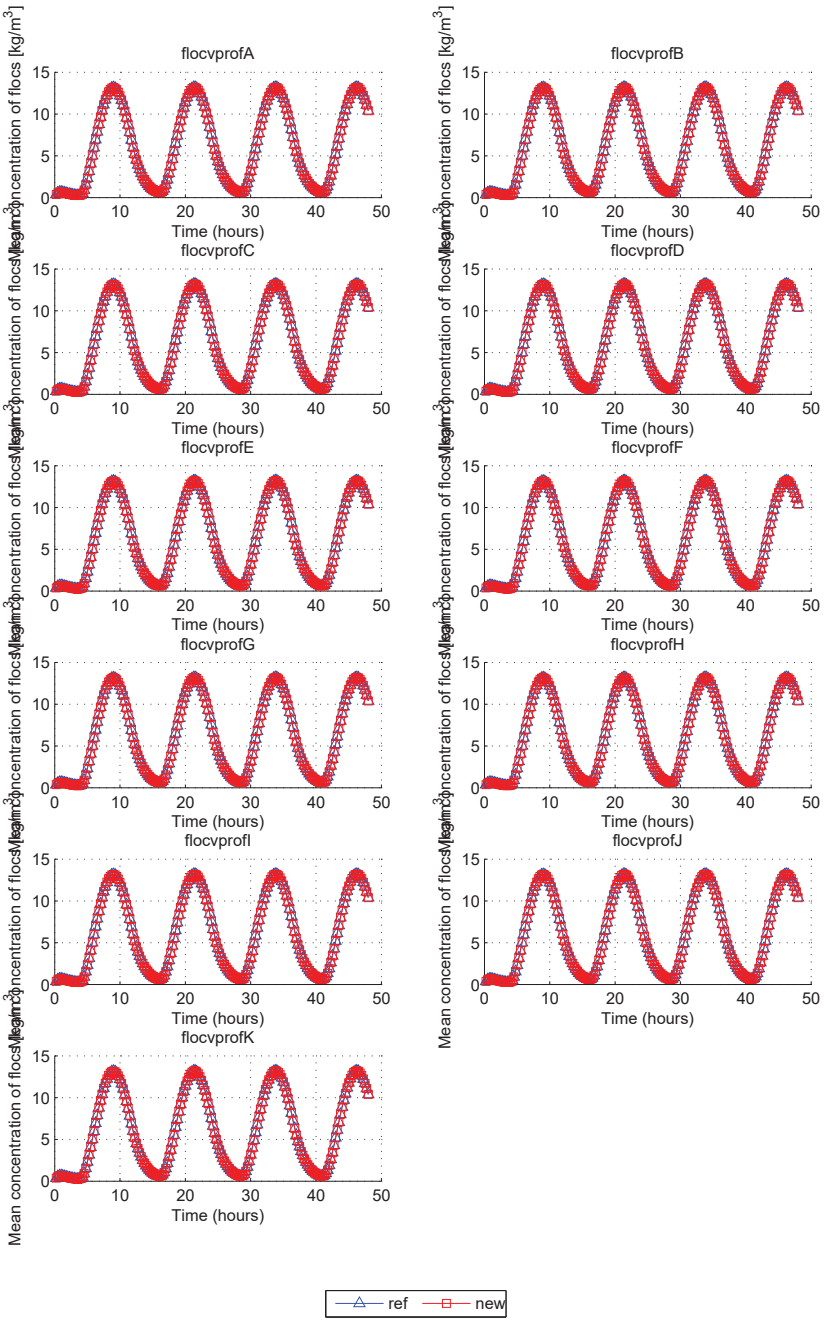


*Figure 10.63:* ***flocvprof****: Time series (hours) of the vertical mean concentration of flocs* floc_F_mean *(Pa).*

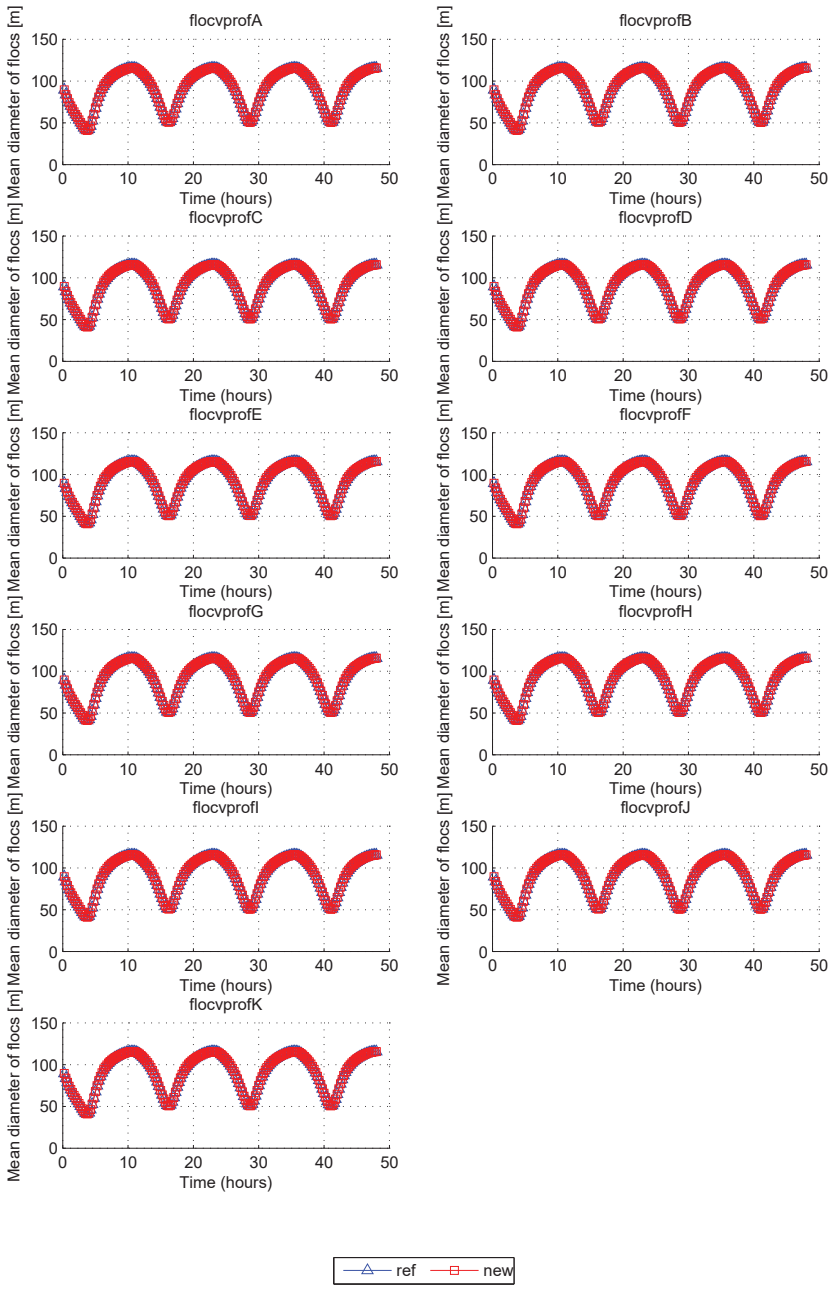


*Figure 10.64:* ***flocvprof****: Time series (hours) of the vertical mean of the floc diameter* floc_dia_mean *(m).*

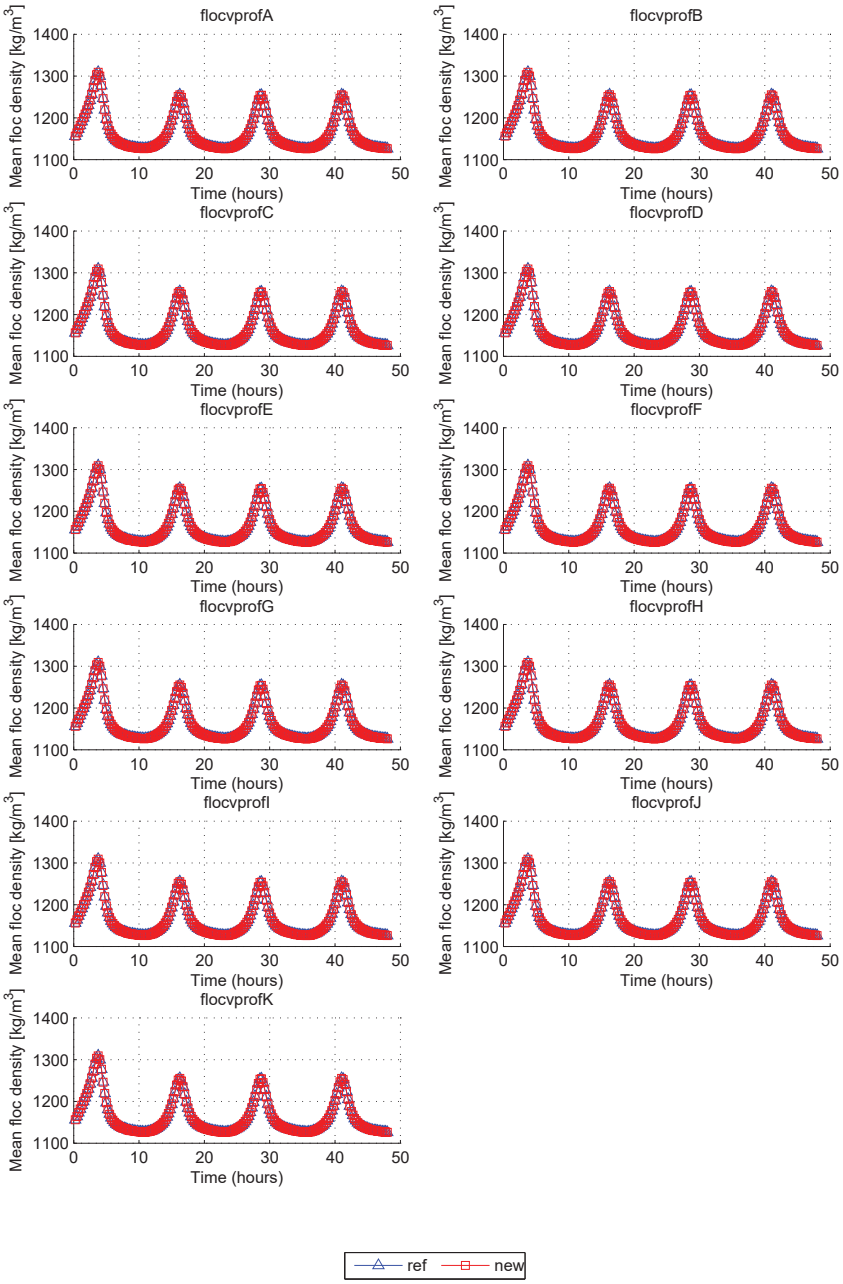


*Figure 10.65:* ***flocvprof****: Time series (hours) of the vertical mean of the floc density* floc_dens_mean *(m).*

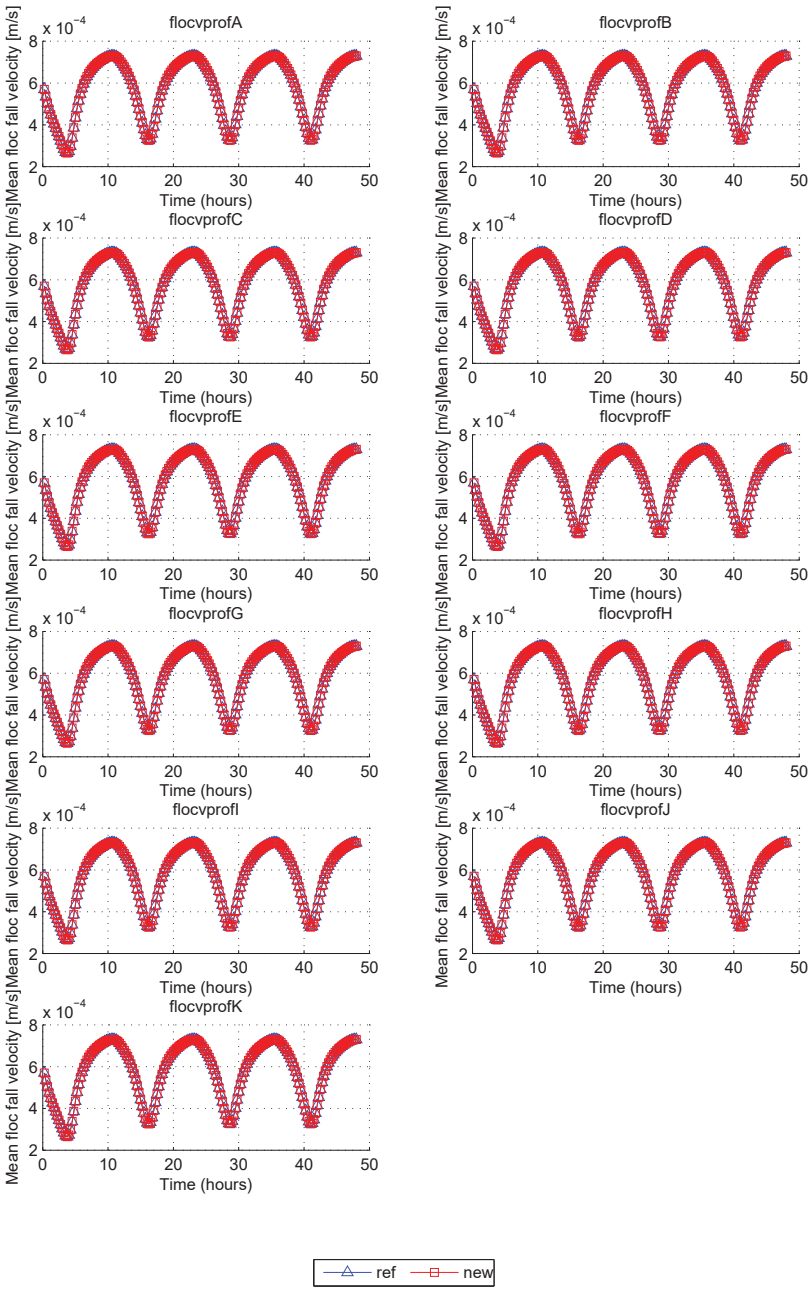


*Figure 10.66:* ***flocvprof****: Time series (hours) of the vertical mean of the floc fall velocity* floc_ws_mean *(m/s).*

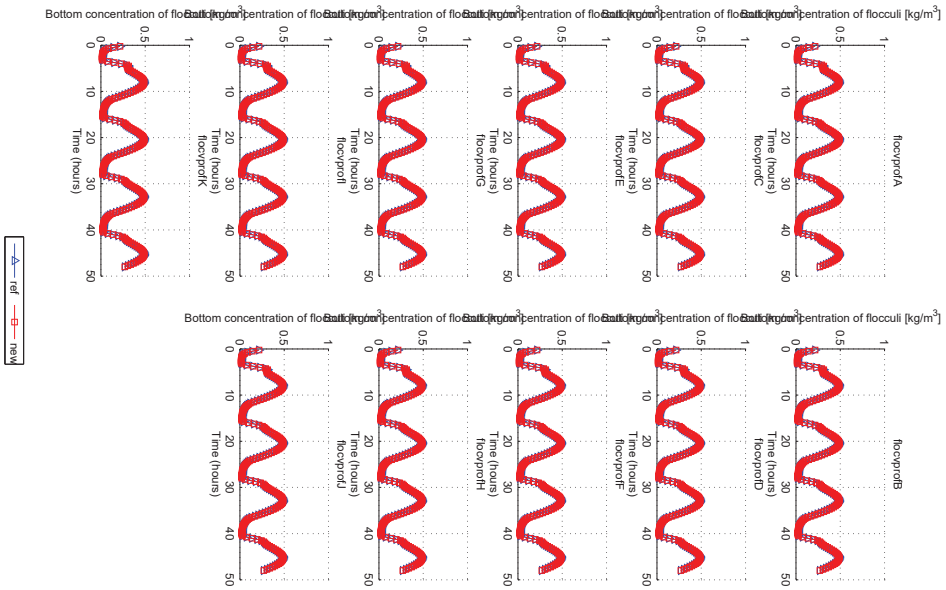


*Figure 10.67:* ***flocvprof****: Time series (hours) of the bottom concentration of flocculi* floc_P_bot *(Pa).*

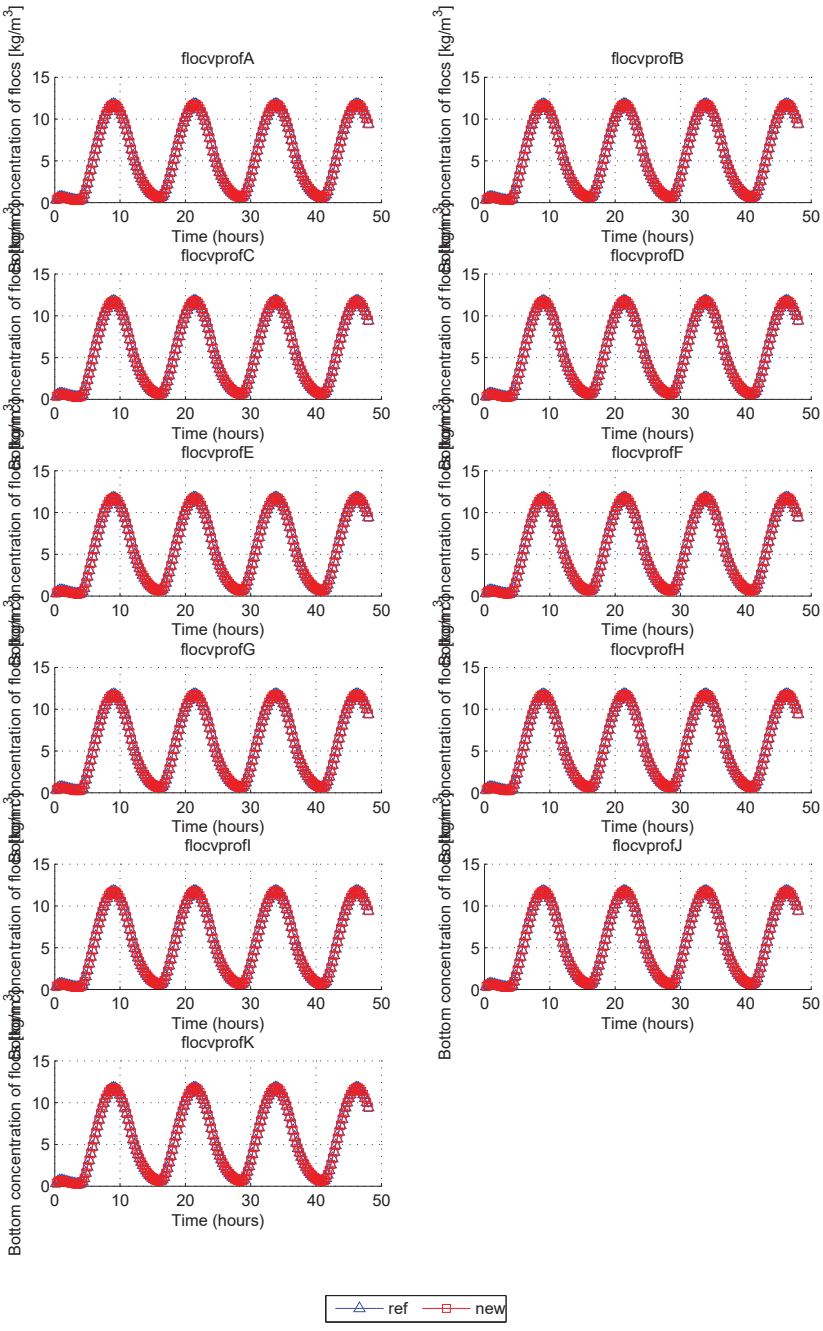


*Figure 10.68:* ***flocvprof****: Time series (hours) of the bottom concentration of flocs* floc_F_bot *(Pa).*

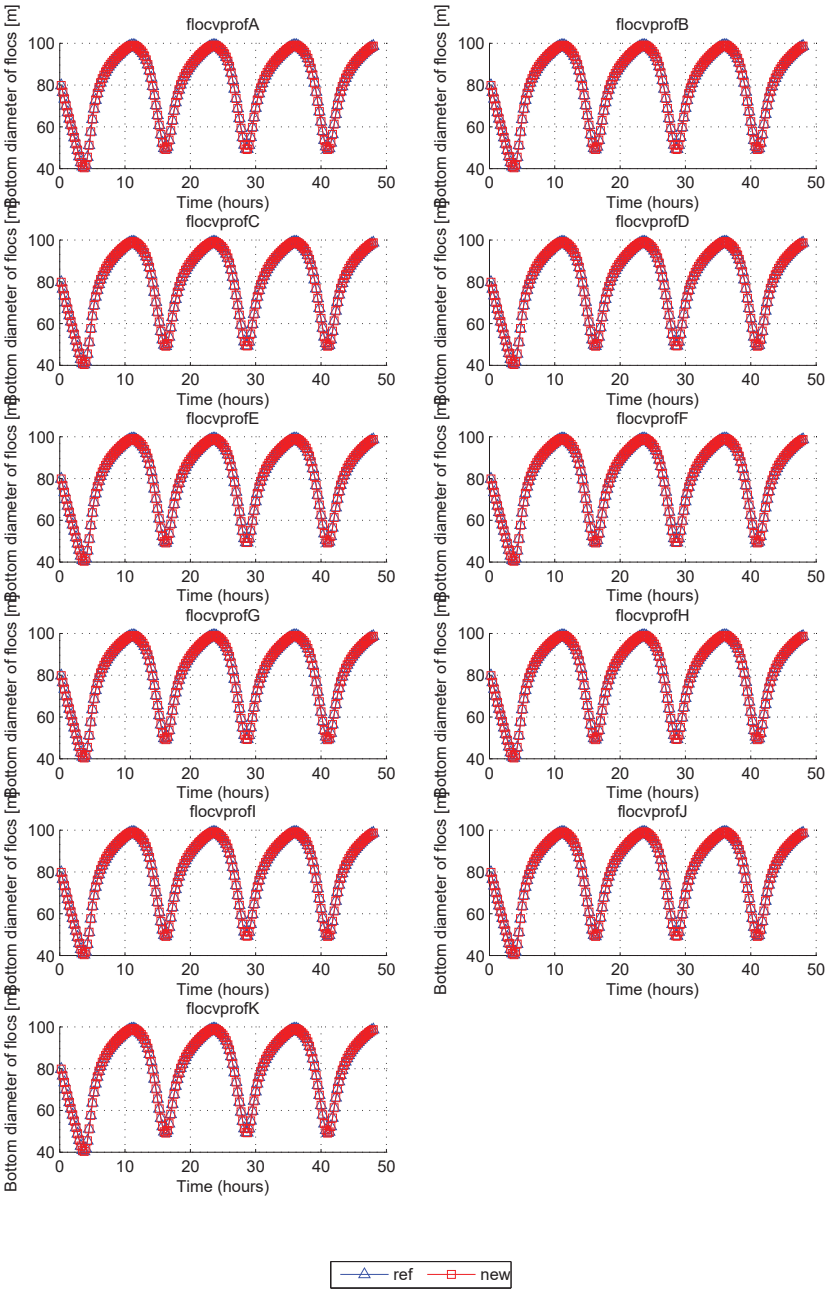


*Figure 10.69:* ***flocvprof****: Time series (hours) of the bottom floc diameter* floc_dia_bot *(m).*

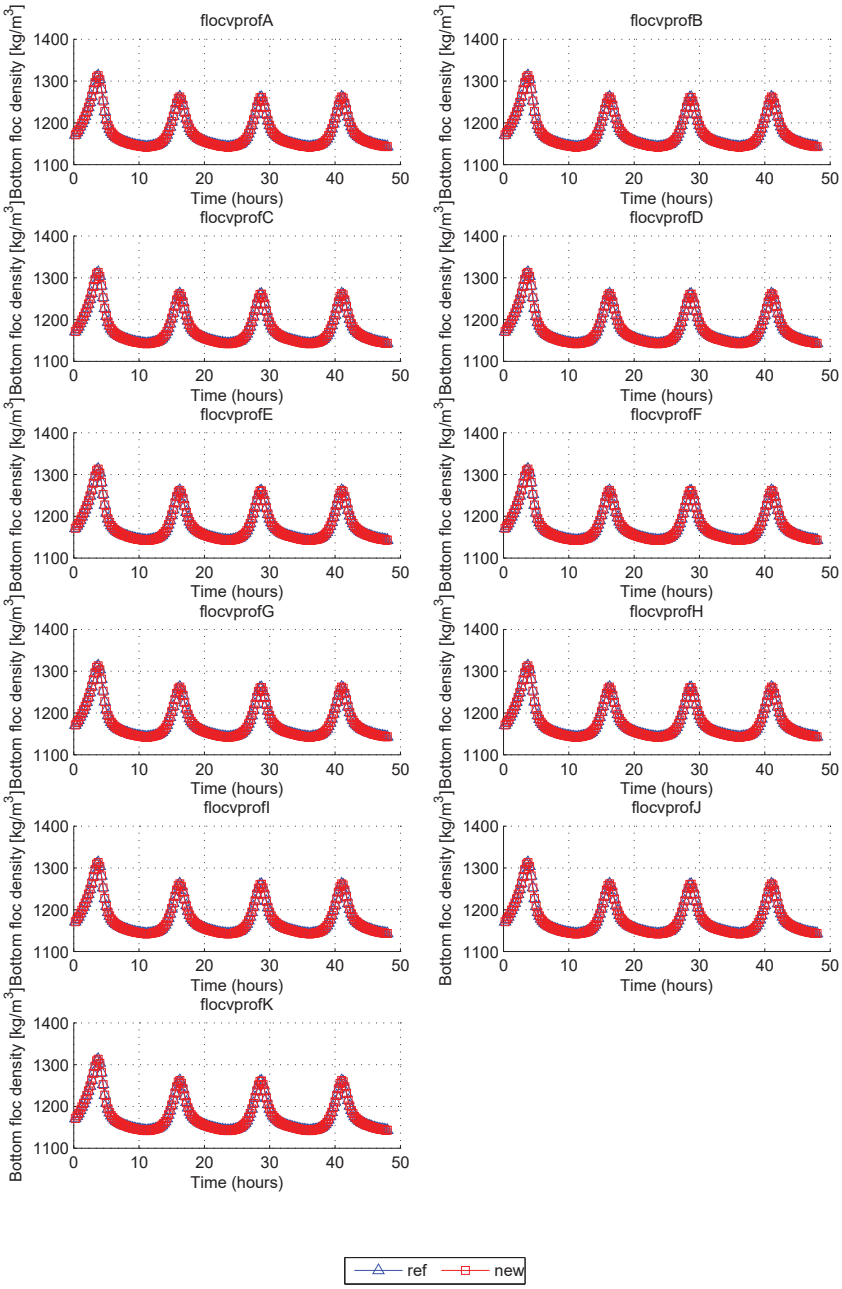


*Figure 10.70:* ***flocvprof****: Time series (hours) of the bottom floc density* floc_dens_bot *(m).*

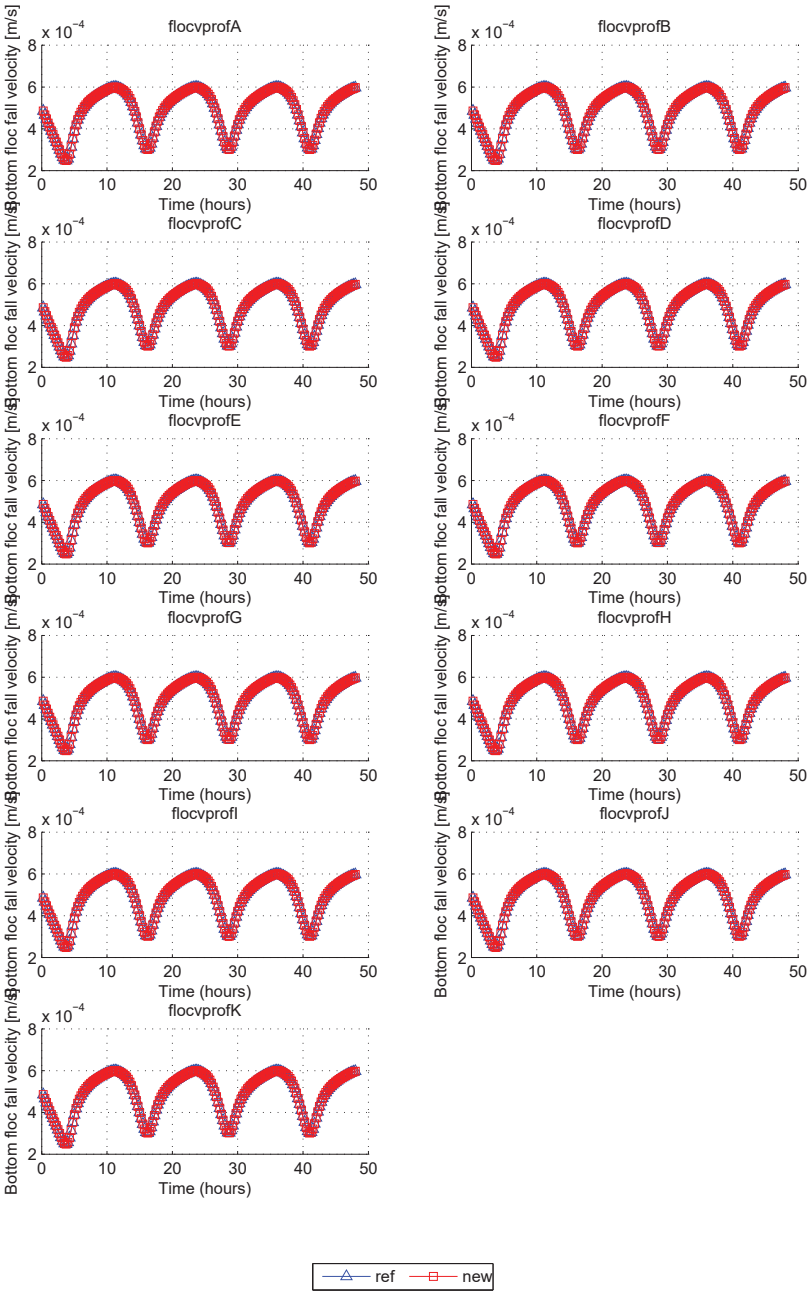


*Figure 10.71:* ***flocvprof****: Time series (hours) of the bottom floc fall velocity* floc_ws_bot *(m/s).*

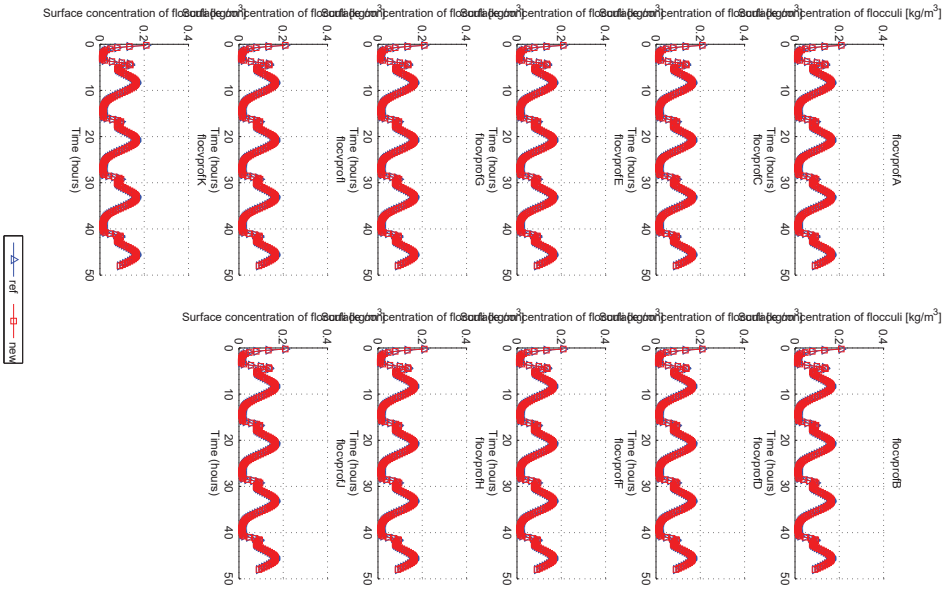


*Figure 10.72:* ***flocvprof****: Time series (hours) of the surface concentration of flocculi* floc_P_sur *(Pa).*

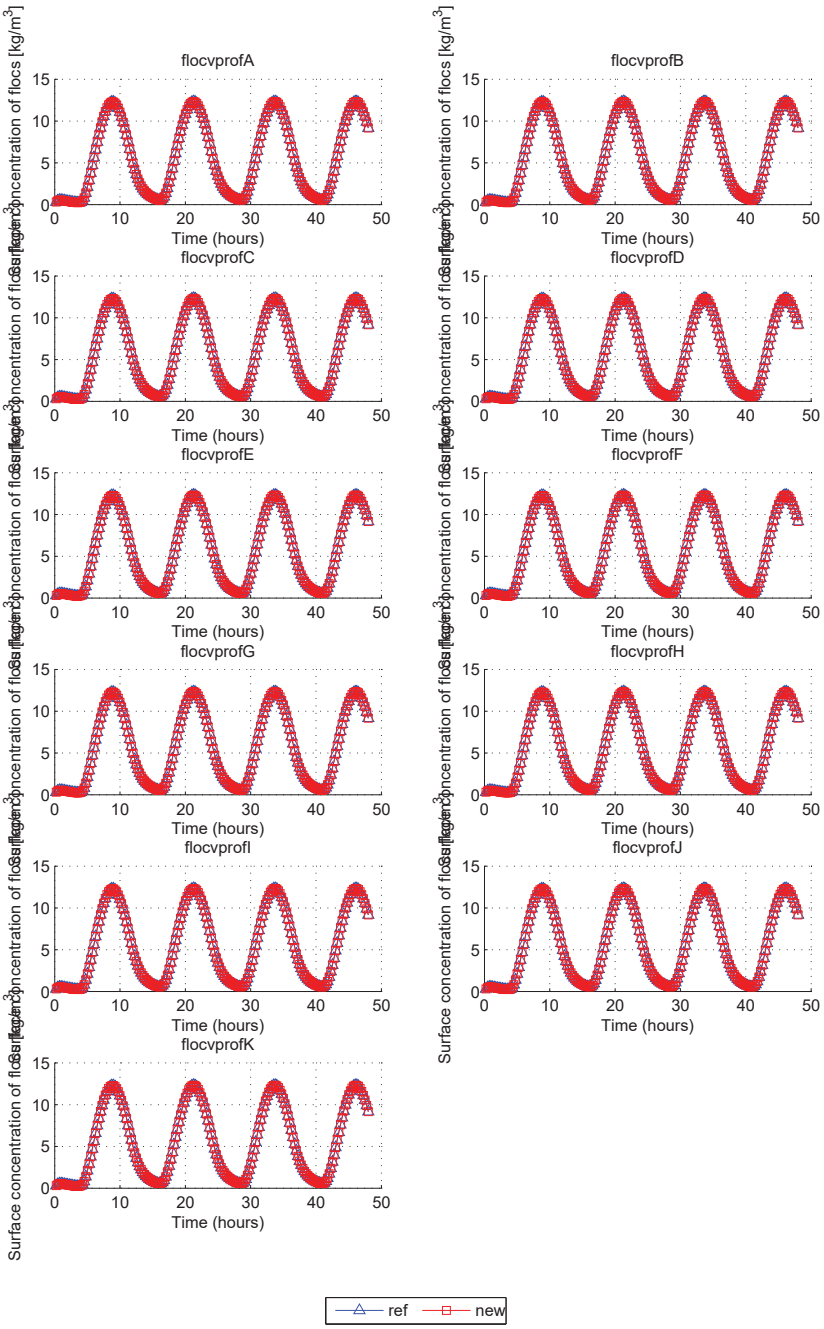


*Figure 10.73:* ***flocvprof****: Time series (hours) of the surface concentration of flocs floc_F_sur (Pa).*

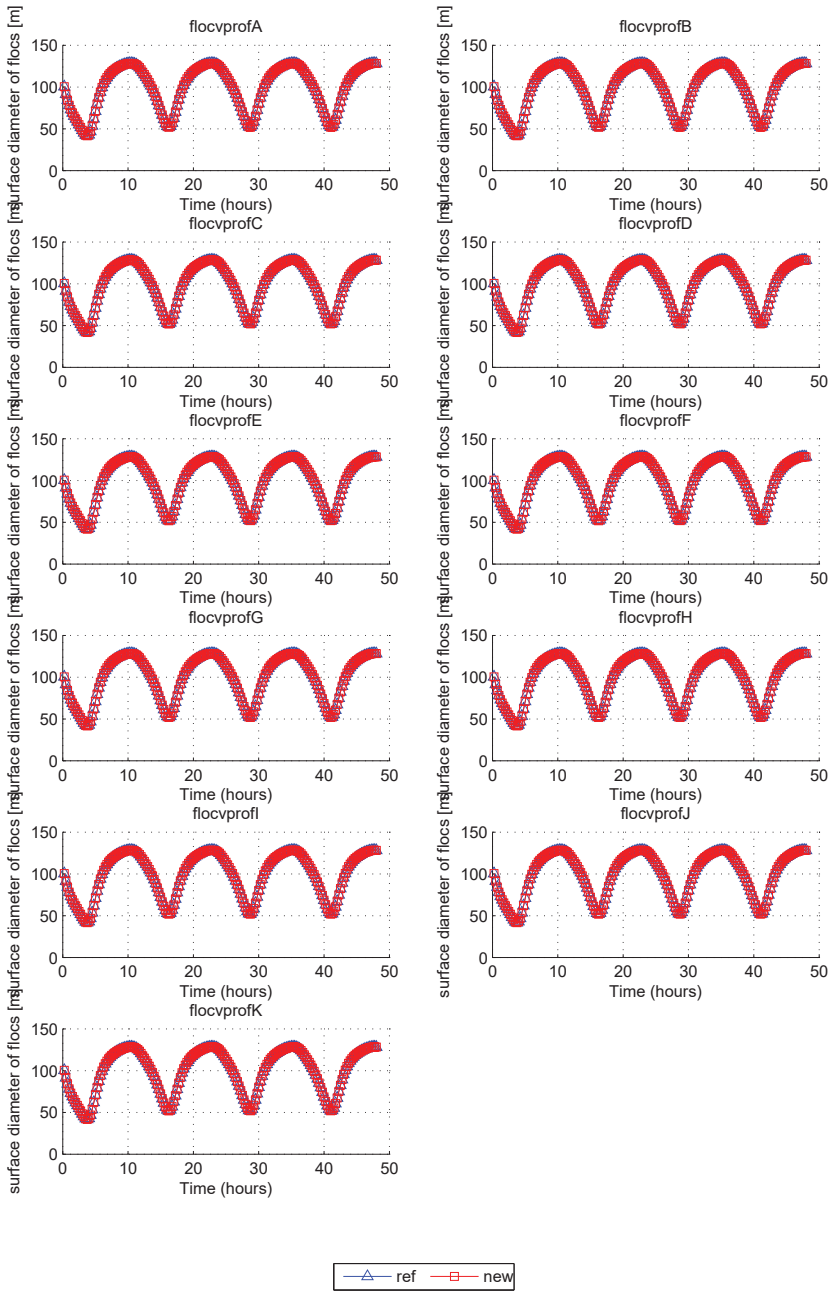


*Figure 10.74:* ***flocvprof****: Time series (hours) of the surface floc diameter* floc_dia_sur *(m).*

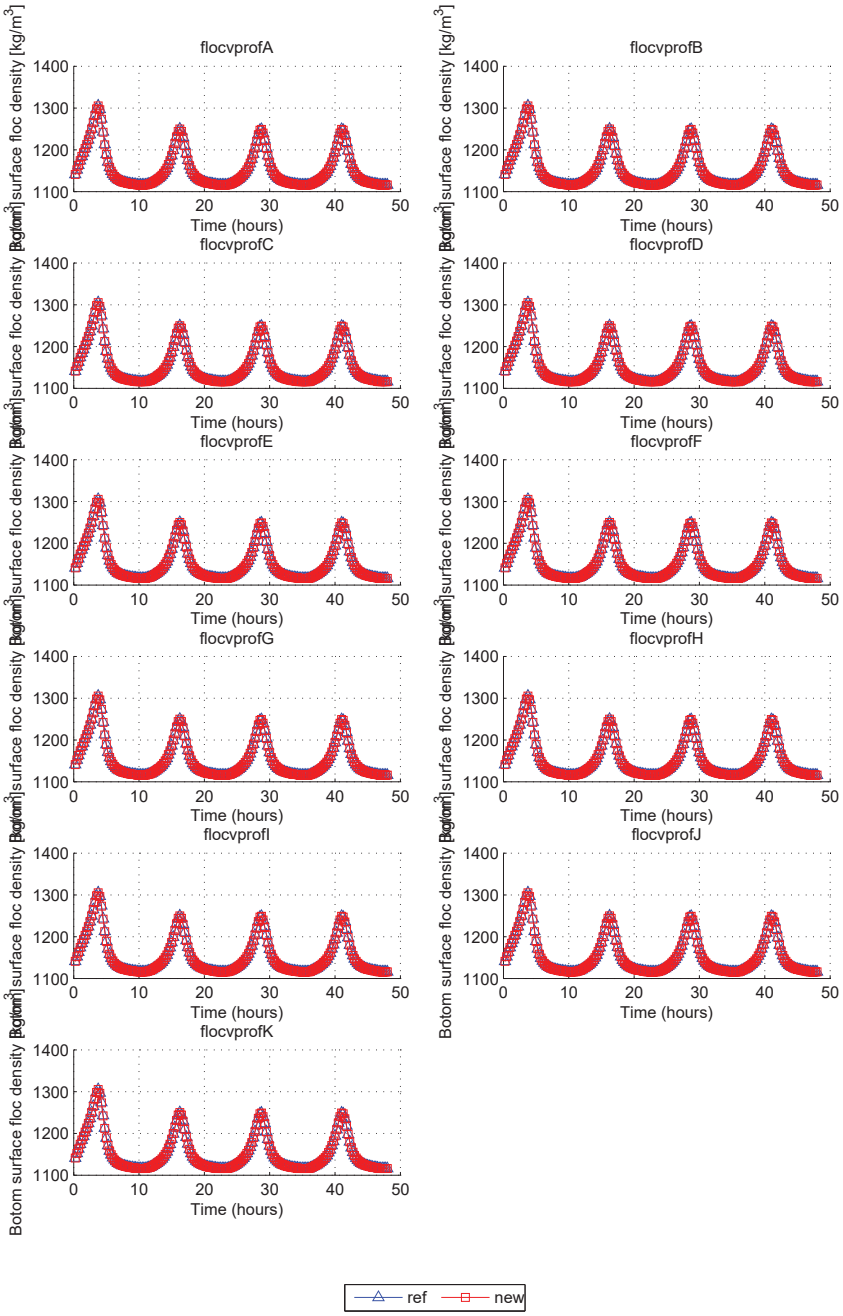


*Figure 10.75:* ***flocvprof:*** *Time series (hours) of the surface floc density* floc_dens_sur *(m).*

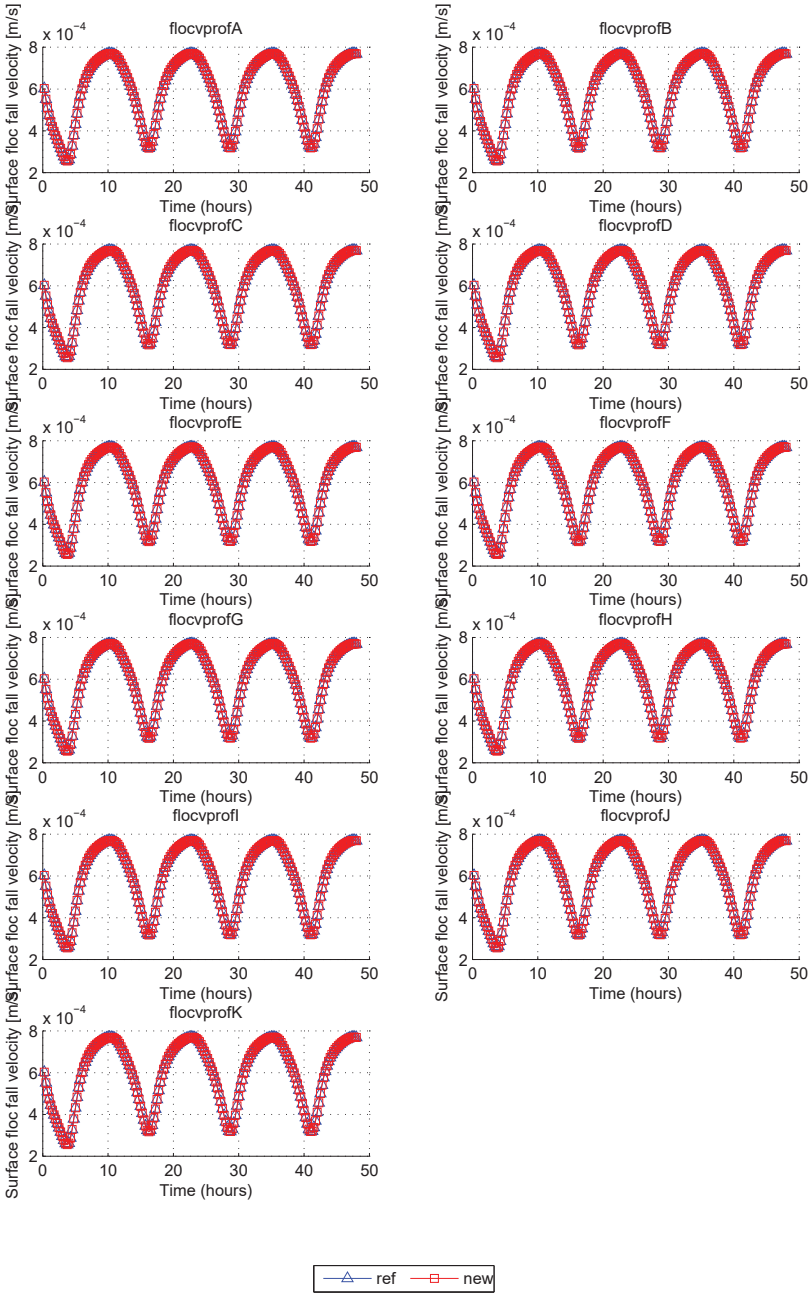


*Figure 10.76:* ***flocvprof****: Time series (hours) of the surface floc fall velocity* floc_ws_sur *(m/s).*

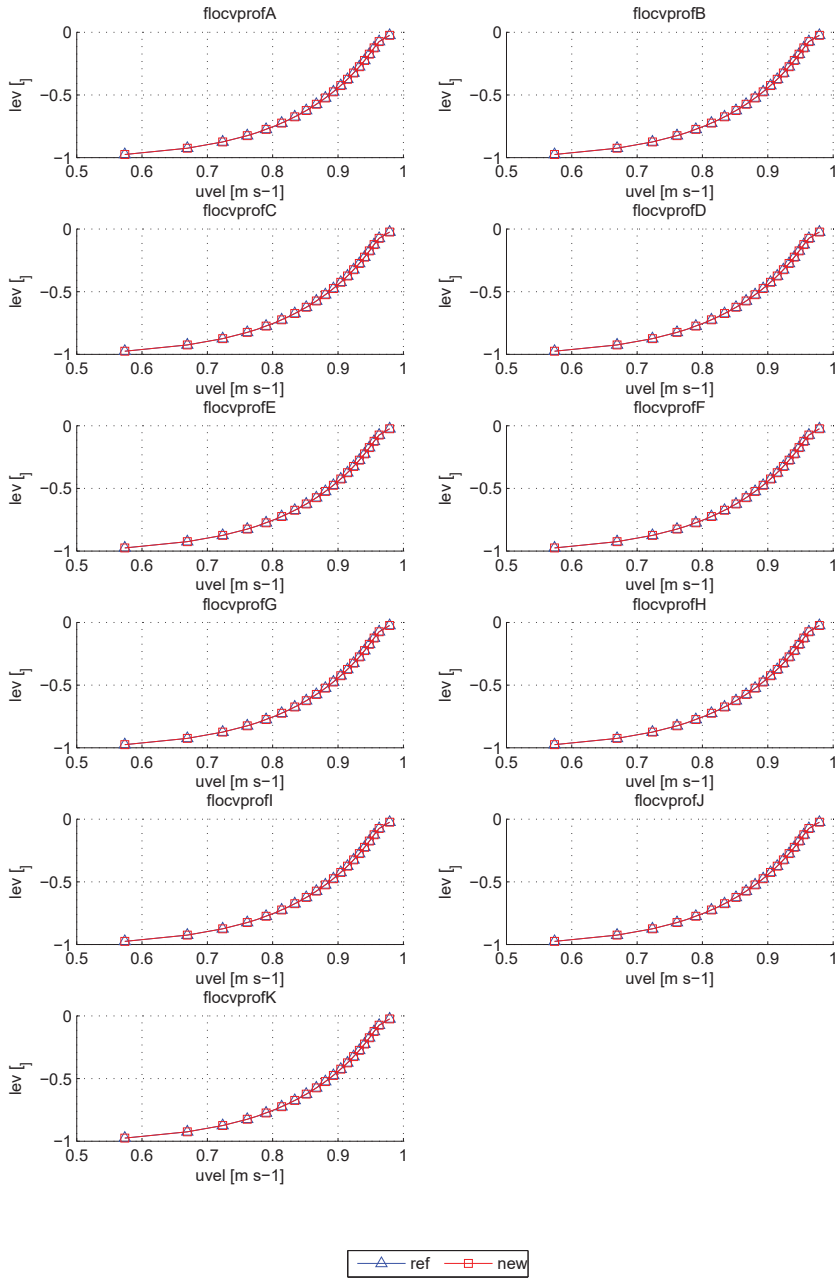


*Figure 10.77:* ***flocvprof****: Vertical profile of the current (m/s) at the end of the simulation.*

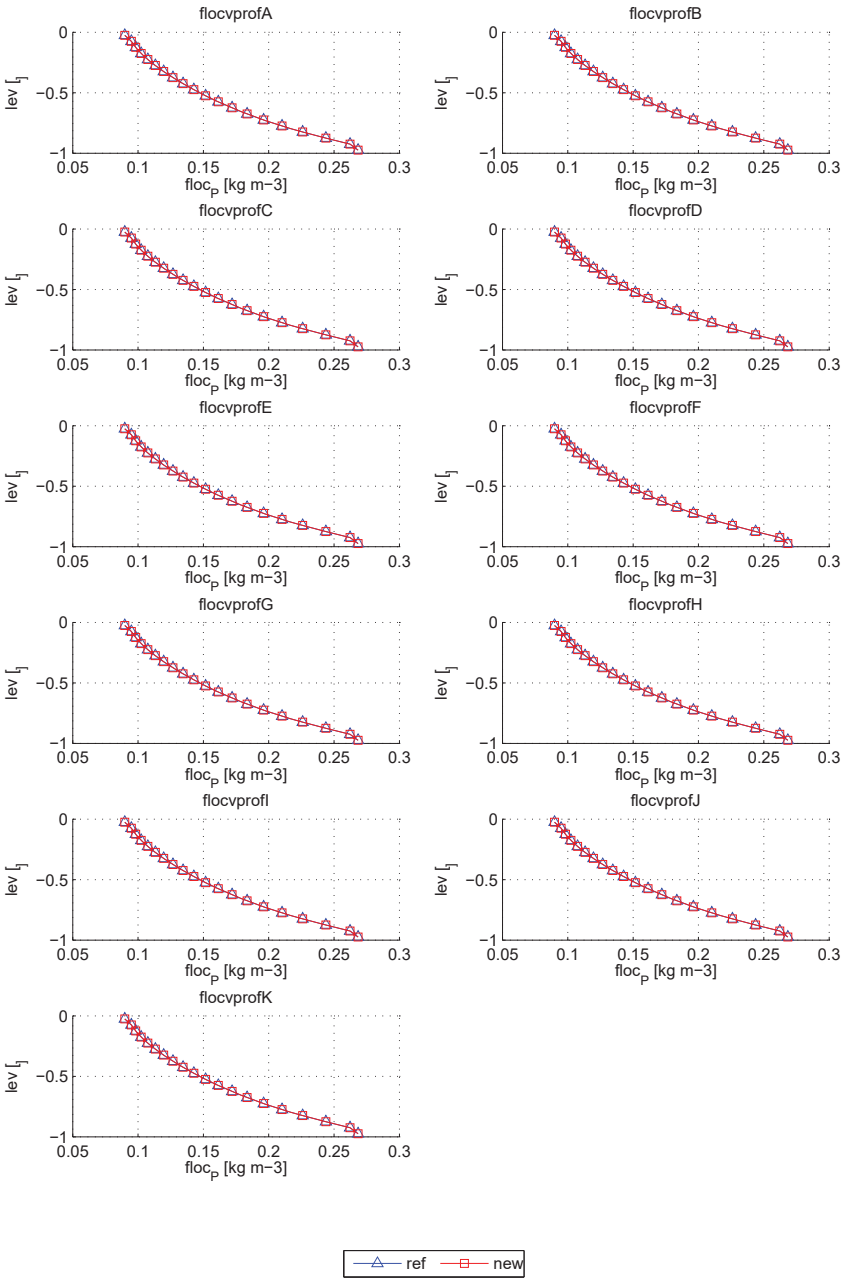


*Figure 10.78:* ***flocvprof****: Vertical profile of the flocculi concentration (kg/m$^3$) at the end of the simulation.*

### 10.8.4 Calculation time

Tables 10.15, 10.16 and 10.17 compare the time spent by COHERENS in each module called for each run of the test case, both for the reference and the new version. Results are given in percentage of the total time. The sum of all percentages is greater than 100% because the calulation time in a routine includes the time spent in all the routines called within this routine.

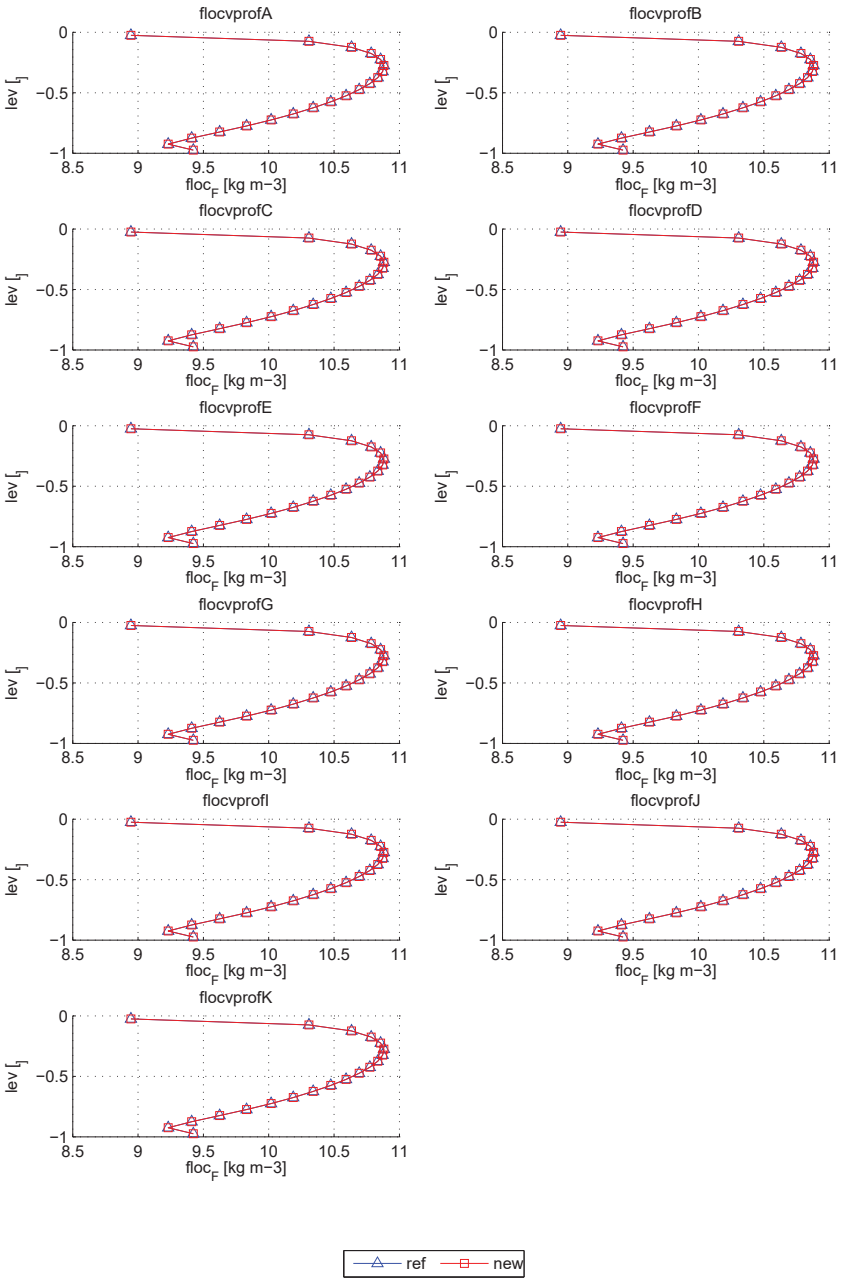


*Figure 10.79:* ***flocvprof****: Vertical profile of the floc concentration (kg/m$^3$) at the end of the simulation.*

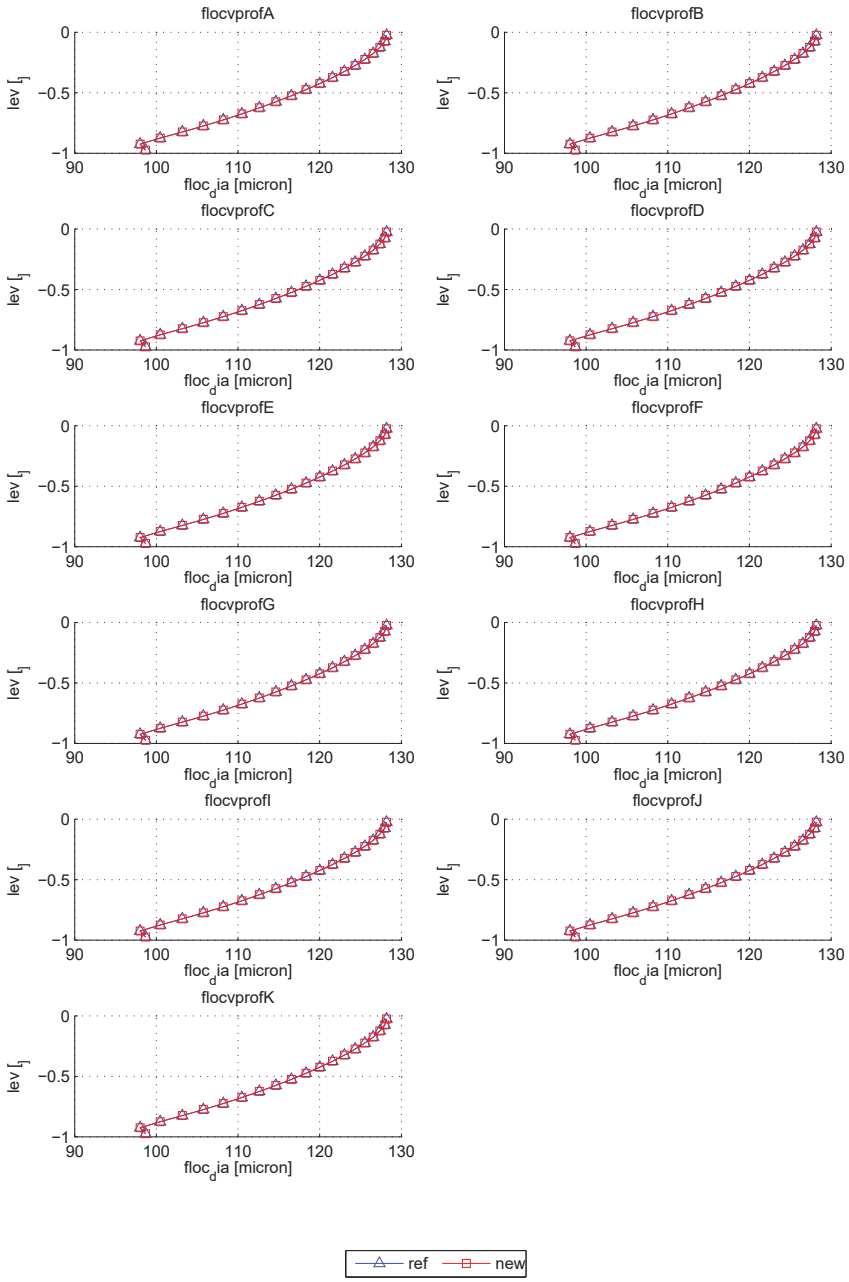


*Figure 10.80:* ***flocvprof****: Vertical profile of the floc diameter (m) at the end of the simulation.*

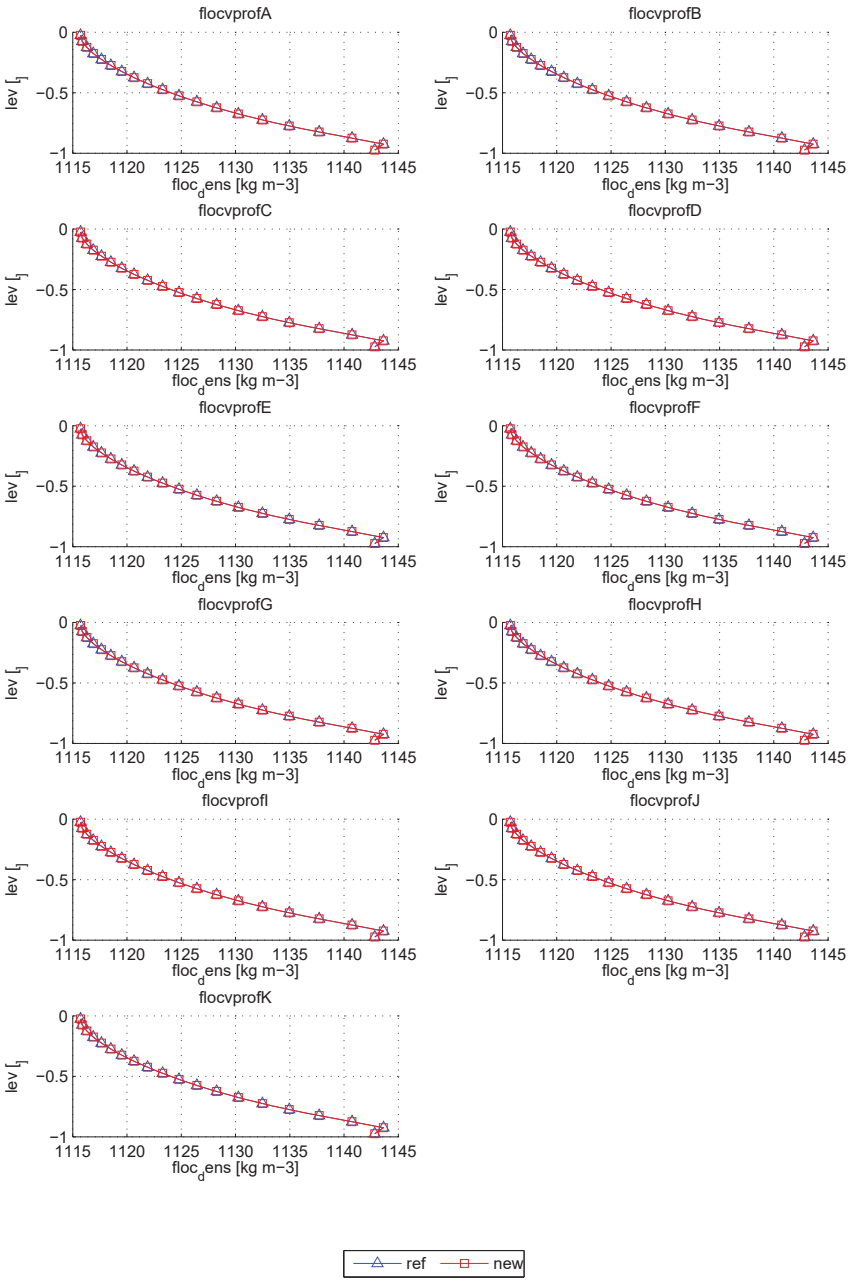


*Figure 10.81:* ***flocvprof****: Vertical profile of the floc density (kg/m$^3$) at the end of the simulation.*

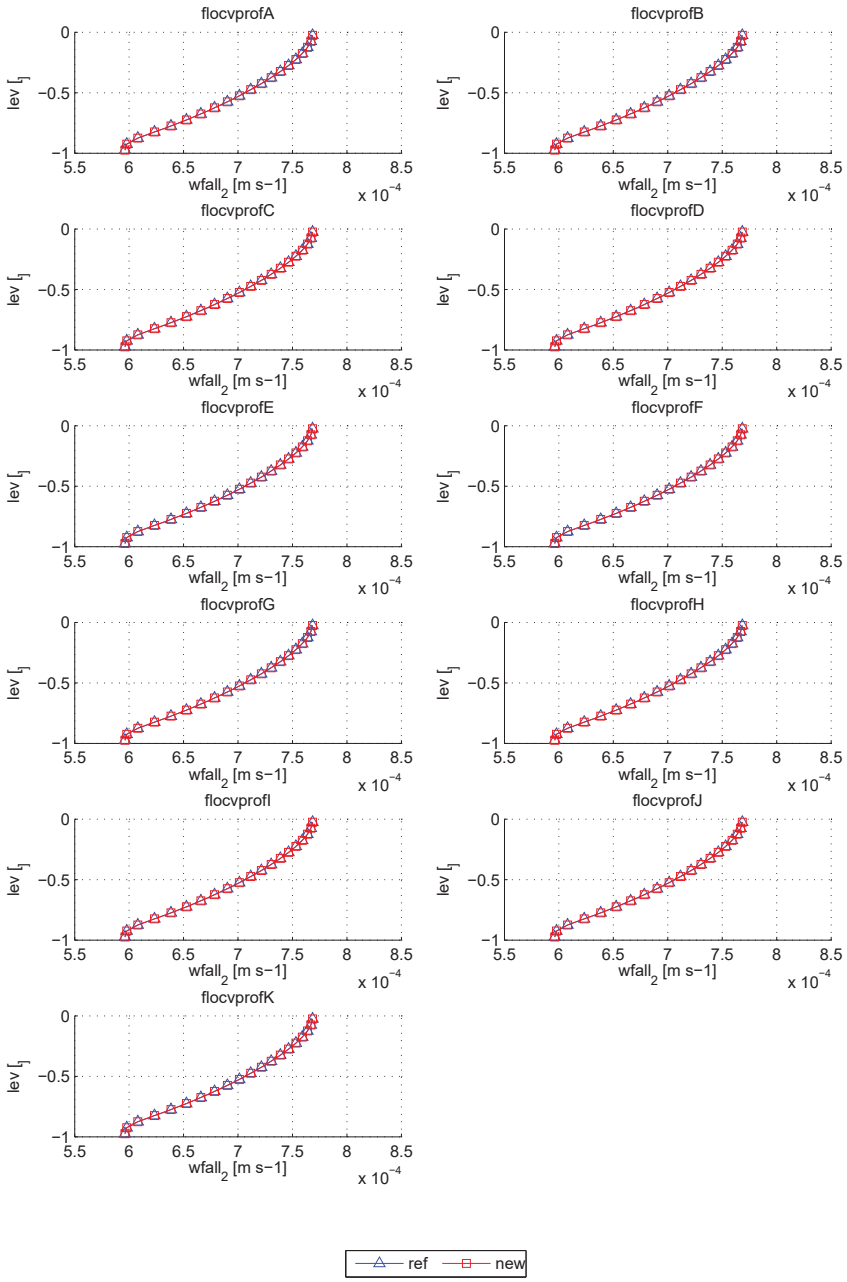


*Figure 10.82:* ***flocvprof****: Vertical profile of the floc fall velocity (m/s) at the end of the simulation.*

| Run name | flocvprof1A | | flocvprof1B | | flocvprof1C | | flocvprof1D | |
|---|---|---|---|---|---|---|---|---|
| | ref | new | ref | new | ref | new | ref | new |
| Hydrodynamics | 23.4 % | 27.4 % | 23.5 % | 23.7 % | 27.3 % | 27.2 % | 23.6 % | 27.4 % |
| 1D mode | 18.2 % | 21.8 % | 18.4 % | 18.2 % | 21.2 % | 21.1 % | 18.3 % | 21.3 % |
| 3D mode | 17.9 % | 21.4 % | 18.0 % | 17.9 % | 20.9 % | 20.7 % | 18.0 % | 21.0 % |
| Density | 2.5 % | 2.7 % | 2.5 % | 2.5 % | 3.0 % | 3.1 % | 2.7 % | 2.9 % |
| Initialisation | 0.1 % | 0.1 % | 0.1 % | 0.1 % | 0.1 % | 0.1 % | 0.2 % | 0.1 % |
| Transport | 47.3 % | 54.3 % | 46.6 % | 46.9 % | 54.6 % | 54.3 % | 47.0 % | 54.4 % |
| Advection | 13.9 % | 16.4 % | 13.9 % | 14.0 % | 16.3 % | 15.8 % | 13.9 % | 15.6 % |
| Vertical diffusion | 24.7 % | 28.3 % | 24.8 % | 24.5 % | 28.0 % | 28.9 % | 24.5 % | 28.5 % |
| Input | 0.0 % | % | 0.0 % | % | % | % | 0.0 % | % |
| Output | 0.1 % | 0.1 % | 0.1 % | 0.2 % | 0.1 % | 0.1 % | 0.2 % | 0.2 % |
| Input/output | 0.1 % | 0.1 % | 0.1 % | 0.2 % | 0.1 % | 0.1 % | 0.2 % | 0.2 % |
| netCDF calls | 0.1 % | 0.1 % | 0.1 % | 0.1 % | 0.1 % | 0.1 % | 0.2 % | 0.2 % |
| Array interpolation | 7.8 % | 10.0 % | 8.3 % | 8.1 % | 9.8 % | 9.1 % | 8.5 % | 9.4 % |
| User calls | 0.2 % | 0.2 % | 0.2 % | 0.3 % | 0.3 % | 0.2 % | 0.2 % | 0.4 % |
| Library calls | 4.3 % | 5.1 % | 4.3 % | 4.2 % | 5.1 % | 4.7 % | 4.4 % | 5.0 % |
| Boundary conditions | 2.2 % | 2.4 % | 2.2 % | 2.4 % | 2.6 % | 2.6 % | 2.2 % | 2.5 % |
| Sediment | 44.4 % | 50.9 % | 43.7 % | 43.9 % | 50.7 % | 50.7 % | 43.6 % | 50.7 % |
| **Total time** | 14$s$.820 | 12$s$.469 | 14$s$.708 | 14$s$.715 | 12$s$.561 | 12$s$.387 | 14$s$.673 | 12$s$.049 |

*Table 10.15:* ***flocvprof****: Total calculation time and percentage of total time spent by* COHERENS *in each module (part 1).*

| Run name | flocvprof1E | | flocvprof1F | | flocvprof1G | | flocvprof1H | |
|---|---|---|---|---|---|---|---|---|
| | ref | new | ref | new | ref | new | ref | new |
| Hydrodynamics | 27.3 % | 27.1 % | 23.7 % | 27.3 % | 27.0 % | 27.0 % | 26.6 % | 23.2 % |
| 1D mode | 21.4 % | 21.2 % | 18.6 % | 21.1 % | 21.0 % | 21.2 % | 21.0 % | 18.2 % |
| 3D mode | 21.0 % | 20.7 % | 18.3 % | 20.8 % | 20.5 % | 20.9 % | 20.6 % | 17.8 % |
| Density | 3.1 % | 2.8 % | 2.6 % | 3.1 % | 2.9 % | 3.0 % | 3.0 % | 2.6 % |
| Initialisation | 0.1 % | 0.1 % | 0.1 % | 0.1 % | 0.1 % | 0.2 % | 0.1 % | 0.1 % |
| Transport | 54.7 % | 54.4 % | 46.7 % | 54.1 % | 54.7 % | 54.8 % | 54.5 % | 46.7 % |
| Advection | 16.2 % | 15.5 % | 13.2 % | 15.9 % | 16.1 % | 16.6 % | 16.2 % | 13.5 % |
| Vertical diffusion | 28.8 % | 28.4 % | 24.7 % | 28.6 % | 28.8 % | 28.7 % | 28.8 % | 24.7 % |
| Input | 0.0 % | 0.0 % | % | 0.0 % | 0.0 % | 0.0 % | 0.0 % | 0.0 % |
| Output | 0.1 % | 0.1 % | 0.1 % | 0.2 % | 0.1 % | 0.1 % | 0.1 % | 0.1 % |
| Input/output | 0.1 % | 0.1 % | 0.1 % | 0.2 % | 0.1 % | 0.2 % | 0.1 % | 0.1 % |
| netCDF calls | 0.1 % | 0.1 % | 0.1 % | 0.1 % | 0.1 % | 0.1 % | 0.1 % | 0.1 % |
| Array interpolation | 9.6 % | 9.6 % | 8.6 % | 9.2 % | 9.3 % | 9.2 % | 9.3 % | 8.0 % |
| User calls | 0.2 % | 0.2 % | 0.2 % | 0.2 % | 0.3 % | 0.3 % | 0.3 % | 0.2 % |
| Library calls | 4.8 % | 5.1 % | 4.4 % | 5.0 % | 5.2 % | 4.8 % | 4.8 % | 4.4 % |
| Boundary conditions | 2.5 % | 2.4 % | 2.2 % | 2.4 % | 2.4 % | 2.5 % | 2.5 % | 2.0 % |
| Sediment | 51.0 % | 50.6 % | 43.5 % | 50.7 % | 50.9 % | 50.7 % | 51.2 % | 43.7 % |
| **Total time** | 13*s*.627 | 12*s*.068 | 14*s*.628 | 12*s*.542 | 12*s*.096 | 13*s*.526 | 12*s*.136 | 14*s*.522 |

*Table 10.16:* ***flocvprof****: Total calculation time and percentage of total time spent by* COHERENS *in each module (part 2).*

| Run name | flocvprof1I | | flocvprof1J | | flocvprof1K | |
|---|---|---|---|---|---|---|
| | ref | new | ref | new | ref | new |
| Hydrodynamics | 27.3 % | 27.2 % | 27.1 % | 23.1 % | 27.0 % | 27.4 % |
| 1D mode | 21.2 % | 21.1 % | 20.9 % | 17.8 % | 21.1 % | 21.4 % |
| 3D mode | 20.8 % | 20.8 % | 20.6 % | 17.5 % | 20.8 % | 21.1 % |
| Density | 3.1 % | 3.1 % | 3.1 % | 2.5 % | 3.1 % | 3.1 % |
| Initialisation | 0.1 % | 0.1 % | 0.2 % | 0.1 % | 0.1 % | 0.1 % |
| Transport | 54.4 % | 53.9 % | 54.8 % | 47.6 % | 53.7 % | 54.0 % |
| Advection | 15.8 % | 15.9 % | 16.1 % | 13.9 % | 15.9 % | 16.0 % |
| Vertical diffusion | 29.5 % | 28.1 % | 29.3 % | 25.1 % | 29.2 % | 28.9 % |
| Input | 0.0 % | % | % | 0.0 % | % | % |
| Output | 0.2 % | 0.1 % | 0.2 % | 0.1 % | 0.2 % | 0.2 % |
| Input/output | 0.2 % | 0.1 % | 0.2 % | 0.1 % | 0.2 % | 0.2 % |
| netCDF calls | 0.1 % | 0.1 % | 0.1 % | 0.1 % | 0.2 % | 0.1 % |
| Array interpolation | 9.4 % | 9.3 % | 9.2 % | 8.1 % | 9.5 % | 9.6 % |
| User calls | 0.3 % | 0.3 % | 0.3 % | 0.2 % | 0.3 % | 0.3 % |
| Library calls | 4.6 % | 4.8 % | 4.9 % | 4.5 % | 5.0 % | 5.0 % |
| Boundary conditions | 2.4 % | 2.3 % | 2.6 % | 2.1 % | 2.6 % | 2.5 % |
| Sediment | 50.9 % | 50.9 % | 50.8 % | 44.6 % | 50.6 % | 50.1 % |
| **Total time** | 12$s$.226 | 12$s$.649 | 12$s$.126 | 15$s$.668 | 12$s$.313 | 12$s$.595 |

*Table 10.17:* ***flocvprof****: Total calculation time and percentage of total time spent by* COHERENS *in each module (part 3).*

## 10.9 *flocest*

### 10.9.1 Description

The flloculation module is applied to an estuarine configuration. The hydrodynamic setup is the same as experiment ***D*** of the test case ***obcest***.
The following experimenst are defined

**A:** Initial concentrations of flocculi and flocs are set to zero. Diameter and density of the flocculi are set to respectively 5 $\mu$m and 1600.0 $kg/m^3$15. Critical shear stress is 0.001 $m^2/s^2$.

**B:** As experiment ***A*** except that an initial concentrations of flocculi and flocs are prescribed respectively in the estuary and the river channel.

**C:** As experiment ***A*** except that the flocculi mow have of diameter of 30 $\mu$m.

**D:** As experiment ***A*** except that the critical shear stress is set to 0.002 $m^2/s^2$.

**D:** As experiment ***A*** now including turbidity flow.

The following test case parameters are defined. The non-global parameters are obtained at 9 stations.

| | |
|---|---|
| Pintmass | Volume integrated mass [tons] of flocculi. |
| Fintmass | Volume integrated mass [tons] of flocs. |
| Sedintmass | Volume integrated mass [tons] of all sediment. |
| Pdens | Concentration [kg/m$^3$] of flocculi. |
| Fdens | Concentration [kg/m$^3$] of flocs. |
| floc_dens | Floc mass density [kg/m$^3$]. |
| floc_dia | Floc diameter [$\mu$m]. |
| floc_nc | Number of flocculi within flocs. |
| Fwfal | Fall velocity of flocs [cm/s]. |

### 10.9.2 Log files

This section contains the COHERENS *log* files reporting errors (*errlog*) and warnings (*warlog*) encountered while running the test case.
An *errlog* contains the list of critical errors encountered causing the simulation to stop. It is created by COHERENS at the beginning of the simulation

and deleted in case of successful completion. An empty *errlog* also indicates that something went wrong.
A *warlog* contains a list of changes in setup variables and switches automatically performed by COHERENS during initialisation and warnings for "suspect" model settings.
Errlogs of reference version:

```
no errlog/warlog file
```

Errlogs of new version:

```
no errlog/warlog file
```

Warlogs of reference version:

```
flocest0.warlog
WARNING: value of integer parameter iopt_waves_pres is set from 1 to 0
WARNING: value of integer parameter iopt_fld_alpha is set from 1 to 0
WARNING: value of integer parameter iopt_meteo_pres is set from 1 to 0
WARNING: value of real parameter theta_sur is set from   0.5000000 to
    0.000000
WARNING: value of integer parameter itsimp is set from 0 to 1
WARNING: value of integer parameter nprocsx is set from 0 to 1
WARNING: value of integer parameter nprocsy is set from 0 to 1

flocestA.warlog
WARNING: value of integer parameter iopt_waves_pres is set from 1 to 0
WARNING: value of integer parameter iopt_fld_alpha is set from 1 to 0
WARNING: value of integer parameter iopt_meteo_pres is set from 1 to 0
WARNING: value of real parameter theta_sur is set from   0.5000000 to
    0.000000
WARNING: value of integer parameter nprocsx is set from 0 to 1
WARNING: value of integer parameter nprocsy is set from 0 to 1
WARNING: value of integer parameter iopt_sed_bedeq is set from 1 to 0
WARNING: value of integer parameter iopt_sed_toteq is set from 1 to 0
WARNING: value of integer parameter iopt_sed_type is set from 1 to 2
WARNING: value of integer parameter nrquad_wav is set from 10 to 1
WARNING: value of integer parameter nf is set from 1 to 3
WARNING: using default initial conditions for sediments

flocestB.warlog
WARNING: value of integer parameter iopt_waves_pres is set from 1 to 0
WARNING: value of integer parameter iopt_fld_alpha is set from 1 to 0
WARNING: value of integer parameter iopt_meteo_pres is set from 1 to 0
WARNING: value of real parameter theta_sur is set from   0.5000000 to
    0.000000
WARNING: value of integer parameter nprocsx is set from 0 to 1
WARNING: value of integer parameter nprocsy is set from 0 to 1
WARNING: value of integer parameter iopt_sed_bedeq is set from 1 to 0
WARNING: value of integer parameter iopt_sed_toteq is set from 1 to 0
WARNING: value of integer parameter iopt_sed_type is set from 1 to 2
WARNING: value of integer parameter nrquad_wav is set from 10 to 1
WARNING: value of integer parameter nf is set from 1 to 3

flocestC.warlog
WARNING: value of integer parameter iopt_waves_pres is set from 1 to 0
WARNING: value of integer parameter iopt_fld_alpha is set from 1 to 0
WARNING: value of integer parameter iopt_meteo_pres is set from 1 to 0
```

```
WARNING: value of real parameter theta_sur is set from   0.5000000 to
    0.000000
WARNING: value of integer parameter nprocsx is set from 0 to 1
WARNING: value of integer parameter nprocsy is set from 0 to 1
WARNING: value of integer parameter iopt_sed_bedeq is set from 1 to 0
WARNING: value of integer parameter iopt_sed_toteq is set from 1 to 0
WARNING: value of integer parameter iopt_sed_type is set from 1 to 2
WARNING: value of integer parameter nrquad_wav is set from 10 to 1
WARNING: value of integer parameter nf is set from 1 to 3
WARNING: using default initial conditions for sediments

flocestD.warlog
WARNING: value of integer parameter iopt_waves_pres is set from 1 to 0
WARNING: value of integer parameter iopt_fld_alpha is set from 1 to 0
WARNING: value of integer parameter iopt_meteo_pres is set from 1 to 0
WARNING: value of real parameter theta_sur is set from   0.5000000 to
    0.000000
WARNING: value of integer parameter nprocsx is set from 0 to 1
WARNING: value of integer parameter nprocsy is set from 0 to 1
WARNING: value of integer parameter iopt_sed_bedeq is set from 1 to 0
WARNING: value of integer parameter iopt_sed_toteq is set from 1 to 0
WARNING: value of integer parameter iopt_sed_type is set from 1 to 2
WARNING: value of integer parameter nrquad_wav is set from 10 to 1
WARNING: value of integer parameter nf is set from 1 to 3
WARNING: using default initial conditions for sediments

flocestE.warlog
WARNING: value of integer parameter iopt_waves_pres is set from 1 to 0
WARNING: value of integer parameter iopt_fld_alpha is set from 1 to 0
WARNING: value of integer parameter iopt_meteo_pres is set from 1 to 0
WARNING: value of real parameter theta_sur is set from   0.5000000 to
    0.000000
WARNING: value of integer parameter nprocsx is set from 0 to 1
WARNING: value of integer parameter nprocsy is set from 0 to 1
WARNING: value of integer parameter iopt_sed_bedeq is set from 1 to 0
WARNING: value of integer parameter iopt_sed_toteq is set from 1 to 0
WARNING: value of integer parameter iopt_sed_type is set from 1 to 2
WARNING: value of integer parameter nrquad_wav is set from 10 to 1
WARNING: value of integer parameter nf is set from 1 to 3
WARNING: using default initial conditions for sediments
```

Warlogs of new version:

```
flocest0.warlog
WARNING: value of integer parameter iopt_vdif_rot is set from 1 to 0
WARNING: value of integer parameter iopt_waves_pres is set from 1 to 0
WARNING: value of integer parameter iopt_fld_alpha is set from 1 to 0
WARNING: value of integer parameter iopt_meteo_data is set from 1 to 0
WARNING: value of integer parameter iopt_meteo_heat is set from 1 to 0
WARNING: value of integer parameter iopt_meteo_pres is set from 1 to 0
WARNING: value of integer parameter iopt_meteo_stres is set from 1 to 0
WARNING: value of real parameter theta_sur is set from   0.5000000 to
    0.000000
WARNING: value of integer parameter itsimp is set from 0 to 1
WARNING: value of integer parameter nprocsx is set from 0 to 1
WARNING: value of integer parameter nprocsy is set from 0 to 1

flocestA.warlog
WARNING: using default initial conditions for sediments

flocestB.warlog
```

```
flocestC.warlog
WARNING: using default initial conditions for sediments

flocestD.warlog
WARNING: using default initial conditions for sediments

flocestE.warlog
WARNING: using default initial conditions for sediments
```

### 10.9.3 Comparison graphs

The following figures are plotted for each of the five experiments in the ***flocest*** test (each containing the data of the reference version and of the new version):

- Time series (hours) of volume integrated mass (tons) of flocculi Pintmass.
- Time series (hours) of volume integrated mass (tons) of flocs Fintmass.
- Time series (hours) of volume integrated mass (tons) of all sediment Sedintmass.
- Time series (hours) of flocculi bottom concentration (kg/m$^3$) Pdens at station 3.
- Time series (hours) of floc bottom concentration (kg/m$^3$) Fdens at station 6.
- Time series (hours) of floc bottom concentration (kg/m$^3$) floc_dens at station 9.
- Time series (hours) of surface floc diameter (m) floc_dia at station 4.
- Time series (hours) of mid-water number of flocculi within flocs floc_nc at station 5.
- Time series (hours) of mid-water floc fall velocity (cm/s) Fwfall at station 8.
- Horizontal profile of the bottom concentration (kg/m$^3$) of flocculi along a mid-channel transect at the end of the simulation.
- Horizontal profile of the bottom concentration (kg/m$^3$) of flocs along a mid-channel transect at the end of the simulation.

- Horizontal profile of the mid-water floc diameter (m) along a mid-channel transect at the end of the simulation.
- Horizontal profile of the surface floc mass density (kg/m$^3$) along a mid-channel transect at the end of the simulation.
- Horizontal profile of the mid-water floc fall velocity (m/s) along a mid-channel transect at the end of the simulation.

### 10.9.4 Calculation time

Tables 10.18 and 10.19 compare the time spent by COHERENS in each module called for each run of the test case, both for the reference and the new version. Results are given in percentage of the total time. The sum of all percentages is greater than 100% because the calulation time in a routine includes the time spent in all the routines called within this routine.

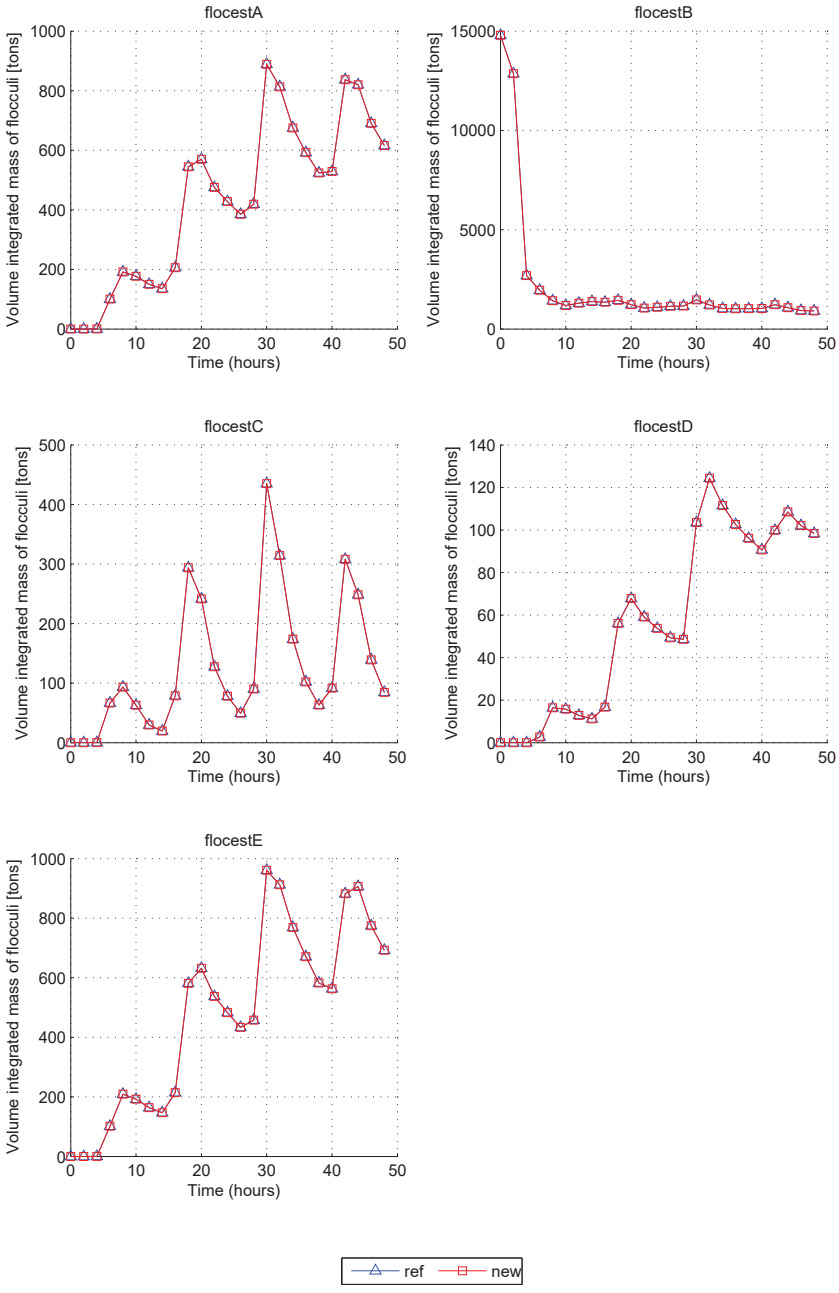


*Figure 10.83:* ***flocest****: Time series (hours) of volume integrated mass (tons) of flocculi* Pintmass.

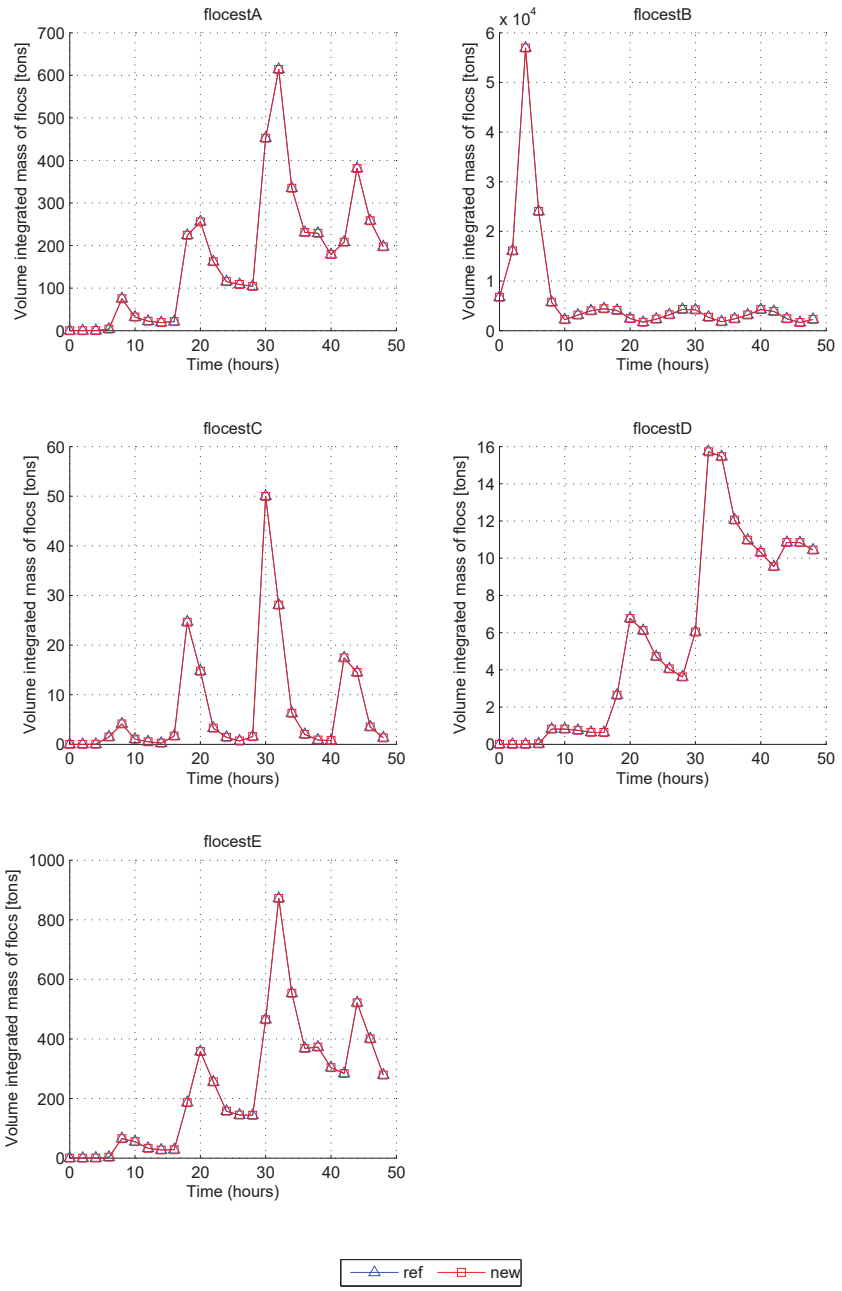


*Figure 10.84:* ***flocest****: Time series (hours) of volume integrated mass (tons) of flocs* Fintmass.

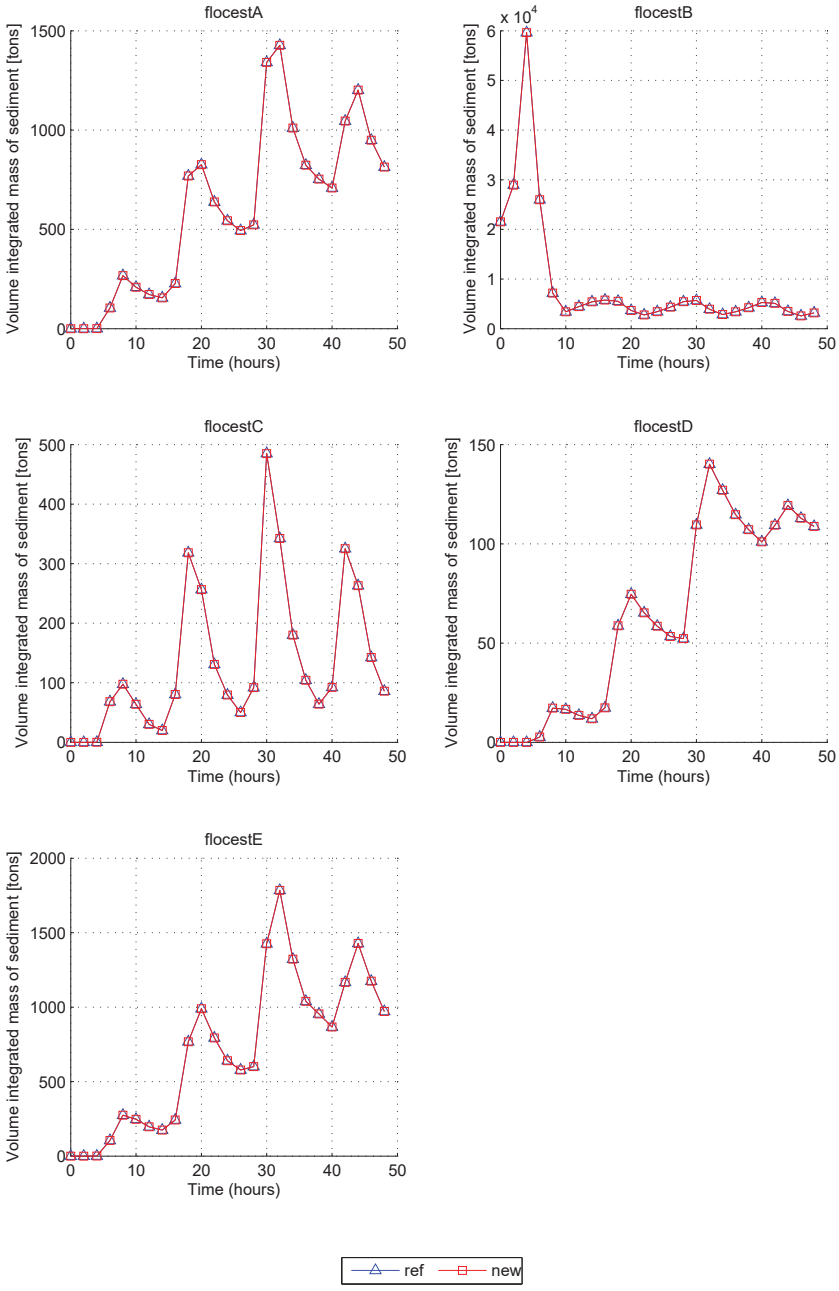


*Figure 10.85:* ***flocest****: Time series (hours) of volume integrated mass (tons) of all sediment* Sedintmass.

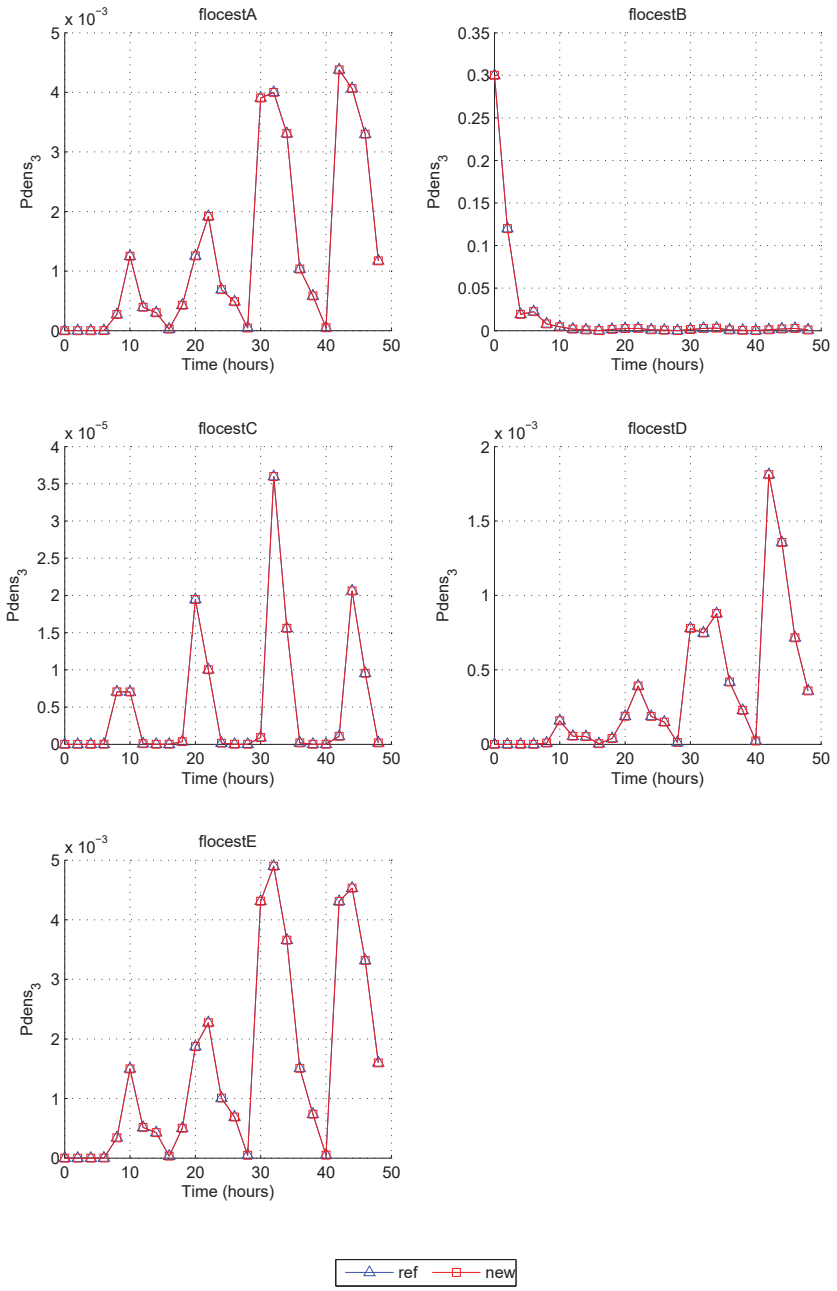


*Figure 10.86:* ***flocest****: Time series (hours) of flocculi bottom concentration (kg/m$^3$)* Pdens *at station 3.*

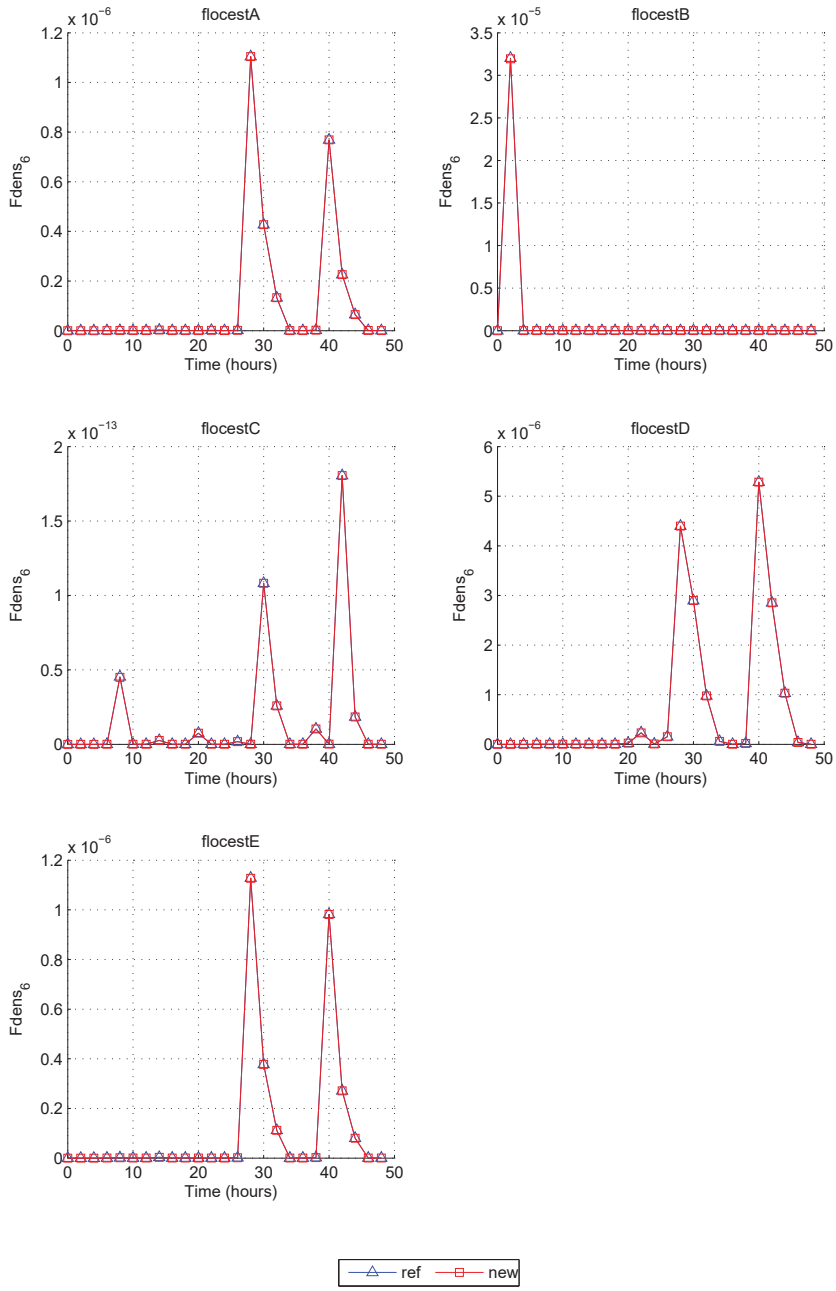


*Figure 10.87:* ***flocest****: Time series (hours) of floc bottom concentration (kg/m$^3$)* Fdens *at station 6.*

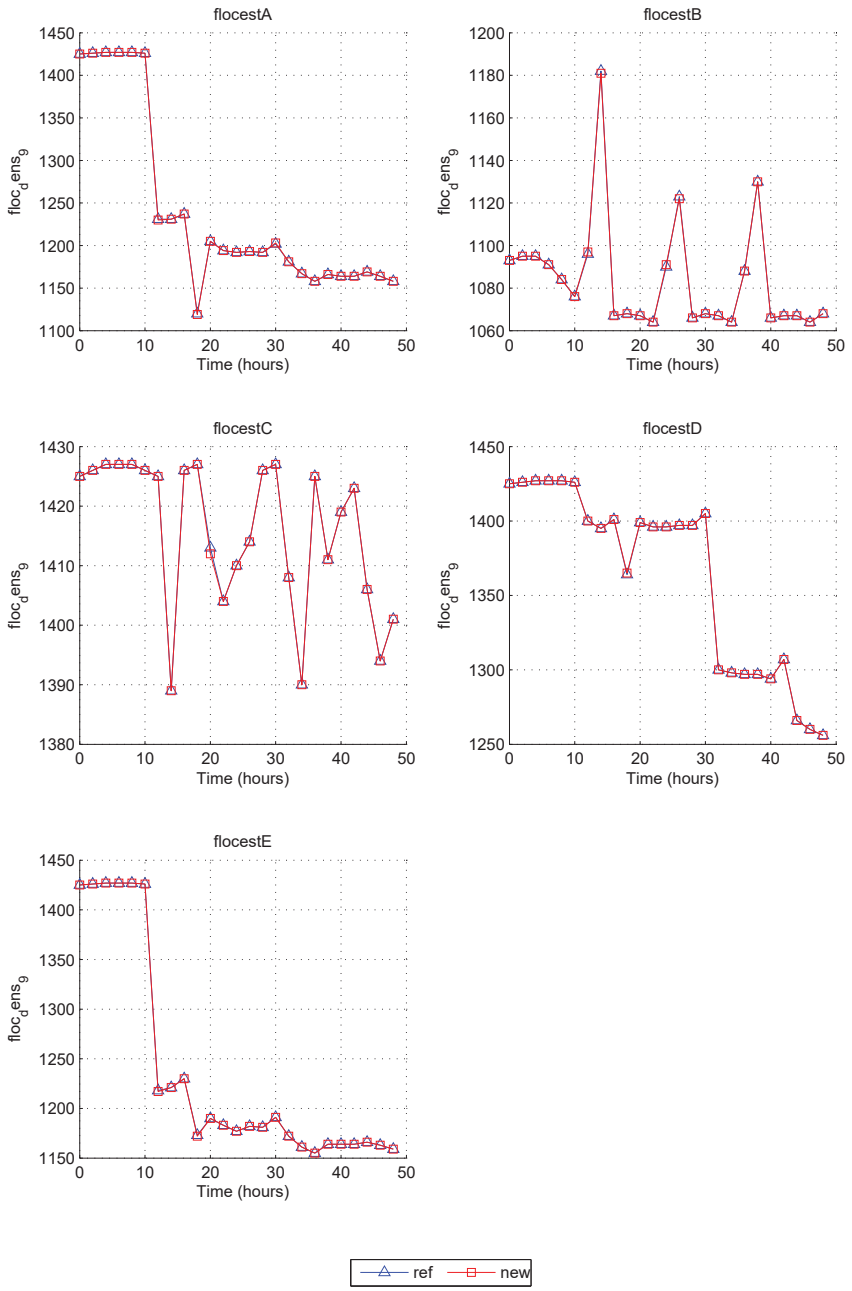


*Figure 10.88:* ***flocest****: Time series (hours) of floc bottom concentration (kg/m$^3$)* floc_dens *at station 9.*

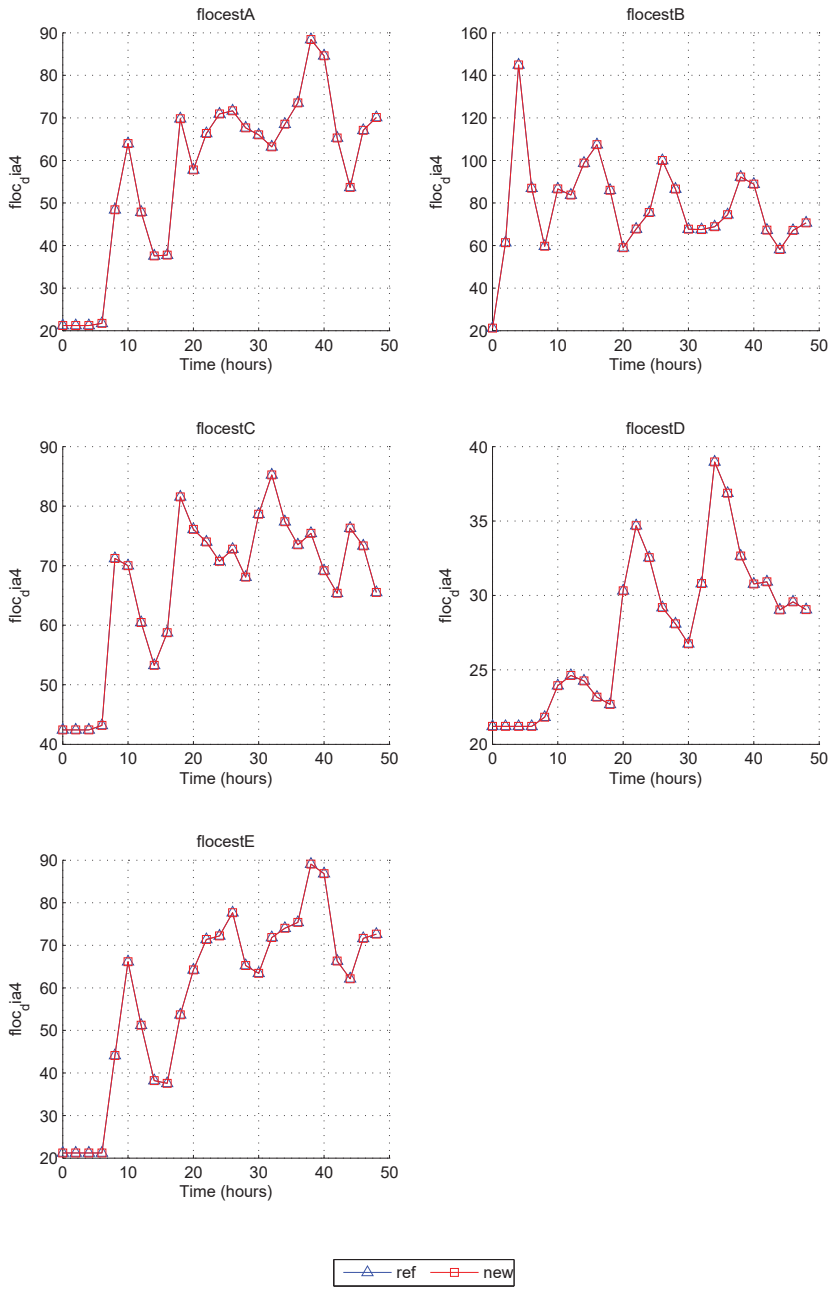


*Figure 10.89:* ***flocest****: Time series (hours) of surface floc diameter (m)* floc_dia *at station 4.*

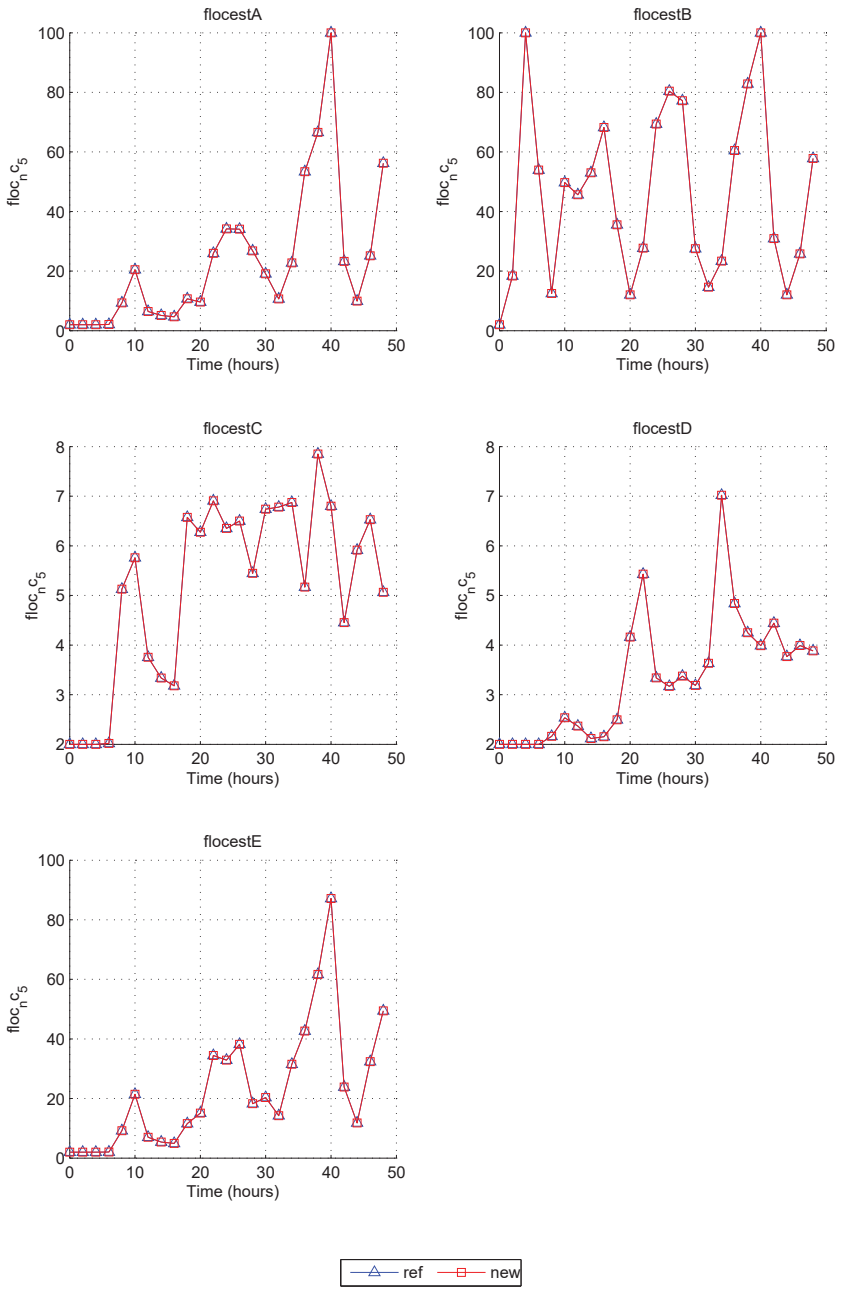


*Figure 10.90:* ***flocest****: Time series (hours) of mid-water number of flocculi within flocs* floc_nc *at station 5.*

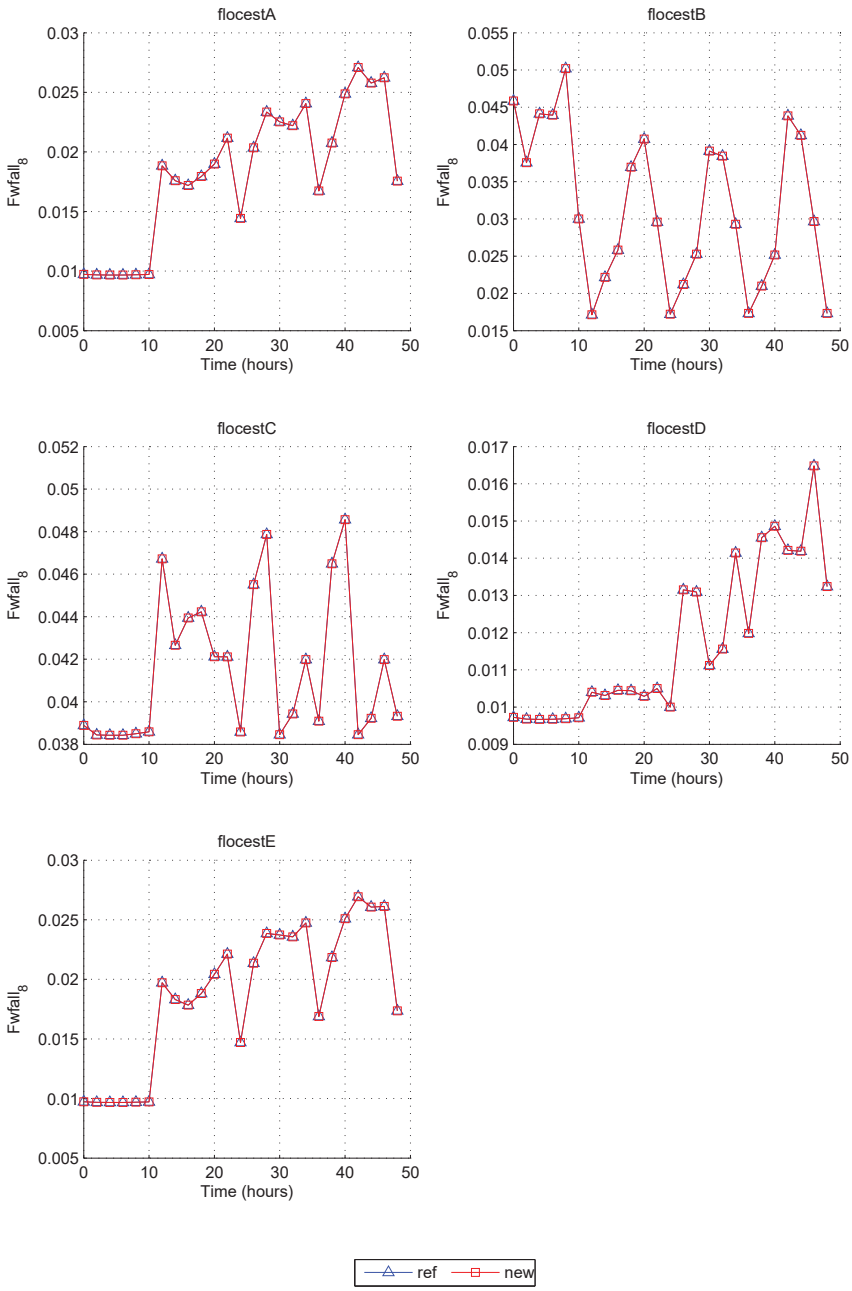


*Figure 10.91:* ***flocest****: Time series (hours) of mid-water floc fall velocity (cm/s)* Fwfall *at station 8.*

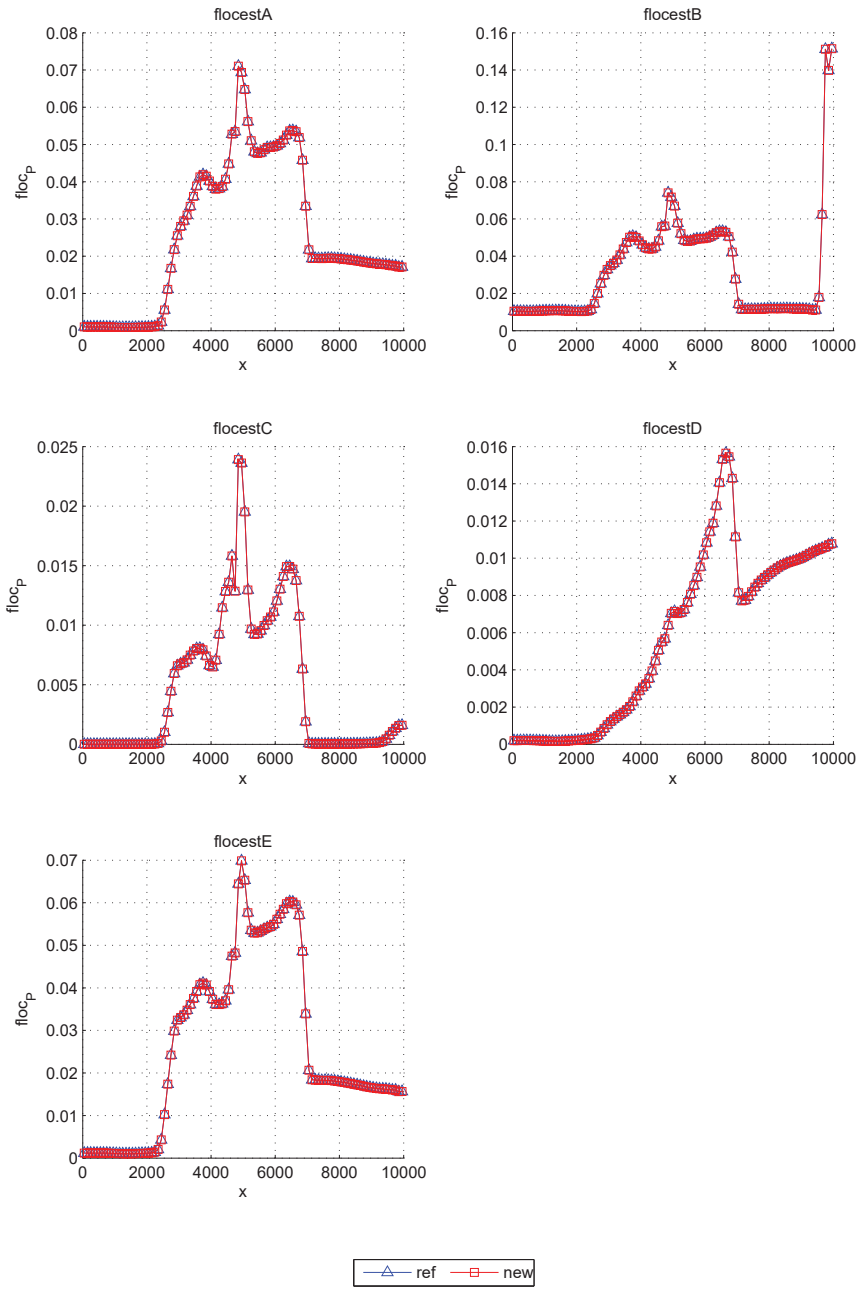


*Figure 10.92:* ***flocest****: Horizontal profile of the bottom concentration ($kg/m^3$) of flocculi along a mid-channel transect at the end of the simulation.*

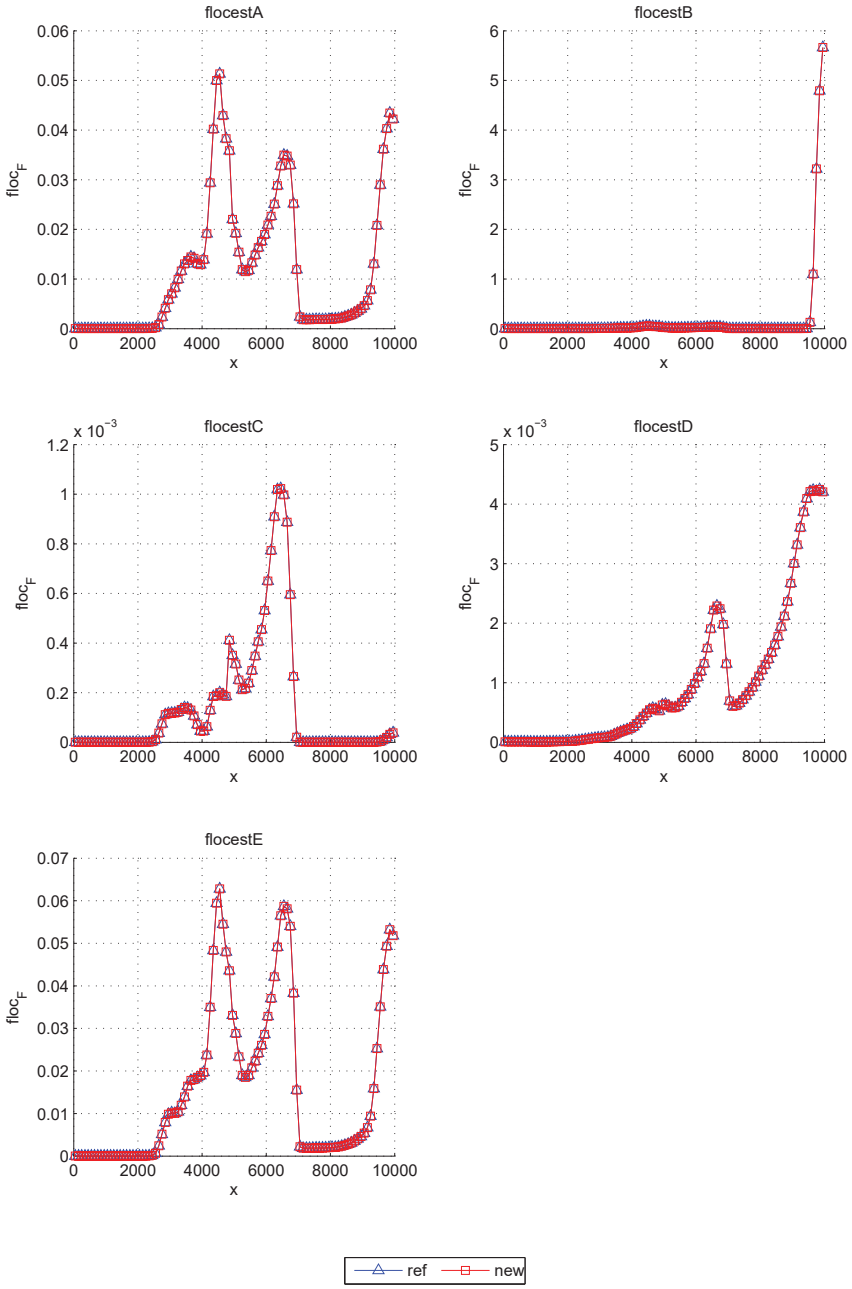


*Figure 10.93:* ***flocest****: Horizontal profile of the bottom concentration ($kg/m^3$) of flocs along a mid-channel transect at the end of the simulation.*

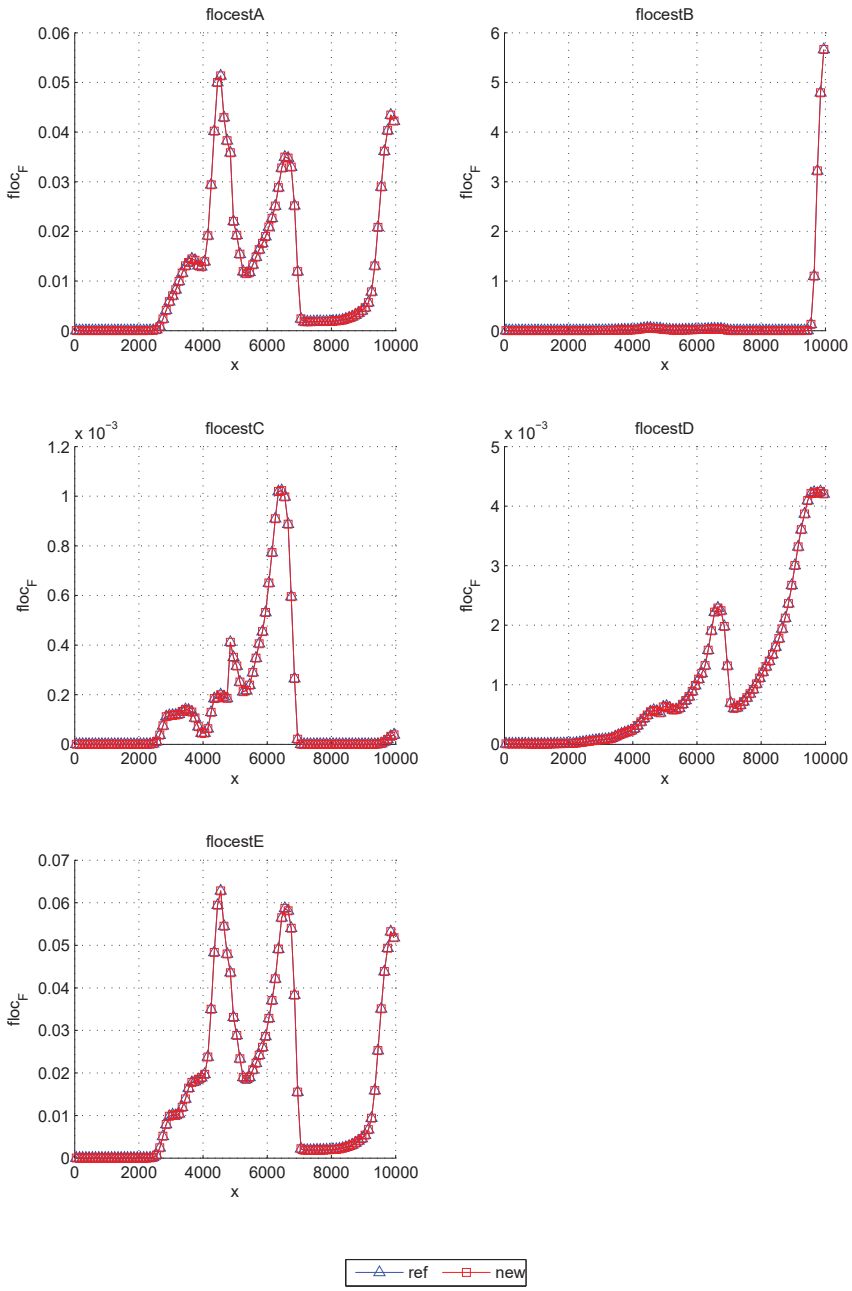


*Figure 10.94:* ***flocest****: Horizontal profile of the mid-water floc diameter (m) along a mid-channel transect at the end of the simulation.*


*Figure 10.95:* ***flocest****: Horizontal profile of the surface floc mass density ($kg/m^3$) along a mid-channel transect at the end of the simulation.*

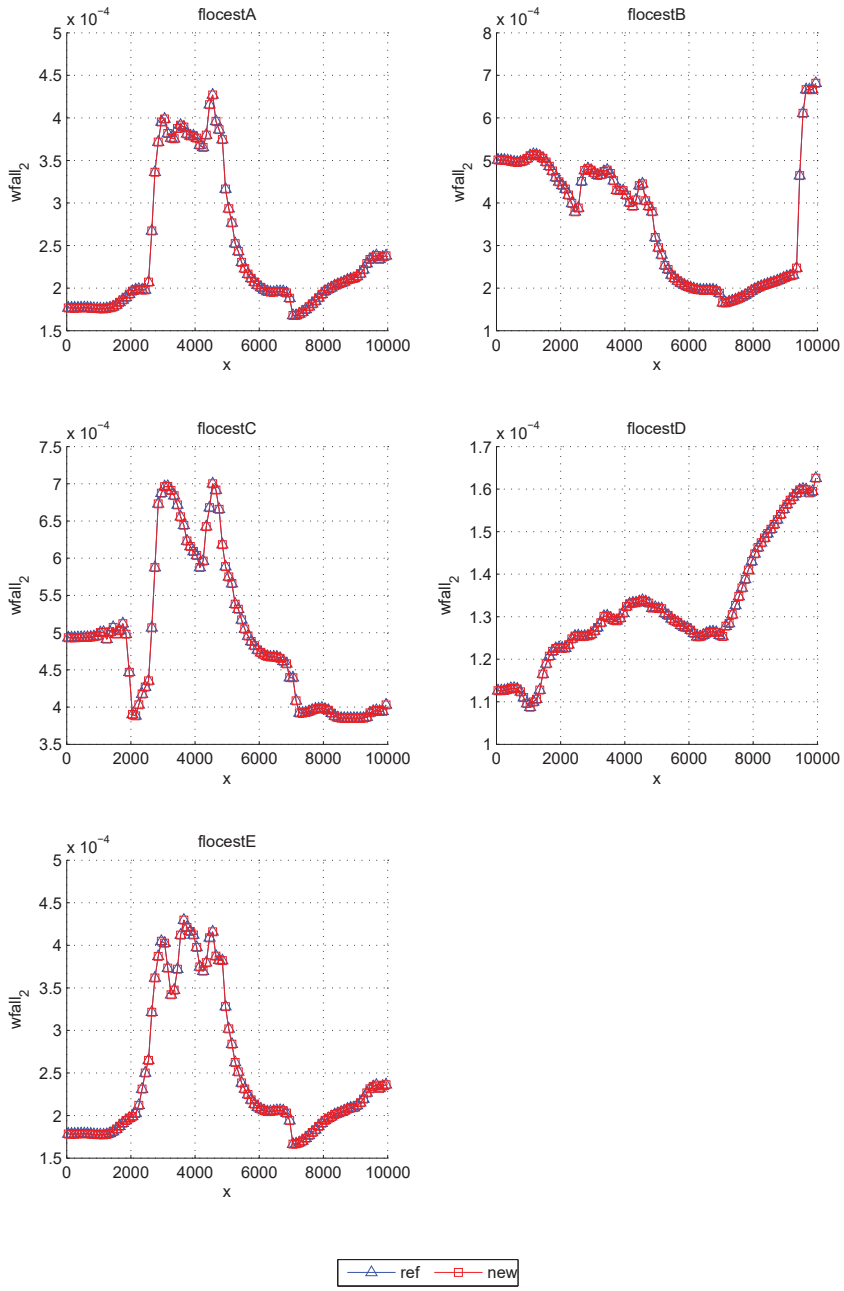


*Figure 10.96:* ***flocest****: Horizontal profile of the mid-water floc fall velocity (m/s) along a mid-channel transect at the end of the simulation.*

| Run name | flocest0 | | flocestA | | flocestB | | flocestC | |
|---|---|---|---|---|---|---|---|---|
| | ref | new | ref | new | ref | new | ref | new |
| Hydrodynamics | 60.9 % | 61.6 % | 34.8 % | 26.7 % | 34.8 % | 26.7 % | 34.7 % | 26.8 % |
| 2D mode | 8.4 % | 8.5 % | 5.2 % | 4.0 % | 5.1 % | 4.0 % | 5.1 % | 4.0 % |
| 3D mode | 49.6 % | 50.1 % | 27.8 % | 21.3 % | 27.8 % | 21.3 % | 27.8 % | 21.4 % |
| Density | 26.9 % | 27.1 % | 21.6 % | 40.0 % | 21.5 % | 40.0 % | 21.6 % | 40.0 % |
| Salinity | 19.4 % | 19.5 % | 10.7 % | 8.2 % | 10.7 % | 8.2 % | 10.7 % | 8.2 % |
| Initialisation | 0.0 % | 0.0 % | 0.0 % | 0.0 % | 0.0 % | 0.0 % | 0.0 % | 0.0 % |
| Transport | 71.9 % | 72.7 % | 70.5 % | 53.9 % | 70.5 % | 53.8 % | 70.3 % | 54.0 % |
| Advection | 48.9 % | 49.6 % | 47.4 % | 36.3 % | 47.5 % | 36.3 % | 47.2 % | 36.3 % |
| Vertical diffusion | 19.7 % | 19.8 % | 15.6 % | 11.9 % | 15.6 % | 11.9 % | 15.6 % | 11.9 % |
| Baroclinic pressure | 3.0 % | 3.0 % | 6.8 % | 5.2 % | 6.6 % | 5.1 % | 6.8 % | 5.2 % |
| Array interpolation | 10.2 % | 10.3 % | 8.1 % | 6.2 % | 8.0 % | 6.1 % | 8.0 % | 6.2 % |
| Library calls | 4.7 % | 4.8 % | 3.3 % | 2.5 % | 3.2 % | 2.4 % | 3.3 % | 2.5 % |
| Boundary conditions | 0.4 % | 0.4 % | 0.3 % | 0.2 % | 0.2 % | 0.2 % | 0.2 % | 0.2 % |
| Output | % | % | 0.0 % | 0.0 % | 0.0 % | 0.0 % | 0.0 % | 0.0 % |
| Input/output | % | % | 0.0 % | 0.0 % | 0.0 % | 0.0 % | 0.0 % | 0.0 % |
| netCDF calls | % | % | 0.0 % | 0.0 % | 0.0 % | 0.0 % | 0.0 % | 0.0 % |
| User calls | % | % | 0.2 % | 0.1 % | 0.2 % | 0.1 % | 0.2 % | 0.1 % |
| Sediment | % | % | 37.1 % | 28.3 % | 36.9 % | 28.1 % | 36.9 % | 28.3 % |
| **Total time** | 214*s*.463 | 213*s*.069 | 538*s*.358 | 701*s*.329 | 534*s*.842 | 702*s*.144 | 535*s*.499 | 699*s*.058 |

*Table 10.18:* ***flocest****: Total calculation time and percentage of total time spent by* COHERENS *in each module (part 1).*

| Run name | flocestD | | flocestE | |
|---|---|---|---|---|
| | ref | new | ref | new |
| Hydrodynamics | 34.9 % | 26.8 % | 36.7 % | 27.8 % |
| 2D mode | 5.2 % | 4.0 % | 5.4 % | 4.1 % |
| 3D mode | 27.9 % | 21.4 % | 29.3 % | 22.2 % |
| Density | 21.6 % | 39.9 % | 17.1 % | 37.3 % |
| Salinity | 10.8 % | 8.2 % | 11.3 % | 8.5 % |
| Initialisation | 0.0 % | 0.0 % | 0.0 % | 0.0 % |
| Transport | 70.5 % | 54.1 % | 74.3 % | 56.1 % |
| Advection | 47.4 % | 36.4 % | 49.8 % | 37.7 % |
| Vertical diffusion | 15.7 % | 11.9 % | 16.1 % | 12.0 % |
| Baroclinic pressure | 6.8 % | 5.2 % | 1.9 % | 1.4 % |
| Array interpolation | 8.1 % | 6.2 % | 6.2 % | 4.7 % |
| Library calls | 3.2 % | 2.5 % | 3.4 % | 2.6 % |
| Boundary conditions | 0.2 % | 0.2 % | 0.3 % | 0.2 % |
| Output | 0.0 % | 0.0 % | 0.0 % | 0.0 % |
| Input/output | 0.0 % | 0.0 % | 0.0 % | 0.0 % |
| netCDF calls | 0.0 % | 0.0 % | 0.0 % | 0.0 % |
| User calls | 0.2 % | 0.1 % | 0.2 % | 0.1 % |
| Sediment | 37.0 % | 28.3 % | 39.1 % | 29.5 % |
| **Total time** | 532*s*.142 | 697*s*.218 | 507*s*.794 | 673*s*.984 |

*Table 10.19:* ***flocest****: Total calculation time and percentage of total time spent by* COHERENS *in each module (part 2).*

# APPENDIX 3

**Bijdrage voor**

**EGU Conferentie 7-12 April, Wenen (Oostenrijk)**

Geophysical Research Abstracts
Vol. 21, EGU2019-16185, 2019
EGU General Assembly 2019


# A population balance model for multi-class floc size distributions of cohesive sediments in Belgian coastal zones

Xiaoteng Shen (1,2,3), Erik Toorman (1), Michael Fettweis (4), and Byung Lee (5)

(1) Hydraulics Laboratory, Department of Civil Engineering, KU Leuven, Kasteelpark Arenberg 40, B-3001 Leuven, Belgium (xiaoteng.shen@kuleuven.be), (2) College of Harbour, Coastal and Offshore Engineering, Hohai University, Nanjing 210098, China, (3) State Key Laboratory of Estuarine and Coastal Research, East China Normal University, Shanghai 200062, China, (4) Operational Directorate Natural Environment, Royal Belgian Institute of Natural Sciences, Rue Vautier 29, 1000 Brussels, Belgium, (5) School of Construction and Environmental Engineering, Kyungpook National University, 2559 Gyeongsang-daero, Sangju, Gyeongbuk 742-711, Korea

To manage coastal and estuarine waters, it is critical to accurately predict the movements of cohesive and non-cohesive sediments. There are well-established methods to estimate the behavior of non-cohesive sediments; however, without extensive knowledge on flocculation processes it remains difficult to predict the behavior of cohesive sediments. Flocculation is one of the main processes (e.g., erosion, deposition, settling, consolidation and flocculation) in cohesive sediment dynamics. The study of flocculation is an interdisciplinary work since it relates to various physical (e.g., transport, settling and deposition), chemical (e.g., contaminant uptake and transformation) and biological (e.g., community structure activities and metabolism) activities. Nevertheless, a widely-accepted flocculation model that can quantitative simulating the Floc Size Distributions (FSDs) for a relatively large study domain has not yet been fully developed. In this study, a multi-class population balance flocculation model was developed to address the occurrence of suspended microflocs, macroflocs and megaflocs in Belgian coastal waters (southern North Sea). The floc size distributions were represented by the size and mass fraction of each particle group. The representative sizes of macroflocs and megaflocs are unfixed and migrated between classes mainly due to the effects of turbulent shear, differential settling and biofilm growth. Specifically, the growth of an aggregate because of biofilm attachment and extracellular polymeric substance glue is averaged to each elementary particle, with its growth rate response to various bio-activities. This simple bio-flocculation model has been successfully coupled in the open source TELEMAC modeling system with five passive tracers in a quasi-1D vertical case. It was validated by observation data at the station MOW1 close to Zeebrugge harbor during both peak algae bloom and low biomass periods. It shows that when the biomass is abundant the predictions of the mean settling velocities are largely underestimated when the biological effect is neglected. This model will enhance our knowledge of the dynamics of suspended particulate matters, especially the biophysical influences on the fate and transport of estuarine aggregates.

# APPENDIX 4

**Fettweis M et al. 2019. Uncertainties associated with in situ long-term observations of suspended particulate matter concentration using optical and acoustic sensors. Progress in Oceanography, 178, 102162**

Progress in Oceanography 178 (2019) 102162

Contents lists available at ScienceDirect

Progress in Oceanography

journal homepage: www.elsevier.com/locate/pocean

# Uncertainties associated with in situ high-frequency long-term observations of suspended particulate matter concentration using optical and acoustic sensors

Michael Fettweis[a,*], Rolf Riethmüller[b,*], Romaric Verney[c], Marius Becker[d], Joan Backers[a], Matthias Baeye[a], Marion Chapalain[c], Styn Claeys[e], Jan Claus[f], Tom Cox[g], Julien Deloffre[h], Davy Depreiter[f], Flavie Druine[h,i], Götz Flöser[b], Steffen Grünler[j], Frédéric Jourdin[k], Robert Lafite[h], Janine Nauw[l], Bouchra Nechad[a], Rüdiger Röttgers[b], Aldo Sottolichio[m], Tom Van Engeland[g], Wim Vanhaverbeke[a], Hans Vereecken[e]

[a] Royal Belgian Institute of Natural Sciences, OD Nature, Rue Vautier 29, 1000 Brussels, Belgium
[b] Helmholtz-Zentrum Geesthacht, Institute for Coastal Research, Max-Planck-Str. 1, 21502 Geesthacht, Germany
[c] IFREMER, Laboratoire DHYSED, CS10070, 29280 Plouzané, France
[d] Christian-Albrechts-Universität, Institute of Geosciences, Otto-Hahn-Platz 1, 24118 Kiel, Germany
[e] Flanders Hydraulics Research, Berchemlei 115, 2140 Antwerp, Belgium
[f] IMDC, Van Immerseelstraat 66, 2018 Antwerp, Belgium
[g] University of Antwerp, Ecosystem Management Research Group, Universiteitsplein 1C -C.0.32, 2610 Wilrijk, Belgium
[h] Normandie University Rouen, UNIROUEN, UNICAEN, CNRS, M2C, 76000 Rouen, France
[i] University of Tours, EA GéoHydrosystèmes continentaux, Parc Grandmont, 37200 Tours, France
[j] Federal Waterways Engineering and Research Institute (BAW), Wedeler Landstr. 157, 22559 Hamburg, Germany
[k] Service Hydrographique et Océanographique de la Marine (SHOM), 13 rue du Chatellier, 29228 Brest, France
[l] Royal Netherlands Institute for Sea Research, Department of Coastal Systems and Utrecht University, PO Box 59, 1790 AB Den Burg Texel, the Netherlands
[m] University of Bordeaux, EPOC, UMR5805, 33600 Pessac, France

ARTICLE INFO

*Keywords:*
Suspended particulate matter
Measurement uncertainty
Regression
Optical and acoustical sensors

ABSTRACT

Measurement of suspended particulate matter concentration (SPMC) spanning large time and geographical scales have become a matter of growing importance in recent decades. At many places worldwide, complex observation platforms have been installed to capture temporal and spatial variability over scales ranging from cm (turbulent regimes) to whole basins. Long-term in situ measurements of SPMC involve one or more optical and acoustical sensors and, as the ground truth reference, gravimetric measurements of filtered water samples. The estimation of SPMC from optical and acoustical proxies generally results from the combination of a number of independent calibration measurements, as well as regression or inverse models. Direct or indirect measurements of SPMC are inherently associated with a number of uncertainties along the whole operation chain, the autonomous field deployment, to the analyses necessary for converting the observed proxy values of optical and acoustical signals to SPMC. Controlling uncertainties will become an important issue when the observational input comprises systems of sensors spanning large spatial and temporal scales. This will be especially relevant for detecting trends in the data with unambiguous statistical significance, separating anthropogenic impact from natural variations, or evaluating numerical models over a broad ensemble of different conditions using validated field data.

The aim of the study is to present and discuss the benefits and limitations of using optical and acoustical backscatter sensors to acquire long-term observations of SPMC. Additionally, this study will formulate recommendations on how to best acquire quality-assured SPMC data sets, based on the challenges and uncertainties associated with those long-term observations. The main sources of error as well as the means to quantify and reduce the uncertainties associated with SPMC measurements are also illustrated.

* Corresponding authors.
*E-mail addresses:* mfettweis@naturalsciences.be (M. Fettweis), rolf.riethmueller@hzg.de (R. Riethmüller).

https://doi.org/10.1016/j.pocean.2019.102162
Received 5 July 2018; Received in revised form 8 August 2019; Accepted 10 August 2019
Available online 12 August 2019
0079-6611/ 

## 1. Introduction

Water clarity is an important parameter to understand marine ecosystems and is mainly controlled by suspended particulate matter concentration (SPMC). To detect variability in SPMC, networks of observational platforms have been installed worldwide using optical and acoustical sensors (e.g. Butman et al., 1979; Grabemann and Krause, 1989 Fettweis et al., 1998; Guézennec et al., 1999; Ganju and Schoellhamer, 2006; Badewien et al., 2009; Palinkas et al., 2010; Garel and Ferreira, 2011; Nauw et al., 2014; Anastasiou et al., 2015; Jalón-Rojas et al., 2015; Many et al., 2016; Druine et al., 2018) as well as sensors or samples that give information on the shape, size and composition of the SPM (e.g. Krivtsov et al., 2008; Cartwright et al., 2009; Gray and Gartner, 2009; Fettweis and Baeye, 2015; van der Hout et al., 2015; Chapalain et al., 2019). In addition to these sensors gravimetric measurements of filtered water samples are generally used as ground truth reference (e.g. Neukermans et al., 2012a). The infrastructure on which the sensors are attached includes fixed (piles, benthic landers, tripods, moored lines and buoys) and moving platforms (vessels, gliders, AUV, ROV, floats) or a combination of both (Baschek et al., 2017), and the SPMC may cover the whole range of coastal environments from oligotrophic to hyperturbid conditions.

Long-term and high frequency data series of SPMC are typically collected indirectly with autonomous sensors that measure either the optical beam attenuation as a percentage of light transmission (Moody et al., 1987; Spinrad et al., 1989; Agrawal and Pottsmith, 2000), the back- or sidescatter intensity of light in volt or factory calibrated turbidity units, or the acoustic backscatter in counts or volts (Thorne and Hanes, 2002; Downing, 2006; Rai and Kumar, 2015). The measuring frequency should at least be able to resolve the dominant variations (often the tidal cycle) and might be as high as to record finer scale variations such as turbulence. The time span of long-term measurements should cover variations ranging from lunar to seasonal and interannual cycles.

The combination of different sensors measuring in environments with high spatiotemporal variability implicitly demands adapted pre- and post-measurement procedures in order to obtain homogenous data sets. Conversion of the sensor output to physical units (e.g. mass or volume concentration of particles) results from laboratory and field calibrations, as well as data post processing procedures. The whole procedure requires direct measurements in the laboratory using standard turbidity solutions for calibration, and in the field using SPMC determined through filtration of water samples. The way the sensor output is transformed to SPMC (in g/l) depends on the modelling techniques used to relate sensor output to SPMC and is further complicated by the significant variability of the inherent optical (IOP) and acoustical properties (IAP) of the SPM (e.g. Slade et al., 2011; Woźniak et al., 2011; Sahin et al., 2017). To guarantee quality and repeatability the laboratory procedures and the measuring process need to be documented from the planning of the measurements to the post processing of the data (Lane et al., 2000; Waldmann et al., 2010; Bolanos et al., 2011; Gil et al., 2016).

Direct or indirect measurements of SPMC are inherently associated with a number of uncertainties along the whole operational chain: from the laboratory work, to system problems due to the autonomous nature of the sensor deployments, to converting the observed proxy values of optical and acoustic signals to SPMC. Guidelines for good practice for fluvial sediment transport measurements can be found in e.g. Rasmussen et al. (2009). However, limited information exists in guidelines or standards that can be applied to long term observation programs of SPMC in marine and estuarine environments. Recent literature highlights only part of the uncertainties or problems related to the use of optical and acoustical sensors (Rai and Kumar, 2015; Rymszewicz et al., 2017). This study goes further as it reviews and discusses the benefits, limitations, and problems of present practices as they relate to the use of optical and acoustical sensors in long-term deployments, and formulates recommendations for acquiring the best quality-assured SPMC data possible. Other uncertainties or biases in the observation, which are for example related to the representativeness of the measuring location within the regional context, the interactions of the measuring infrastructure with the environment, or the disturbances by human activities are not part of this study.

## 2. Methods for long-term in situ SPMC measurements

### 2.1. Terminology

SPM is a mixture of clay to sand-sized particles that can be detected in suspension and that consists of varying amounts of minerals from physico-chemical and biogenic origin, living and non-living organic matter, and particles from human origin, see Table 1. The particles are considered to be in suspension as long as they do not form an interconnected matrix of bonds that prevents their mobility; this is the case when the concentration is below the gelling point (McAnally et al., 2007). The inherent properties of SPM (i.e. the concentration, size and composition) may change over time depending on the seafloor composition (cohesive and non-cohesive sediments), the hydrodynamics, the measuring height above the bed and biological activity. Sand grains are generally limited to the near-bed layer (bed-load), while fine-grained sediments can be found throughout the water column. Charged particles such as clays and polymers may become attached to each other to form fragile structures known as flocs. The composition, size, density, structural complexity, and settling velocity of flocs vary as a function of turbulence, chemical environment (salinity) and bio-chemical composition (e.g. Eisma, 1986; Dyer and Manning, 1999; Droppo et al., 2005; Fettweis and Lee, 2017).

Long-term in situ measurements of SPMC in coastal seas and estuaries involve one or more optical and acoustical sensors and, as the ground truth reference, gravimetric measurements of filtered water samples. The combination of indirect and reference measurements requires two main calibration steps (sensor and model parameter calibration) at different moments during the workflow to extract reliable and homogeneous SPMC. These calibration steps are essential for

**Table 1**
Bulk mineralogical composition (in %) of the SPM in the English Channel and southern North Sea sampled with a centrifuge during transect or anchoring of the vessel. Offshore Somme mouth, Dover Strait, Calais, Zeebrugge and north of the Rhine mouth. Qtz = Quartz; Kspar = K-feldspar; Plag = Plagioclase; Carb = Sum of Calcite, Mg-rich Calcite, Dolomite, Aragonite; Am = Amorphous fraction (organic matter and biogenic opal); Hal = Halite; NClays = Sum of non-clay minerals; Kaol = Kaolinite; Chl = Chlorite; 2:1 = Sum of 2:1 clays and micas; Clays = Sum of Kaol + chl + 2:1. The samples have been collected with a centrifuge (water intake about 4 m below surface) and analysed with XRD (data from Adriaens et al., 2018).

| | Qtz | Kspar | Plag | Carb | Am | Hal | NClays | Kaol | Chl | 2:1 | Clays |
|---|---|---|---|---|---|---|---|---|---|---|---|
| Somme | 29 | 2 | 3 | 30 | 15 | 5 | 86 | < 1 | < 1 | 10 | 10 |
| Dover Strait | 22 | 3 | 2 | 21 | 18 | 7 | 84 | 2 | 4 | 20 | 26 |
| Calais | 10 | 1 | < 1 | 29 | 22 | 3 | 66 | < 1 | 2 | 31 | 33 |
| Zeebrugge | 20 | 1 | 5 | 24 | 10 | 2 | 61 | 2 | 4 | 33 | 39 |
| Rhine offshore | 29 | 4 | 1 | 21 | 12 | 3 | 70 | 1 | 2 | 27 | 30 |
| Rhine nearshore | 17 | 4 | 2 | 21 | 16 | 1 | 61 | 2 | 1 | 35 | 38 |

relating changes in calibration constants (both sensor and model-parameter constants) to either sensor degradation or to natural variability in SPM inherent properties. Changes in SPM properties and concentration might be related to seasonal and geographical variations. The latter is typically occurring along the gradients from the estuary, coastal zone towards the offshore (Fettweis et al., 2006; Becker et al., 2013; Maerz et al., 2016; Many et al., 2016).

**Sensor calibration** refers to the comparison of the output signal of an optical or acoustical sensor against laboratory standards (e.g. Thorne et al., 1991; Downing, 2006). For turbidity this is usually formazine or an alternative standard (AMCO clear®, StablCal®), while for acoustical backscatter intensity a solution of standard spheres with a given size distribution, concentration and at a given distance from the transducer is used. Acoustic sensor calibration is not commonly applied for long-term measurements due to practical difficulties in setting up a laboratory device. Sensor calibration is necessary to convert the sensor output to various turbidity units (see below) or decibels (dB). During long-term field operations the sensor calibration constants, relative to a standard may change. Any of these changes in the sensor calibration constants are inherent to the sensors and not to the environment.

**Model parameter calibration** refers to the regression between the sensor signal after sensor calibration and the corresponding real SPMC. The calibration should ideally be carried out in situ. This type of calibration is well distinguished from sensor calibration as it relies on natural particles and has to be carried out regularly, as well as each time the SPM inherent properties change significantly. If the sensors have been well-calibrated, then any changes in model calibration constants are caused by changes in SPM inherent properties.

**Sample SPMC** is the SPMC obtained from filtration and gravimetric measurements of water samples. As the real, in situ SPMC cannot be measured by any direct method we will use the sample SPMC as our reference, as it is less influenced by the inherent particle properties of the SPM (Neukermans et al., 2012a; Röttgers et al., 2014).

**Sensor SPMC** is a surrogate obtained by an acoustical or optical backscatter sensors or other type of sensors.

**Turbidity** refers to the optical water cloudiness caused by suspended particles and dissolved substances, which scatter and absorb light (Downing, 2005; Ziegler, 2003; Gray and Gartner, 2009). Turbidity does not have a SI unit, is not uniquely defined and depends strongly on the applied protocols. It is thus an arbitrary unit that is incomparable to measurements taken at other times and places or with different turbidity meters, which diminishes the comparability of turbidity data for scientific purposes (Downing, 2006). There are two international recognized methodologies for determining turbidity: the ISO Method 7027 (ISO, 1999) and the American EPA Method 180.1 (EPA, 1993). Both estimate turbidity, for the ISO method it is in formazine Nephelometric Units (FNU), and for the EPA method in Nephelometric Turbidity Units (NTU), respectively, and in both methods, the optical sensor to be used is a nephelometer that must measure side-scattered light at 90°. There are, however, some differences between the two methodologies. Turbidity following the EPA method is poorly defined. The strengths of the ISO method include the use of a stable monochromatic near infrared light source of 860 nm with low absorbance interference with samples, which is critical in reducing the impact of particulate and coloured dissolved organic matter absorption and in having low amounts of stray light (Sadar, 1999). Sensors designed according to the ISO definition of turbidity provide thus a better basis for the comparability of measurements than those designed following the EPA specification (Barter and Deas, 2003, Nechad et al., 2009; Bright et al., 2018). The ISO compliant sensors are therefore recommended when no legal regulations require other protocols.

As previously stated, both protocols refer to a formazine-equivalent turbidity value. If an alternative to formazine is used as the standard, it should be explicitly stated that turbidity refers to the alternative standard-equivalent NU or TU. The unit of the formazine (or alternative) standard is generally given in NTU, despite the fact that the standard solution can be created by following either the ISO or EPA protocol. In an ISO-compliant formazine solution of 1000 “NTU” an ISO-compliant side-scattering sensor will measure 1000 FNU, whereas an EPA-compliant side-scattering sensor will measure another value in NTU. The difference between FNU and NTU is mainly due to the spectral range of lights that are emitted by the instruments. For example, in waters with particles highly absorbing in the blue-green range, an EPA-compliant instrument measures lower turbidity values than an ISO-compliant instrument.

Optical Backscatter Sensors (OBS) measure the particle backscattering of light at different angles of detection (120–165°, or even including side and forward scattering depending on the type of sensor); although highly correlated, the turbidity measured by an OBS and a Nephelometer is not necessarily the same. For example, Nechad et al. (2016) report a large variability in the relationship between in situ side- and back-scattering coefficients in the lower turbidity range (< 20 FNU) and a convergence with increasing turbidity. Turbidity from backscatter devices should be expressed in Formazine Backscatter Units (FBU, or BU with indication of the alternative standard used) for the near IR (830–890 nm) light (ISO Method 7027) and Backscatter Turbidity Units (BTU) for the EPA Method 180.1 (Dogliotti et al., 2016; Nechad et al., 2016). Often FTU (Formazine Turbidity Unit) or NTU are used as unit without specifying how the instrument measures the sample (side, back or forward scattering) or which protocol it follows (ISO or EPA). By adapting the correct units, the confusion on protocol or scattering angle can be avoided.

### 2.2. Sensors used to obtain long-term SPMC time series

#### 2.2.1. Sensitivity of optical sensors to inherent particle properties

Various measurements of IOPs, which are defined as properties of the water column that are independent of the ambient light field, are used as proxies for SPMC. Optical sensors rely on the interaction of SPM with light at a given wavelength λ through absorption $a(\lambda)$ and scattering $b(\lambda)$. For long-term measurements, the attenuation or the scattering at a given angle are mainly used to obtain the SPMC surrogates. Details on the optical properties of particles can be found e.g. in the Ocean Optics Web Book (2018). Available sensors can differ in wavelength and backscattering angle. The backscattering of light by particles, $b_b(\lambda)$, is theoretically calculated as the integration of the volume scattering function (VSF; denoted as $\beta(\lambda, \theta)$ [$m^{-1}$ $sr^{-1}$] with $\theta$ representing the scattering angle), over all backward directions. Boss and Pegau (2001) and Berthon et al. (2007) showed that $b_b$ is highly correlated to $\beta$ at angles between 120° and 140°, while Chami et al. (2006) found that the increase of $\beta$ at $\theta > 150°$ can significantly impact the backscattering. The backscattering of particles at large wavelengths ($\lambda > 700$ nm) gives the best estimations for SPMC (Downing, 2006; Boss et al., 2009a). The effect of absorption by particles and coloured dissolved organic matter is higher at shorter wavelengths (Yentsch, 1962) which can impact (back)scattering or turbidity estimation by sensors that emit light at short wavelengths, as was highlighted by Sutherland et al. (2000) and Downing (2005). In more turbid waters, high amounts of particle absorption can influence the estimation of backscattering coefficient, even at longer wavelengths and should be properly corrected for (Doxaran et al., 2016).

As mentioned above, ISO Method 7027 (ISO, 1999) and EPA Method 180.1 (EPA, 1993) estimate turbidity $T$ in Formazine Nephelometric Units (FNU) or Nephelometric Turbidity units (NTU), respectively, such as $T = \frac{\beta(90°)}{\beta^F(90°)}$ where $\beta^F(90°)[m^{-1}]$ is the VSF at 90° of a unit of formazine. As has been outlined above, other types of optical sensors such as backscatter sensors are widely used to measure turbidity and hence to estimate SPMC. In terms of sensor calibration based on successive dilution of a standard solution, this use of multiple sensor types does not cause problems as the sensor output will be compared, and then associated, to the standard solution that can be expressed in a

turbidity unit. This calibration must then be used for quality control and to ensure the stability of the intrinsic sensor performance, and possible drifts induced by electronic failure or damages on optical windows that may induce maintenance and repair. The main issue comes when these instruments measure turbidity in situ or from natural water samples as IOPs (i.e. scattering efficiency $K$), in that case the VSF are dependent on particles shape (Slade et al., 2013), particles size and density, refractive index (Mishchenko et al., 2002; Boss et al., 2004), and colour (Sutherland et al., 2000; Hatcher et al., 2000; Bright et al., 2018).

Generally, $b(\lambda) = K(\lambda, r)N(r)\pi r^2$, where $K$ is the scattering efficiency factor for non-absorbing particles, $N$ the number of particles, and $r$ the particle radius. For spherical particles $SPMC = \frac{4}{3}N\rho\pi r^3$, where ρ is the dry density (i.e. particle mass divided by the particle volume), resulting in a ratio of turbidity to SPMC that is inversely proportional to the particle radius and density (Sutherland et al., 2000; Babin et al., 2003):

$$b(\lambda) = \frac{3}{2}K(\lambda, r)\frac{SPMC}{\rho r} \tag{1}$$

The SPM dry density (proportional to the excess density) can, depending on the particle composition, be anywhere in between the range of well below 100 kg m$^{-3}$ for the organic flocs and up to 2650 kg m$^{-3}$ or more for the individual mineral particles. In case the SPM consists of flocs the variations in density and size can be very large, with the densest flocs having the smallest size and vice versa. The consequence of this is that the dependence of $b(\lambda)$ on $\rho r$ is weaker than its dependence on $1/r$ (Bowers et al., 2009) but can still be significant (Gibbs, 1985; Babin et al., 2003; Baker and Lavelle, 1984). This demonstrates that a change in the composition of particles and/or their shape, size and density affects the turbidity measured by a side- and backscatter sensor (e.g. Binding et al., 2005; Druine et al., 2018; Neukermans et al., 2012b; Zhang et al., 2014), but also indicates that the model parameter calibration of optical backscatter instruments using a single optical property (backscattering coefficient or beam attenuation) against sample SPMC is often successful over a wide range of particle sizes (Boss et al., 2009b; Bowers et al., 2017) as long as SPM characteristics do not change significantly over the observed period.

### 2.2.2. Sensitivity of acoustic sensors to particle properties

Some acoustics devices commonly used in coastal areas, such as ADVs or ADCPs are primarily designed for current velocity measurement, while others (ABS) are specifically designed for measuring SPMC at a single point (Guerrero and Di Federico, 2018) or in a vertical profile (Hay and Sheng, 1992). Analogously to optical devices, the emitted acoustic wave, at a given frequency, interacts with particles in suspension while propagating in the medium and are backscattered to the receivers (Thorne and Hanes, 2002). The recorded volume backscattering strength ($S_v$, in dB) is a proxy of the SPMC, but is also strongly modulated by SPM features such as size, density and shape, depending on the acoustic wavelength. Originally used in sandy environments (Sheng and Hay, 1988; Thorne and Hanes, 2002), these devices are now routinely deployed in fine sediment environments (e.g. Gartner, 2004; Hoitink and Hoekstra, 2005; Merckelbach, 2006; Merckelbach and Ridderinkhof, 2006; Tessier et al., 2008; Sahin et al., 2017). The sonar equation (Urick, 1975) is commonly used to relate $S_v$ (in dB) and SPMC concentration, including acoustic signal correction for geometry compensation, spherical spreading, and water and particle attenuation:

$$\frac{S}{N} = SL - 20log_{10}(\psi R^2) - 2\int_0^R (\alpha_w(r) + \alpha_s(r))dr + S_v + 10log_{10}\left(\varphi R^2\frac{WS}{2}\right) \tag{2}$$

and

$$S_v = 10log_{10}\left(\frac{SPMC\ \sigma}{\rho_s v_s}\right) \tag{3}$$

where $S/N$ is the signal to noise ratio (dB) received by the device. After Gostiaux and Van Haren (2010), Mullison (2017) specifies the values of $S/N$ in function of the raw echo readings (in counts) of the ADCP devices. $SL$ is the source level (dB); $R$ is the along-beam distance from transducers, $a_w$ and $a_s$ respectively the water and sediment attenuation, $\varphi$ the angular aperture; $WS$ the cell size and $\psi$ the near field correction. $\sigma$, $\rho_s$ and $v_s$ are particle features: backscattering cross section, particle dry density and volume respectively.

Comparably to optical devices, the relationship between the acoustic backscatter and SPMC strongly depends on the nature, size, density and shape of the particles, both for the estimation of the particle attenuation and for the calculation of the backscattering cross section (Fugate and Friedrichs, 2002; Ha et al., 2009; Salehi and Strom, 2011; Rouhnia et al., 2014), achieved using theoretical acoustic models (Stanton, 1989; Thorne and Hanes, 2002; Thorne et al., 2014). However, contrary to optical devices, the sensor calibration is not routinely (often never) operated due to the difficulty to access requested laboratory facilities. Hence this step is often skipped and quality check is based on comparison with other in situ sensors or SPMC samples.

### 2.2.3. Conversion of acoustical and optical sensor output to SPMC

The relationship between OBS or nephelometer signal and SPMC is almost linear as long as the sensor is not deployed in highly concentrated waters (Downing, 2006), and the simplest model is a linear regression model. The same holds for single point acoustical sensors (ADV) or for the first bin of a profiling acoustical sensor, where the target volume is very close to the sensors. As far as SPMC are lower than several g/l, a direct empirical relationship can be built such as $log_{10}(SPMC) \sim S_v$, where $S_v$ can be related to the signal/noise ratio (Fugate and Friedrichs, 2002; Voulgaris and Meyer, 2004; Verney et al., 2007; Ha et al., 2009; Salehi and Strom, 2011).

For profiling acoustic sensors, the sonar equation should be considered to correct for the signal loss along the acoustic path. The conversion factor from counts to dB, as commonly used in acoustics, is typically provided by the manufacturer. Close to the transducer, the acoustic signal has to be corrected for near-field effects (Downing et al., 1994) and for ringing effects that may affect the first bins, in particular when blank distance is set too small in the configuration parameters. Corresponding data cannot be corrected and should be discarded (Muste et al., 2006). A formulation for the water absorption coefficient was proposed by e.g. Francois and Garrison (1982a,b) and later simplified by Ainslie and McColm (1998), who showed that their result did not differ from the original equation more than the accuracy error. The sonar equation yields the so-called water-corrected backscatter, which is a property of the suspension at all locations along the acoustic path. Subsequent processing depends on the SPMC. In case of moderately turbid environment, i.e. lower than 100 mg/l, sound attenuation by SPM is usually neglected as it is one or two orders of magnitude lower than the water absorption coefficient (Ha et al., 2011). SPMC is then either determined by applying an appropriate calibration, similar to single point optical sensors, or by a theoretical acoustic model. In the latter case, physical properties of the transducer and of the SPM must be exactly known, which are rarely available. If SPMC exceeds 100 mg/l, sediment absorption should be considered. However, this term is a function of the SPMC, which is also the unknown of the calculation. The inversion problem is solved by iterative methods (Thorne et al., 1994; Holdaway et al., 1999). This technique is efficient but requires assumption or knowledge about SPM characteristics (size, density) and is based on the choice of an acoustic model adapted to the observed SPM, and may in some specific case exponentially propagate uncertainties and fail to estimate SPMC (Becker et al., 2013).

Theoretical acoustic models were originally built to simulate the physical interactions between particles and the acoustic signal (Sheng

and Hay, 1988, Medwin and Clay, 1998) and were applied to sand particles in suspensions (Thorne and Hanes, 2002). These models were later adapted to represent low density aggregates of SPM (Stanton, 1989; MacDonald et al., 2013; Thorne et al., 2014). Differences between models mainly appear in the methodology to calculate the total scattering and backscattering cross section as well as the compressibility of flocs and their ability to interact with sound. Merckelbach and Ridderinkhof (2006) and Nauw et al. (2014) observed that at strong currents (> 1 m/s) acoustical backscatter exceeds the linear relationship to sample SPMC noted at lower currents. This was not due to changes in the particle-sizes and the non-linearity was compensated for, based on a model that suggests a transition from random phase to coherent particle backscatter by turbulence-induced variability in in the spatial distribution of SPMC (Merckelbach, 2006). More research is however required to understand the cause of this effect.

### 2.3. Existing international guidelines and standards

In the European framework guidelines for SPMC determination consider only the collection of water samples. OSPAR's Joint Assessment and Monitoring Programme JAMP (2012) refers to the ICES TIMES report by Yeats and Brügmann (1990). The Trilateral Monitoring and Assessment Program for the Wadden Sea (TMAP) refers in their handbook on nutrients (TMAP, 2009) explicitly to the corresponding guidelines of JAMP. HELCOM (2015) treats SPMC as a co-factor in water analysis and keeps its determination by filtration according to ISO (1997). In a global framework, the IOC-EU-BSH-NOAA-(WDC-A) International Workshop on Oceanographic Biological and Chemical Data Management did not include SPMC in the list of bio-geochemical bulk parameters (IOC, 1996). For the ARGO programme, Quality Control (QC) manuals for Bio-Argo particle backscattering measurements are yet in development (Schmechtig et al., 2015), the main purpose of these measurements is the use of the backscattering coefficient as proxy for POC concentration (IOCCG, 2011). The National Oceanic and Atmospheric Administration NOAA does not provide standards for SPMC measurements in official documents. In some technical reports, however, the methods to obtain SPMC are described, always using gravimetric analyses of water samples (e.g. Pait et al., 2015). For the large-scale integrated ocean and coastal ocean observatories, such as IOOS in the United States (www.ioos.us) and IMOS in Australia (www.imos.org.au), no guidelines for best practice of SPMC measurements are put forward. The U.S. Geological Survey provides a number of documents comprising guidelines for the sampling (Edwards and Glysson, 1999), for the lab analysis of the samples (Matthes et al., 1992; Shreve and Downs, 2005), for the proper layout and operation of field stations and sensors to meet accuracy and precision requirements (Wagner et al., 2006). They also describe how to compute time series of SPMC and their related loads using proper statistical regression models (Rasmussen et al., 2009, Topping and Wright, 2016). These guidelines were developed for measurements in rivers, but many of them can be transferred to estuaries and coastal seas in a straightforward way, except that estuarine and coastal SPM exhibits much higher variability on texture and composition.

## 3. Sources of uncertainties

Uncertainties, as described in Ramsey and Ellison (2007) and ISO (2008; 2017), hamper data quality and may arise from mal-functioning of sensors (3.1), the environment influencing the sensors without changes in SPMC (3.2), SPMC sample collection and analysis (3.3), modelling of sensor output to sample SPMC (3.4), and additional uncertainties arising from human error and uncontrolled environmental boundary conditions (3.5).

### 3.1. Sensor

Sensor related uncertainties occur if the sensor output changes over time unrelated to changes in inherent particle properties or SPMC. Concerning optical backscatter sensors this is caused by variations in voltage supply, changes in the transmittance of the window that is the interface between the sensor and the water or other degradations. Concerning acoustical backscatter sensors, the main sensor related uncertainty is related to battery power. The reason that no other sensor related uncertainties are documented is due to the limited availability of facilities to test acoustic sensors in a lab, and that in contrast to optical sensor, no standards and norms exists so far to test and calibrate acoustical backscatter sensors. Other uncertainties may arise from the drift of the internal clock of the sensor or the data logger in particular in case of long-term monitoring.

#### 3.1.1. Drift with time

Optical sensors are subject to gradual decreasing transmittance of the sensor window during deployment due to scratches caused by the collision of particles. Therefore, the factory calibration parameters should be used with care and be checked regularly. The damage of the transmission and detection windows is often not visible by visual inspection. A re-calibration of 11 Seapoint turbidity sensors operated by HZG in the laboratory for example revealed that the average slope between factory calibration and formazine recalibration agreed within 1%, but the individual slopes showed discrepancies up to ± 30% with a standard deviation of 15%. Fig. 1 shows a comparison between an OBS3+ factory calibration and a sensor calibration obtained after 329 and 421 days highly turbid (SPMC > 1 g/l) sea water. Using the factory calibration constants without recalibration would indicate an

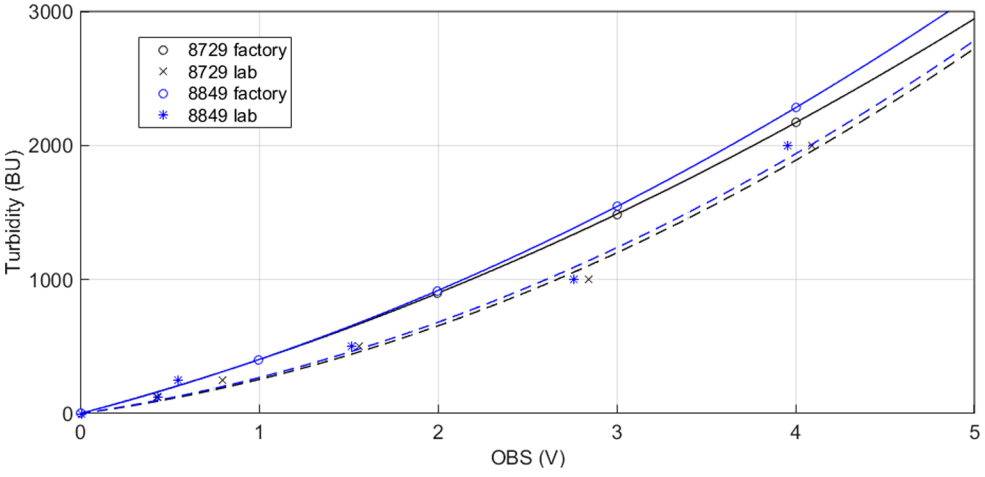


**Fig. 1.** Factory and in lab sensor calibration of two OBS3+ (8729 and 8849). The laboratory calibration was done after 421 (8729) and 329 (8849) days of measurements in high turbid (SPMC > 1 g/l) sea water during the period 2014–2016. The solid lines are the 2nd order polynomial fittings provided by the factory, the dashed lines are the 2nd order fittings after recalibration.

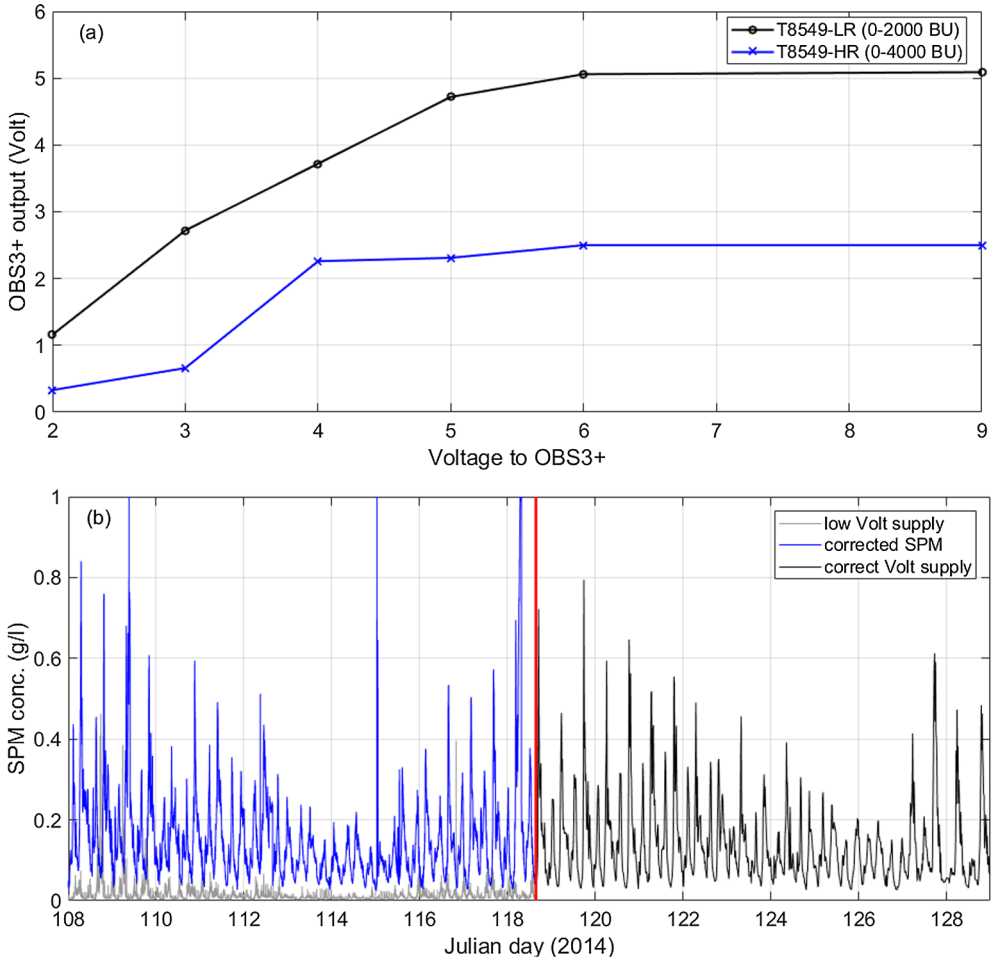


**Fig. 2.** (a) Power provided by an external source to a OBS3 + (T8549) measuring in high and low range in a standard solution of 2000 AMCO Clear® equivalent BU. When the voltage drops below 6 V, the sensor registers low voltage output values. (b) SPMC time series from the Belgian nearshore measured with a OBS3 + that was attached to a SonTek Hydra data logging system for storage and battery supply. The system was replaced on day 118.7 by a similar system. The first system was not providing the minimum of 6 V to the OBS, the second system worked correctly. In blue is shown the corrected time series.

apparent increase of the turbidity. Any of these changes in the calibration constants are inherent to the sensors itself and the need of recalibration has to be specified by the user based on the required precision.

Variations in voltage supply result in a drift, which is unrelated to variations in SPMC or inherent particle properties. In clear water the output of for example an OBS3 + will be a minimum voltage, increasing to a maximum voltage at the maximum turbidity range. The sensor needs to be fed by a constant minimum voltage in order to give good data. Lower voltage supply results in an apparent decrease in turbidity. Fig. 2a shows an OBS3 + in low (0–2000 BU) and high (0–4000 BU) range that has been fed with different input voltages while measuring in a standard of 2000 AMCO Clear®-equivalent BU. For an input voltage of more than 6 V the low range registers a constant value of 5.1 V (saturation), while the high range registers about half of it (2.5 V). If the supplied voltage decreases, the signal registered by the OBS3 + decreases as well. An example of a time series collected with an OBS that received a low battery voltage and another one with a normal voltage supply is illustrated in Fig. 2b. The recorded SPMC signal of the first sensor was on average about 90% lower than it should be. After sensor calibration with lower voltage supply the data could be corrected. Battery power affects also acoustical backscatter sensors (Tessier et al., 2008). From the registered battery voltage during the deployment the emitted power can be converted into the correction factor $P_{dbw}$ calculated as $P_{dbw} = 10log(P^2)/R$, with $R$ the electrical resistance. If only one of the transducers of profiling acoustical sensors supplies more or less power than the others, then this can be corrected using the other transducers (Tessier, 2006).

### 3.1.2. Sensitivity

Some optical backscatter sensors, such as an OBS3 +, are dual range sensors having both a low- and a high-range output. The two measuring ranges increase the resolution of the measurements, but each output is more accurate when its designed turbidity range matches its calibrated range. The RMS error between high and low range output depends on the turbidity. For example, for an averaged turbidity around 20 the low range (500 BU) recordings during a tidal cycles differed by about 2% with the high range ones (2000 BU). When increasing the ranges (low: 1000 BU, high 4000 BU) then the relative difference increased to 24%. The optimal range is to be chosen according to the expected range of turbidity values in the field.

### 3.1.3. Inter-sensor variabilities

The aim of multi-sensor calibration is to generate a reliable model parameter calibration to estimate SPMC at long-term monitoring stations by repeated field surveys and to record variabilities caused by the use of similar types of sensors. Fig. 3 shows the result of a simultaneous calibration of three OBS3 + sensors during a tidal cycle. The RMSE between the three OBS3 + sensors, which have been calibrated against the same sample SPMC, was 2.6% for 1 Hz sampling and 2% for an averaging over 60 s. The difference between sensor outputs is changing during the course of the measurements. This points to small-scale

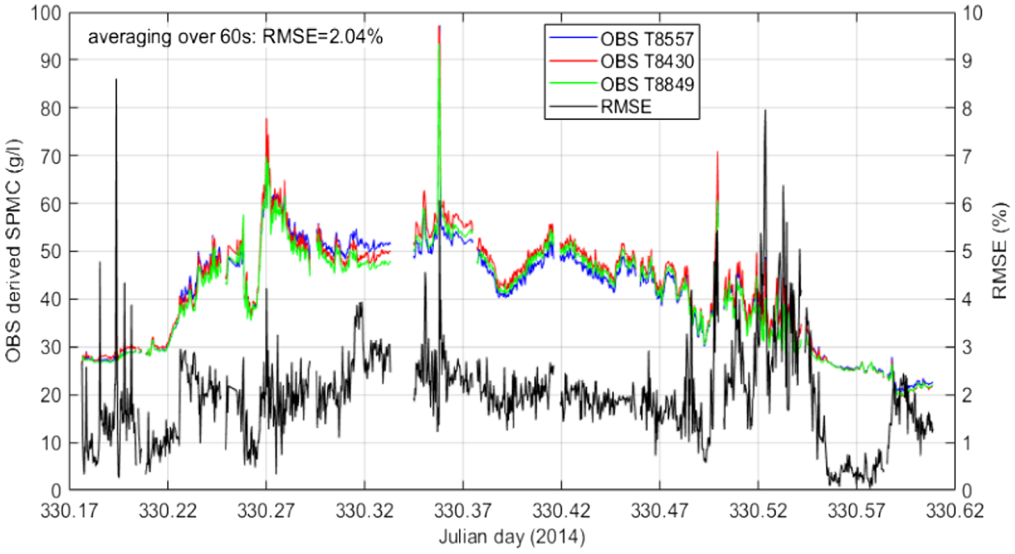


**Fig. 3.** Inter-sensor variability between three OBS3+ sensors measuring at about 50 cm from each other during a tidal cycle (Belgian nearshore area). The sensors have been calibrated using the same sample SPMC. The differences between the OBS's are not constant but change during the course of the tide. This points possibly to variations in the SPMC (sensor are located about 50 cm from each other) or to different sensitivities of the individual sensors.

variations in the SPMC (sensors are located about 50 cm from each other) and to different sensitivities of the individual sensors. These examples presented strengthen the necessity of sensor calibration (difficult to achieve for profiling acoustic sensors) and model calibration for each sensor separately.

### 3.2. Environmental related uncertainties

Environmental related uncertainties occur when the sensor output changes over time unrelated to changes in inherent particle properties or SPMC. This occurs when the signal is for example attenuated by biofouling or the occurrence of air bubbles. Another environmental uncertainty is specific to optical sensors and occurs when the emitted light beam is strongly attenuated and backscattered light decreases with increasing sediment concentration.

#### 3.2.1. Biofouling

Biofouling or other type of fouling can limit the accuracy and quality of long-term SPMC measurements within a week, depending on the season and the environment. Biofouling occurs in four phases starting with the development of an organic film, followed by primary and secondary micro colonizers and finally tertiary colonizers attach to the micro-fouling film (Abarzua and Jakubowski, 1995). The impact of these different phases on the recorded signal remains difficult to estimate and can result in a temporary or permanent increase of the backscattered signal due to additional reflection or a decrease due to attenuation (Kerr et al., 1998; Delauney et al., 2010). Increase of the backscattered signal can also be caused by plant or artificial (e.g. fishnet) filaments trapped by the measuring infrastructure and constantly or ephemerally influencing the detection volume. There are several methods and reasons to protect the sensors against biofouling (Ridd and Larcombe, 1994; Manov et al., 2004; Whelan and Regan, 2006). The most obvious reason is to obtain good quality data. Another one is that the fouling development on the whole measuring infrastructure can disturb the properties of the study site. For example, the growth of epi-fauna on the infrastructure may influence the measurements as they trap, accumulate and temporarily release SPM (Baeye and Fettweis, 2015). Effectively biofouling results in a gradual and continuous drift of the signal over time together with an apparent decrease in sensitivity (Dolphin et al., 2000; Downing, 2006). Permanent biofouling events will gradually change the backscatter intensity and can only be corrected if a non-affected reference sensor is at hand. The reference sensor can be single beam acoustic or optical backscatter sensor or a not-affected beam of an acoustic profiler. The onset of a change in the SPMC signal due to biofouling is difficult to identify and therefore should be based on the hypothesis that the observed changes cannot any more be explained by known physical behaviour of SPMC variations.

Fig. 4 is an example of epifauna (barnacles) growing on an OBS that resulted in an increase of backscatter intensity until saturation and thus an overestimation of the SPMC. The timing of biofouling was estimated at the point where the ratio of the affected sensor to a non-affected one

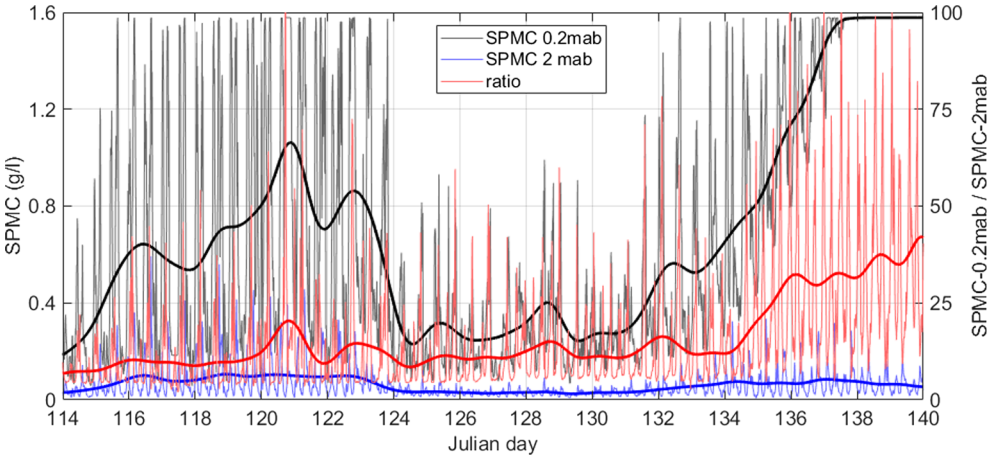


**Fig. 4.** The time series collected in the Belgian nearshore area show the OBS derived SPMC at 0.2 and 2 mab (left axis) and the ratio between SPMC at 0.2 and at 2mab (right axis). The thick lines are the low-passed filtered data. The OBS at 0.2 mab was covered by barnacles, while the one at 2 mab was not affected by biofouling. The low-pass filtered ratio indicates that biofouling started to affect the OBS at 0.2 mab from about day 134 onward. The OBS at 0.2 mab saturated during the measuring period when the SPMC exceeded about 1.6 g/l.

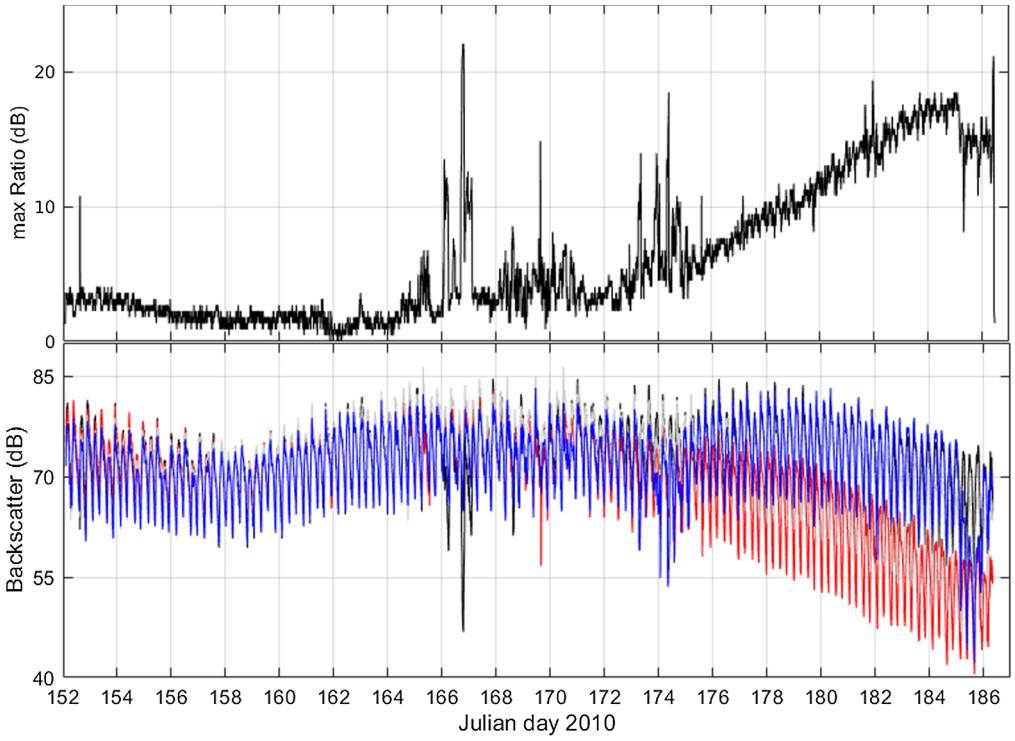


**Fig. 5.** 35-day time series of cross-beam backscatter ratio (up) and the acoustic backscatter intensity (down) recorded by an upward-looking 1.2 MHz RDI ADCP (5th bin at about 1.5 m above the ADCP is shown) moored offshore the Belgian coast. Changes in the cross beam backscatter ratio, $R_v$, occurred from day 165 onward and from day 172 a gradual increase is observed. Superposed are quarter-diurnal variations in $R_v$ of the order of 2–3 dB that result from the deposition of fine sediments during slack water and the subsequent erosion during increasing currents. The recovered ADCP was massively fouled by barnacles, tube building worms and hydrozoa.

started to increase monotonically. Biofouling has also been observed on moored up-ward looking ADCPs. A straightforward identification of these events is possible by computing the cross-beam backscatter ratio. Expressed in dB, this ratio is computed as the difference between the maximum and the minimum of all backscatter intensities recorded at a given depth by all beams of the sensor. In case of an ADCP, each ratio value is then computed over a typical ensemble composed by three or four data points (Jourdin et al., 2014, their Eq. (10)). Hence, in a homogeneous medium and in absence of biofouling, measured values of the cross-beam backscatter ratio are close to the sensor noise (typically 1 dB). But a drop of up to 10 dB has been observed in ADCP moorings deployed off the French coast (Jourdin et al., 2014), while in an ADCP mooring off the Belgian coast a gradual drop of more than 20 dB in acoustic backscatter intensity have been recorded. A value of 10 dB leads to under-estimation of the suspended sediment concentration by one order of magnitude, over the entire acoustic profile. If only one beam of an ADCP is affected by biofouling, this can be corrected by applying the median function to all beams as explained in Jourdin et al. (2014). Fig. 5 provides an example of permanent biofouling resulting in a gradually decrease of the acoustic backscatter intensity during the mooring, while in Fig. 6 episodic biofouling events are shown. In any case, acoustic and optical instrument should be serviced at least once a month and at higher frequency during periods of strong seasonal bloom (van der Hout et al., 2017).

### 3.2.2. Saturation and ambiguity problems

SPMC in the field may vary from several mg/l to a few g/l. At these ranges, the OBS output increases with SPMC, and the gain setting is adjusted by the manufacturer for an optimized sensitivity at the expected concentrations in the field. However, for too high SPMC values, saturation occurs and the OBS output will show a plateau as illustrated in Fig. 4 (the OBS at 0.2 mab from day 137 onward). The individual setting of certain probes can be adjusted (see Section 3.1.2) to broaden the range of SPMC before saturation.

For many OBS probes, beyond the saturation range, the output signal decreases with increasing concentration as was firstly observed in the field by Kineke and Stenberg (1992). They attributed this trend to the partial blockage of the emitted beam by highly concentrated suspensions, the reduction of the scattering volume relative to the area of detection. Fig. 7 shows typical bell-shaped backscatters curve, meaning that a given OBS output can correspond to two possible SPMC values. The two values that can be obtained (i.e. the up and over response) depend on the sensitivity of the individual sensor. This bell-shaped response can be particularly useful when measuring near-bed very high concentrations (Sottolichio et al., 2011). However, because of this ambiguity, the determination of SPMC in highly concentrated waters ($>$ 4 g/l) with a single-point measurement is not always possible. A correction is possible in case of vertical profiles, because SPMC is continuously increasing downward and the decrease of the near-bed OBS output can be readily related with an increase of SPMC (Kineke and Sternberg, 1992). However, this does not help in case of time series, obtained by one probe at fixed height above the bed. The use of a second probe above the other could help to solve the ambiguity of one of the two probes (Fig. 7). Acoustic backscattering sensors show the same type of response than optical probes, and the ambiguity issue applies thus also to acoustic devices, such as single point ADV sensors (Ha et al., 2009; Sottolichio et al., 2011).

### 3.2.3. Air/gas bubbles

Due to the high acoustic impedance or the very different refractive indices between gas and water, the volumetric backscattering strength measured by acoustical sensors or the scattering efficiency measured by an optical sensor is sensitive to the presence of air or gas microbubbles (1–500 μm in radius) in water. These bubbles are mainly generated at the sea surface by wave breaking or white-capping (e.g. Schwendeman and Thomson, 2015) and as a consequence the subsurface scattering is perturbed by the sea state (e.g. Klein, 2003; Downing, 2006; Puleo et al., 2006) from surface up to depth (in m) that approximately equals the wind speed (in m/s) squared divided by 15 (Wang et al., 2016) or in the vicinity of bubble plumes (Nauw et al., 2015). Indeed, the finest bubble population of typical size less than 50 μm in radius penetrates within the water column where it can remain in near-equilibrium suspension (e.g. Randolph et al., 2014). Outside the surf zone, bubbles can be carried down in form of plumes or patches by convergent fronts or

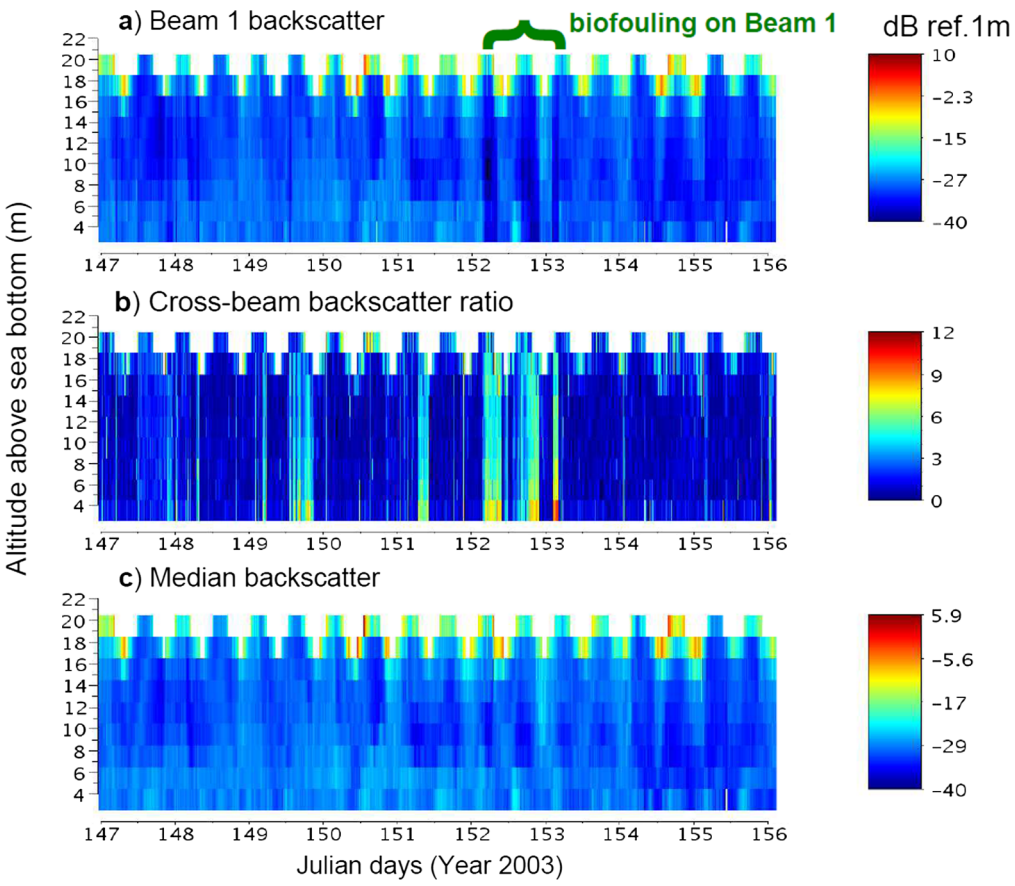


**Fig. 6.** 9-day time series of the backscattering strength vertical profile recorded by an upward-looking 500 kHz ADCP (Nortek ADP) moored on the sea bottom at 20 m depth in the Bay of Vilaine, South of Brittany (France). The surface oscillation corresponds to the tidal elevation. (a) Volume backscatter strength measured by the transducer 1. At day 152 a biofouling event caused a sudden drop in all backscatter values of the profile, by nearly 10 dB. Following, backscatter values rise again and drop again until day 153. (b) Cross-beam backscatter ratio $R_v$. Biofouling events on other transducers are identified at days 149 and 151. (c) Median acoustic backscatter intensity. The median allows a computation of a backscattering strength without perturbations by the biofouling.

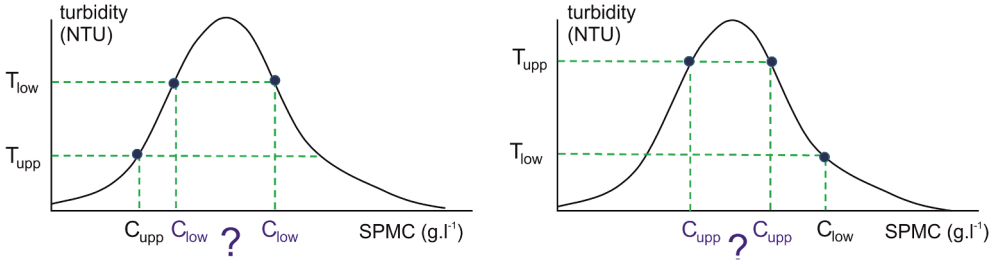


**Fig. 7.** Typical bell-shaped backscatters curve of an OBS (Sottolichio et al., 2011), meaning that a given OBS output can correspond to two SPMC values. The figure shows how this ambiguity can be solved by using two superimposed sensors. Left: when the upper probe records lower turbidity than the lower probe, upper concentration is solved, but the lower remains unsolved. Right: when the upper probe records higher turbidity than the lower one, lower concentration is solved, but the higher remains ambiguous and unsolved.

wind-induced down-welling to depths up to 30 m. The vertical distribution of wave bubbles decays exponentially with depth resulting in a similar decrease of the backscattering strength at lengths scales of 0.5–5 m (Wang et al., 2016). Expressed in decibels the backscattering intensity displays a linear decrease with depth (e.g. Wang et al., 2011) and this property together with measurements of the wind speed ($U_{10}$) and wave height in parallel can be used to discard parts of profiles affected by wave bubbles, see the example in Jourdin et al. (2014).

### 3.2.4. Density stratification

As reminded in Eq. (2), acoustic backscatter inversion requires first correction for water attenuation, which is a function of the acoustic frequency, temperature, salinity and depth (Lurton, 2010). In estuaries and coastal seas, strong density stratification can be observed, and may introduce noise in the backscatter intensity inversion if not corrected properly: for a 1200 kHz ADCP, the water attenuation coefficient can vary from 0.2 dB/m to 0.55 dB/m. For a given average temperature, the water attenuation coefficient variability is around 0.1 dB/m for a 1200 kHz. The uncertainty introduced by stratification was examined using ADCP and CTD measurements in the Seine estuary, where strong temporal and vertical stratification are observed as shown in Fig. 8 (Sahin et al., 2017). In the given example, not considering water salinity/temperature variability may induce uncertainty on absolute acoustic backscatter intensity of the order of 1 dB, which results in a systematic error of about ± 40%. Similar uncertainties can be expected offshore, as salinity/temperature variability is lower but depths are larger.

### 3.3. Sample related uncertainties

Sample related uncertainties occur during collection and analysis of the sample SPMC, i.e. the filtering and weighing. A diversity of methods and equipment are used to collect water samples, such as Niskin bottles, Go-Flow bottles and stand-alone or on-board sea water pump or suction systems. The bottles attached to a profiling frame, or the intake for the pump system should be close enough to the detection volume of the sensors, which are deployed for model calibration. Whereas the occurrence of SPM in plumes creates random scatter in the relation

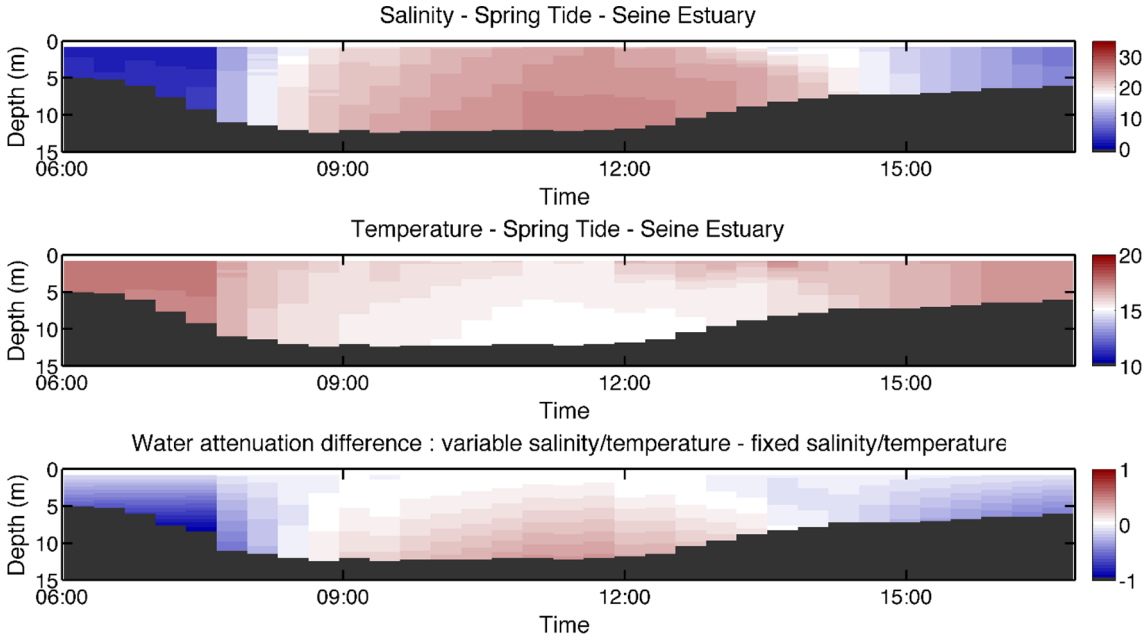


**Fig. 8.** Salinity (top panel) and temperature (°C, middle panel) variability in the Seine Estuary turbidity maximum zone during spring tide. The lower panel shows the water attenuation correction differences (in dB) with and without consideration of salinity and temperature variability.

between filter weights and sensor outputs, the occurrence of permanent gradients causes systematic errors. Therefore, one should take beforehand knowledge of the spatial gradients to define "close enough". It is not possible to present a general number here, as the gradients are dependent on the spatial extension of the studied basins or estuaries or the typically prevailing hydrodynamic energy inputs. In most cases samplers are mounted on the same frames as the sensor packages. Scales of horizontal gradients are normally in the order of more than 10 m and therefore less critical than vertical that are typically in the order of a meter or less.

Standard protocols for dry mass SPMC determination (Strickland and Parsons, 1968; Pearlman et al. 1995) and additional procedures to partition SPMC into its organic and inorganic content (e.g. loss on ignition, element analysis) are straightforward: They include filtering a specific volume through a pre-weighed filters, washing of sample filters and filter edges with deionized water (or MilliQ water) to remove salt, drying, and weighing of the filter to determine the dry mass of the SPMC. In early years, paper filters were used; later membrane filters (Banse et al., 1963) have been in use, while nowadays often glass-fibre filters (type GF/F or GF/C) are used. The removal of the salt in filters is a critical source of uncertainty, which if not well done, will lead to an overestimation of the SPMC (Neukermans et al., 2012a). Additional uncertainties are related to the determination of the dry mass and filter volume and the amount of structural water in minerals (Barillé-Boyer et al., 2003). Most uncertainties are related to a constant mass offset (salt, weight and volumetric determination) and are, hence, relatively small when enough mass of particulates (several milligram) is collected on the filter. The collection of a sufficient mass is easy to achieve in turbid nearshore or estuarine waters dominated by mineral material, but more difficult in low turbid organic-rich waters or for example during a *Phaeocystis* bloom. In the latter case the gelatinous algal colonies may clog the filter before enough material is collected and prevent the removal of the salt. In cases were the sample mass on the filter is not very high, errors due to salt are significant (Banse et al., 1963; Stavn et al., 2009; Röttgers et al., 2014). In cases were the sample is turbid (> 100 mg/l), the main uncertainty is often caused by the difficulty to homogenize the sample prior to subsampling and filtration (Fettweis 2008). Methodological improvements include the optimization of the filtration volume and cleaning of the filter margin after the funnel is removed (Neukermans et al., 2012a); the correction of the salt mass bias using procedural control filters (Stavn et al., 2009), the filling of the filter margin with salt-free water before filtration and the determination of a SPMC free of the salt-bias using a set of different sample volumes (Röttgers et al., 2014).

The uncertainty in sample SPMC decreases with increasing SPMC as shown for a data set of about 2500 sample SPMC from the Belgian nearshore obtained with the method of triplicates with the same volume using GF/C filters. The uncertainty (expressed as the RMSE of the triplicates divided by the mean value) is highest (8.5%) for sample SPMC lower than 5 mg/l and decreases with increasing SPMC to 6.7% (< 10 mg/), 3.5% (10–50 mg/l) and 2.1% (> 100 mg/l). This error corresponds to the uncertainty introduced if only one replica was used instead of three replicas. In case of triplicates the error is limited by excluding sample SPMC with a RMSE exceeding a threshold value. The need of subsamples with different volumes versus subsamples with the same volume has been checked from samples collected in three stations with different turbidity in the southern North Sea. The estimated slope, i.e. the SPMC, has an uncertainty that can be higher than 1 mg/l (> 30%) for clearer waters (SPMC about 3 mg/l) and then it drops to about 0.3 mg/l for SPMC of about 11 mg/l (3%) or 25 mg/l (1%). Using the method with the same volume, the uncertainty is about 0.3 mg/l (10%) for the clearest sample, about 0.4 mg/l (4%) for SPMC around 11 mg/l and about 0.8 mg/l (3%) for SPMC of around 25 mg/l. The relative difference between the estimated SPMC using this method and the different volume method (applied three times, and averaged) is about 11% for clear waters, 6% and 4% for higher levels of turbidity. One should consider that the uncertainty (standard deviation) of the SPMC through averaging of triplicates with the same volume is not the same uncertainty as that obtained via the slope determination using the different volume method. The latter includes a random and a systematic error due to the offset by salt, while the same volume method provides only a measurement error. The systematic error is not detected in the same volume method, which explains the apparent lower uncertainty of this method, especially at low SPMC as compared to the different volume method. The method with different volumes is more accurate, the latter holds especially in low SPMC waters, where the effect of salt is important (Röttgers et al., 2014).

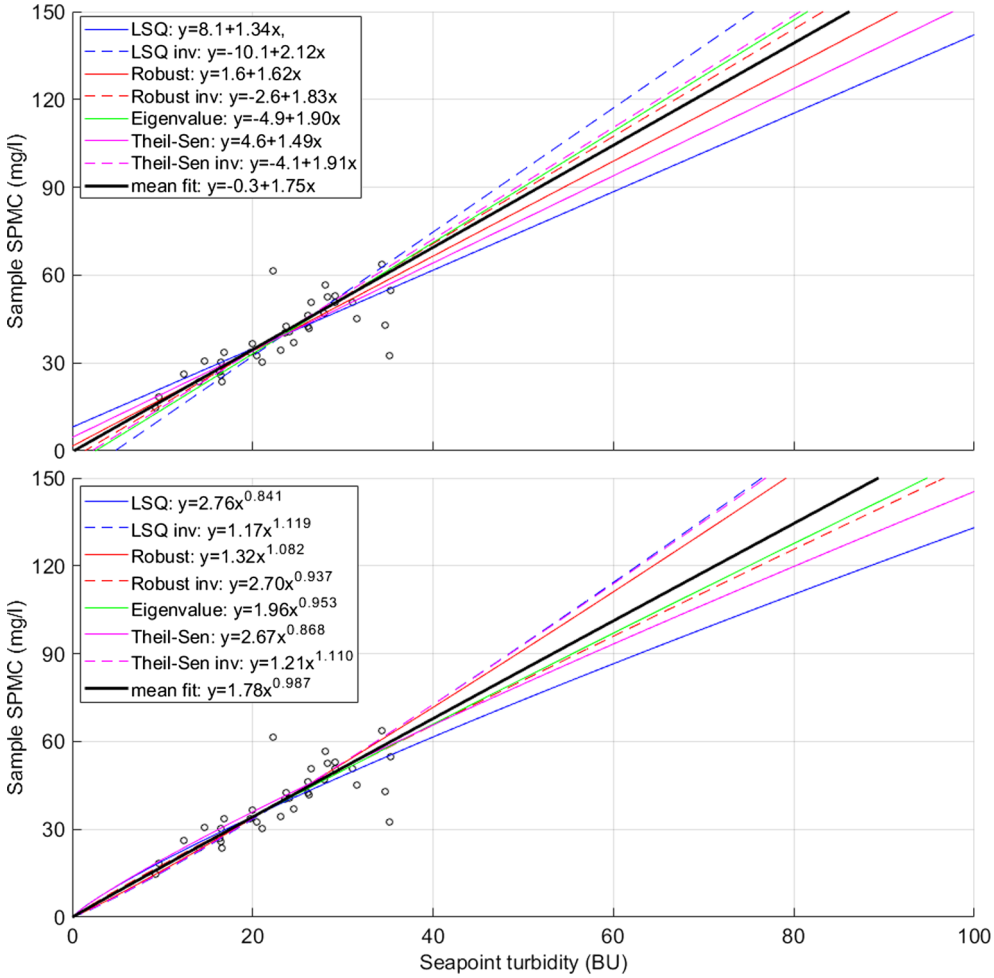


**Fig. 9.** Relating sample SPMC to sensor output using different linear regression models for the actual and the log transformed data ($R^2 = 0.61$, 26 samples). The data have been collected in the Belgian nearshore area and consist of 26 sample SPMC and corresponding turbidity values from a Seapoint OBS. The solid lines correspond to the relationship BU = f(sample SPMC) and the dash lines to sample SPMC = f(BU). The bold line is the mean of the 7 regressions and represents a baseline to show the variability of the different regression models (compare Sections 3.4.2 and 4.1.4).

### *3.4. Relating sensor output to sample SPMC*

Modelling techniques establish a statistical relationship between turbidity or acoustical backscatter intensities and reference SPMC data, i.e. the sample SPMC (ISO, 2014). This relationship is applied to convert the time-series of turbidity or acoustical backscattered signal into SPMC. However, for acoustic devices such as an ADCP a calibration against in situ water samples is challenging, as samples are often difficult to collect next to the profiling sensor and as the property of the SPM may change over the water column. For these cases the SPMC derived from optical sensors measuring close to the ADCP is often used as reference SPMC. It must be noted that the sample SPMC or the optical-derived SPMC is collected at a given location in a confined volume, while the acoustic backscatter signal from a profiling sensor is the mean of a user-defined volume, which is generally much larger than the one of the sample SPMC. This procedure will add additional uncertainty to the model.

The first two sections deal with a purely technical aspect, i.e. the biases involved with the choice of the linear regression model. The third section addresses uncertainties that are caused by systematic changes of the particle IOPs or IAPs that will result in varying proportional factors between the detected signal and SPMC that are not detected during the generally short calibration periods. A general bias in the model parameter calibration relation may be caused by the spatiotemporal mismatch between the sample and the sensor, by local changes in the turbulence and floc size caused by the sampling device or by the calibration period that is not necessarily representative for the whole unsupervised time series. The fourth section deals with the inconsistencies between parallel optical and acoustical data that are caused by the uncorrelated and random variations in the IOPs and IAPs.

#### *3.4.1. Modelling techniques*

The relationship between optical sensor output to SPMC or the acoustic backscatter to the $10\log_{10}$(SPMC) can be modelled using a linear model (see Section 2.2). The model can be applied to the linear domain or the log-log transformed domain (the latter only for turbidity data). Mostly, after quality checks of the data, linear regression finds optimal regression parameters by minimization of the squared differences between the values of the dependent variable and the regression line ($X^2$ method, further called LSQ). In general, however, different options for the linear regression method can be considered that lead to different values in the regression parameters for the same data set and different levels of predictability of SPMC from optical turbidity or acoustic backscatter intensity.

The first option is the choice of the independent (explanatory) and dependent (response) variable. As one finally wants SPMC as a function of turbidity, mostly SPMC is used as dependent variable. On the other hand, as turbidity depends on SPMC and not vice versa, this requires turbidity as dependent variable and then compute SPMC from turbidity using the inverse of the calibration regression. As another option, one

may regard both SPMC and turbidity not strictly causal dependent on each other. This situation may be adequate for cases where water sampling locations and turbidity detections volumes differ by typically more than the coherence lengths of the SPMC in the observation area. Then the minimization of the difference between data and regression line should take place perpendicularly to the regression line solving an Eigenvalue problem. This method leads to symmetric results no matter whether SPMC or turbidity is the dependent or independent variable.

In most real data sets, the assumptions for linear regressions are not met (e.g. Gilbert, 1987) and ordinary least-squares fitting can have undesired sensitivities both in best model parameter or confidence interval estimations. In this study, two examples of robust fitting are contrasted with ordinary least-squares, i.e. the Theil-Sen estimator (e.g. Wilcox, 2010) and the "iteratively reweighted least squares" (further called Robust) method (Press et al., 1989).

To overcome the problems with data heteroscedasticity, $\log_{10}$ -transformations of the variables can be applied, a decision that should be based on the examination of the model residuals (Helsel and Hirsch, 2002). This transformation has also the advantage that the distribution of data along the independent variable is more homogeneous as there is very often a bias in the coastal water sample data sets towards lower SPMC. The re-transformation of the regression line into the original units introduces a bias that arises as the regression estimates are computed from means in log units unequal to the mean in original units. Helsel and Hirsch (2002) recommend the usage of the non-parametric "smearing" estimator

$$BCF = \frac{\sum_{i=1}^{n} 10^{e_i}}{n} \tag{4}$$

introduced by Duan (1983) as bias correction factor (BCF) with $n$ the number of samples, and $e_i$ the residual of sample $i$ in log-units. This BCF is not symmetric when using the Eigenvalue regression in the log space as SPMC and turbidity have different units.

Fig. 9 shows the calibration of an OBS against sample SPMC for the different methods and the exchange of dependent and independent variables. It also shows that outside the data range available for calibration, the uncertainty may increase significantly. In the next example, the direct calibration of an ADCP (1 MHz Nortek AWAC) against sample SPMC in a moderately turbid environment (< 100 mg/l), is shown (Fig. 10). The direct calibration with sample SPMC was performed for the surface and bottom samples separately as they originate from different population of particles in suspension, i.e. surface plume and bottom resuspension. The data are from a coastal observatory located at the mouth of the Seine estuary and consists of a bottom station equipped with an ADCP and a Wetlabs NTUSB optical backscatter sensor (Wetlabs OBS) and a surface buoy measuring turbidity with a similar Wetlabs NTUSB sensor.

In Fig. 11 the model calibration of two acoustic sensors (3 MHz Sontek ADP with series number M284 and M947) is shown using the OBS-derived SPMC as the reference SPMC. The data is from a one-year time series in 2013 collected in the turbid Belgian nearshore area at about 2 m above the bed (Fettweis et al., 2016). Both acoustic sensors have measured about half of the period at a burst rate of 15 min and all the available OBS and ADP data pairs have been used for the model calibration (M284: 12280; M947: 14923). The OBS sensors have been calibrated twice during the period against sample SPMC. The model calibration (M284: $R^2 = 0.4$; M947: $R^2 = 0.6$) shows strong scatter in the data and thus a high uncertainty in the acoustic derived $10\log_{10}$(SPMC) versus acoustical backscatter in dB. This is indicated by the dashed lines in Fig. 11 representing the results of 7 different regression models. Their slopes differ by a factor of 1.8 and the associated uncertainties by even a factor of 3 within the data range when the OBS-SPMC data are re-transformed to SPMC. Other studies report similar (up to 0.8) ranges of $R^2$ (Fugate and Friedrichs, 2002; Gartner 2004; Dufois et al., 2014). The difference between OBS and ADCP estimates of SPMC during a one-week deployment in San Francisco Bay was 8–10% relative to OBS range and about 35–40% relative to OBS mean (Gartner, 2004).

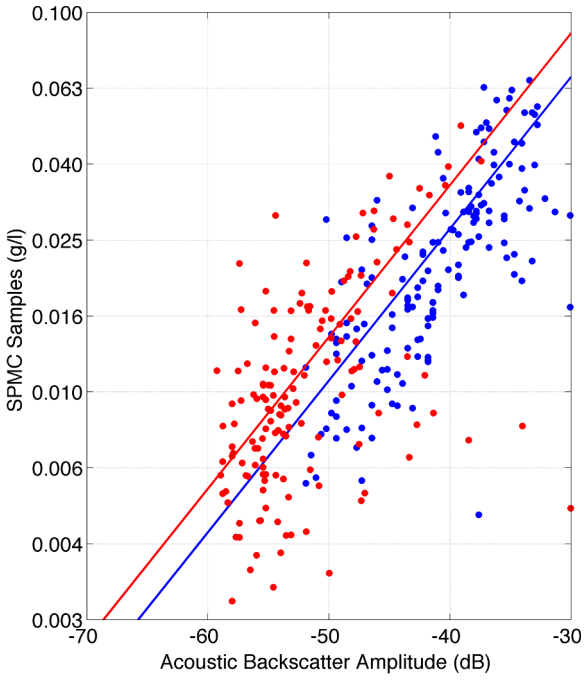


**Fig. 10.** Direct calibration of a profiling acoustic sensor (Nortek AWAC) against sample SPMC in a moderately turbid environment (< 100 mg/l) located at the mouth of the Seine estuary (red dots: surface samples, blue dots: bottom samples).

### 3.4.2. The choice of the linear regression model

To estimate the uncertainties introduced by the choice of a specific regression method, we applied the different regression methods as described in Section 3.4.1 to eleven data sets with $R^2$ between 0.58 and 0.99. With three minimisation schemes (LSQ, Eigenvalue and Robust fit) plus the Theil-Sen estimator, exchanging turbidity and SPMC as independent variable and taking the data with and without $\log_{10}$ -transformations we obtain 15 combinations per data set, as for the non-transformed data the eigenvalue method is symmetric to the choice of abscissa and ordinate. The data sets consist of pairs of sample SPMC and turbidity collected at various location with Hach nephelometers (North Sea, English Channel, Mediterranean Sea, French Guiana coast, Gironde estuary, Rio de la Plata) and Seapoint sensors (Wadden Sea, North Sea, Oosterschelde estuary, Weser estuary). As an example for a field data set ($R^2 = 0.61$, 26 samples), Fig. 9 depicts the 15 regressions. Within the range of the calibration data, the different model results differ by some 20%, but they increase significantly beyond the data sample range. In the following, we define Regression Spread (RS) as the percentage difference between SPMC computed from the regression models with highest and lowest slope as a function of turbidity. In Fig. 12a the RS derived from the seven regression models for the non-transformed (i.e. linear scale) sample-SPMC/turbidity data pairs is plotted versus data set $R^2$. Fig. 9 exemplifies that within each data set RS depends on the value of the turbidity relating to the mean turbidity. To make the regressions of all data sets comparable, RS was computed for different z-transformed (standardized) turbidities, $T_{z-std}$ defined as

$$T_{z-std} = (T - \bar{T})/std(T) \tag{5}$$

where $T$ is turbidity and $\bar{T}$ the average and *std(T)* the standard deviation of the turbidities in each data set. For $T_{z-std}$, six values between −0.5 and 8 (see Fig. 12) were chosen to cover the turbidity range from close to the origin to far beyond the range of the calibration data pairs.

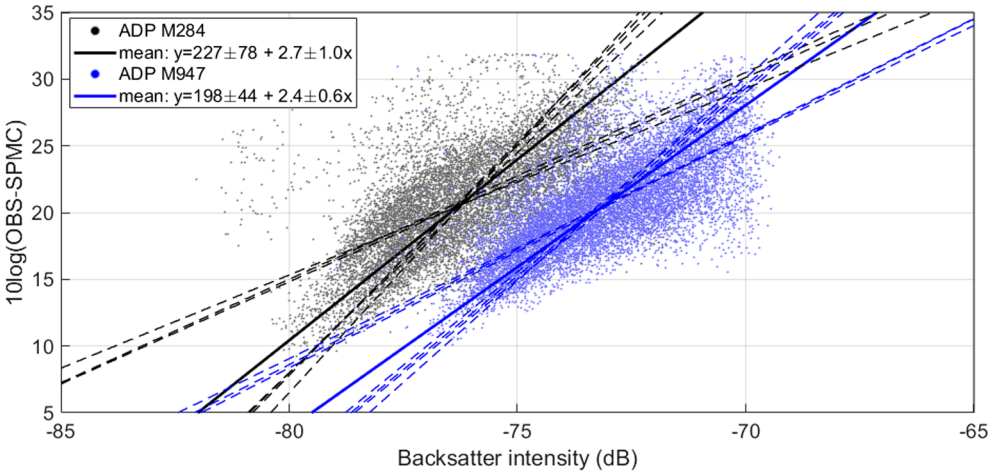


**Fig. 11.** Relating OBS derived SPMC to the backscatter intensity of the first bin of two Sontek 3 MHz ADP profilers (M284, M947) using linear regression models. The data set consists of about one-year data collected in 2013 in the Belgian nearshore area; every sensor measured about half of the period (M284: R2 = 0.4; M947: $R^2$ = 0.6). The dashed lines represent the regressions of 7 different models (see text) and the bold lines show the mean over the regressions, which is our baseline to show the variability of the different regression models (compare Sections 3.4.2 and 4.1.4).

For $T_{z-std}$ = 2 (typically the 95% percentile of the turbidities in the calibration data sets) RS increases significantly with decreasing $R^2$ from nearly 0% for $R^2$ close to 1, to 10% for $R^2$ = 0.93 and 30% for $R^2$ = 0.60. For $T_{z-std}$ = 0 (centre of the turbidities in the calibration data sets), RS is close to zero, as expected. For $T_{z-std}$ = 8 and $R^2$ < 0.6, RS amounts to more than 50%.

Fig. 12b and c display slopes and intercepts by linear regression (Eigenvalues method) of RS for the six $T_{z-std}$. Their dependence can be closely fitted by exponentials and yields the following formula for RS as a function of $R^2$ and $T_{z-std}$:

$$RS = 140(e^{-0.35T_{z-std}} - 135)R^2 + 140(1 - e^{-0.44T_{z-std}}) - 5 \quad (6)$$

This formula predicts the percentage spreading within 5% with an $R^2$ of 0.91 and can be used to estimate the uncertainties involved with the choice of the regression method applied based only on $R^2$ and dependent on the value of $T_{z-std}$ for any data set.

We further investigated RS of each regression method for the exchange of independent and dependent variables, as this, according to Fig. 9, is the main control for the magnitude of RS. For each data set, we created the mean of all seven linear scaled data regressions as a baseline and computed for each regression method the Regression model choice Uncertainty (RU), defined as the relative differences of SPMC to the baseline value as a function of $T_{z-std}$. In Fig. 13a RU averaged over the data sets with $R^2$ < 0.75 and in Fig. 13b RU averaged over the data sets with $R^2$ > 0.90 versus $T_{z-std}$ is shown. At $T_{z-std}$ = 0, RU is nearly zero for all methods, whereas towards negative $T_{z-std}$ it diverges sharply reaching more ± 40% at $T_{z-std}$ = −1 (the 10% percentile of the turbidities in the calibration data set), as the computed absolute SPMC differences in the denominator of RU are approaching zero. With increasing $T_{z-std}$, these differences remain confined to ± 15% ($R^2$ < 0.75) and ± 5% ($R^2$ > 0.9) within the calibration data range below $T_{z-std}$ = 1.6 (90% percentile). However, further increasing $T_{z-std}$ results in even higher RU that depends both of the $R^2$ of the data set and the regression method. For data sets with $R^2$ > 0.90, this plateau remains below ± 5% for all regression methods, but raises to nearly ± 20% for data sets with $R^2$ < 0.75. Here, the regression methods differentiate distinctively from each other, see Fig. 13a. The LSQ method for example, with turbidity as dependent variable and SPMC computed from the inverse of the regression, deviates from the baseline by +20%, whereas the Eigenvalue and inverse robust fit regression still remain close to +5%. All inverse regressions have a positive bias with respect

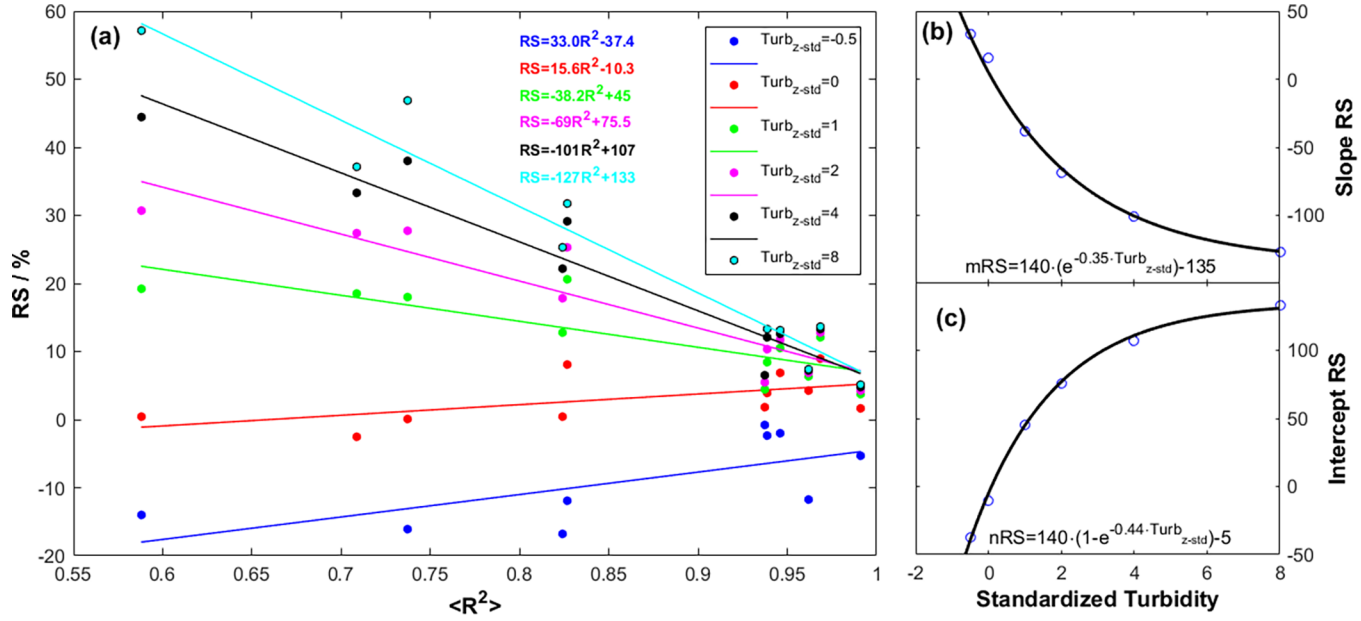


**Fig. 12.** (a) Regression spread (RS) versus $R^2$ for 11 sample-SPMC/turbidity data calibration sets. Coloured dots denote values for different standardized turbidities $T_{z\text{-std}}$ (see Section 3.4.2), coloured lines the corresponding results of the Eigenvalue regressions. (b) Slopes of the regression functions shown in panel (a) versus $T_{z\text{-std}}$. The line shows the result of the exponential fit. (c) The same as (b) for the intercepts.

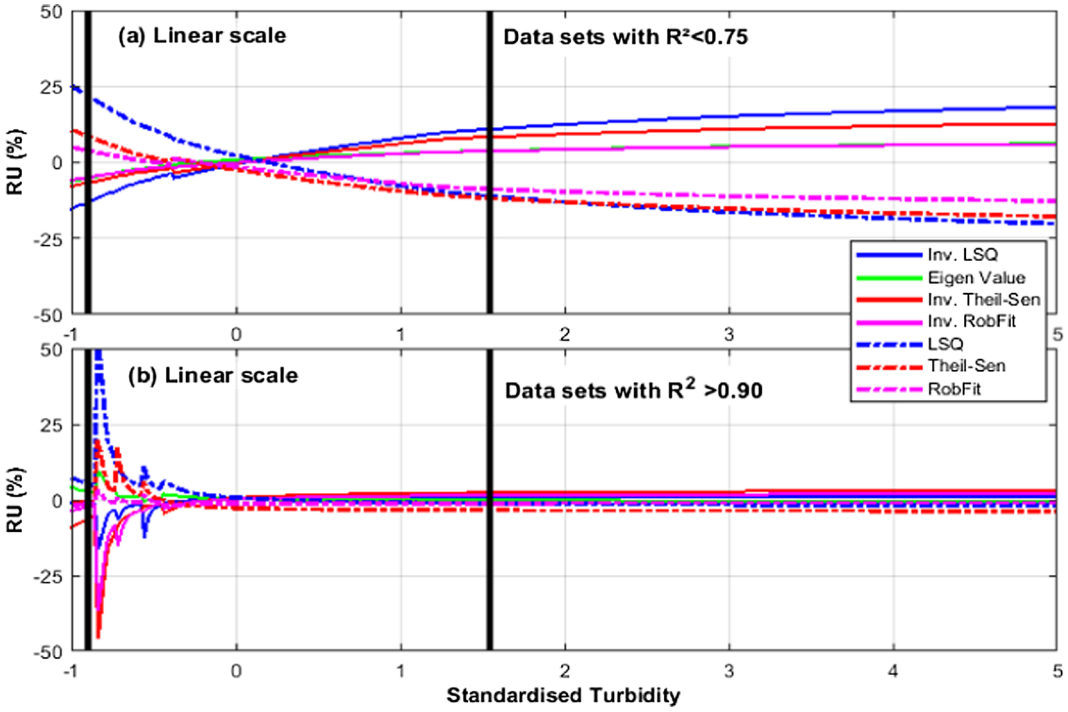


**Fig. 13.** Regression model choice uncertainty (RU) for the different regression models as a function of standardized turbidity ($T_{z\text{-std}}$) for the linear scale. The examples show RU averaged over data sets with $R^2 < 0.75$ (upper panels) and $R^2 > 0.90$ (lower panels). The black lines represent the 10 and 90% percentiles of $T_{z\text{-std}}$ averaged over all calibration data sets. Note the different limits in the ordinates of the left and the right panels.

to the mean, whereas the regressions with SPMC as dependent variable have a negative bias of the same amount.

The situation is quite different for the regressions performed with $\log_{10}$-transformed data. The slope of the regression may deviate from 1, resulting in a non-linear power function after re-transformation. This may result in quite large RU at high $T_{z-std}$, see Fig. 14. For data sets with $R^2 < 0.75$, the RU exceeds by more than ± 50% at $T_{z-std} = 8$ with no signs to reach a plateau limit at higher $T_{z-std}$. For $R^2 > 0.9$, the RU is much lower with ± 20% at most and reaching the plateau at $T_{z-std} = 6$. This value still is four times higher than for the regressions with not-transformed data. Within the calibration data range the uncertainties are still higher by a factor of 2 compared to the not transformed cases. At the lower end of the of $T_{z-std}$, the RU of all models are more or less identical and remain low as all regressions are forced to cross the origin point.

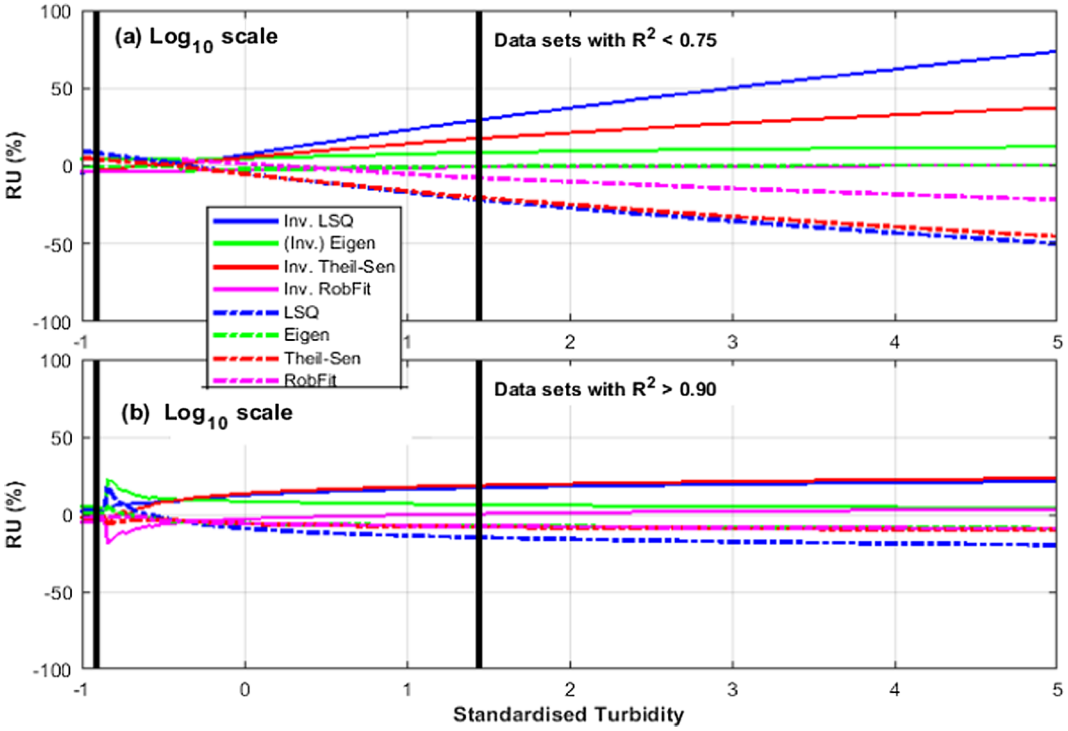


**Fig. 14.** Idem Fig. 13 but now for the log10 – transformed data.

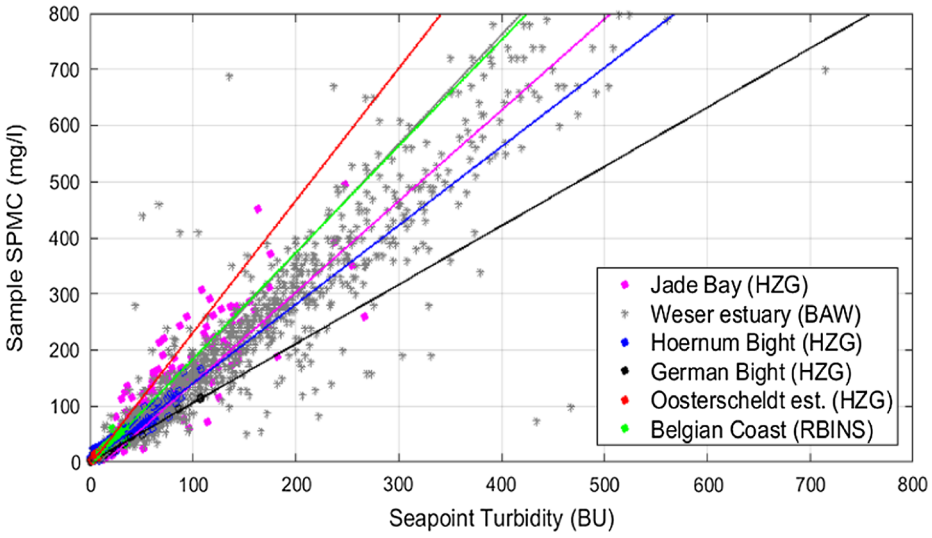


**Fig. 15.** Sample SPMC as a function of Seapoint turbidity collected at various locations in the southern North Sea. The regression is calculated with the Eigenvalue model. The mean regressions are (SPMC = ax + b): all data ($R^2$ = 0.88; a = 1.53, b = −1); Jade Bay ($R^2$ = 0.83; a = 1.95, b = −17), Weser estuary ($R^2$ = 0.83; a = 1.62, b = −21); Hoernum Bight ($R^2$ = 0.95; a = 1.41, b = 0); German Bight ($R^2$ = 0.99, a = 1.05, b = 1); Oosterschelde estuary ($R^2$ = 0.74; a = 2.34, b = −3); Belgian coast (data from Fig. 9, R2 = 0.61, a = 1.90, b = −5).

Of course, the results shown here are valid for any data set independent of the meaning of the variables. This means that the uncertainties involved with the model calibration of acoustical backscatter data against an OBS derived $10\log_{10}$(SPMC) are much larger as the examples in Figs. 10 and 11 show, where the $R^2$ is 0.4 and 0.6 respectively. The situation is even aggravated after raising the data to the power of 10, where the uncertainties will increase accordingly and likely exceed 100%.

### 3.4.3. Variabilities in SPM inherent properties

Variabilities in IOPs may occur between different geographical areas or within a same measuring location. The former is illustrated in Fig. 15, where the relation between sample SPMC and Seapoint turbidity is shown for different areas in the North Sea. The spreading in the data is caused by variabilities in inherent particle properties between the areas. Additional causes of the differences are inter-sensor variabilities and uncertainties due to the sampling and filtration protocols. The latter are thought to be of lesser importance as the differences in slope of the regression lines (German Bight: 1.05 and Oosterschelde estuary: 2.34) is larger than these additional uncertainties. Local variation in the IOPs have thus to be considered when regional turbidity data are compiled into SPMC maps.

Intra-tidal variabilities in IOPs at a same location have been observed at various locations. Fig. 16a shows that the specific backscatter ratio (i.e. turbidity divided by sample SPMC) is oscillating with the tides (Becherer et al., 2016) and that this may be largely assigned to the organic content of the particles that increases with the specific backscatter ratio (Fig. 16b). The magnitude and the tidal signal of the ratio nearly persisted after the storm even though sample SPMC at maximum currents increased threefold. With respect to the tidal mean this would result in a systematic over- and underestimation of the SPMC by 60% over the tidal cycle. Variation in the specific backscatter ratio may also occur on seasonal time scales as observed in Liverpool Bay (Jafar-Sidik et al., 2017). These variations are caused by the seasonality of the primary production and turbulence regime and have changed the ratio by a factor 2.

Another example shows intra-tidal variations in acoustical and optical inherent particle properties due to occurrence of mixed particles (i.e. sand and mud) in suspension at a muddy and sandy bed site located in the main tidal channel of a brackish marsh in the Scheldt estuary (Schwarz et al., 2017). The optical sensor was calibrated with sample SPMC and the optical derived SPMC was subsequently used to calibrate the acoustic backscatter sensor. The muddy bed site shows a strong correlation in contrast with the sandy bed site between acoustical and optical backscatter during the two tidal cycles (Fig. 17). These observations indicate constant particle properties during a tide at the muddy site and changing particle properties at the sandy site, indicating that the SPM at the muddy site consists mostly of muddy flocs resuspended from the bed, while at the sandy site sand grains with diameters comparable to those of flocs are eroded into suspension at high flow velocities. Their intermittent abundance will lead to changes in the IOP's of the SPM due to their higher specific density, i.e. the increase of $\rho$ will lower the ratio of turbidity to sample SPMC (see Eq. (1)). A storm event recorded at an observation pole in the Elbe river (Baschek et al., 2017, Kappenberg et al., 2018), discloses a further example of significant changes in this ratio due to sand grains entrained into the water column. The ratio of optical turbidity to SPMC derived from water samples taken hourly over a period of 12 h before, during and after the storm varied from 0.4 during the moderate wind phases to 0.12 just after the peak of the wind speed (Fig. 18). Grain-size analysis of the samples revealed a significant increase of mainly sand around the 90 μm fraction. As a consequence, optical turbidity remained in the range of average tidal variability during the storm, whereas sample SPMC exceeded this by a factor of five. Similar observations have been made at other locations where mixed sediments and/or strong changing current and wave conditions caused sandy material or particle with other erosion characteristics to be resuspended up to the detection volumes of the acoustic and optical sensors (see e.g. Fugate and Friedrichs, 2002; Fettweis et al., 2012).

The sample SPMC and the sensor data should preferably be collected in situ as it represents the actual inherent properties of the SPMC and is thus more reliable than in laboratory model calibrations (ISO, 2014). In case no in situ samples can be collected or if the range of sample SPMC is too small, in laboratory model calibration can be applied with representative samples. Bollen et al. (2006) describes a laboratory model calibration using a representative in situ bed sample taken near the monitoring station. The bed sample was sieved on a 63 μm sieve, followed by desalination and drying, to finally produce standard solutions with defined SPMC. The regression model using in situ data has a larger slope and overestimates the sensor output by about 10%. The difference is most probably caused by changes of the laboratory versus in situ IOP of the SPM.

The examples demonstrated that in situ calibration with samples is necessary at all representative locations and phases of the local hydrodynamic and biogeochemical conditions to take the varying composition of the suspended particles into account.

### 3.4.4. Comparison between optical and acoustical derived SPMC

A comparison of the modelled SPMC was performed from different optical and acoustical sensors, based on the data from the mouth of the

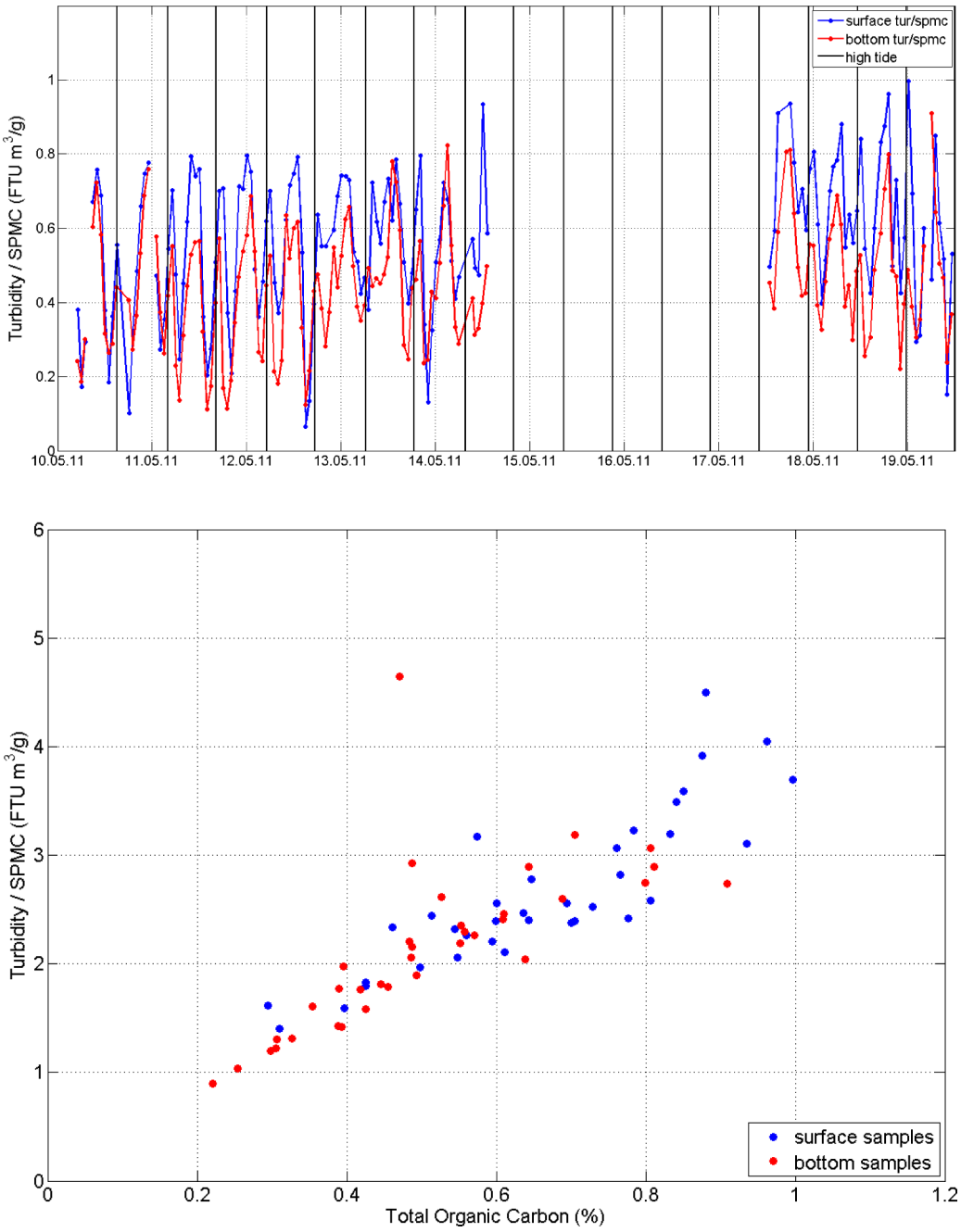


**Fig. 16.** Sample SPMC and turbidity collected in the tidal inlet between two islands in the German Wadden Sea between 10 and 19 May 2011 (Becherer et al., 2016). Sample SPMC ranged between 7 mg/l and 500 mg/l, during the storm (14–17/05) no samples have been taken. (a) Time series of the ratio turbidity/sample SPMC and (b) dependence of the specific backscatter b = turbidity/sample SPMC on total organic carbon. All samples shown are taken after the storm, from 17th through 19th May. Surface data are taken 1 m below water surface.

Seine estuary (Fig. 10). The same sample SPMC was used to build models for a moored Wetlabs OBS, a profiling OBS3+ and a moored ADCP (1 MHz Nortek AWAC) and the modelled optical derived SPMC was further used as reference SPMC to build a model for the moored ADCP in order to estimate and compare model performance and associated uncertainties (Fig. 19). Results show that the optical sensors have highest accuracy against sample SPMC (OBS3+: 10%, Wetlabs OBS: 40%) and that the acoustical derived SPMC compare well with the OBS3+ profiles for the period where both sensors have been calibrated against sample SPMC. In the same figure the acoustic derived SPMC is compared with the SPMC time series derived from the Wetlabs OBS's, thus for periods that are not covered by the field campaigns dedicated for calibration. The optical and acoustic derived SPMC values significantly differ, the ADCP underestimating large optical derived SPMC and overestimating the lower ones. The acoustic sensor has the larger uncertainty at lowest (400% for SPMC $<$ 5 mg/l) and highest values; in the mid-range the uncertainty is about 100% (5 mg/l $<$ SPMC $<$ 10 mg/l) and below 50% (SPMC $<$ 75 mg/l). The results also show that the error of the reference SPMC propagates into the uncertainty of the acoustic derived SPMC, as can be seen when comparing the ADCP derived SPMC from Wetlabs OBS (20–150%) and OBS3+ (20–50%).

High uncertainties between acoustic and OBS derived SPMC have been observed in the data from the Belgian nearshore, see Fig. 20. The normalized RMSE associated with the regression model varies between 100 and 500% (mean regression is 170%) for the M284 ADP and

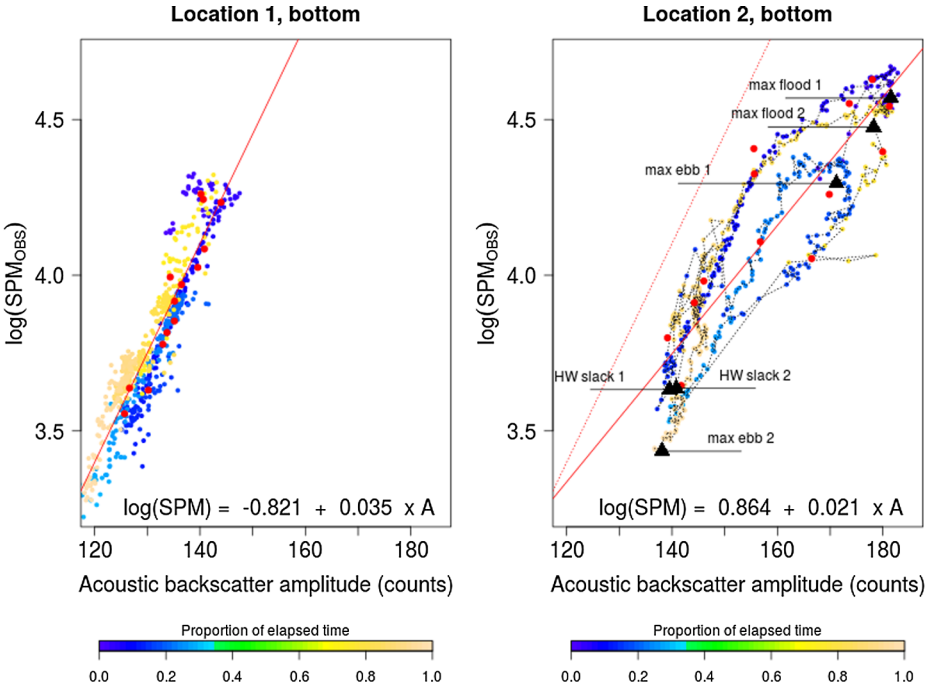


**Fig. 17.** Relation between optical (YSI, type 6920 V2) and acoustical backscatter sensor (ADV (Nortek, 6 MHz) at a muddy (location 1) and a sandy bed site (location 2) located 1200 m apart in the main tidal channel of a brackish marsh located in the Scheldt estuary during 2 tidal cycles (Schwarz et al., 2017).

90–140% (mean regression is 90%) for the M947 ADP. The uncertainty is lowest in the mid-range SPMC (100–1000 mg/l), with normalized RMSE between 50 and 70% (M284) and 45–60% (M947) for the best regression models and higher for the lower and higher SPMC values.

Both examples indicate that the differences between acoustic and optic derived SPMC can be very large and that these uncertainties increase when long time series are used for calibration. These differences are probably caused by variabilities in inherent acoustical and optical properties of the SPM that occurred over time scales longer than the sampling surveys, by differences in built-in sensor technology or due to time-delay between sensor measurements and sample time. Further differences may also be caused by the presence of coloured dissolved organic matter (CDOM) that affects the optical measurements (Bright et al., 2018) and that may change the size and density of the flocs and thus the inherent properties of the particles (Lee et al., 2019). In order to improve the correlation, the inherent acoustic and optical properties of the particles, and the presence of dissolved OM should be incorporated into the model calibrations.

### 3.5. Additional uncertainties

Additional uncertainties are caused by the direct and indirect human interference in the chain of operation. These includes errors directly caused by the human variability, by the specific problems associated with working in the sea or by the effects of human activities not related to the operational chain that have an impact on the SPMC. Many of these errors are often only detected after the field campaign and should therefore be discarded, see for example the occurrence of outliers in the model parameter calibration that cannot be explained by natural processes.

## 4. Towards best practice

To come to best practice for long-term monitoring activities of SPMC an accurate documentation of the successive operations and of the accumulating effect of uncertainties is required. An overview of the generic succession of operations required to run long-term or large-

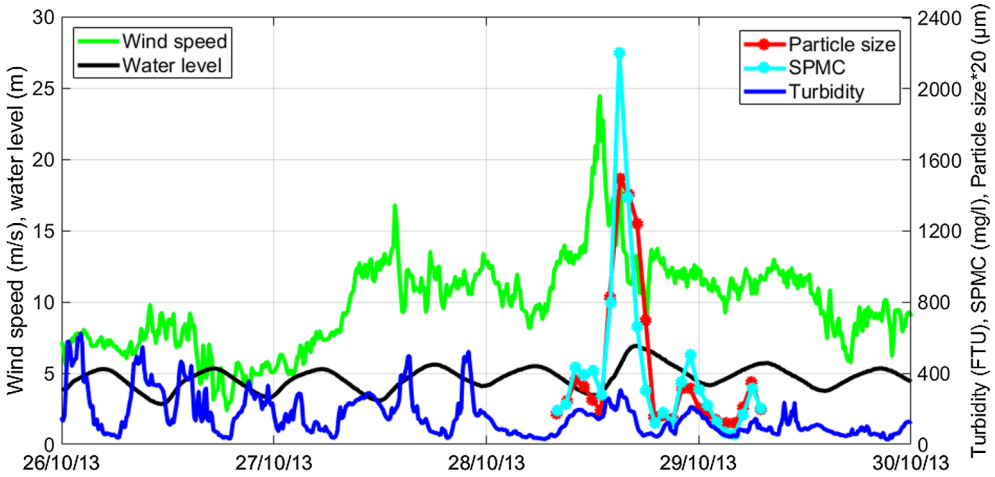


**Fig. 18.** Changes in the ratio of turbidity to sample SPMC from 0.4 to 0.12 during a storm period in the Elbe estuary caused by the resuspension of sand grains.

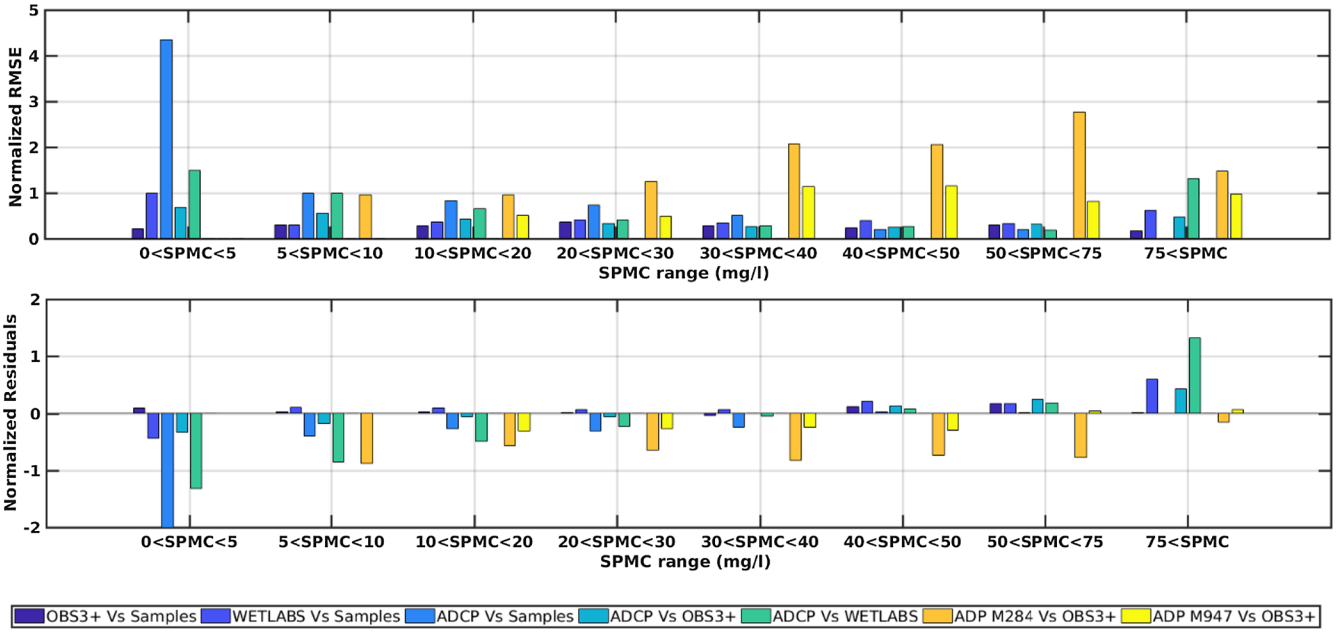


**Fig. 19.** The model SPMC uncertainty (normalized RMSE and residuals) as a function of the reference SPMC (sample or sensor derived SPMC) and SPMC range (see the dataset shown in Figs. 10 and 11) for an acoustical and some optical backscatter sensors. The reference SPMC is from sample or OBS3+ derived SPMC.

scale measurements of SPMC is depicted in Fig. 21. In long-term observations the pre-measurement, measurement and post-measurement phases and activities are not in strict sequence but interleave.

Beforehand knowledge on the magnitudes in SPMC will guide the choice of instrumentation and define the need for adjoined measurements of state variables such as particle size, shape and composition, salinity, temperature, current velocity or turbulence, see Table 2. Before field usage, all sensors should be calibrated in the laboratory against standards to manifest a reference against any possible changes in sensor response after recovery.

During the measurement phase the observing system is impacted by processes that may disturb the sensor outputs with respect to the preceding sensor and model calibration, as presented in chapter 3. A functional understanding of the interrelation between inherent particle properties, system state conditions and sensor SPMC will only be achieved if sufficient surveys are carried out to estimate the source and magnitude of changes in the sensor SPMC between the in situ calibration activities.

Post-measurement phase starts with the raw data retrieval and their conversion into ascii-based data and archiving information that collate all so far undertaken calibration, accuracy and precision measures (Tzeng et al., 2016). After recovery from the field, optical and (if possible) acoustical sensors should be calibrated against the lab reference to quantify any changes in sensor response due to electronic drift or

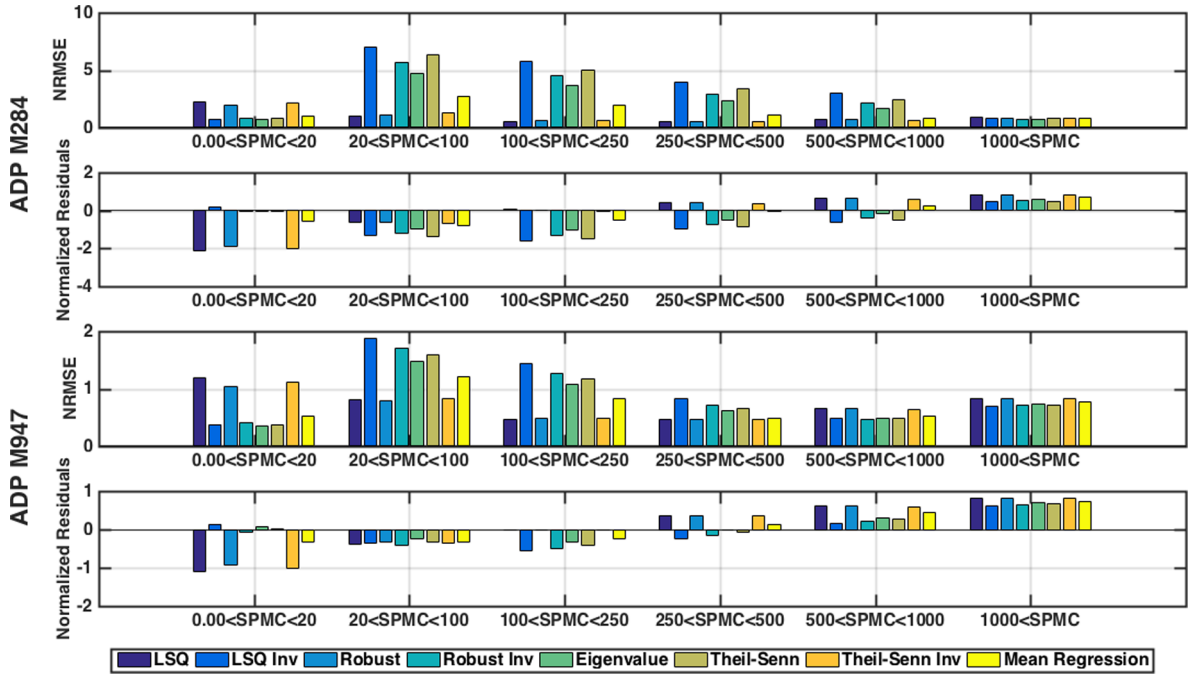


**Fig. 20.** The model SPMC uncertainty for the ADP's of Fig. 11 expressed as normalized RMSE and normalized residual for different regression models and as a function SPMC. Negative residuals have a higher ADP-derived SPMC than the OBS-derived one.

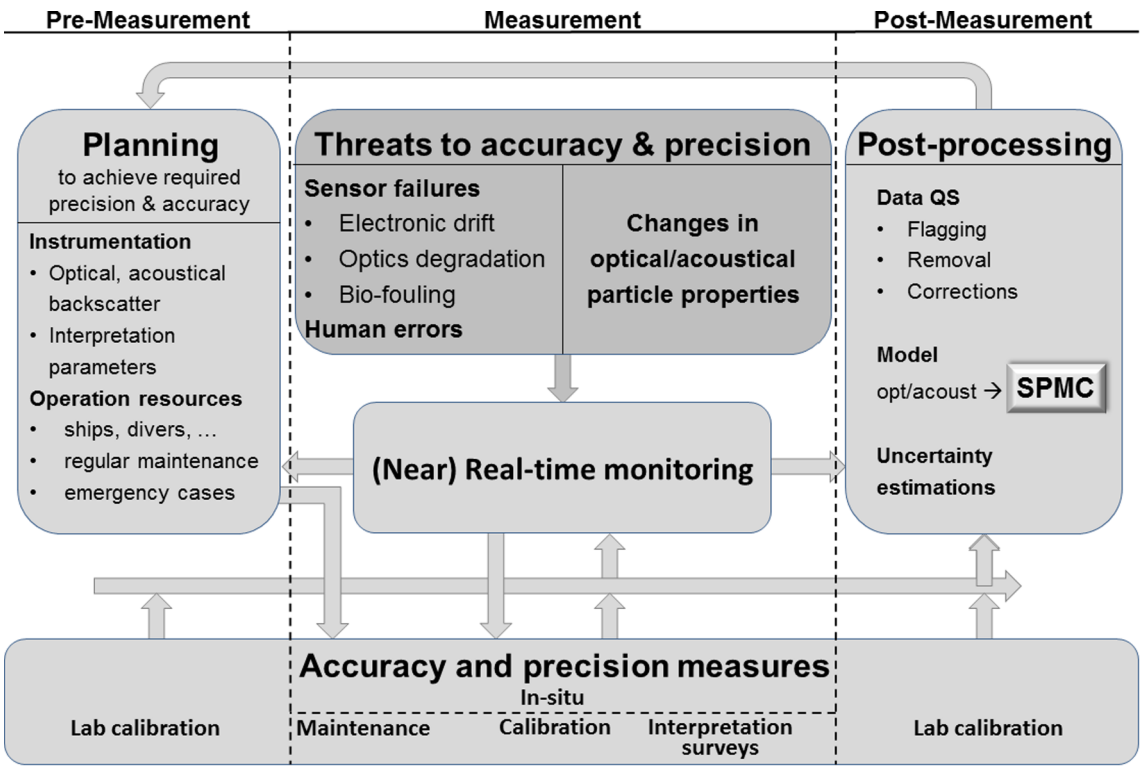


**Fig. 21.** Workflow of activities and tasks to be performed in long-term SPMC measurements. The arrows indicate the flow information between the tasks and activities over the measurement phases. The measurement phases are plotted in serial order, but may overlap in the course of long-term installations.

**Table 2**
List of additional state parameter and their measuring methods that are necessary to interpret the results of long-term SPMC measurements with more accuracy and completeness (sensor: instrument that can be used in long-term measurements; water/centrifuge sample: can be measured occasionally; station: nearby meteorological, tidal, or wave station; LoI = loss on ignition, POC = particulate organic carbon, PON: particulate organic nitrate, XRD: x-ray diffractometer).

| State parameter | Method | Type |
|---|---|---|
| Particle size in situ | laser diffractometer, holography, optical camera systems | sensor |
| Particle size in lab | Grain size analysis (primary particle size) | water sample, centrifuge sample |
| Particle composition | LOI: Organic matter<br>Element analysis: POC, PON<br>XRD: Mineral composition<br>Pigment analysis: Chlorophyll<br>Colorimetric analysis: TEP concentration<br>Electron microscopy | water sample, centrifuge sample |
| Particle composition | Fluorimeter: Fluorescence<br>Primary production: Fast Repetition Rate Fluorimeter | sensor |
| Particle shape | Holography, floc camera<br>Electron microscopy | sensor<br>water sample |
| Turbulence | High frequency Acoustic Doppler Sensor | sensor |
| Currents | Acoustical Doppler Sensor | sensor |
| Waves | Acoustic Doppler Profiler, Wave rider, floater | sensor or station |
| Density | Conductivity, Temperature | sensor |
| Water level | Pressure sensor; tide gauge | sensor, station |
| Distance to bed | Acoustic altimeter | sensor |
| Meteorology | from relevant meteorological stations | station |

optical window damages. In post-processing the data should first undergo an expert judgement to flag occurrences of spikes, stuck values or unreliable magnitudes. The resulting set of accepted and corrected data together with sample SPMC acts as input for the computation of the sensor SPMC. The associated error estimates are due to the measurement procedures themselves and yield only the errors at the observing point and for the calibration periods of the time series.

### 4.1. Discussion and ranking of the uncertainties

The overall error of the SPMC data set consists of random errors that lead to uncertainties of individual SPMC but approximate the accurate value with increasing amount of data; and systematic errors (biases) that lead to an average over- or underestimation of all data. There exist two types of biases: one that is constant or independent of observing times and locations (e.g. the choice of the regression method, as discussed in Section 3.4.2) and another one that changes with time and location (Section 3.4.3). Some kinds of errors can be detected, and to some extent corrected, whereas, others are inherently associated with the applied technologies and its interference with the environment and remain spurious and difficult to quantify or to control. The first types of errors are related to the sensors, sampling and lab protocols or the modelling techniques, while the latter are mainly related to systematic, often gradually changing natural variability in SPM inherent properties. Table 3 lists the sources of uncertainties as described in chapter 3. The listed uncertainties represent typical values that indicate their relative importance for the overall error. The following discussion continues along the vertical order of Table 3 and relates to the major items of the workflow depicted in Fig. 21.

As the errors and their mitigation or correction measures are quite dependent on the site conditions, we did not give a set of specific guidelines. In our view, regular sensor calibration against a standard solution, field inter-calibrations of sensors against reference sensors, biofouling, splitting up the sample into different volumes for filtration at SPMC $< 3$ mg/l, the choice of the regression model and long-term

**Table 3**
Quantification and nature (random or bias) of uncertainties (in % based on normalized RMSE) from the examples described in chapter 3. Negative (positive) bias corresponds to an underestimation (overestimation) of the actual value.

| Source of uncertainty | Detectable | Correctable | Uncertainty without correction | | Uncertainty with correction | | Comment |
|---|---|---|---|---|---|---|---|
| | | | random | bias | random | bias | |
| *3.1 Sensor* | | | | | | | |
| 3.1.1 Factory calibration | yes | yes | – | ± 15% | – | less than ± 2% | not fully conclusive, as sensors were checked after intense usage |
| 3.1.1 Optical degradation | yes | yes | – | 20% | – | ± 5% | Fig. 1 |
| 3.1.1 Voltage supply | yes | yes | | −90% | | ± 10% | Fig. 2 |
| 3.1.2. Sensitivity of sensor | yes | no | < 25% | | no example | no example | depends on measuring range |
| 3.1.3 Inter-sensor variability | yes | no | 2% | no example provided | no example provided | no example provided | Fig. 3<br>Comparing sensors of same type and applying the same set of sensor output to sample SPMC calibration constants for all sensors |
| *3.2 Environment* | | | | | | | |
| 3.2.1 Biofouling | yes | no[1], yes[2] | – | positive, large (up to > 100%)[1]<br>negative[2] | f(no of beams)[2] | data loss[1]<br>partial data loss[2] | [1]optical sensors<br>[2]acoustical sensors with > 3 beams |
| 3.2.2 Saturation | yes | no | | Negative[1] | – | – | [1]numerically not specified |
| 3.2.2 Ambiguity | yes | yes | not specified | – | – | – | |
| 3.2.3 Air bubbles | yes | no | – | – | – | [1]data loss | [1]optical and acoustical sensors |
| 3.2.4 Density stratification | yes | yes | | less than ± 43% | | – | acoustical sensors |
| *3.3 Sample* | | | | | | | |
| one filter | yes[1] | no | 2–10% | 1–50%[3] | - | not correctable | [1] only random uncertainty |
| triplicate filter | yes[1] | | 1–6% | | - | not correctable | [2] random + bias |
| volume method | yes[2] | | 3% | | - | < 5%[3] | [3] random bias per sample ; depends on SPMC (> 50 to < 1 mg/l) |
| *3.4 Model* | | | | | | | |
| 3.4.2 Regression model | yes | no | 10–60%[1] | 0 to > 30%[1,2] | | | [1]depends on $R^2$ and $T_{z\text{-}std}$<br>[2]depends on regression model |
| 3.4.3 Inherent particle properties | yes[1] | partly | | ± 50%[2]<br>40–60%[3]<br>50–200%[4]<br>± 10%[5] | | | [1]only with reference SPMC<br>[2]geographical variation, Fig. 15<br>[3]organic content, Fig. 16<br>[4]sand in suspension, Fig. 17 + 18<br>[5]in lab vs in situ calibration |
| 3.4.4 Optic vs. acoustic sensors | yes | no | 50–100%[2] | 40%[1]<br>O(**100%**)[2] | | | [1]acoustic sensor calibrated with sample SPMC, Fig. 19<br>[2]acoustic sensor calibrated with OBS, Figs. 19 and 20 |

changes in the IOPs are the most critical elements in the workflow.

#### 4.1.1. Sensor related uncertainties

Most sensor related sources of uncertainty can be deduced from the correct ratio of the sensor signal to a standard solution. Any deviation from the 1:1 ratio results in a bias of potentially ± 15% that will pass through the whole workflow and needs to be detected and corrected for. Controlling the sensor drift will require either the close follow up of the battery voltage and indirect field inter-calibration against a well calibrated reference sensor operated in parallel very close to the long-term observing location, or by regular re-calibration checks in the laboratory with formazine or other reference solutions after recovery of the sensor.

The usage of sensors that are not adapted to the range of turbidity values of the site, as shown in Section 3.1.2, may reduce the overall accuracy of the output in general by a bias of about 2% up to 24%. The limited turbidity resolution may also increase the random or steady changes in IOPs and thus in the ratio of sample SPMC to turbidity.

The comparison of the SPMC derived from different OBS3 + sensors (Section 3.1.3) shows that inter-sensor variability for identical sensor types can be reduced to natural random fluctuations in the water bodies, if all sensors are calibrated separately against sample SPMC. If inter-comparing different types of sensors, it is not evident beforehand that even separate calibration leads to the same results for longer time series, as different sensors may react differently to changes in the IOPs of the SPM. This may result in time-dependent biases and has to be investigated case by case.

#### 4.1.2. Environmental related uncertainties

Biofouling represents an important challenge for accurate measurements of turbidity and in some cases of acoustical backscatter intensity in the field. If not detected and flagged, the bias (positive for turbidity; negative for acoustical backscatter) can easily reach many tens of percent. Especially optical sensor output is sensitive to increasing coverage of the sensors material disturbing the light pathways or scatter detection volume. Although technologies exist to mitigate the impact of fouling, regular cleansing of the sensors remains a necessity and needs to be accompanied by sensor inter-calibration against a reference device or solution. As long as the effect of biofouling is limited, corrections by means of independent not-affected devices is sometimes possible. In many cases, however, tagging and discarding bio-fouled data is the only option.

Discarding the very high SPMC that saturate the sensor output will introduce a bias. Modelling the gaps by extending the power spectrum of the time series will lead to more realistic values, however, the degree of uncertainty depends on the specific situation and the applied interpolation model.

#### 4.1.3. Sample related uncertainties

The determination of sample SPMC is through three steps, sampling, filtering and subsequent weighing. The main uncertainties involved are related to the filtering procedure at SPMC < 3 mg/l, because the

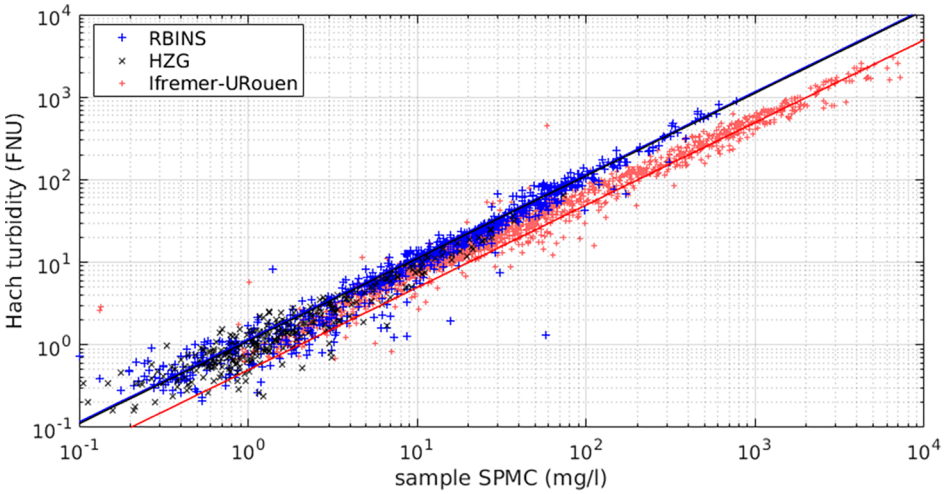


**Fig. 22.** Scatterplot of sample SPMC (mg/l) versus turbidity measurements from various waters around the world. The turbidity data from RBINS and HZG have been collected with a Hach 2100S and those from Ifremer and University of Rouen by a Hach 2100N IS. HZG measurements were collected from 2009 to 2013, RBINS data are from 2007 to 2015 and Ifremer and University of Rouen data from 2015 to 2016.

weights of the filter loadings are in the order of the sample specific filter offset. So far the most accurate protocol to determine this offset is the method with different filter volumes by Röttgers et al. (2014). At SPMC $>$ 25 mg/l the error without knowing the filter offset amounts to 3%, but raises to 50% for SPMC $<$ 3 mg/l. When the filter offset is known then the uncertainties reduce to less than 10% for SPMC $<$ 3 mg/l. For SPMC $>$ 25 mg/l the impact of the filter offset becomes negligible. Using only one filter in this range bears the risk that faulty sample SPMC cannot be identified and show up as outliers in the scatter plots that cannot be removed from the calibration data set. This can be avoided by working with triplicates and removing the sample that differs from the other two by more than a pre-defined value which reduces the random error by a factor of 2 down to the order of 5% or less.

A simple method to evaluate the quality of the sample SPMC compared with in situ optical measurements consist in using a Hach turbidimeter in addition to the filtration. Large inconsistency between the Hach sample turbidity measured on board, the in situ turbidity from a sensor and the sample SPMC will designate this sample as unreliable.

#### 4.1.4. Choice of the linear regression model

The choice of the linear regression model including the choice of the dependent and independent variable has some significance as it is systematic and leads to SPMC that are too high or too low. To our knowledge, publications involving SPMC estimated from optical turbidity or acoustical backscatter do not consider this issue. It is quite evident and quantified in Figs. 13 and 14 that a calibration data set within an $R^2 > 0.9$ should be achieved to keep uncertainties involved with the choice of a specific regression model well below 10%, independent of the model and the range of the calibration data compared to the complete data set. However, under circumstances of variable IOPs or IAPs in the sample calibration period, such a high $R^2$ may not be achievable.

From the three regression methods that are sensitive to the exchange of dependent and independent variables, it is the Robust fit that in our examples shows the least sensitivity to this exchange, followed by the Theil-Sen estimator and the LSQ method as exemplified by Figs. 13 and 14. A recommendation for the best, i.e. least sensitive regression model is not straightforward. The reason is that although prominent outliers in the calibration data set may suggest the preference for a robust method, they bear the risk of creating biases in the regression if they are caused by erratic variations in the inherent particle properties (see Section 3.4.3) and not by sensor, sampling or human related faults. In the absence of substantial, not removable outliers, Eigenvalue regression may be the proper option, as both SPMC and turbidity/acoustical backscatter, averaged over the sampling period, have errors of comparable magnitude. As another option, the regression average of a method with exchanged ordinate and abscissa may be used. The random error statistics of this approach may be generated by a boot-strap method. Regressions with $\log_{10}$-transformed data exhibit a generally higher sensitivity to the model choice for $T_{z-std} > 0$ that increase substantially for turbidities above the calibration data range. In this respect they bear the risk of substantial biases in the SPMC computed from higher optical or acoustical backscatter data.

#### 4.1.5. Variabilities in SPM inherent optical and acoustical properties

Uncertainties due to undetected changes in inherent particle properties of the SPM are difficult to quantify during long-term SPMC measurements, however, they may be significant for specific sites or periods. All of them can be ascribed to changes in particle size, shape, composition and density and to the occurrence of coloured dissolved organic substances. Regular water sampling to compare the sample SPMC with sensor output will provide insight into the stability of models used to estimate sensor SPMC over time and/or space (e.g. Druine et al., 2018). The examples of Section 3.4.3 show that even intra-tidal variations or events of several hours lead to systematic uncertainties of 50–200%. Therefore, it is recommended to add further sensors to the observing system that give direct indication for changes in the inherent particle properties (Table 2).

When measuring in the benthic boundary layer the SPMC may reach values that exceed the calibration data range. The calibration data set does not cover the sensor SPMC data range and may result in high uncertainty for the largest SPMC value. For these situations a model calibration in the laboratory allows extending the calibration data range (see Section 3.4.3). This is meaningful if the associated uncertainty is lower than the one from an in situ model calibration at large $T_{z-std}$.

### 4.2. Water sample turbidity as a surrogate for SPMC?

#### 4.2.1. Uncertainty between SPMC and turbidity

To separate variability due to measurement errors from variability due to natural variations in IOPs, protocols that use the same water sample for filtration and for turbidity estimation should be used in parallel to the in situ procedures. Fig. 22 shows a collection of sample SPMC versus turbidity measurements of the same water sample recorded with a portable ISO Hach 2100P nephelometer from various waters around the world (North Sea, English Channel, Mediterranean Sea, Rio de la Plata, French Guiana nearshore, Gironde estuary, Scheldt estuary, see Table 3), collected by the RBINS (Dogliotti et al., 2015; Knaeps et al., 2015) and HZG (Röttgers et al., 2014). The protocols for

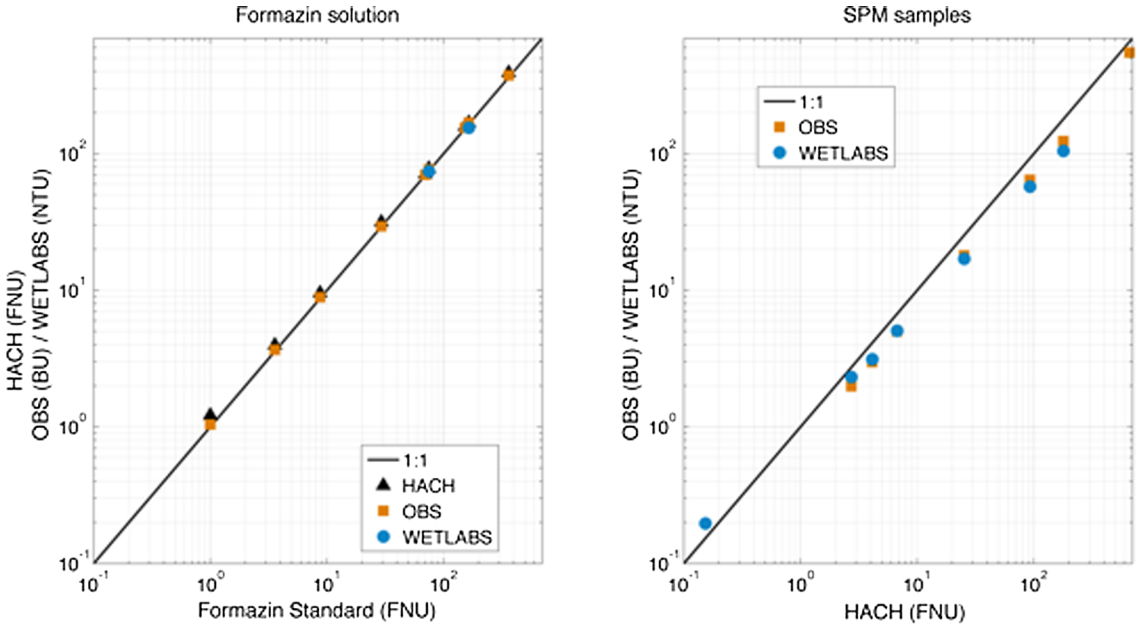


**Fig. 23.** The performance of different sensors (side-scattering: Hach; backscattering: OBS3+ and Wetlabs) during sensor calibration with different formazine solutions (left) and as compared with natural SPM samples.

sample SPMC and turbidity measurements are those described in Neukermans et al. (2012a) for RBINS and Röttgers et al. (2014) for HZG. The figure shows that the ratio between sample SPMC and Hach turbidity is quite stable within an uncertainty of 20% throughout the regions. In this collection, 4.1% of couples fail outside of the 95% confidence interval regarding the t-distribution of sample SPMC/turbidity in the logarithmic space. The outlying couples probably reflect the tails of the combined natural variability of particles mass-specific side-scattering coefficient, and sampling and filtration errors. The average ratio of sample SPMC to turbidity from all data is about 1.13 mg/l/FNU (RBINS data), and 1.19 mg/l/FNU (HZG data).

Despite calibration to a formazine reference solution and the use of ISO-normed optical sensors, model calibration may vary considerably in recorded turbidity for a same SPMC solution across different instruments resulting in instrument-specific turbidity-SPMC relations, see Fig. 23. Although different types of optical sensors have been calibrated against the same reference solution, they yield up to 20% differences results in the field. Another example concerns data collected by Ifremer and the University of Rouen at different locations in the Seine estuary (Druine et al., 2018) with a ISO Hach 2100N nephelometer (same constructor, but different type as the above mentioned 2100P) give significant different turbidity values for the same SPMC. Given the consistency of the Hach 2100P data pairs from two institutes over a wide range of areas we assume that the differences are mainly caused by the instrument specificities. The latter was confirmed during intercalibration of both ISO standardized nephelometers with StablCal® and with SPMC solutions. The inter comparison revealed that the 2100N measures about 13% lower turbidity values for the same StablCal® solution than the 2100P. This strengthens further that any turbidity unit should be referred to the instrument used and the protocol applied (see Section 2.1).

#### *4.2.2. Need for further sample SPMC?*

The above results prohibit the comparison of turbidity values measured by different types of optical sensors. Turbidity as a surrogate of SPMC is only reliable, as long as site-specific (model) and instrument-specific (sensor) calibrations are carried out. On the other hand, the quiet stable relationship between the ISO Hach water sample turbidity and the sample SPMC in Fig. 22 throughout different localities suggests that this relationship could be used as an estimate of SPMC in two ways. Firstly, it adds a third independent measurement and helps to separate model-calibration outliers due to natural fluctuations from sample or human faults. Secondly, the stable ratio of Hach derived turbidity to sample SPMC could be used instead of sample SPMC for in situ turbidity data. This introduce an individual random uncertainty of some 20%, which could be compensated by less laboratory effort and therefore more available calibration data. The site specific regressions for sample SPMC versus Hach turbidity vary by only 20% in the RBINS data set shown in Fig. 22. Using the global fit at different sites still reproduces the sample SPMC within less than 20% with an average bias of 3%. Especially given the high uncertainties of low sample SPMC due to the filter offsets, a 20% random error for Hach-derived SPMC seems to be a suitable and cheap alternative to filter weights.

## 5. Conclusions and outlook

Optical and acoustical sensors have proved invaluable in the study of SPM dynamics in marine and estuarine environments as they allow collecting easily in situ, high frequency SPMC time series over long periods of time. The payback is the availability of large homogeneous data set of SPMC from various locations on the globe; the drawback is that the quality or certainty of the data and thus also the inter-comparability depends on factors that are only to a certain level avoidable.

Long-term observations of SPMC are the result of a complex ladder of operations that involve field, laboratory and modelling methods. Each step contributes its own random and systematic errors to the overall uncertainties of the sensor SPMC. Systematic errors related to the functioning of the sensors, the environment, the collection and processing of calibration samples and faulty human operations are detectable and sometimes correctable. As long as protocols for sample analysis and sensor calibration are carefully obeyed, uncertainties can be confined within ± 5%, otherwise they may reach up to ± 20%. Biofouling may add a further bias of 100% (positive for optical, negative for acoustical sensors), and their detection in generally leads to a loss of data. A good understanding of the processes that are causing changes in SPMC and particle inherent properties (size, shape, density and composition) is required in order to estimate their importance and to possibly rescale the sensor data to some reference particle properties. Variations in these properties may result in over- or underestimation of the SPMC by up to a factor 2 or more. Based on the uncertainties, listed

in Table 3, one can achieve random errors below 25% and biases below 40% only with substantial efforts in technologies that indicate the changes in inherent particle properties.

Acoustical and optical sensors require both the conversion of the sensor output (after sensor calibration) to a mass concentration. This is done by relating the sensor output to a reference SPMC, which is preferably the sample SPMC. The choice of the regression method, the dependent and independent variable, and the error associated with the reference SPMC determines the coefficient of determination. We have built a model that based on the $R^2$ and the normalized turbidity/dB quantifies the uncertainty of the sensor derived SPMC in the calibration range and outside of it. The model shows that the Robust fit and the Eigenvalue regression have less prediction bias than the Theil-Sen estimator and the ordinary LSQ. This bias is not an issue for $R^2 > 0.9$ and remains below 10%, but it becomes significant for lower $R^2$ and can amount to 30%. Short-term variabilities in the model-regressions generally show up as random noise limiting the $R^2$ of the calibration data set, but the extrapolation of the regression parameters to longer periods or larger areas may introduce biases of more than 50%.

The site specific regressions for sample SPMC versus Hach turbidities vary by 20% between different coastal regions and even less within the same region. This relationship could be a cheap alternative to filter weights as less laboratory effort is needed as long as the same nephelometer is used. Indeed, our study confirms that the relation between turbidity and sample SPMC is depending on protocols (EPA, ISO), technology (scattering angle) and the manufacturer, and even may differ between sensors of the same type (e.g. Downing, 2006; Rai and Kumar, 2015; Rymszewicz et al., 2017). The relation between the output of an acoustical sensor and SPMC is even more variable. In spite of these uncertainties, turbidity is still often used as a proxy for water clarity or SPMC as is the dB of acoustical sensors. We advise to not use turbidity (or dB) for scientific purposes as it diminishes the comparability of the data. Instead, the sensor output should be transformed into a mass concentration, a unit that is comparable in time and between regions. If this is not possible, then the turbidity data should always be referred to the instrument used and the protocol applied. The problem aggravates when turbidity data that have been collected using different technologies and protocols over long periods of time and regional scales are stored in international data bases (e.g. turbidity in EMODnet, see http://www.emodnet.eu), and used to derive conclusive trends of the environmental status of marine and estuarine areas. We hope that the uncertainty analysis presented here will serve as a basis for the validation of historical turbidity and SPMC data and that it offers guidelines to obtain inter-comparable high quality long-term SPMC time series.

## Acknowledgements

This work was initiated on a meeting held in February 2016. As an outcome a number of recommendations were formulated that have been compiled in the text. The first four authors have structured compiled and written large parts of the text. The other authors have provided examples, data and have contributed to the writing. The research was supported by the Belgian Science Policy (BELSPO) within the BRAIN-be program (INDI67 project), the Maritime Access Division of the Flemish Ministry of Mobility and Public Works (MOMO project), the Helmholtz Association of German Research Centres, the research and development programme of the Federal Waterways Engineering and Research Institute (BAW) and the Seine Aval Research Program (SUSPENSE and PHERSQUES projects). Ship time for the RBINS data collection was provided by BELSPO and RBINS–OD Nature.

## References

Abarzua, S., Jakubowski, S., 1995. Biotechnological investigation for the prevention of biofouling. I Biological and biochemical principles for the prevention of biofouling. Mar. Ecol. Prog. Ser. 123, 301–312.

Adriaens, R., Zeelmaekers, E., Fettweis, M., Vanlierde, E., Vanlede, J., Stassen, P., Elsen, J., Środoń, J., Vandenberghe, N., 2018. Quantitative clay mineralogy as provenance indicator for recent muds in the southern North Sea. Mar. Geol. 398, 48–58. https://doi.org/10.1016/j.margeo.2017.12.011.

Agrawal, Y.C., Pottsmith, H.C., 2000. Instruments for particle size and settling velocity observations in sediment transport. Mar. Geol. 168, 89–114.

Ainslie, M.A., McColm, J.G., 1998. A simplified formula for viscous and chemical absorption in sea water. J. Acoust. Soc. Am. 103, 1671–1672.

Anastasiou, S., Sylaios, G.K., Tsihrintzis, V.A., 2015. Suspended particulate matter estimates using optical and acoustic sensors: application in Nestos River plume (Thracian Sea, North Aegean Sea). Environ. Monit. Assess. 187, 1–17. https://doi.org/10.1007/s10661-015-4599-y.

Babin, M., Morel, A., Fournier-Sicre, V., Fell, F., Stramski, D., 2003. Light scattering properties of marine particles in coastal and open ocean waters as related to the particle mass concentration. Limnol. Oceanogr. 48, 843–859. https://doi.org/10.4319/lo.2003.48.2.0843.

Badewien, T.H., Zimmer, E., Bartholomä, A., Reuter, R., 2009. Towards continuous long-term measurements of suspended particulate matter (SPM) in turbid coastal waters. Ocean Dyn. 59, 227–238. https://doi.org/10.1007/s10236-009-0183-8.

Baeye, M., Fettweis, M., 2015. In situ observations of suspended particulate matter plumes at an offshore wind farm. Geo-Mar. Lett. 35, 247–255. https://doi.org/10.1007/s00367-015-0404-8.

Baker, E.T., Lavelle, J.W., 1984. The effect of particle size on the light attenuation coefficient of natural suspensions. J. Geophys. Res. 89 (C5), 8197–8203.

Banse, K., Falls, C.P., Hobson, L.A., 1963. A gravimetric method for determining suspended matter in sea water using Millipore filters. Deep Sea Res. Oceanogr. Abstr. 639–642.

Barillé-Boyer, A.-L., Barillé, L., Massé, H., Razet, D., Héral, M., 2003. Correction for particulate organic matter as estimated by loss on ignition in estuarine ecosystems. Estuar. Coast. Shelf Sci. 58, 147–153. https://doi.org/10.1016/S0272-7714(03)00069-6.

Barter, P.J., Deas, T., 2003. Comparison of portable nephelometric turbidimeters on natural waters and effluents. N. Z. J. Mar. Freshwater Res. 37, 485–492.

Baschek, B., Schroeder, F., Brix, H., Riethmüller, R., Badewien, T.H., Breitbach, G., Brügge, B., Colijn, F., Doerffer, R., Eschenbach, C., Friedrich, J., Fischer, P., Garthe, S., Horstmann, J., Krasemann, H., Metfies, K., Merckelbach, L., Ohle, N., Petersen, W., Pröfrock, D., Röttgers, R., Schlüter, M., Schulz, J., Schulz-Stellenfleth, J., Stanev, E., Staneva, J., Winter, C., Wirtz, K., Wollschläger, J., Zielinski, O., Ziemer, F., 2017. The coastal observing system for northern and arctic seas (COSYNA). Ocean Sci. 13, 379–410. https://doi.org/10.5194/os-13-379-2017.

Becherer, J., Flöser, G., Umlauf, L., Burchard, H., 2016. Estuarine circulation versus tidal pumping: sediment transport in a well-mixed tidal inlet. J. Geophys. Res. 121, 6251–6270. https://doi.org/10.1002/2016JC011640.

Becker, M., Schrottke, K., Bartholomä, A., Ernstsen, V., Winter, C., Hebbeln, D., 2013. Formation and entrainment of fluid mud layers in troughs of subtidal dunes in an estuarine turbidity zone. J. Geophys. Res. 118, 2175–2187. https://doi.org/10.1002/jgrc.20153.

Berthon, J.-F., Shybanov, E., Lee, M.E.-G., Zibordi, G., 2007. Measurements and modeling of the volume scattering function in the coastal northern Adriatic Sea. Appl. Opt. 46, 5189–5203. https://doi.org/10.1364/AO.46.005189.

Binding, C.E., Bowers, D.G., Mitchelson-Jacob, E.G., 2005. Estimating suspended sediment concentrations from ocean colour measurements in moderately turbid waters; the impact of variable particle scattering properties. Remote Sens. Environ. 94, 373–383. https://doi.org/10.1016/j.rse.2004.11.002.

Bolanos, R., Amoudry, L., Doyle, K., 2011. Effects of instrumented bottom tripods on process measurements. J. Atmos. Oceanic Technol. 28, 827–837. https://doi.org/10.1175/2010JTECHO816.1.

Bollen, M., Sas, M., Vanlede, J., de Mulder, T., 2006. Measuring High Concentration Benthic Suspensions (HCBS), using a high resolution SiltProfiler. In: Proc. 15th International Congress of the International Federation of Hydrographic Societies. Special Publication, vol. 55, pp. 138–140. www.vliz.be/imisdocs/publications/114165.pdf.

Boss, E., Pegau, W.S., 2001. Relationship of light scattering at an angle in the backward direction to the backscattering coefficient. Appl. Opt. 40, 5503–5507. https://doi.org/10.1364/AO.40.005503.

Boss, E., Pegau, W.S., Lee, M., Twardowski, M.S., Shybanov, E., Korotaev, G., Baratange, F., 2004. The particulate backscattering ratio at LEO 15 and its use to study particle composition and distribution. J. Geophys. Res. 109 (C01014). https://doi.org/10.1029/2002JC001514.

Boss, E., Taylor, L., Gilbert, S., Gundersen, K., Hawley, N., Janzen, C., Johengen, T., Purcell, H., Robertson, C., Schar, D.W.H., Smith, G.J., Tamburri, M.N., 2009a. Comparison of inherent optical properties as a surrogate for particulate matter concentration in coastal waters. Limnol. Oceanogr. Methods 7, 803–810. https://doi.org/10.4319/lom.2009.7.803.

Boss, E., Slade, W., Hill, P., 2009b. Effect of particulate aggregation in aquatic environments on the beam attenuation and its utility as a proxy for particulate mass. Optic Express 17, 9408–9420. https://doi.org/10.1364/OE.17.009408.

Bowers, D.G., Braithwaite, K.M., Nimmo-Smith, W.A.M., Grahams, G.W., 2009. Light scattering by particles suspended in the sea: the role of particle size and density. Cont. Shelf Res. 29, 1748–1755. https://doi.org/10.1016/j.csr.2009.06.004.

Bowers, D.G., McKee, D., Jago, C.F., Nimmo-Smith, W.A.M., 2017. The area-to-mass ratio and fractal dimension of marine flocs. Estuar. Coast. Shelf Sci. 189, 224–234. https://doi.org/10.1016/j.ecss.2017.03.026.

Bright, C.E., Mager, S.M., Horton, S.L., 2018. Predicting suspended sediment concentration from nephelometric turbidity in organic-rich waters. River Res. Appl. 34,

629–639. https://doi.org/10.1002/rra.3305.
Butman, B., Noble, M., Folger, D.W., 1979. Long-term observations of bottom current and bottom sediment movement on the mid-Atlantic continental shelf. J. Geophys. Res. 84 (C3), 1187–1205. https://doi.org/10.1029/JC084iC03p01187.
Cartwright, G.M., Friedrichs, C.T., Dickhudt, P.J., Gass, T., Farmer, F.H. 2009. Using the Acoustic Doppler Velocimeter (ADV) in the MUDBED real-time observing system. OCEANS 2009.
Chami, M., Marken, E., Stamnes, J.J., Khomenko, G., Korotaev, G., 2006. Variability of the relationship between the particulate backscattering coefficient and the volume scattering function measured at fixed angles. J. Geophys. Res. 111 (C5), C05013. https://doi.org/10.1029/2005JC003230.
Chapalain, M., Verney, R., Fettweis, M., Jacquet, M., Le Berre, D., Le Hir, P., 2019. Investigating suspended particulate matter in coastal waters using fractal theory. Ocean Dyn. 69, 59–81. https://doi.org/10.1007/s10236-018-1229-6.
Delauney, L., Compère, C., Lehaitre, M., 2010. Biofouling protection for marine environmental sensors. Ocean Sci. 6, 503–511. https://doi.org/10.5194/os-6-503-2010.
Dogliotti, A.-I., Ruddick, K., Nechad, B., Doxaran, D., Knaeps, E., 2015. A single algorithm to retrieve turbidity from remotely-sensed data in all coastal and estuarine waters. Remote Sens. Environ. 156, 157–168. https://doi.org/10.1016/j.rse.2014.09.020.
Dogliotti, A., Nechad, B., Ruddick, K., Gossn, J.I., 2016. Towards an autonomous turbidimeter network for multi-mission ocean colour satellite validation activities. In: Ouwehand, L. (Ed.), Proc. Living Planet Symposium, ESA-SP Volume 740, ISBN: 978-92-9221-305-3.
Dolphin, T.J., Green, M.O., Radford, J.D.J., Black, K.P., 2000. Biofouling of optical backscatter sensors: prevention and analytical correction of data. J. Coastal Res. SI34, 334–341.
Downing, A., Thorne, P.D., Vincent, C.E., 1994. Backscattering from a suspension in the near field of a piston transducer. J. Acoust. Soc. Am. 97 (3), 1614–1620.
Downing, J., 2005. Turbidity Monitoring. In: Down, R.D., Lehr, J.H., (Eds.), Environmental Instrumentation and Analysis Handbook, John Wiley & Sons Inc. https://doi.org/10.1002/0471473332.ch24.
Downing, J., 2006. Twenty-five years with OBS sensors: the good, the bad, and the ugly. Cont. Shelf Res. 26, 2299–2318. https://doi.org/10.1016/j.csr.2006.07.018.
Doxaran, D., Leymarie, E., Nechad, B., Dogliotti, A., Ruddick, K., Gernez, P., Knaeps, E., 2016. Improved correction methods for field measurements of particulate light backscattering in turbid waters. Opt. Express 24 (4), 3615–3637. https://doi.org/10.1364/OE.24.003615.
Droppo, I., Leppard, G., Liss, S., Milligan, T., 2005. Flocculation in natural and engineered environmental systems. CRC Press, Boca Raton, Fla, pp. 438.
Druine, F., Verney, R., Deloffre, J., Lemoine, J.-P., Chapalain, M., Landemain, V., Lafite, R., 2018. In situ high frequency long term measurements of suspended sediment concentration in turbid estuarine system (Seine Estuary, France): optical turbidity sensors response to suspended sediment characteristics. Mar. Geol. 400, 24–37. https://doi.org/10.1016/j.margeo.2018.03.003.
Duan, N., 1983. Smearing estimate—a nonparametric retransformation method. J Am Stat Assoc 78 (383), 605–610.
Dufois, F., Verney, R., Le Hir, P., Dumas, F., Charmasson, S., 2014. Impact of winter storms on sediment erosion in the Rhone River prodelta and fate of sediment in the Gulf of Lions (North Western Mediterranean Sea). Cont. Shelf Res. 72, 57–72. https://doi.org/10.1016/j.csr.2013.11.004.
Dyer, K.R., Manning, A.J., 1999. Observation of the size, settling velocity and effective density of flocs, and their fractal dimensions. J. Sea Res. 41, 87–95.
Edwards, T.K., Glysson, G.D., 1999. Field methods for measurement of fluvial sediment. U.S. Geological Survey Techniques of Water-Resources Investigations, USGS Survey Book 3, chap. C2, 89 pp.
Eisma, D., 1986. Flocculation and de-flocculation of suspended matter in estuaries. Neth. J. Sea Res. 20, 183–199.
EPA, 1993. Method 180.1 - Determination of turbidity by nephelometry (revision 2.0), Environmental Protection Agency, Cincinnati, 10.
Fettweis, M., Sas, M., Monbaliu, J., 1998. Seasonal, neap-spring and tidal variation of cohesive sediment concentration in the scheldt estuary, Belgium. Estuar. Coast. Shelf Sci. 47, 21–36. https://doi.org/10.1006/ecss.1998.0338.
Fettweis, M., Francken, F., Pison, V., Van den Eynde, D., 2006. Suspended particulate matter dynamics and aggregate sizes in a high turbidity area. Mar. Geol. 235, 63–74. https://doi.org/10.1016/j.margeo.2006.10.005.
Fettweis, M., 2008. Uncertainty of excess density and settling velocity of mud flocs derived from in situ measurements. Estuar. Coast. Shelf Sci. 78, 426–436. https://doi.org/10.1016/j.ecss.2008.01.007.
Fettweis, M., Baeye, M., Lee, B.J., Chen, P., Yu, J.C.R., 2012. Hydro-meteorological influences and multimodal suspended particle size distributions in the Belgian nearshore area (southern North Sea). Geo-Mar. Lett. 32, 123–137. https://doi.org/10.1007/s00367-011-0266-7.
Fettweis, M., Baeye, M., 2015. Seasonal variation in concentration, size and settling velocity of muddy marine flocs in the benthic boundary layer. J. Geophys. Res. 120, 5648–5667. https://doi.org/10.1002/2014JC010644.
Fettweis, M., Baeye, M., Cardoso, C., Dujardin, A., Lauwaerts, B., Van den Eynde, D., Van Hoestenberghe, T., Vanlede, J., Van Poucke, L., Velez, C., Martens, C., 2016. The impact of disposal of fine grained sediments from maintenance dredging works on SPM concentration and fluid mud in and outside the harbor of Zeebrugge. Ocean Dyn. 66, 1497–1516. https://doi.org/10.1007/s10236-016-0996-1.
Fettweis, M., Lee, B.J., 2017. Spatial and seasonal variation of biomineral suspended particulate matter properties in high-turbid nearshore and low-turbid offshore zones. Water 9, 694. https://doi.org/10.3390/w9090694.
Francois, R.E., Garrison, G.R., 1982a. Sound absorption based on ocean measurements. Part I: Pure water and magnesium sulfate contributions. J. Acoust. Soc Am. 72, 896–907.
Francois, R.E., Garrison, G.R., 1982b. Sound absorption based on ocean measurements. Part II: Boric acid contribution and equation for total absorption. J. Acoust. Soc. Am. 72, 1879–1890.
Fugate, D.C., Friedrichs, C.T., 2002. Determining concentration and fall velocity of estuarine particle populations using ADV, OBS and LISST. Cont. Shelf Res. 22, 1867–1886. https://doi.org/10.1016/S0278-4343(02)00043-2.
Ganju, N.K., Schoellhamer, D.H., 2006. Annual sediment flux estimates in a tidal strait using surrogate measurements. Estuar. Coast. Shelf Sci. 69, 165–178. https://doi.org/10.1016/j.ecss.2006.04.008.
Garel, E., Ferreira, O., 2011. Monitoring estuaries using non-permanent stations: practical aspects and data examples. Ocean Dyn. 61, 891–902. https://doi.org/10.1007/s10236-011-0417-4.
Gartner, J.W., 2004. Estimating suspended solids concentrations from backscatter intensity measured by acoustic Doppler current profiler in San Francisco Bay, California. Mar. Geol. 211, 169–187. https://doi.org/10.1016/j.margeo.2004.07.001.
Gibbs, R.J., 1985. Estuarine flocs: their size, settling velocity and density. J. Geophys. Res. 90 (C2), 3249–3251.
Gil, Y., David, C.H., Demir, I., Essawy, B.T., Fulweiler, R.W., Goodall, J.L., Karlstrom, L., Lee, H., Mills, H.J., Oh, J.-H., Pierce, S.A., Pope, A., Tzeng, M.W., Villamizar, S.R., Yu, X., 2016. Toward the geoscience paper of the future: best practices for documenting and sharing research from data to software to provenance. Earth Space Sci. 3, 388–415. https://doi.org/10.1002/2015EA000136.
Gilbert, R.O., 1987. Statistical Methods for Environmental Pollution Monitoring. Van Nostrand Reinhold Company Inc., New York, pp. 320.
Gostiaux, L., van Haren, H., 2010. Extracting meaningful information from uncalibrated backscattered echo intensity data. J. Atmos. Oceanic Technol. 27, 943–949. https://doi.org/10.1175/2009JTECHO704.1.
Grabemann, I., Krause, G., 1989. Transport processes of suspended matter derived from time series in a tidal estuary. J. Geophys. Res. 94 (C10), 14373–14379. https://doi.org/10.1029/JC094iC10p14373.
Gray, J.R., Gartner, J.W., 2009. Technological advances in suspended-sediment surrogate monitoring. Water Resour. Res. 45, W00D29. https://doi.org/10.1029/2008WR007063.
Guerrero, M., Di Federico, V., 2018. Suspended sediment assessment by combining sound attenuation and backscatter measurements – analytical method and experimental validation. Adv. Water Resour. 113, 167–179. https://doi.org/10.1016/j.advwatres.2018.01.020.
Guézennec, L., Lafite, R., Dupont, J.P., Meyer, R., Boust, D., 1999. Hydrodynamics of suspended particulate matter in the tidal freshwater zone of a macrotidal estuary (the Seine Estuary, France). Estuaries 22, 717–727.
Ha, H.K., Hsu, W.-Y., Maa, J.P.-Y., Shao, Y.Y., Holland, C.W., 2009. Using ADV backscatter strength for measuring suspended cohesive sediment concentration. Cont. Shelf Res. 29, 1310–1316. https://doi.org/10.1016/j.csr.2009.03.001.
Ha, H.K., Maa, J.P.-Y., Park, K., Kim, Y.H., 2011. Estimation of high-resolution sediment concentration profiles in bottom boundary layer using pulse-coherent acoustic Doppler current profilers. Mar. Geol. 279, 199–209. https://doi.org/10.1016/j.margeo.2010.11.002.
Hatcher, A., Hill, P., Grant, J., Macpherson, P., 2000. Spectral optical backscatter of sand in suspension: effects of particle size, composition and colour. Mar. Geol. 168, 115–128. https://doi.org/10.1016/S0025-3227(00)00042-6.
Hay, A.E., Sheng, J., 1992. Vertical profiles of suspended sand concentration and size from multifrequency acoustic backscatter. J. Geophys. Res. 97, 15661–15677.
Helsel, D.R., Hirsch, R.M. 2002. Statistical Methods in Water Resources. Techniques of Water-Resources, Investigations of the US Geological Survey, Book 4, Hydrologic Analysis and Interpretation, 510pp. https://pubs.usgs.gov/twri/twri4a3/.
HELCOM, 2015. Manual for Marine Monitoring in the COMBINE Programme of HELCOM, 466pp. http://helcom.fi/action-areas/monitoring-and-assessment/manuals-and-guidelines/combine-manual.
Hoitink, A.J.F., Hoekstra, P., 2005. Observations of suspended sediment from ADCP and OBS measurements in a mud-dominated environment. Coast. Eng. 52, 103–118. https://doi.org/10.1016/j.coastaleng.2004.09.005.
Holdaway, G.P., Thorne, P.D., Flatt, D., Jones, S.E., Prandle, D., 1999. Comparison between ADCP and transmissometer measurements of suspended sediment concentration. Cont. Shelf Res. 19 (3), 421–441. https://doi.org/10.1016/S0278-4343(98)00097-1.
IOCCG, 2011. Bio-optical sensors on ARGO floats. In: Claustre, H. (Ed.), Reports of the International Ocean-Colour Coordinating Group, No. 11, IOCCG, Dartmouth, Canada. http://www.ioccg.org/reports/IOCCG_Report11.pdf.
IOC, 1996. Workshop Report No. 122, IOC-EU-BSH-NOAA-(WDC-A) International Workshop on Oceanographic Biological and Chemical Data Management, Intergovernmental Oceanographic Commission Hamburg, Germany, 20–23 May 1996.
ISO, 1997. Water quality – determination of suspended solids by filtration through glass-fibre filters. ISO Standard 11923:1997, International Organization for Standardization, Geneva, Switzerland.
ISO, 1999. Water Quality – Determination of Turbidity, ISO Method 7027. International Organization for Standardization, Geneva, Switzerland.
ISO, 2008. Evaluation of measurement data — guide to the expression of uncertainty in measurement. ISO/IEC Guide 98-3:2008 (JCGM/WG1/100) International Organization for Standardization, Geneva, Switzerland.
ISO, 2014. Hydrometry – suspended sediment in streams and canals – determination of concentration by surrogate techniques. ISO 11657:2014, International Organization for Standardization, Geneva Switzerland.
ISO, 2017. Guidance for the Use of Repeatability, Reproducibility and Trueness Estimates

in Measurement Uncertainty Estimation, ISO 21748. International Organization for Standardization, Geneva, Switzerland.
Jafar-Sidik, M., Gohin, F., Bowers, D., Howarth, J., Hull, T., 2017. The relationship between Suspended Particulate Matter and turbidity at a mooring station in a coastal environment: consequences for satellite-derived products. Oceanologia 59, 365–378. https://doi.org/10.1016/j.oceano.2017.04.003.
Jalón-Rojas, I., Schmidt, S., Sottolichio, A., 2015. Turbidity in the fluvial Gironde Estuary (southwest France) based on 10-year continuous monitoring: sensitivity to hydrological conditions. Hydrol. Earth Syst. Sci. 19, 2805–2819. https://doi.org/10.5194/hess-19-2805-2015.
JAMP, 2012. Eutrophication monitoring guidelines: Chlorophyll a in Water. OSPAR Joint Assessment & Monitoring Programme, Agreement 2012-11.
Jourdin, F., Tessier, C., Le Hir, P., Verney, R., Lunven, M., Loyer, S., Lusven, A., Filipot, J.-F., Lepesqueur, J., 2014. Dual-frequency ADCPs measuring turbidity. Geo-Mar. Lett. 34, 381–397. https://doi.org/10.1007/s00367-014-0366-2.
Kappenberg, J., Berendt, M., Ohle, N., Riethmüller, R., Schuster, D., Strotmann, T., 2018. Variation of hydrodynamics and water constituents in the mouth of the Elbe estuary, Germany. Civil Eng. Res. J. 4, 555643. https://doi.org/10.19080/CERJ.2018.04.555643.
Kerr, A., Cowling, M.J., Beveridge, C.M., Smith, M.J., Parr, A.C.S., Head, R.M., Davenport, J., Hodgkiess, T., 1998. The early stages of marine biofouling and its effects on two types of optical sensors. Environ. Int. 24, 331–343.
Kineke, G.C., Sternberg, R.W., 1992. Measurements of high concentration suspended sediments using the optical backscatterance sensor. Mar. Geol. 108, 253–258.
Klein, H., 2003. Investigating sediment re-mobilisation due to wave action by means of ADCP echo intensity data Field data from the Tromper Wiek, western Baltic Sea. Estuar. Coast. Shelf Sci. 58, 467–474. https://doi.org/10.1016/S0272-7714(03)00113-6.
Knaeps, E., Ruddick, K.G., Doxaran, D., Dogliotti, A.I., Nechad, B., Raymaekers, D., Sterckx, S., 2015. A SWIR based algorithm to retrieve total suspended matter in extremely turbid waters. Remote Sens. Environ. 168, 66–79. https://doi.org/10.1016/j.rse.2015.06.022.
Krivtsov, V., Howarth, M.J., Jones, S.E., Souza, A.J., Jago, C.F., 2008. Monitoring and modelling of the Irish Sea and Liverpool Bay: an overview and an SPM case study. Ecol. Model. 212, 37–52. https://doi.org/10.1016/j.ecolmodel.2007.10.038.
Lane, A., Riethmüller, R., Herbers, D., Rybaczokv, P., Günther, H., Baumert, H., 2000. Observational data sets for model development. Coast. Eng. 41, 125–153.
Lee, B.J., Kim, J., Hur, J., Choi, I.H., Toorman, E., Fettweis, M., Choi, J.W., 2019. Seasonal dynamics of organic matter composition and its effects on suspended sediment flocculation in river water. Water Resour. Res. https://doi.org/10.1029/2018WR024486.
Lurton, Xavier (Ed.), 2010. An Introduction to Underwater Acoustics. Springer Berlin Heidelberg, Berlin, Heidelberg.
MacDonald, I.T., Vincent, C.E., Thorne, P.D., Moate, B., 2013. Acoustic scattering from a suspension of flocculated sediments. J. Geoph. Res. 118, 2581–2594. https://doi.org/10.1002/jgrc.20197.
Maerz, J., Hofmeister, R., van der Lee, E.M., Gräwe, U., Riethmüller, R., Wirtz, K.W., 2016. Maximum sinking velocities of suspended particulate matter in a coastal transition zone. Biogeosciences 13, 4863–4876. https://doi.org/10.5194/bg-13-4863-2016.
Manov, V., Chang, G.C., Dickey, T.D., 2004. Methods for reducing biofouling of moored optical sensors. J. Atmospheric Ocean Technol. 21, 958–968.
Many, G., Bourrin, F., Durrieu de Madron, X., Pairaud, I., Gangloff, A., Doxaran, D., Ody, A., Verney, R., Menniti, C., Le Berre, D., Jacquet, M., 2016. Particle assemblage characterization in the Rhone River ROFI. J. Mar. Syst. 157, 39–51. https://doi.org/10.1016/j.jmarsys.2015.12.010.
Matthes, W.J., Sholar, C.J., George, J.R., 1992. Quality assurance plan for the analysis of fluvial sediment by laboratories of the U.S. Geological Survey. USGS Numbered Series 91–467 31. Available from: https://doi.org/10.3133/ofr91467.
McAnally, W.H., Friedrichs, C., Hamilton, D., Hayter, E., Shrestha, P., Rodriguez, H., Sheremet, A., Teeter, A.M., 2007. Management of fluid mud in estuaries, bays, and lakes. I: Present state of understanding on character and behavior. J. Hydraul. Eng. 133, 9–22.
Medwin, H., Clay, C.S., 1998. Fundamentals of Acoustical Oceanography. Academic Press, New York, pp. 712.
Merckelbach, L.M., 2006. A model for high-frequency acoustic Doppler current profiler backscatter from suspended sediment in strong currents. Cont. Shelf Res. 26, 1316–1335. https://doi.org/10.1016/j.csr.2006.04.009.
Merckelbach, L.M., Ridderinkhof, H., 2006. Estimating suspended sediment concentration using backscatterance from an acoustic Doppler profiling current meter at a site with strong tidal currents. Ocean Dyn. 56, 153–168. https://doi.org/10.1007/s10236-005-0036-z.
Mishchenko, M.I., Travis, L.D., Lacis, A.A., 2002. Scattering, Absorption, and Emission of Light by Small Particles. Cambridge University Press, Cambridge.
Moody, J.A., Butman, B., Bothner, M.H., 1987. Near-bottom suspended matter concentration on the continental shelf during storms: estimates based on in-situ observations of light transmission and a particle size dependent transmissometer calibration. Cont. Shelf Res. 7, 609–628.
Mullison, J., 2017. Backscatter estimation using Broadband Acoustic Doppler Current Profilers – updated. ASCE Hydraulic Measurements & Experimental Methods Conference, Durham, NH (USA). July 9–12.
Muste, M, Kim, D., Burkhardt, A., Brownson, Z., 2006. Near-transducer errors in Acoustic Doppler Current Profiler measurements. World Environmental and Water Resources Congress, Omaha (Nebraska, USA), May 21–25. http://doi.org/10.1061/40856(200)164.
Nauw, J.J., Merckelbach, L.M., Ridderinkhof, H., van Aken, H.M., 2014. Long-term ferry-based observations of the suspended sediment fluxes through the Marsdiep inlet using acoustic Doppler current profilers. J. Sea Res. 87, 17–29. https://doi.org/10.1016/j.seares.2013.11.013.
Nauw, J., Linke, P., Leifer, I., 2015. Bubble momentum plume as a possible mechanism for an early breakdown of the seasonal stratification in the northern North Sea. Mar. Pet. Geol. 68, 789–805. https://doi.org/10.1016/j.marpetgeo.2015.05.003.
Ocean Optics Web Book, 2018. A collaborative web-based book on optical oceanography http://www.oceanopticsbook.info/.
Nechad, B., Ruddick, K., Neukermans G., 2009. Calibration and validation of a generic multisensor algorithm for mapping of turbidity in coastal waters. In: Proceedings SPIE "Remote Sensing of the Ocean, Sea Ice, and Large Water Regions", SPIE Vol. 7473, 74730H.
Nechad, B., Dogliotti, A., Ruddick, K., Doxaran, D., 2016. Particulate backscattering retrieval from remotely-sensed turbidity in various coastal and riverine turbid waters. In: Ouwehand, L. (Ed.), Proc. Living Planet Symposium, ESA-SP Volume 740, ISBN: 978-92-9221-305-3.
Neukermans, G., Ruddick, K., Loisel, H., Roose, P., 2012a. Optimization and quality control of suspended particulate matter concentration measurement using turbidity measurements. Limnol. Oceanogr. Methods 10, 1011–1023.
Neukermans, G., Loisel, H., Mériaux, X., Astoreca, R., McKee, D., 2012b. In situ variability of mass-specific beam attenuation and backscattering of marine particles with respect to particle size, density, and composition. Limnol. Oceanogr. 57, 124–144. https://doi.org/10.4319/lo.2011.57.1.0124 1.
Pait, A.S., Galdo Jr, F.R., Hartwell, S.I., Mason, A.L., Apeti, D.A., Jeffrey, C.F.G., Hoffman, A.M., Pittman, S.J., 2015. An assessment of nutrients, sedimentation, and total suspended solids (TSS) in the St. Thomas East End Reserves (STEER). NOAA Technical Memorandum NOS/NCCOS 184. Silver Spring, MD. 66pp.
Palinkas, C.M., Ogston, A.S., Nittrouer, C.A., 2010. Observations of event-scale sedimentary dynamics with an instrumented bottom boundary-layer tripod. Mar. Geol. 274, 151–164. https://doi.org/10.1016/j.margeo.2010.03.012.
Pearlman, S.R., Costa, H.S., Jung, R.A., McKeown, J.J., Pearson, H.E., 1995. Solids (section 2540). In: Eaton, A.D., Clesceri, L.S., Greenberg, A.E. (Eds.), Standard Methods for the Examination of Water and Wastewater. American Public Health Association, Washington DC, USA, pp. 2-53–2-64.
Press, W.H., Flannery, B.P., Teukolsky, S.A., Vetterling, W.T., 1989. Numerical Recipes. Cambridge University Press, pp. 702.
Puleo, J.A., Johnson, R.V., Butt, T., Kooney, T.N., Holland, K.T., 2006. The effect of air bubbles on optical backscatter sensors. Mar. Geol. 230, 87–97. https://doi.org/10.1016/j.margeo.2006.04.008.
Rai, A.K., Kumar, A., 2015. Continuous measurement of suspended sediment concentration: technological advancement and future outlook. Measurements 76, 209–227. https://doi.org/10.1016/j.measurement.2015.08.013.
Ramsey, M.H., Ellison, S.L.R., (Eds.). 2007. Measurement uncertainty arising from sampling: A guide to methods and approaches. Eurachem/EUROLAB/ CITAC/Nordtest/AMC Guide.
Randolph, K., Dierssen, H.M., Twardowski, M., Cifuentes-Lorenzen, A., Zappa, C.J., 2014. Optical measurements of small deeply penetrating bubble populations generated by breaking waves in the Southern Ocean. J. Geophys. Res. Oceans 119, 757–776. https://doi.org/10.1002/2013JC009227.
Rasmussen, P.P., Gray, J.R., Glysson, G.D., Ziegler, A.C., 2009. Guidelines and procedures for computing time-series suspended-sediment concentrations and loads from in-stream turbidity-sensor and streamflow data: U.S. Geological Survey Techniques and Methods Book 3, chap. C4, 53 pp.
Ridd, P., Larcombe, P., 1994. Biofouling control for optical backscatter suspended sediment sensors. Mar. Geol. 116, 255–258.
Röttgers, R., Heymann, K., Krasemann, H., 2014. Suspended matter concentrations in coastal waters: methodological improvements to quantify individual measurement uncertainty. Estuar. Coast. Shelf Sci. 151, 148–155. https://doi.org/10.1016/j.ecss.2014.10.010.
Rouhnia, M., Keyvani, A., Strom, K., 2014. Do changes in the size of mud flocs affect the acoustic backscatter values recorded by a Vector ADV? Cont. Shelf Res. 84, 84–92. https://doi.org/10.1016/j.csr.2014.05.015.
Rymszewicz, A., O'Sullivan, J.J., Bruen, M., Turner, J.N., Lawler, D.M., Conroy, E., Kelly-Quinn, M., 2017. Measurement differences between turbidity instruments, and their implications for suspended sediment concentration and load calculations: a sensor inter-comparison study. J. Environ. Manage. 199, 99–108. https://doi.org/10.1016/j.jenvman.2017.05.017.
Sadar, M., 1999. Turbidimeter instrument comparison: Low-level sample measurements technical information series. Hach Company, report D90.5, 55pp.
Sahin, C., Verney, R., Sheremet, A., Voulgaris, G., 2017. Acoustic backscatter by suspended cohesive sediments: field observations, Seine Estuary, France. Cont. Shelf Res. 134, 39–51. https://doi.org/10.1016/j.csr.2017.01.003.
Salehi, M., Strom, K., 2011. Using velocimeter signal to noise ratio as a surrogate measure of suspended mud concentration. Cont. Shelf Res. 31, 1020–1032. https://doi.org/10.1016/j.csr.2011.03.008.
Schmechtig, C., Thierry, V., the Bio Argo Team, 2015. Argo quality control manual for biogeochemical data. http://doi.org/10.13155/40879.
Schwarz, C., Cox, T.J.S., Van Engeland, T., Van Oevelen, D., Van Belzen, J., van de Koppel, J., Soetaert, K., Bouma, T.J., Meire, P., Temmerman, S., 2017. Field estimates of floc dynamics and settling velocities in a tidal creek with significant along-channel gradients in velocity and SPM. Estuar. Coast. Shelf Sci. 197, 221–235. https://doi.org/10.1016/j.ecss.2017.08.041.
Schwendeman, M., Thomson, J., 2015. Observations of whitecap coverage and the relation to wind stress, wave slope, and turbulent dissipation. J. Geophys. Res. Oceans 120, 8346–8363. https://doi.org/10.1002/2015JC011196.
Sheng, J., Hay, A.E., 1988. An examination of the spherical scatterer approximation in

aqueous suspensions of sand. J. Acoust. Soc. Am. 83, 598–610.
Shreve, E.A., Downs, A.C., 2005. Quality-assurance plan for the analysis of fluvial sediment. U.S. Geological Survey Kentucky Water Science Center Sediment Laboratory, USGS Open-File Report 2005-1230, 28pp.
Slade, W.H., Boss, E., Russo, C., 2011. Effects of particle aggregation and disaggregation on their inherent optical properties. Opt. Express 19, 7945–7959. https://doi.org/10.1364/OE.19.007945.
Slade, W.H., Agrawal, Y.C., Mikkelsen, O.A., 2013. Comparison of measured and theoretical scattering and polarization properties of narrow size range irregular sediment particles. Presented at Oceans, San Diego, 23–7.
Sottolichio, A., Hurther, D., Gratiot, N., Bretel, P., 2011. Acoustic turbulence measurements of near-bed suspended sediment dynamics in highly turbid waters of a macrotidal estuary. Cont. Shelf Res. 31, S36–S49. https://doi.org/10.1016/j.csr.2011.03.016.
Spinrad, R.W., Yentsch, C.M., Brown, J., Dortch, Q., Haugen, E., Revelante, N., Shapiro, L., 1989. The response of beam attenuation to heterotrophic growth in a natural population of plankton. Limnol. Oceanogr. 34, 1601–1605.
Stanton, T.K., 1989. Simple approximate formulas for backscattering of sound by spherical and elongated objects. J. Acoust. Soc. Am. 86, 1499–1510.
Stavn, R.H., Rick, H.J., Falster, A.V., 2009. Correcting the errors from variable sea salt retention and water of hydration in loss on ignition analysis: implications for studies of estuarine and coastal waters. Estuar. Coast. Shelf Sci. 81, 575–582. https://doi.org/10.1016/j.ecss.2008.12.017.
Strickland, J.D.H., Parsons, T.R., 1968. A practical handbook of seawater analysis. Bulletin 167. Fisheries Research Board of Canada, Ottawa, Canada, 181–184.
Sutherland, T.F., Lane, P.M., Amos, C.L., Downing, J., 2000. The calibration of optical backscatter sensors for suspended sediment of varying darkness levels. Mar. Geol. 162, 587–597. https://doi.org/10.1016/S0025-3227(99)00080-8.
Tessier, C., 2006. Charactérisation et dynamique des turbidités en zone côtière: l'exemple de la région marine Bretagne Sud. PhD thesis Université de Bordeaux, France, 400pp.
Tessier, C., Le Hir, P., Lurton, X., Castaing, P., 2008. Estimation de la matière en suspension à partir de l'intensité acoustique rétrodiffusée des courantomètres acoustiques à effet Doppler (ADCP). C.R. Geosci. 340, 57–67.
Thorne, P.D., Vincent, C.E., Hardcastle, P.J., Rehman, S., Pearson, N., 1991. Measuring suspended sediment concentrations using acoustic backscatter devices. Mar. Geol. 98, 7–16.
Thorne, P.D., Hardcastle, P.J., Holdaway, G.P., Born, A.J., 1994. Analysis of results obtained from a triple frequency acoustic backscatter system for measuring suspended sediments. In: Proceedings of the 6th International Conference on Electronic Engineering in Oceanography, vol. 394, pp. 83–89.
Thorne, P.D., Hanes, D.M., 2002. A review of acoustic measurement of small-scale sediment processes. Cont. Shelf Res. 22, 603–632. https://doi.org/10.1016/S0278-4343(01)00101-7.
Thorne, P.D., MacDonald, I.T., Vincent, C.E., 2014. Modelling acoustic scattering by suspended flocculating sediments. Cont. Shelf Res. 88, 81–91. https://doi.org/10.1016/j.csr.2014.07.003.
TMAP, 2009. Monitoring Handbook: Eutrophication – Nutrients (version 16.09.2009, TMAG 09-2). http://www.waddensea-secretariat.org/monitoring-tmap/manual-guidelines.
Topping, D.J., Wright, S.A., 2016, Long-term continuous acoustical suspended-sediment measurements in rivers—Theory, application, bias, and error. U.S. Geological Survey, USGS Professional Paper 1823, 98 pp. http://doi.org/10.3133/pp1823.
Tzeng, M.W., Dzwonkowski, B., Park, K., 2016. Data processing for a small-scale long-term coastal ocean observing system near Mobile Bay, Alabama. Earth Space Sci. 3, 510–522. https://doi.org/10.1002/2016EA000188.
Urick, R.J., 1975. Principles of Underwater Sound, second ed. McGraw-Hill Book Company, New York.
van der Hout, C.M., Gerkema, T., Nauw, J.J., Ridderinkhof, H., 2015. Observations of a narrow zone of high suspended particulate matter (SPM) concentrations along the Dutch coast. Cont. Shelf Res. 95, 27–38. https://doi.org/10.1016/j.csr.2015.01.002.
van der Hout, C.M., Witbaard, R., Bergman, M.J.N., Duineveld, G.C.A., Rozemeijer, M.J.C., Gerkema, T., 2017. The dynamics of suspended particulate matter (SPM) and chlorophyll-a from intratidal to annual time scales in a coastal turbidity maximum. J. Sea Res. 127, 105–118. https://doi.org/10.1016/j.seares.2017.04.011.
Verney, R., Deloffre, J., Brun-Cottan, J.-C., Lafite, R., 2007. The effect of wave-induced turbulence on intertidal mudflats: Impact of boat traffic and wind. Cont. Shelf Res. 27, 594–612. https://doi.org/10.1016/j.csr.2006.10.005.
Voulgaris, G., Meyer, S.T., 2004. Temporal variability of hydrodynamics, sediment concentration and sediment settling velocity in a tidal creek. Cont. Shelf Res. 24, 1659–1683. https://doi.org/10.1016/j.csr.2004.05.006.
Wagner, R.J., Boulger Jr, R.W., Oblinger, C.J., Smith, B.A., 2006. Guidelines and standard procedures for continuous water-quality monitors—Station operation, record computation, and data reporting. U.S. Geological Survey, USGS Techniques and Methods 1–D3, 51 pp. http://pubs.water.usgs.gov/tm1d3.
Waldmann, C., Tamburri, M., Prien, R.D., Fietzek, P., 2010. Assessment of sensor performance. Ocean Sci. 6, 235–245. https://doi.org/10.5194/os-6-235-2010.
Wang, D.W., Wijesekera, H.W., Teague, W.J., Rogers, W.E., Jarosz, E., 2011. Bubble cloud depth under a hurricane. Geophys. Res. Lett. 38, L14604. https://doi.org/10.1029/2011GL047966.
Wang, D.W., Wijesekera, H.W., Jarosz, E., Teague, W.J., 2016. Turbulent diffusivity under high winds from acoustic measurements of bubbles. J. Phys. Oceanogr. 46, 1593–1613. https://doi.org/10.1175/JPO-D-15-0164.1.
Whelan, A., Regan, F., 2006. Antifouling strategies for marine and riverine sensors. J. Environ. Monit. 8, 880–886. https://doi.org/10.1039/b603289c.
Wilcox, R.R., 2010. Fundamentals of Modern Statistical Methods - Substantially Improving Power and Accuracy, second ed. Springer, New York Dordrecht Heidelberg London, pp. 249. https://doi.org/10.1007/978-1-4419-5525-8.
Woźniak, S.B., Meler, J., Lednicka, B., Zdun, A., Stoń-Egiert, J., 2011. Inherent optical properties of suspended particulate matter in the southern Baltic Sea. Oceanologia 53, 691–729. https://doi.org/10.5697/oc.53-3.691.
Yeats, P.A., Brügmann, L., 1990. Suspended particulate matter: collection methods for gravimetric and trace metal analysis. ICES Techniques in Marine. Environ. Sci. 7, 9.
Yentsch, C.S., 1962. Measurement of visible light absorption by particulate matter in the ocean. Limnol. Oceanogr. 7, 207–217.
Zhang, X., Stavn, R.H., Falster, A.U., Gray, D., Gould Jr, R.W., 2014. New insight into particulate mineral and organic matter in coastal ocean waters through optical inversion. Estuar. Coast. Shelf Sci. 149, 1–12. https://doi.org/10.1016/j.ecss.2014.06.003.
Ziegler, A.C., 2003. Breakout session 1 – Definition of optical methods for turbidity and data reporting. In: Gray, J.R., Glysson, G.D., (Eds.), Proceedings of the Federal Interagency Workshop on Turbidity and Other Sediment Surrogates, U.S. Geological Survey, USGS Circular 1250, 9–13. http://water.usgs.gov/pubs/circ/2003/circ1250/.

# APPENDIX 5

**Montereale-Gavazzi et al. 2019. Insight into short term tidal variability of multibeam backscatter from field experiments on different seafloor types. Geosciences 2019, 9, 34**

geosciences

MDPI

Article

# Insights into the Short-Term Tidal Variability of Multibeam Backscatter from Field Experiments on Different Seafloor Types

**Giacomo Montereale-Gavazzi [1,2,*], Marc Roche [3], Koen Degrendele [3], Xavier Lurton [4], Nathan Terseleer [1], Matthias Baeye [1], Frederic Francken [1] and Vera Van Lancker [1,2]**

1 Royal Belgian Institute of Natural Sciences, Operational Directorate of Nature, Gulledelle 100, B, 1200 Brussels, Belgium; nterseleerlillo@naturalsciences.be (N.T.); mbaeye@naturalsciences.be (M.B.); ffrancken@naturalsciences.be (F.F.); vera.vanlancker@naturalsciences.be (V.V.L.)

2 Department of Geology, Renard Centre of Marine Geology, Ghent University, Krijgslaan 281 s.8, B-9000 Gent, Belgium

3 Federal Public Service Economies, Continental Shelf Service, Boulevard du Roi Albert II, 16, 1000 Brussels, Belgium; Marc.Roche@economie.fgov.be (M.R.); Koen.Degrendele@economie.fgov.be (K.D.)

4 Ifremer, Underwater Acoustics Laboratory, IMN/NSE/AS, CS 10070, 29280 Plouzané, France; Xavier.Lurton@ifremer.fr

* Correspondence: gmonterealegavazzi@naturalsciences.be

Received: 4 December 2018; Accepted: 2 January 2019; Published: 10 January 2019


**Abstract:** Three experiments were conducted in the Belgian part of the North Sea to investigate short-term variation in seafloor backscatter strength (BS) obtained with multibeam echosounders (MBES). Measurements were acquired on predominantly gravelly (offshore) and sandy and muddy (nearshore) areas. Kongsberg EM3002 and EM2040 dual MBES were used to carry out repeated 300-kHz backscatter measurements over tidal cycles (~13 h). Measurements were analysed in complement to an array of ground-truth variables on sediment and current nature and dynamics. Seafloor and water-column sampling was used, as well as benthic landers equipped with different oceanographic sensors. Both angular response (AR) and mosaicked BS were derived. Results point at the high stability of the seafloor BS in the gravelly area (<0.5 dB variability at 45° incidence) and significant variability in the sandy and muddy areas with envelopes of variability >2 dB and 4 dB at 45° respectively. The high-frequency backscatter sensitivity and short-term variability are interpreted and discussed in the light of the available ground-truth data for the three experiments. The envelopes of variability differed considerably between areas and were driven either by external sources (not related to the seafloor sediment), or by intrinsic seafloor properties (typically for dynamic nearshore areas) or by a combination of both. More specifically, within the gravelly areas with a clear water mass, seafloor BS measurements where unambiguous and related directly to the water-sediment interface. Within the sandy nearshore area, the BS was shown to be strongly affected by roughness polarization processes, particularly due to along- and cross-shore current dynamics, which were responsible for the geometric reorganization of the morpho-sedimentary features. In the muddy nearshore area, the BS fluctuation was jointly driven by high-concentrated mud suspension dynamics, together with surficial substrate changes, as well as by water turbidity, increasing the transmission losses. Altogether, this shows that end-users and surveyors need to consider the complexity of the environment since its dynamics may have severe repercussions on the interpretation of BS maps and change-detection applications. Furthermore, the experimental observations revealed the sensitivity of high-frequency BS values to an array of specific configurations of the natural water-sediment interface which are of interest for monitoring applications elsewhere. This encourages the routine acquisition of different and concurrent environmental data together with MBES survey data. In view of promising advances in MBES absolute calibration allowing more straightforward data comparison, further investigations of the drivers of BS variability and sensitivity are required.

**Keywords:** multibeam echosounder; seafloor; backscatter; monitoring; short-term variability; sensitivity; high-frequency

## 1. Introduction

The North Sea is amongst the most highly impacted areas of the marine biome [1]. This is particularly the case for its Belgian part, where a multitude of anthropogenic activities, including intense routed navigation, dredging and disposal of dredged material, marine aggregate extraction, bottom trawling by commercial fisheries and extensive infrastructural, engineering and management developments (e.g., telecommunication cables, pipelines, wind energy and beach nourishment), take place over a limited spatial extent of ~3600 km$^2$ along a ~65 km coastline [2]. In this regard, knowledge of the seafloor composition and of its spatio-temporal evolution is of great relevance to monitor human impacts on benthic habitats (of which substrate type is a fundamental abiotic component and surrogate for biota [3]). At the European level, the monitoring is mandated by the European Marine Strategy Framework Directive to achieve *Good Environmental Status* (GES) of marine waters by 2020 (see [4] and references therein). Twelve GES descriptors were put forward for which each EU Member State defined indicators with associated monitoring programmes. For the Belgian part of the North Sea (BPNS), one of them relates to changes in the extent of seabed habitats for which multibeam echosounding (MBES) was selected for the monitoring [5].

The use of MBES systems to acoustically characterize the seafloor has developed at a fast pace over the past three decades [6,7]. Co-registration of depth (signal travel-time) and reflectivity (backscattered intensity of the echo signals, hereafter BS) measured over a large range of angles (swathe) and at very high resolution is possible using this technology. MBES BS depends on many factors, including ([8]): (1) sediment type and its geotechnical characteristics dictating the seawater-seafloor impedance contrast (e.g., porosity, roughness, grain size and sediment inner homogeneity), (2) the sonar operating frequency, and (3) the signal angle of incidence. Due to the various sound-scattering properties of different seafloor substrates, BS can be used as a proxy aiding in the determination of bottom type at the water-sediment interface (e.g., [9,10]) and possibly the inference of some of its physical characteristics [11,12]. Mapping this interface over vast areas allows extending information from local observations (in situ ground-truth measurements) or transect-based information, that need interpolation/extrapolation [13], to the spatial continuum of the seafloor. This is valuable as an input to Marine Spatial Planning and Ecosystem Based Management and aids in the creation of efficient analytical, managerial and decision-making tools [14–17].

Backscatter data obtained from MBES surveys are usually considered at two processing levels: angular response (AR—signal processing) and mosaicked images (image-analysis). The AR describes the backscattering strength variation with angle of incidence and is retained as an intrinsic property of the seafloor directly relating to physical quantities of interest [18]. This "raw" format of backscatter is a promising seabed classification feature with a high potential for sediment discrimination, as reported in a range of studies ([19,20] and references therein). The AR forms a shape ("the AR curve") which reflects the dominant acoustic phenomena occurring along the angular domains: high-intensity specular reflection around the nadir and lower-level scattering at oblique angles, strongly decreasing at shallow grazing angles. Where absolute calibration of the BS is achievable, the BS AR is to be considered as an objective measurement for which different methods exist ([21] and references therein). The mosaic backscatter is a further derivative of the backscatter data, where BS levels are presented, usually in a georeferenced frame, in the form of a grayscale image with the angular dependence removed via statistical compensation. As such, the complete scene seems to be observed from the same incidence angle which is generally obtained by normalizing the data and referencing it to a conventional angle or a limited range of angles. Typically, this is around 45° where the angular dependence is weakest and where the sediment response dominates [12]. Both BS data forms (AR

and mosaicked images) have been used to predict seafloor type, on their own, or in combination with other MBES data types [20,22]. The main differences between these two formats are the spatial resolution and the type of information they contain. The BS AR is obtained by averaging a set of consecutive pings and processing them over the swath extent or over areas of interest, resulting in a resolution approximating that of the area selected. The BS mosaic resolution is considerably finer, given that it can be gridded as a function of the bathymetric resolution. Here, identification of small-scale features (down to decimetric orders of magnitude for high-frequency MBES operated in shallow waters) is feasible and is particularly valuable to ecological modelling requiring detailed discrimination of substrate distribution, down to the spatial-unit level of single patches [23–25]. However, due to its inherent compensation of angle dependency, the mosaicking process leads to a loss of quantitative/physical information, making immediate ground truthing critical for effective relation to seabed properties. On the other hand, the AR can be interpreted via modelling of the response and fitting of parameters (see [26] and references therein) which directly relate to the physical nature of the underlying substrate. Inversion of the AR into sedimentologically relevant information is a principle known for long which is currently hindered by a lack of high-frequency geoacoustic models dedicated to solving the "inversion problem" and should be perceived as an advancing application within the realm of acoustical oceanography. However, it remains promising considering the rapid advances in MBES system absolute [21,27,28] and relative calibration [29] and in stability and repeatability controls [30], together promoting the comparability of data in space and time. This would also allow compiling acoustic inventories that are calibrated against substrate types (and of associated features and combinations) to be used more globally. Alternatively, ground-truthing developments allow an increasingly detailed characterization of the acoustic observations and thus the potential development of models otherwise constrained by the need for a priori knowledge. In the long term, the scientific community would largely benefit from the development of detailed high-frequency geoacoustic models offering the advantage of directly exploiting the remotely sensed data, thus reducing labour-intensive and often expensive ground-truthing operations. Methods exploiting the AR demonstrated the utility of inverting radiometrically calibrated and geometrically corrected backscatter data into relevant sedimentological parameters [22]. However, the latter were related to well-sorted and homogeneous sediments only, evidencing the need to enhance the understanding of the relations between naturally complex sediment configurations and the retrieved acoustic signatures and to ground truth the acoustics to avoid misleading interpretation (regardless the type of BS product and approach used).

Environmental monitoring, based on the acquisition of MBES time series [31,32], requires investigating and understanding the repeatability and variability of the data. Besides the instrumental constraints (aimed at ensuring the consistency of measured data from different campaigns and/or sensors), multiple sources of environmental factors must be considered for their impact on the consistency and accuracy of backscatter data measurement. This is particularly the case in nearshore/coastal and continental shelf zones where seafloor and water-column variability may be high at diverse scales in space and time. Therefore, it is important to evaluate whether changes in the average backscatter level between different surveys reflects actual changes in sediment properties or in the conditions of the water medium [33] and of other dynamic parameters. A similar concern was already identified in terrestrial remote-sensing applications [34,35]. In this regard, it is critical that the survey-design phase of any such investigation considers all possible sources of variation which may contribute to unwanted fluctuations of the backscatter strength. This is needed to confidently quantify seafloor type and change based on the acoustic returns.

Depending on the MBES survey environment, a range of factors can be responsible for unwanted signal fluctuations in the acoustic measurements. First, the azimuthal dependence is driven by the orientation of small-scale bed forms relative to the navigation heading (hence the acoustic line of sight; see [10,36–39]), as well as by seafloor mobility under the effect of hydrodynamic forcing driving the roughness polarization. Second, the dissipative nature of the water medium leads to absorption of acoustic energy during the signal propagation; this depends on the seafloor-target

range, frequency and physico-chemical properties, such as temperature and salinity driving the viscous-thermal status [40–42]. The concentration and particle size and shape of suspended particulate matter (SPM) also contribute to the total two-way transmission loss of the acoustic signal; it can be significant in nearshore and shelf environments (particularly over relatively long distances, i.e., typically beyond 100 m—see [43]). Finally, biological activity, occurring in the water column (e.g., the Deep Scattering Layer—see [44]) or at the benthic level (referring to epibenthic and infaunal activity—see [37,45]), as well as near-bed advection of submerged aquatic vegetation ([17]) can affect MBES measurements. Additionally, there is a need to better understand the effects of the intrinsic dynamicity of given substrates and how near-bed (also referred to as boundary and/or water-sediment interface and benthic zone) sediment transport affects the seafloor sonar detection. Ideally, all of these variables are accounted for when comparing datasets in space and time.

This study presents a set of observations originating from three experimental datasets acquired to understand and quantify the external and seafloor-intrinsic sources of variance that may lead, while surveying, to biases in the seafloor backscatter acquired by high-frequency (300 kHz) multibeam sonar systems. Repeated measurements (multi-pass MBES surveys) using EM3002D and EM2040D echosounders are interpreted based on seafloor and water-column data acquired by grab sampling, optical observations and a multi-sensor benthic lander, in combination with a drop-down frame. Altogether, these data are used to assess the sensitivity of the BS and how its short-term variability can affect the detection of actual changes in the seabed.

## 2. Materials and Methods

### 2.1. Description of MBES and Survey Areas

Multibeam data were collected using Kongsberg EM3002D and EM2040D echosounders, respectively installed on *RV A962 Belgica* (http://odnature.naturalsciences.be/belgica) and *RV Simon Stevin* (http://www.vliz.be/en/rv-simon-stevin). Table 1 reports the parameters used to operate the echosounders during the experiments.

**Table 1.** MBES specifications and main settings, and associated ancillary sensors.

| Parameter/Echosounder | Kongsberg Maritime EM3002D | Kongsberg Maritime EM2040D |
|---|---|---|
| Number of soundings per ping | 508 | 800 |
| Central frequency | 300 kHz | 300 kHz |
| Pulse length | 150 µs | 108 µs |
| MBES Mode | Normal | Normal |
| Rx Beam spacing | High density equidistant | High density equidistant |
| Tx × Rx Beam width | 1.5° × 1.5° | 1° × 1° |
| Positioning System | MGB Tech with Septentrio AsteRx2eH RTK heading receiver | MGB Tech with Septentrio AsteRx2eL RTK receiver |
| Motion Sensor | Seatex MRU 5 | XBlue Octans |
| Sound Velocity Probe | Valeport mini SVS and SVP | Valeport mini SVS and SVP |

Three surveys were conducted during spring-tide regime: in February 2015, March 2016 and November 2017, respectively on the Kwinte swale, Westdiep swale and MOW 1 areas, featuring distinct seafloor substrates. Locations are displayed in Figure 1 and general environmental conditions are given in Table 2. Within the areas, study sites were selected with homogeneous acoustic signatures, based on previous surveys and ancillary data.

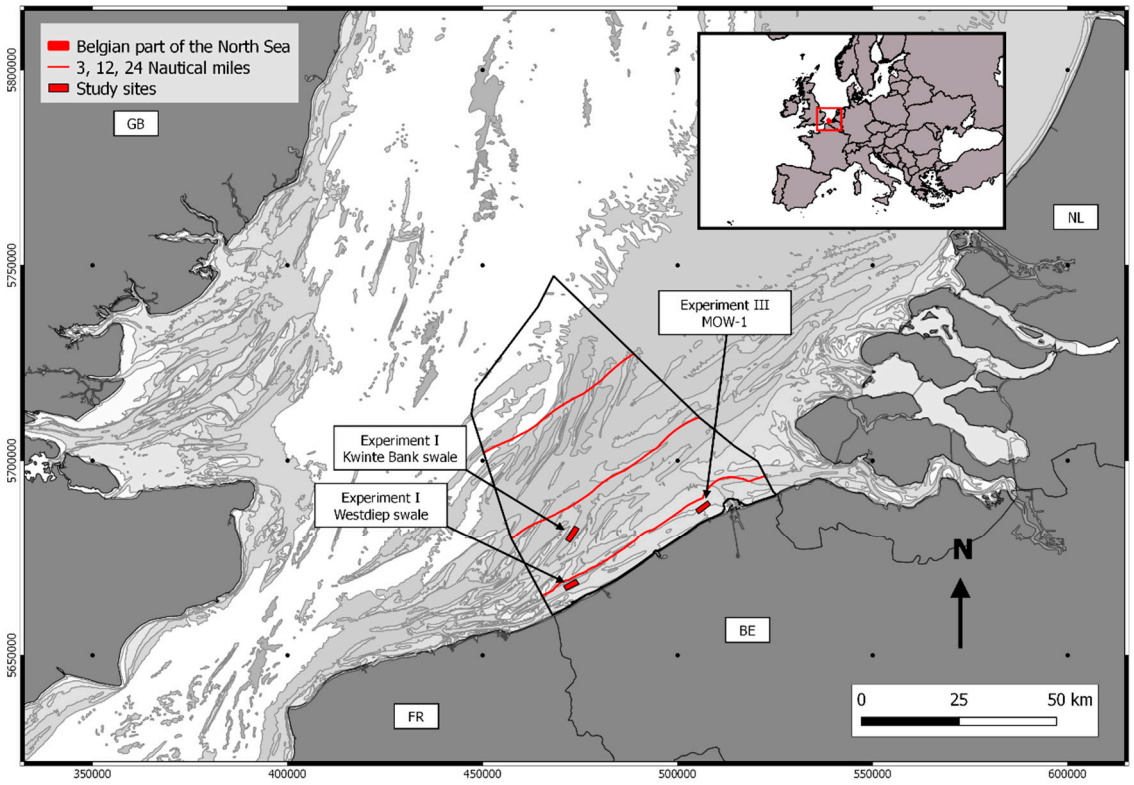


**Figure 1.** Location of selected study sites within the Belgian part of the North Sea: (1) Kwinte swale area (central coordinate: N 51° 17.2717, E 002° 37.7035), (2) Westdiep swale area (N 51° 09.1230, E 002° 34.6806), (3) Zeebrugge, MOW 1 pile area (N 51° 21.6697, E 003° 06.5798). The inset shows the location of the Belgian part of the North Sea within the European geographical zone. Data are projected in World Geodetic System 84 (WGS 84) in Universal Transverse Mercator Zone 31 N (UTM—31N). This coordinate system is used throughout the rest of the document.

**Table 2.** Environmental characteristics of the three experimental areas, each having distinct seafloor substrate properties. MLLWS: Mean Lowest Low Water at Spring tide.

| Area | Depth and Sediment Dynamics * | Habitat Type (EUNIS Level 3 **) | Details on Environmental Setting |
|---|---|---|---|
| Kwinte swale | Depth (MLLWS): 25 m<br>Water mass type: clear seawater<br>Magnitude of sediment transport during Spring tide: <0.5 tonnes $m^{-1}d^{-1}$ | Offshore circalittoral gravelly hummocky/hillocky terrain (relatively well sorted medium sand with gravel) | In [30,46] |
| Westdiep swale | Depth (MLLWS): 15 m<br>Water mass type: clear seawater<br>Magnitude of sediment transport during Spring tide: 0.5–1 tonnes $m^{-1}d^{-1}$ | Circalittoral sandy/siliciclastic terrain (well sorted fine to medium sand) | In [47] |
| Zeebrugge, MOW1 pile | Depth (MLLWS): 10 m<br>Water mass: Turbidity maximum zone<br>Magnitude of sediment transport during Spring tide: >1 tonnes $m^{-1}d^{-1}$ | Circalittoral muddy sediments | [48,49] |

* From [50,51]. ** European Nature Information System level III categories—see [52].

## 2.2. Survey Methodology and Data Processing

The surveying principle designed to capture short-term backscatter variability over the same seafloor patch is presented in Figure 2. It consists of a series of repetitive MBES measurements

performed over the duration of a tidal cycle (~13 h). The same reference survey-line (~2 km) was followed using the same heading and crossing the centre of a region of interest (ROI—approximately 500 × 200 m for the first two experiments and 200 × 50 m in the third one). While deviations from the planned track line could happen for several reasons, this did not occur significantly during the experiments, and the homogeneity of the selected ROIs ensures the spatio-temporal consistency of the data across all insonified angles. Runtime acquisition parameters used in the Kongsberg Seafloor Information System software suite [53] were kept rigorously unchanged throughout the duration of each experiment, avoiding introducing extra sources of variance in the data.

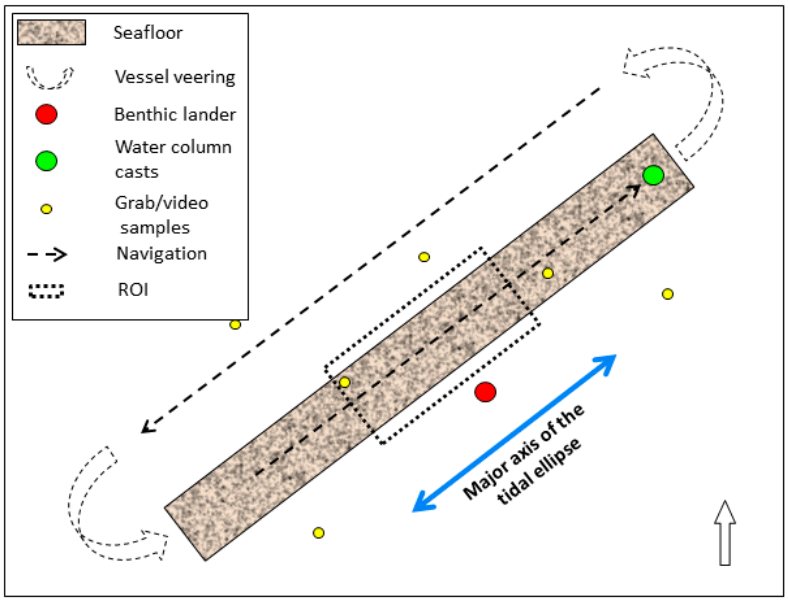


**Figure 2.** Schematic representation (not to scale) of the surveying principle designed to capture the short-term backscatter variability over a homogeneous region of interest (ROI). See main text for explanations.

Each experiment consists in the acquisition of a short-term backscatter and bathymetry time series according to the described strategy. To interpret the acoustic data, different strategies were put forward to quantify environmental variables during the experiments; these are listed hereafter for each experiment.

#### 2.2.1. Experiment 1—Kwinte Swale Area

The first experiment alternated MBES measurements with vertical profiling of oceanographic variables using a drop-down frame over a 13-h tidal cycle. The area was selected because of its high stability in MBES-measured BS, based on previous investigations. Meanwhile, this site was proposed as a natural reference area to control the BS stability prior to any surveying operation in the Belgian Part of the North Sea (BPNS) [30]. The oceanographic data relating to this experiment are discussed in [33,54]. They show negligible effects of water-column processes and of near-bed sediment transport on the backscatter measurements. Here, only the MBES data are discussed.

#### 2.2.2. Experiment 2—Westdiep Swale Area

The second experiment was extended with the deployment of a benthic lander equipped with oceanographic sensors (Figure 3; Table 3) from which variables relating to the lower ~2.4 m above seabed (*mab*) were derived. The lander was moored at ~120 m distance from the nadir of the MBES track line. This was the minimum distance allowed to keep a safe navigation buffer from the instrument's signalling buoy. Given the similar morpho-sedimentary characteristics over the

survey area, the information sampled by the lander was considered as representative of the processes occurring within the MBES ROI.

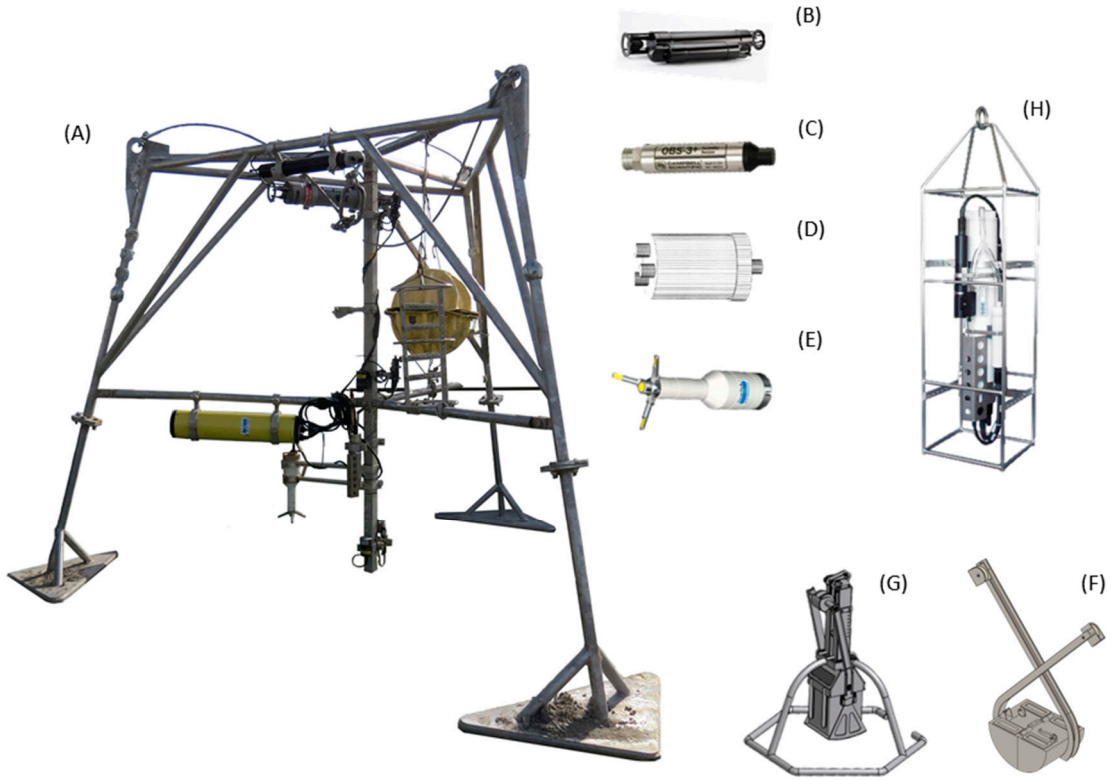


**Figure 3.** (**A**) Benthic lander equipped with a set of oceanographic sensors (see Table 1 for details about the instrumentation) deployed during the second experiment in the Westdiep study site. A similar lander was deployed for the third experiment. A chain of OBS+ sensors at 0.3, 1 and 2.4 m above bottom (mab) was present during the third experiment. In this image: (**A**) Benthic lander frame, (**B**) laser in situ transmissometer, (**C**) optical backscatter sensor, (**D**) acoustic backscatter sensor, (**E**) acoustic doppler velocimeter; and on-board winch-operated instruments, (**F**) Van Veen grab, (**G**) Reineck boxcore, (**H**) CTD frame, equipped with a OBS+ and a Niskin bottle.

Measurements of suspended particulate matter concentration (SPMc) were derived using optical and acoustic backscattering sensors (OBS and ABS). Field calibrations of the OBS were carried out during previous *RV Belgica* cruises following the methodology described in [55]. Despite the calibration locations being different, derived SPMc are sufficiently representative of water-column processes occurring at 2.35 mab in the current study area. The multi-frequency ABS was equally used to determine SPMc, as well as median grain size (D50), in a 1-m profile above the bed and per bins of 1 cm. This sensor was chosen due to its suitability to measure in sandy environments. Calibration is provided by the manufacturer (implicit calibration methods; see [56]), and is based on the use of glass spheres being representative of quartz/siliciclastic particles present in this study area. Along with MBES and benthic lander data, an SBE 19+ SeaCAT Profiler CTD, equipped with a 5L Niskin bottle, was regularly down-casted at the end of the MBES transect to obtain measurements of SPMc, salinity, depth and temperature in the water column up until ~3 mab. This was performed approximately every hour. From each water sample, three sub-samples were filtered on board using pre-weighed filters (Whatman GF/C type). In turn, they were subsequently washed with 50 mL of Milli-Q water to remove salt, dried and weighted to derive SPMc. MBES and all benthic lander data were referenced to a uniform timestamp (the mean time of acquisition within the defined ROI) to enable later inter-comparison.

**Table 3.** Summary of the oceanographic sensors installed on the benthic lander used to quantify the driving processes of variability in the MBES backscatter measurements.

| Sensor | Measurements/Variables | Distance of Measurement from Seabed | Temporal/Spatial Resolution | Further Instrument Specifications | Calibration |
|---|---|---|---|---|---|
| ADV Ocean velocimetry @ 5 mHz | Current in x,y,z; Direction; Altimetry; Temperature; Salinity; Velocity | 0.2 mab | Bursts of 15 min.<br>2 × 2 cm measuring cell | www.sontek.com | NA |
| ABS Acoustic Backscatter Sensor @ 0.5, 1, 2, 4 MHz | SPMc; particle size | 1 mab | Bursts of 30 min.<br>1 cm bins over 1 m profile | www.aquatecgroup.com | Manufacturer calibration (implicit method) |
| Sequoia Scientific LISST 100-X (type-C) | Particle size and distribution; transmission; volume concentration | 2.4 mab | Bursts of 1 min. | www.sequoiasci.com | NA |
| OBS+ | SPMc | 2.35 mab | Bursts of 15 min. | www.campbellsci.com/d-a-instruments | Previous campaign calibration using in situ water samples (gravimetric analysis) |
| SBE 19+ SeaCAT Profiler CTD—OBS+ and 5L Niskin bottle | Temperature, Salinity, hydrostatic pressure; SPMc (from water filtrations of Niskin bottles) | ~2/3 mab | ~Every 1 h | www.campbellsci.com/d-a-instruments and www.seabird.com | OBS NTU * vs SPMc Calibration = $R^2$ 0.56 @ 3 ~ mab |

** NTU: Nepheloid turbidity units.*

Additionally, a set of reconnaissance Van Veen grab samples ($n$ = 7, replicate = 3) were acquired in the surroundings of the experiment site and were analysed for grain size by means of a Malvern Master-sizer 3000 (www.malvern.com). Before the analysis, organic matter and calcium carbonate ($CaCO_3$) were removed using $H_2O_2$ (35%) and HCl (10%), respectively. To describe sediment types, the Folk and Ward [57] nomenclature is used throughout the rest of the document.

#### 2.2.3. Experiment 3—Zeebrugge, MOW 1 Pile Area

The third experiment was carried out in the proximity of a fixed monitoring station (MOW 1—http://departement-mow.vlaanderen.be) where a benthic lander is deployed regularly by the Royal Belgian Institute of Natural Sciences as part of a long-term sediment dynamics monitoring programme [48]. The benthic lander allowed obtaining SPMc from a set of turbidity meters installed at 0.3, 1 and 2.4 mab. The OBS signals were related to mass concentration after calibration using mass-filtered water samples, taken during a 13-h tide cycle.

Furthermore, during this experiment, a time series of Reineck box cores was also collected to quantify changes in surficial sediment composition over the duration of the experiment. Overall, 12 samples were collected (approximately one every hour). They were taken from a relatively homogeneous seafloor patch and within a buffer zone with a radius of ~100 m. Particle sizes were analysed, and their nature was described as specified in the previous section. To obtain data relating to the immediate seabed surface of the samples, a 1-cm slicing was carried out on-board; the first three centimetres were kept for analysis.

Additionally, two full-coverage surveys (covering approximately 350 m × 1.5 km) were acquired over this study site on 21 and 24 November 2017 (experiment taking place before the second survey on the 24th November). Similarly to the acquisition of the time-series datasets, surveys were conducted by maintaining fixed runtime parameters and following the same set of navigation lines. Furthermore, both surveys were carried out during the same tide-window: around peak ebb flow. Following a routine to objectively find the statistical number of classes in the datasets (i.e., Within Group Sum of Squared Distances plot), maps were classified using the unsupervised k-means clustering algorithm [58] and assessed for changes by means of simple algebraic change detection (i.e., image

differencing). This was carried out to appraise the short-term spatial sediment dynamics of the study area.

Considering the muddy and soft nature of the water-sediment interface of this study site and the chance to have ephemeral deposition of unconsolidated sediments [49], the Kongsberg Quality Factor (QF) was computed within the ROI to assist in the interpretation of the BS temporal/tidal oscillation. The QF is a metric relating to the relative bathymetry uncertainty and is expressed by the ratio between the scaled standard deviation of the range detection divided by the detected range [59]: the smaller the QF values, the smaller the uncertainty, implying a more accurate bottom detection. In this instance, the QF can be interpreted as a proxy of changes in the water-sediment interface, and thus for variability/sensitivity of the BS. Values of SPMc and QF are later related to the MBES BS time series by means of correlation and regression analysis.

### 2.3. MBES Processing

Different BS products were derived from the Kongsberg datagrams by using different software tools. All BS data were taken within the selected ROIs. Similarly to the acquisition phase, a rigorous standardized processing procedure was maintained to avoid variability induced by changes in software parameters [30]. Using the *QPS FMGT*© module [60], time series of 1-m horizontal resolution mosaicked backscatter were produced. The default *FMGT Geocoder* compensation algorithm compensates the data over the angular interval from 30° to 60°. Secondly, using the *SonarScope*© software suite [61], time series of AR curves were derived from the *Beam intensity* datagrams. The seafloor angular backscatter strength is computed from the following sonar equation liking the transmitted and received signal levels with the transmission losses and the backscattering process:

$$EL\,(R, \theta) = SL + D_{TR}\,(\theta) - 2TL\,(R) + 10 \log A\,(R, \theta) + BS\,(\theta), \quad (1)$$

where $EL$ is the Echo Level (referenced to 1 µPa) measured at the receiver as a function of the sonar-to-target range $R$ and the angle of incidence $\theta$ of the signal onto the seafloor, $SL$ is the Source Level (in dB re 1 µPa @ 1 m), $2TL$ is the two-way Transmission Loss accounting for both geometrical spherical spreading (i.e., 40 log $R$) and absorption ($2\alpha_w R$—see [40,41]), $A$ is the instantaneously insonified area, delimited by the MBES beam aperture and/or signal duration, and $BS$ is the Backscatter Strength of the seafloor target at the observation angle $\theta$. The data reduction scheme relating to the AR data-type is reported in Table 4 and, despite being relative, is considered to be the best estimate of the raw BS angular response [28,30]. Figure 4 shows the differences between AR prior and after removing the Kongsberg built-in *Lambertian* and *specular adaptive* corrections (the latter is removed a priori in the *SonarScope*® processing workflow). Time series of bathymetry for each experiment were also derived using *QPS QIMERA*© [62]. Tidal corrections using data from the closest tide-gauges were applied for the EM3002D datasets whereas a higher accuracy RTK (Real Time Kinematic) correction was applied to the EM2040D data.

The bathymetric time series were needed to assess morphological changes from 2D-depth profiles and 3D visualisation (for example between ebb and flood tidal phases). The vertical accuracy (at a 95% confidence level from descriptive statistics of the conducted measurements) of the EM3002D is ±4 cm, similarly to the value reported in [63] and compliant with the accuracy obtained by the Continental Shelf Service of Belgium conducting periodically repeated measurements over a lock situated in the harbour of Zeebrugge and where the absolute depth is known. The vertical accuracy for the EM2040D data is yet not determined. Its IHO confidence interval ([64]) is around ±15 cm, which is too large to account for decimetric vertical changes. A 1-m pixel horizontal resolution was chosen as a good balance between the size of the insonified area at nadir and that insonified at shallow grazing angles.

**Table 4.** Backscatter processing steps after [30] for the AR time-series dataset (*SonarScope*© processing).

| | |
|---|---|
| 1. | Correction for sound absorption based on surface seawater properties (from the RV Belgica On-board Data Acquisition System—https://odnature.naturalsciences.be/belgica/en/odas) |
| 2. | Correction of the instantaneous insonified area using the real incidence angle as from the tide-corrected terrain model of the study site: the bathymetric surfaces are used to correctly allocate the backscatter snippet traces from single pings to their true seabed position. |
| 3. | Removal of all angle-dependent corrections introduced by the manufacturer (e.g., the Lambert and specular corrections in Kongsberg Maritime MBES data). |
| 4. | Per ROI: Computation of AR curves. |

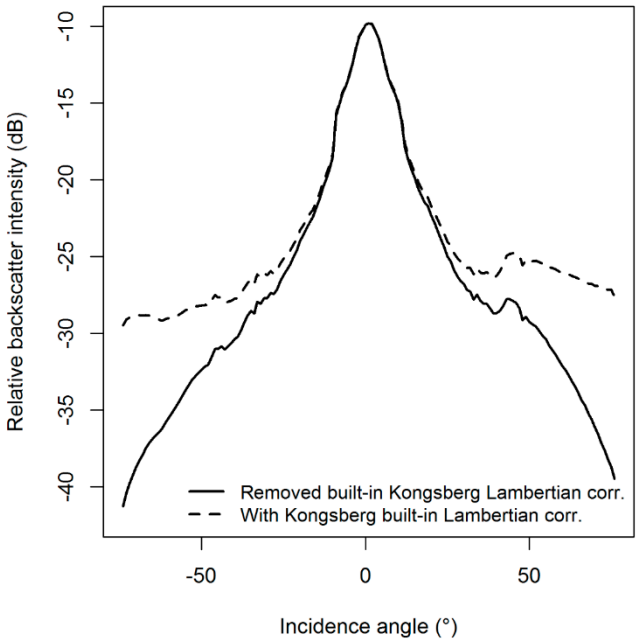


**Figure 4.** Illustration of the difference between angular response curves provided by the Kongsberg manufacturer after correction in *SonarScope*© to remove the specular correction (dashed line, applied by default in *SonarScope*© processing routine) and the Lambertian correction (solid line, backscatter status 1 in *SonarScope*©). The solid line is the type of angular response data used in the present investigation and is believed to be the best estimate of the raw intrinsic seafloor backscatter response. The type of BS data output particularly suits the study of variability (i.e., relying on an artefact- and bias-free dataset) since the built-in specular-adaptive and Lambertian corrections are computed on a ping-to-ping basis, hence possibly introducing biases due to the local seafloor configuration.

### *2.4. Transmission Losses*

Different mechanisms beyond the inherent geometrical (spherical) spreading of the sound wave control the attenuation during the propagation in seawater and can be responsible for unwanted signal fluctuations and degradation of the signal-to-noise ratio [12]. Retrieval of the correct target backscatter strength must account on the dissipative nature of the seawater medium absorbing part of the acoustic energy via chemical reactions, viscosity and scattering [12]. Overall, attenuation losses (i.e., accounted by empirically derived absorption coefficients within the 2TL term of the sonar equation) result from the contributions of: (1) absorption in clear seawater ($\alpha_w$) *sensu* [40,41] and (2) viscous absorption ($\alpha_v$, [65]) and (3) scattering due to the presence of suspended particulate matter ($\alpha_s$, [43,66]).

The uncertainty introduced by the attenuation of sound (in dB/km) in seawater only was estimated for each experiment for nadir (0°), oblique (45°) and fall-off angular regions (70°). For the second experiment, the absorption model by [40,41] was applied to the set of water-column profiles ($n$ = 10) obtained by the CTD frame down-casts; for the two other experiments, only surface values of absorption coefficient were considered.

Using the modelling approach in [43,66], sound absorption due to presence of suspended sediment (that due to combined viscosity and scattering) was estimated for the second and third experiments based on the available data (the routine was implemented in MATLAB©). For the second experiment, this uncertainty was estimated for the 1-m profile above the seafloor using the vertically averaged ABS-derived SPMc and median particle size (D50) for the duration of the experiment.

Additionally, uncertainty was estimated along the quasi-continuous sediment profile (~15 m depth) that was reconstructed combining observations from the various sensors (i.e., filtrations from the Niskin samples and the benthic lander mounted OBS and ABS sensors). The profile was reconstructed, and assumptions were made to represent a worst-case scenario, thereby selecting the data from the moments of maximal volume concentration. As such, the profile relates to 0.05 g/L from surface to 3 mab, 0.1 g/L from 3 to 0.5 mab and 0.3 g/L from 0.5 to seafloor. To appraise the effect of particle size, the D50 of the lower part of the profile was altered from 100 to 400 µm (reflecting the sand particles potentially resuspended in the near-bed of this area during spring tide). Despite a lack of data necessary to carry out a similar analysis in the third experiment, the available OBS-derived SPMc time series were coupled to the MBES BS by means of correlation analysis and further descriptive plots to observe relationships. Nonetheless, similarly to the second experiment, the effect over the full water depth was estimated by reconstructing a quasi-continuous sediment profile based on values of volume concentration from the OBS chain and using a fixed D50 of 63 µm (representative of suspended mud particles, characterising the turbidity of this area). Peak concentration values where selected here too, leading to a reconstructed profile of 0.2 g/L from surface to 2.5 mab, 1 g/L from 2.5 to 0.5 mab and 2 g/L for the lowest 0.5 mab. The effect of particle size was investigated here too, changing the D50 of the lowest part of the profile from 63 to 125 µm (approximating to the fine sand observed in the grab samples). For both cases, the transmission losses due to this factor are presented for nadir (0°), oblique (45°) and fall-off angular regions (70°) and for the described profile arrangements (overall 4 for the second experiment and 2 for the third one).

## 3. Results

### 3.1. Results Display

This section presents the results of the three experiments. First, the spatial context is provided through gridded backscatter and bathymetry data products. Next, a synthesis is given on the short-term variability in the backscatter time series. Interpretation of the results is helped by the ground-truth data collected for experiments II and III: for the second experiment, the benthic lander data were summarized and used to produce a set of correlations between backscatter and variables; for the third experiment, interpretation of the BS spatio-temporal behaviour is supported by a Reineck-box core time series, the SPMc obtained by the OBS chain ($n$ = 3, at: 0.3, 1 and 2.4 mab) on the benthic lander, the bathymetric uncertainty metrics and the full-coverage surveys acquired. For each experiment, results relating to the transmission losses are presented in a separate section.

#### 3.1.1. Offshore Gravelly Area—Kwinte Swale

Figure 5A,D shows details of the bathymetry and the backscatter, respectively, for the Kwinte swale area. Sampling stations are also shown in this image (yellow circles). The sediment of this area is medium sand with gravel and bioclastic detritus and the seafloor presents a hummocky/hillocky terrain typical of predominantly gravelly and shelly substrates of gullies (thalwegs) found in between the sandbanks of the BPNS. These substrate features were observable from the video imagery to be homogeneously distributed (with sporadic occurrence of boulders). The backscatter image for this area (Figure 5D) is moderately uniform and presents a relatively high reflectivity throughout. The patterns observable relate to the tidal-ellipse orientation (SW-NE) that follows the main axis of the gully within which the site is situated [67].

The results of repeated MBES data acquisition in this area are shown in Figure 6 (first column). The AR and boxplot time-series plots (Figure 6A,D) denote the high stability of the sediment backscatter in the area over the duration of the tidal cycle. No trend is detectable. The interquartile range is about 2 dB, indicating a high homogeneity. The consistency of the time series (Figure 6A,G) indicates that the short-term backscatter variability remains <0.5 dB across all incidence angles, except for the specular angular region (0°–18°) where the backscatter variability reaches up to ~2 dB. This behaviour is likely explained by a dependence related to the oscillations of micro-ripples (polarization under hydrodynamic forcing) which are beyond the imaging capability of the MBES spatial resolution. Figure 6J illustrates this behaviour as the AR curves at peak ebb and flood diverge more importantly in the specular angular region but converge above 25°. Interestingly, since the variability in the specular region is limited to an angle around 18°, it does not affect the mosaic production in *FMGT Geocoder* engine, which compensates the data based on an angular interval ranging from 30° to 60°. Small depth differences (Figure 6M) remain within the vertical accuracy of the soundings, with only slight differences in profile indentation: this is likely indicative of a polarization (and/or geometrical reorganization) of the micro-roughness under the effect of bottom currents.

#### 3.1.2. Nearshore Sandy Area—Westdiep Swale

Bathymetry and backscatter maps for this area are presented in Figure 5B,E, respectively. The backscatter is relatively homogeneous, although a detailed inspection of the ROI indicates slight variations in backscatter values (~3 dB) between troughs and crests of the mega ripples. This may be indicative of variations in sediment type (granulometric differences) leading to finer fractions in the troughs and coarser ones on the crests and slopes. Figure 8 shows the inverse trend between depth and reflectivity profiles within this ROI. The mega ripples are flood-dominated and are oriented perpendicular to the coastline. In terms of substrate and morphology, this study area can be divided into two distinct sub-areas: the northernmost part (within which the ROI is situated), composed of well- to moderately sorted fine to medium sand and characterized by flood-dominated mega ripples ($\lambda$ = ~20 m, $H$ = ~0.8 m—see Figure 6N) and the southern part (moving coastward), where ripples become progressively smaller ($\lambda$ = ~13 m, $H$ = ~0.3 m) evolving into a very flat (<1°) area, mostly composed of well-sorted medium to coarse sand. While some biological content was present in the northernmost grab samples, considerable amounts of benthic biota were present in the remaining samples. Benthic flatfish, bivalves (*Macoma baltica, Linnaeus 1758*) and abundant (>10 per sample) echinoderms (*Echinocardium cordatum, Pennant 1777)* and brittle stars (*Ophiura* sp) were predominant. High bioturbation characterizes this area which may lead to important modifications of the water-sediment interface over short temporal scales.

The 13-h time series for this site is presented in Figure 6 (second column). In contrast to the very stable Kwinte swale study site, the AR time series for the Westdiep (Figure 6B,H) present very high variability throughout all angles, reaching >3 dB for the entire angular sector ($BS_{0–73°}$) and >2 dB in the oblique sector ($BS_{30–50°}$; Figure 6H). The trend observed in BS (Figure 6E) partly follows the oscillation of the tidal level with a significant and progressive (starting from $T_8$, ~15:00) decrease in mean BS during the ebbing phase of the cycle. During both flood events values remain stable and fluctuate within a $\pm$1 dB range. While the backscatter dependence due to survey azimuth was counteracted by the mono-directional survey strategy, a strong dependence to morphology is observable in this study area and is confirmed by 3D visualization of the mega ripples (Figures 7 and 8). A pattern of ripple-cap inversion between flood and ebb tide flows is observed (Figure 6N), leading to build-up of finer material on the stoss side of the ripples (note the red dashed line in Figure 7, right). This is visible in Figure 6N where the ebb-phase profile shows an accretion (denoted by the white space between the vertical accuracy envelopes) of ~6 cm.

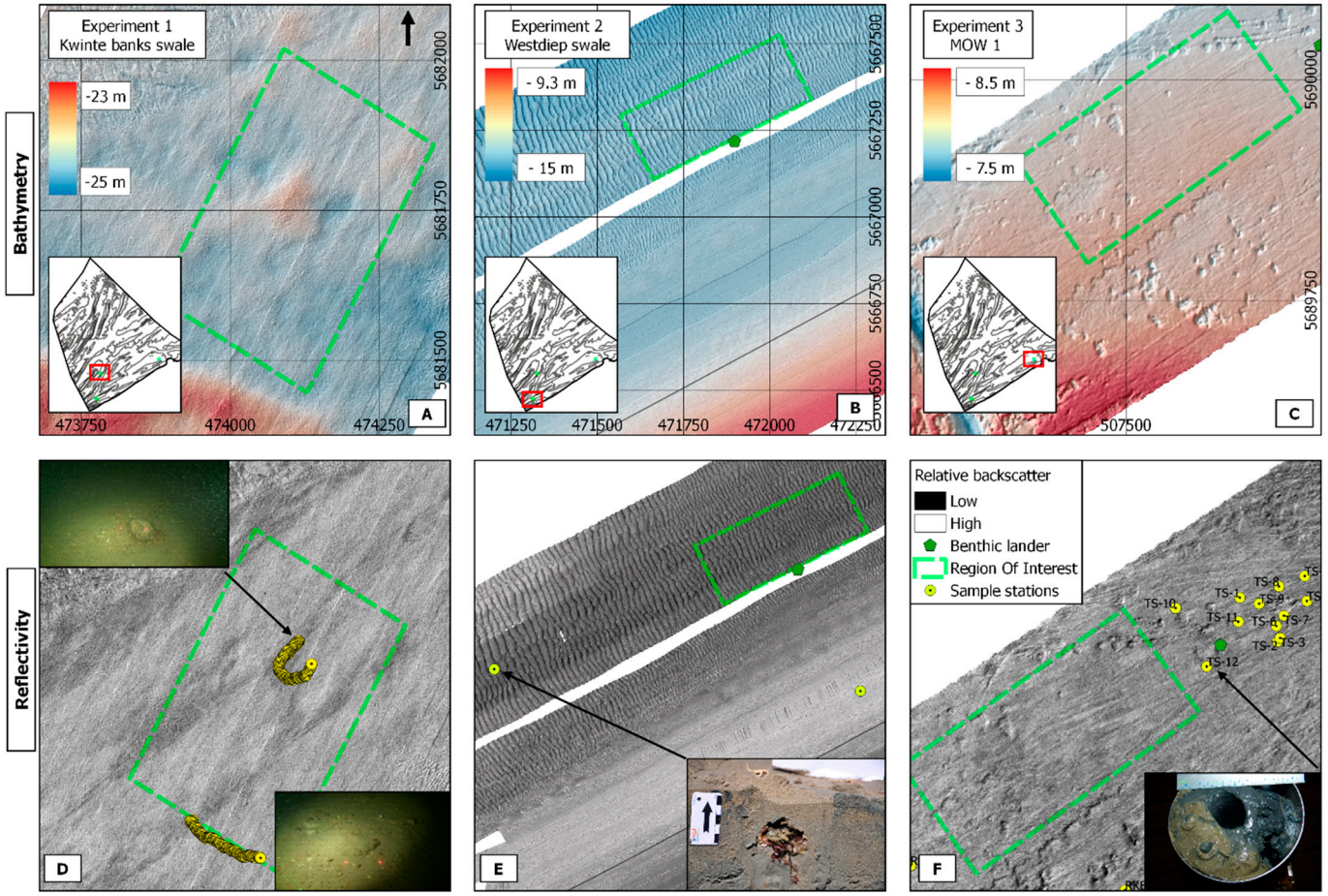


**Figure 5.** Details of the bathymetry (**A**–**C**) and reflectivity maps (**D**–**F**) for each study area. For experiments II (**B**–**E**) and III (**C**–**F**), the location of the benthic lander, equipped with various oceanographic sensors, is denoted by a dark-green pentagon. Ground-truth stations are denoted by yellow circles, whereas the ROIs are denoted by green dashed-line polygons. Photographic details of the substrate types are also shown: for the Kwinte swale area images (**D**), the laser points are 9 cm apart (Courtesy of A. Norro, Royal Belgian Institute of Natural Sciences). Severe modification of the seabed by bottom trawling gears is noticeable at the MOW 1 study site (**C**,**F**): patterns of substrate erosion (elliptical depressions of ~10 to 30 cm in depth and up to 15 m in diameter) occur in the immediate proximity of the trawl marks.

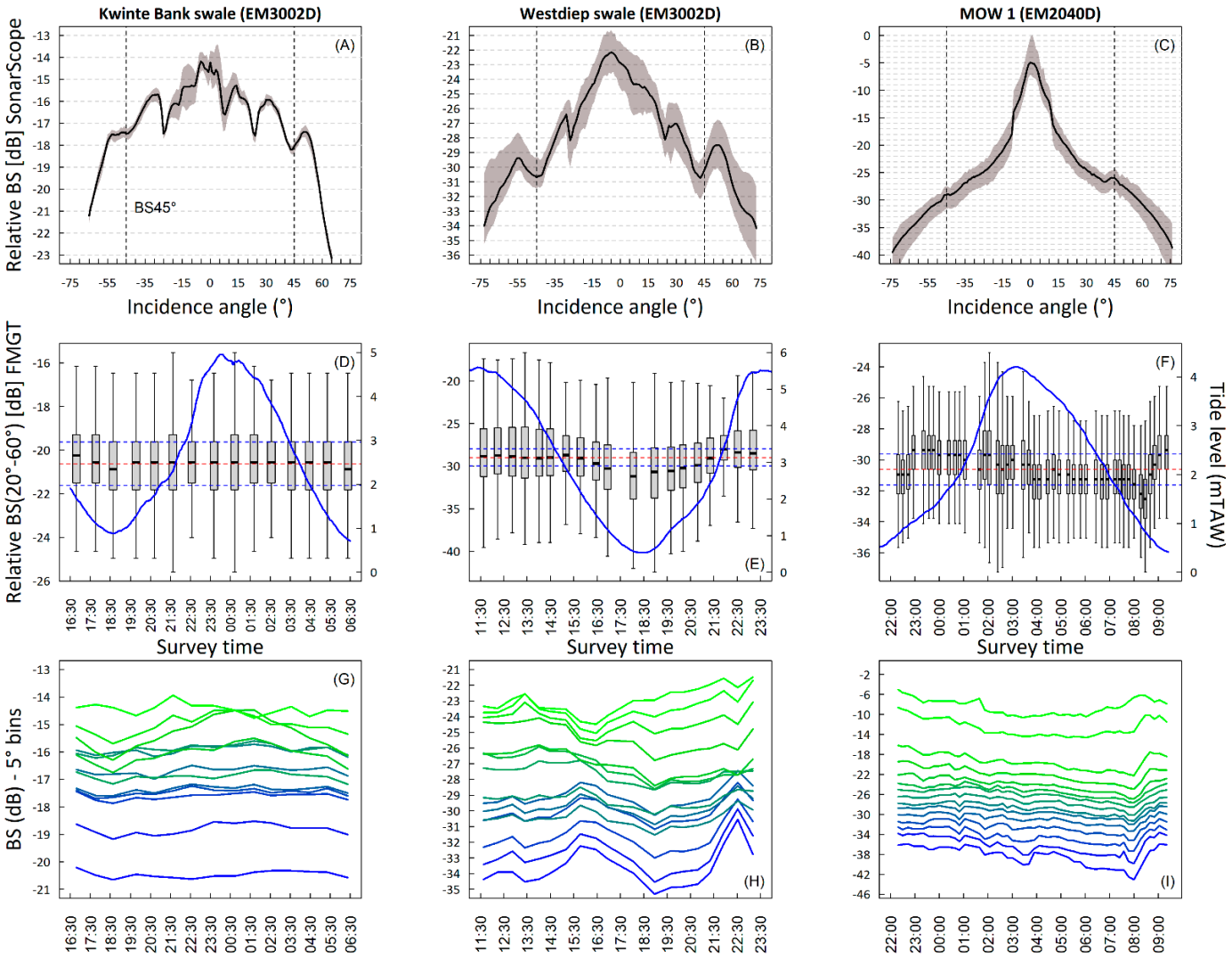


**Figure 6.** *Cont.*

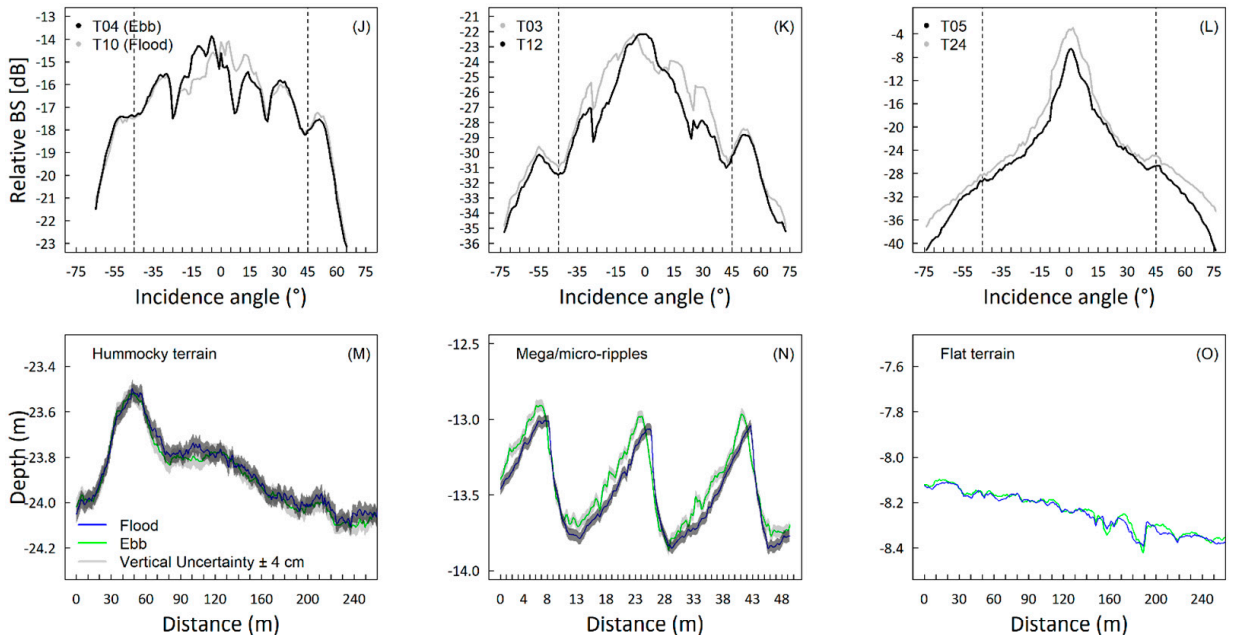


**Figure 6.** Synthesis of the backscatter time series acquired for each experiment. The first plot (**A**–**C**) is the envelope of variability (grey shading) around the average AR (black line) of the full AR BS time series, extracted from the defined ROIs. It describes the variability of backscatter intensity per angle of incidence over the duration of the experiments. The envelope is computed from $n$ = 15, 19 and 47 MBES passes respectively for the 1st, 2nd and 3rd experiment. The processing scheme code for the AR BS dataset is "A4 B1, C2 D1 E5 F3 G2 H3 I0 J0 H2" using the nomenclature proposed in [11]. The second plot (**D**–**F**) is the same time series (though derived from the BS mosaics produced in *FMGT*; $BS_{30\text{-}60^\circ\ @\ 300\ kHz}$) but visualized as boxplots of relative BS (values across the full incidence angle) against the time of acquisition (mean surveying time within the ROI). The overall mean over the full time series, together with the ±1 dB Kongsberg sensitivity threshold [66], are respectively shown as red and blue dashed lines. The tidal level is superimposed to assess a prospective BS trend in respect to the tidal oscillation and its phases. In the boxplots, lower and upper box boundaries are the 25th and 75th percentile respectively, the black central bar the median, whiskers denote the full extent of the data (i.e., min/max). The processing scheme code for the mosaicked BS dataset is "A4 B0 C0 D0 E5 F0" using the nomenclature proposed in [11]. The third plot (**G**,**H**) is the time evolution of the relative BS for areas insonified within a same envelope of incidence angle at a 5° resolution. This provides a more detailed depiction of the variability as a function of the incidence angle, to observe if smaller angular sectors would be less affected by the processes driving the variability. In (**G**,**H**), the blue to green palette represents angular intervals from the fall-off to the specular region in steps of 5°, leading to approximately 15 sub-sectors per experiment. The fourth plot (**J**–**L**) displays the AR curves at the peak flood and ebb tidal phases (the legend mentions the corresponding survey time) during the experiments and is used to establish the presence of roughness-polarization dependence (as proposed in [27,36]). The fifth plot (**M**–**O**) displays bathymetric profiles extracted at nadir within the ROIs at the same peak flood and ebb tidal moments as the previous plot (**J**–**L**). For the Kwinte swale and Westdiep experiments, using the EM3002D echosounder, the ±4 cm vertical accuracy interval is displayed as a grey/transparent envelope.

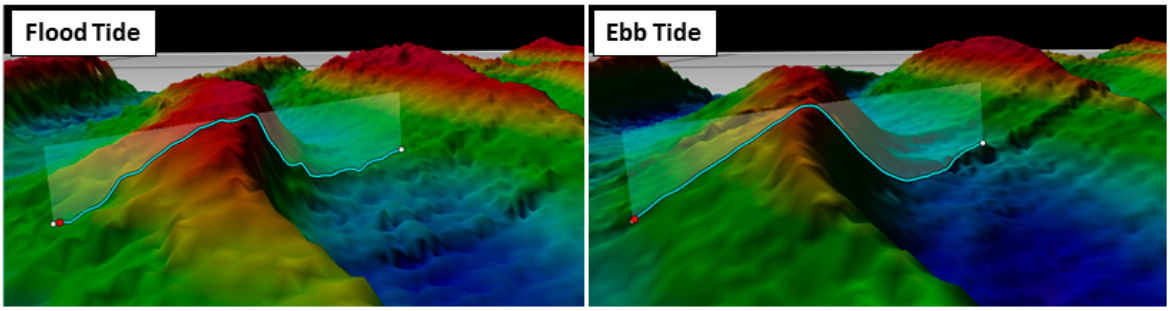


**Figure 7.** 3D models of a mega ripple found within the ROI of the Westdiep experiment (central ripple in Figure 6N; same peak flood and ebb times as in Figure 6K). Vertical exaggeration = 6×. To verify the consistency of this pattern over the entire study area, profiles were extracted from the full transect; different sub-areas of the entire transect and at different angles i.e., nadir, oblique and fall-off angular regions of the swathe (not shown).

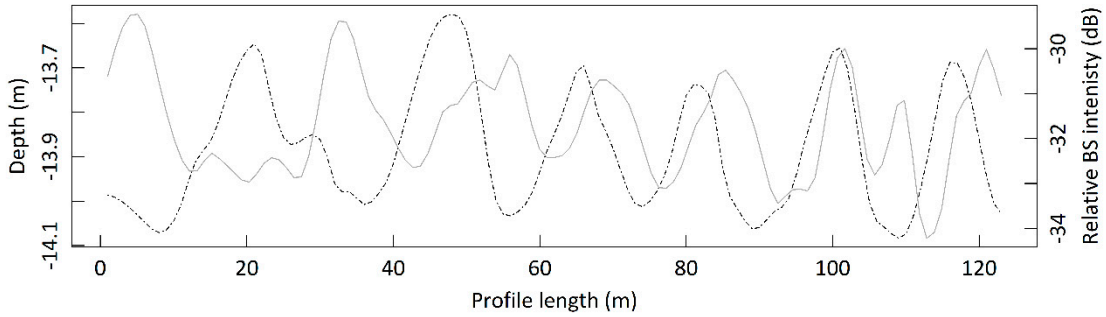


**Figure 8.** 2D profiles of bathymetry and backscatter extracted from 1-m horizontal resolution raster data within the ROI (Experiment II, Westdiep swale). Dotted line is depth, whereas the solid grey line is backscatter. Note the quasi-continuous reverse trend in the two profiles. A ~3 dB difference between troughs (lower BS ~ −33 dB) and crests (higher BS ~ −30 dB) suggesting the presence of different granulometries characterizing the ripples.

For this experiment, several physical processes were captured by the oceanographic sensors mounted on the benthic lander (Figure 9). They provide ground-truth information to understand the dynamics during the experiment and possibly to explain the observed patterns in the MBES-BS data. Non-parametric correlation coefficients obtained by the Spearman $\rho$ rank method are presented in Table 5. While correlation may not directly imply causation, it might be indicative of the processes that drive the variability of the MBES BS at the study site in association to the hydrodynamic forcing. First, significant correlations between the mean MBES-BS, tidal level ($\rho = -0.56$, $p < 0.05$) and the current speed ($\rho = 0.59$, $p = < 0.01$) were found, suggesting that hydrodynamic-related processes played a role in the MBES-BS signal fluctuation. Significant correlations with SPMc at ~2.4 mab (from OBS and LISST sensors; $\rho = -0.66$, $p \leq 0.01$ and $\rho = 0.84$, $p \leq 0.0001$ respectively) were also detected. SPMc was however insufficient to explain the presence of a significant (i.e., >1 dB) absorption event and these correlations are likely indicative of a similarly fluctuating behaviour of the variables. Continuing, the vertical current velocity (in the $z$ axis measured at 0.2 mab) and the alongshore current vector were also significantly correlated with the mean MBES BS with $\rho = 0.75$, $p = < 0.001$ and $\rho = 0.58$, $p = < 0.01$, respectively. This could be explained by the influence of the alongshore hydrodynamic forcing (the cross-shore correlation was weak and not significant) on the sand transport at the boundary layer, modifying the geometry of the bedforms and thus the resulting mean backscatter. Seabed altimetry (measured by the ADV sensor at 0.2 mab) correlated with $\rho = 0.54$, $p = < 0.05$.

**Table 5.** Correlation matrix obtained by the Spearman rank method (lower triangle shown). Significance levels of the correlations are denoted by asterisks: Legend of the significance in the bottom row of the table. Values in italic = > 0.7.

| Variable/Spearman rho | Mean MBES BS |
|---|---|
| Tide level | −0.56 * |
| Curr. speed | 0.59 ** |
| ABS D50 (1 mab) | 0.24 |
| ABS SPM (1 mab) | −0.38 |
| OBS SPM (2.4 mab) | −0.66 ** |
| LISST Trans. (2.4 mab) | 0.84 **** |
| ADV curr. (Z) | 0.75 *** |
| ADV curr. cross-shore | −0.2 |
| ADV curr. alongshore | 0.58 ** |
| ADV altimetry | 0.54 * |

* Significance: $p < 0.0001$ '****'; $p < 0.001$ '***', $p < 0.01$ '**', $p < 0.05$ '*'.

The tide-level trend over the duration of the experiment is reported in Figure 9A, along with its corresponding current velocity. In this area, the amplitude of the spring tidal range is around 5.42 m with both ebb- and flood-peak tidal phases having velocities greater than 0.4 m/s, which can resuspend material [68]. Van Lancker [47] estimated the median particle size able to be resuspended and transported by subtidal alongshore flood and ebb currents in this area being respectively 420 µm (medium sand) and 177 µm (fine sand) under the spring tidal regime. The NE-directed alongshore current vector (Figure 9B) is the dominant component of the flow in this study and is the main driver of sediment mobility and geometrical reorganization of the micro-roughness. This is illustrated by the tidal ellipse (Figure 9C), which presents a SW-NE elongated shape. The vertically averaged ABS SPMc (for the 1 mab profile; Figure 9D) is in close agreement with the tidal level where highest concentrations are observable during both flood tide events (Figure 9A) reaching peak current velocities of up to 0.6 m/s in the alongshore direction (Figure 9B). Potential of deposition/erosion events during the experiment may be assessed by the combined observation of the D50 vectors (from LISST and ABS—Figure 9F,G respectively), seabed altimetry (Figure 9H), and the alongshore current (Figure 9B). During the first slack water window (around 16:00), larger median grain sizes in the suspended sediment are detected reaching ~160 µm and 220 µm, respectively, for ABS and LISST sensors (Figure 9F,G). In the following ebb phase (~19:00), under a significantly weaker alongshore ebb current velocity of about 0.2 m/s, the suspended finer matter may aggregate, sink and settle to the bottom, remaining trapped until the next flood phase (particularly considering the flood-dominated orientation of the study area and the steep lee side of the mega ripples), leading to a ~2 cm difference in seabed altimetry (Figure 9H) and a slight increase in turbidity during the ebb tide (note the OBS SPMc peak around 19:00 in Figure 9E). While this study site is situated beyond the far-field of the turbidity maximum zone, pre- and in-survey meteorological conditions induced a rather turbid ebb flow compared to the flood-incoming water masses (observations based on time series of satellite derived total suspended matter: not shown here). This may possibly introduce fine matter residue into the sandy system [48]. Nevertheless, Figure 9I indicates that throughout the experiment, the water column at ~3 mab (and presumably above this level and up to the surface) was very clear with maximal SPMc of ~0.05 g/L.

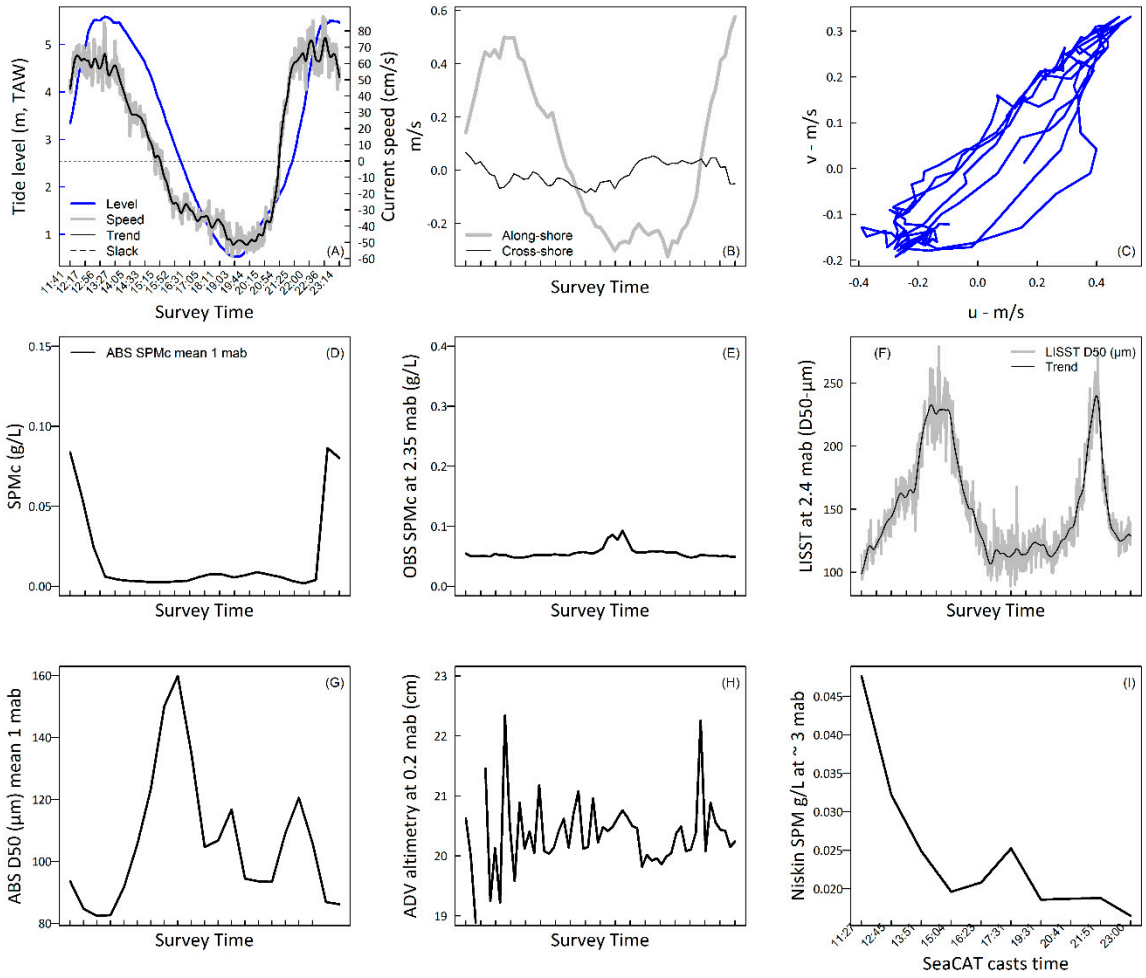


**Figure 9.** Synthesis of the benthic lander dataset of the Westdiep area (second experiment). (**A**) Tidal level with current speed. Slack water indicated by the horizontal dashed line. The trend of the current speed is achieved by fitting of a cubic smoothing spline function: (**B**) Current speed in along- and cross-shore directions; (**C**) Tidal ellipse for the duration of the experiment; (**D**) Vertically averaged SPMc for the 1 mab, as detected by the ABS sensor; (**E**) Same as (**D**), but detected by an OBS installed at 2.35 mab; (**F**) Median particle diameter (D50) detected by the LISST at 2.35 m; trend obtained as in (**A**); (**G**) Vertically averaged D50 as in (**D**); (**H**) Seabed altimetry from an ADV sensor at 0.2 mab; (**I**) SPM ~3 mab, obtained from the water filtrations of the CTD-installed Niskin bottle.

### 3.1.3. Nearshore Muddy Area—Zeebrugge, MOW 1

Bathymetry and backscatter maps for this area are presented in Figure 5C,E, respectively. The substrate type here is muddy sand with the sand part being <200 µm (fine sand). The bathymetry is very flat with <30 cm depth difference within the ROI (Figure 6O). Both in the backscatter and bathymetry images there is evidence of bottom trawling, resulting in regularly spaced striped depressions all over the area. In the immediate proximity of these trawl marks, erosional features appear as relatively small (5 to 15 m in diameter and ~30 cm in depth) concentric/elliptical scours, corresponding to patches of substrate being eroded and washed from the bed likely as a direct consequence of fishing gears' passage enhanced by local hydrodynamic forcing.

The 13-h backscatter time series for this area is presented in Figure 6 (third row). Similarly to the Westdiep site (2nd experiment), the average backscatter fluctuates significantly beyond the ±1 dB sensitivity threshold and a trend consistent to the tidal oscillation is observable (Figure 6F). This study area reaches the highest level of variability: the envelope of variation exceeds 4 dB at 45° and respectively 5 and 7 dB in the specular and fall-off regions (Figure 6C,I). Higher BS averages

occur around the end of the first ebb (~23:00–00:00) and around peak time of the second ebb phase (09:00—interestingly this occurs in concurrence to the higher percentages of sand fraction in the Reineck samples shown in Figure 10A and the strongest ebb current >0.5 m/s). Lower BS averages occur noticeably during the second ebb tide phase, at around slack water time (~08:00).

The interquartile range of the backscatter is about 2 dB (Figure 6F). Comparing angular responses from peak ebb and flood tidal moments (Figure 6L), no azimuthal dependence is detected (no changes in shape) confirming the absence of organized roughness in this flat area (see the 2D profiles in Figure 6O). Despite the shape of the curve remaining unaltered between ebb and flood, differences >2 dB are observable across the full angular range (i.e., a general decrease in reflectivity; Figure 6L), suggesting the transition of this seafloor patch to different states during different phases of the tidal cycle. A set of ground-truth data is presented in Figure 10 to help interpreting the MBES-BS time series. Figure 10A shows the fine sand ($\leq$ 200 μm) and mud ($\leq$ 63 μm) fractions from the first centimetre of the time series of sliced Reineck box core samples (12 samples, 1 approx. every hour). The tide level (blue line) is superimposed together with the corresponding current velocity (black line—from an ADP sensor). During the two ebb-tide phases, prior to slack water, the sand fraction in the samples is globally more important than during the flood tide where, in concurrence to a decrease in current velocity, samples are dominated by mud (up to ~75% content).

Figure 10B shows the bi-temporal image differencing change detection between maps of 21 and 24 November 2017 (pre- and post-experiment) summarized into 3 categories of *persistence* and *from-to* transitions between mud and sand fractions. While persistence is the dominant component of the change, the sand-to-mud change is observable at the central part of the study area where it forms an elongated pattern (where the bathymetry presents a slight channeling depression compared to the surrounding). The mud-to-sand pattern appears as more randomly distributed, forming patch-like features.

In Figure 10C, SPMc from the OBS chain, and the mean MBES BS and QF of the ROI are displayed. Again, the MBES BS acquires a most absorbing character when the SPMc reaches its maximum (around 08:00; ~2.8 g/L at 0.3 mab, 1.3 g/L at 1 mab and ~1 g/L at 2.4 mab) and reversely. The relationship between the mean MBES BS and the near-bed SPMc can be captured by a least-square linear regression ($R^2$ = 0.47, $p < 0.01$) that is significant, as well as by the Spearman correlation coefficients (Table 6). Visualization of these data (Figure 10C) indicates that the least accurate sonar bottom detections (red line) occurred concurrent to the highest SPMc (particularly at 0.3 mab), resulting in the lowest BS averages. Oppositely, during the flood phase of the tide (~T13 to T18—01:00–03:00) the accuracy of the bottom detection increases with decreasing SPMc. This suggests the presence of a dynamic high-concentrated mud suspension (HCMS). Once settled, this could increase the volume of the water-sediment interface (forming a "fluffy" layer which increases the burial volume of the seafloor surface) to which the registration of bottom detection and echo intensity are sensitive to. As such, under this configuration, the active seafloor target considered in bottom detection will change from an extended surface (i.e., the relatively "clean" seafloor surface), to a volume cell (i.e., a "slice" or a truncated prism) populated by point-scatterers, which may raise or attenuate the BS level [12]. The behaviour of this HCMS layer appears as the dominant driver of variability of the MBES-BS time series of this area, leading to short-term and progressive changes in scattering mechanisms (i.e., from a relatively "clean" surface with >50% of sand to a relatively "chaotic" mixed sediment interface topped by a ~30 cm deposition of fluffy material).

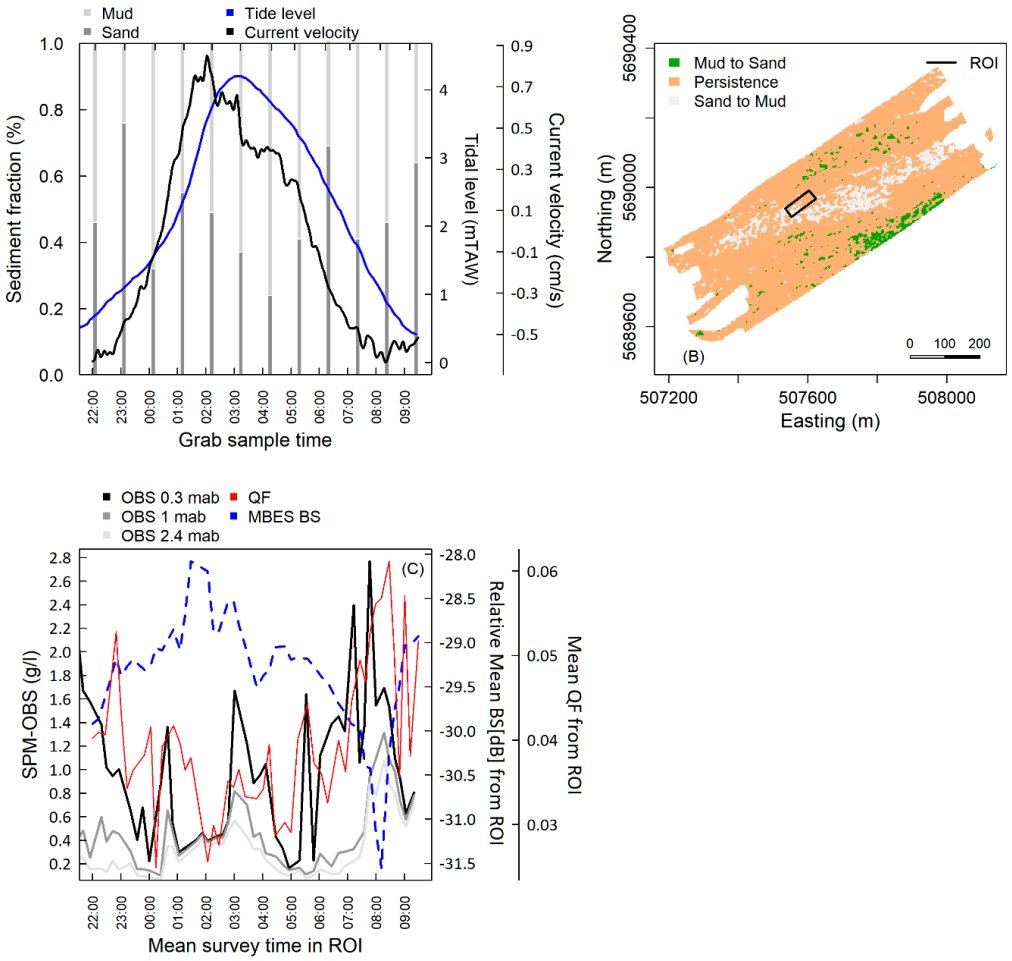


**Figure 10.** (**A**—top left quadrant) Variation in particle size of the first centimetre of the Reineck box-cores time series ($n$ = 12, collected approximately every hour—the above $x$ axis indicates their real position in respect to the tidal cycle), together with the tidal level and the current velocity (respectively blue and black lines, right axis); (**B**) Bi-temporal image differencing (algebraic) change detection between maps of 21st and 24th November 2017 (pre- and post-experiment) summarized into 3 categories of *persistence* and *from-to* transitions. *Green*: Mud to Sand transition; *Orange*: Persistence; and *Grey*: Sand to mud. *Black rectangle*: the ROI; (**C**) SPMc derived from the OBS sensors chain (*continuous lines, left axis*), mean MBES BS from the ROI (*dashed blue line, right axis*) and mean Kongsberg QF (*continuous red line*).

**Table 6.** Correlation matrix obtained by the Spearman rank method (lower triangle shown). Significance levels of the correlations are denoted by asterisks: Legend of the significance in the bottom row of the table.

| Variable/Spearman Rho | Mean MBES BS |
|---|---|
| Mean Kongsberg QF | −0.61 **** |
| OBS SPMc 0.3 mab | −0.69 **** |
| OBS SPMc 1 mab | −0.40 ** |
| OBS SPMc 2.4 mab | −0.35 * |

* Significance: $p < 0.0001$ '****'; $p < 0.001$ '***', $p < 0.01$ '**', $p < 0.05$ '*'.

### 3.2. Transmission Losses

In this section, transmission losses during the experiments are evaluated. The variability of the seawater absorption coefficient [40,41] was computed based on surface temperature and salinity from SBE 21 SeaCAT Thermosalinograph values stored in ODAS (On Board Data Acquisition System; *R/V Belgica*) and from SBE 21 SeaCAT Thermosalinograph and SBE 38 Sea-Bird Digital Oceanographic

Thermometer values stored in MIDAS (Marine Information and Data Acquisition System; *R/V Simon Stevin*) systems. The echo level uncertainty (in dB) was estimated for the average depths of the study sites and for different slant ranges corresponding to nadir (0°), oblique (45°) and grazing (70°) angles (see Table 7). The uncertainty magnitudes resulted as *negligible* (N) for beams at nadir and *small to negligible* (S-N) for beams at 45° and 70° (according to the nomenclature proposed in [69]).

**Table 7.** Table reporting the estimated uncertainty introduced by the seawater absorption coefficient (*sensu* [40,41]) for each experiment and for nadir (0°), oblique (45°) and grazing (70°) angles. This uncertainty estimate was accounted for during acquisition.

| Experiment | Overall $\alpha_W$ Error (dB/km) | Depth (m) | 0° (dB) | 45° (dB) | 70° (dB) | Uncertainty Score * |
|---|---|---|---|---|---|---|
| Kwinte swale | 2 | 30 | 0.11 | 0.17 | 0.35 | S |
| Westdiep swale | 2 | 20 | 0.08 | 0.11 | 0.23 | N-S |
| Zeebrugge MOW 1 | 1 | 10 | 0.02 | 0.028 | 0.05 | N |

* N = Negligible (0.01–0.1 dB), S = Small (0.1–1 dB), M = Moderate (1–3 dB), H = High (3–6 dB), P = Prohibitive (>6 dB). Uncertainty score nomenclature after [68].

For the second experiment (Westdiep area), a set of CTD down-casts allowed investigating in more detail the absorption variability over the water-column profile. Figure 11A–D shows the vertical variability of temperature, salinity, sounds speed and $\alpha_w$ for one CTD down-cast: the variability of these measures is within the instrumental error of the sensors, indicating the high homogeneity of the water column. Figure 11E shows the mean values of the vertically averaged absorption coefficients for each of the 10 CTD casts, individually displayed in Figure 11F. In this environmental setting, the stability of the vertical profiles justifies the use of surface values to correct for absorption during data acquisition.

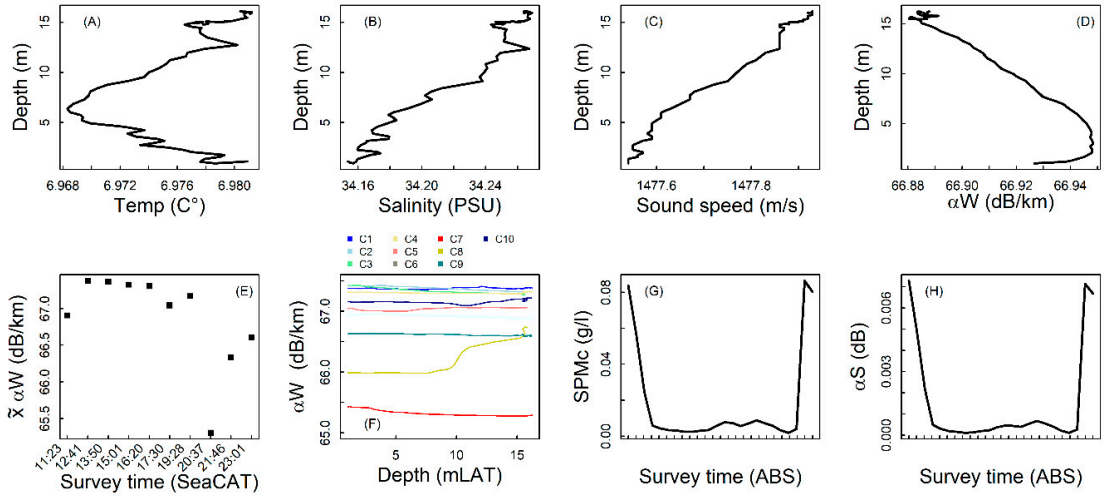


**Figure 11.** Temperature (**A**), salinity (**B**), sound speed (**C**), and absorption coefficient (at 300 kHz) due to seawater (**D**) over depth for one CTD downcast (~15 m). Vertically averaged (**E**) and full profiles (**F**) of $\alpha_w$ coefficients. (**G**) Averaged SPMc (g/L) for the 1 m profile above seabed as obtained by the ABS sensor installed on the benthic lander. (**H**) Absorption due to suspended sediment ($\alpha_s$) for the 1-m profile above seabed computed as a function of vertically averaged SPMc in G and vertically averaged grain size (shown in Figure 7G).

For this second experiment, the SPMc and median grain size (D50) obtained from the ABS sensor (Figure 11G–H) allowed estimation of the transmission losses due to SPMc. Figure 11G reports the vertically averaged SPMc, and Figure 11H shows the dB loss for the 1-m profile. For this experiment and for such sound travel paths, fully negligible *(N)* influences of SPMc on the mean BS level are observed.

Nonetheless, to better appraise the uncertainty potentially introduced by this environmental factor, vertical sediment profiles (approximating to the full travel path of the acoustic signal and

defined in a conservative way maximizing the SPM impact) were reconstructed for the second and third experiments as specified in the "Materials and Methods" section. As in Table 7, Table 8 reports the estimated transmission losses for nadir (0°), oblique (45°) and fall-off slant ranges (70°).

**Table 8.** Table reporting the estimated uncertainty introduced by the suspended sediment absorption coefficient ($\alpha_s$ *sensu* [43,65]) for the 2nd and 3rd experiments and for nadir (0°), oblique (45°) and grazing (70°) angles. Out of the four and two profiles for the 2nd and 3rd experiments respectively, only the worse-case scenarios are shown.

| Experiment | Depth (m) | 0° (dB) | 45° (dB) | 70° (dB) | D50 Upper/Lower (μm) | Uncertainty Score |
|---|---|---|---|---|---|---|
| Westdiep swale | 15 | 0.13 | 0.18 | 0.38 | 100/100 | S |
| Zeebrugge MOW 1 | 10 | 0.35 | 0.48 | 1 | 63/125 | S |

Transmission losses due to suspended sediment remain small for both experiments and for the depths, concentrations and particle sizes assessed. Noticeably, for the second experiment in the sandy and clear-water area (Westdiep swale), losses due to seawater only and those due to suspended sediment show similar magnitudes and increasing the D50 in the lower part of the water-column causes little changes. Oppositely, for the third experiment in the maximal turbidity zone, the echo level attenuation increases significantly reaching up to ~0.5 and 1 dB at oblique and fall-off slant ranges respectively, showing slight increases with increasing particle size.

## 4. Discussion

Mapping for monitoring requires repeated measurements of the same seafloor areas over short-, medium- and long-term time scales (i.e., diel to decadal time scales). Three field experiments were conducted in the BPNS under spring tide regime to investigate the short-term effect of environmental sources of variance on the acoustic signature of predominantly gravelly (Kwinte swale), sandy (Westdiep swale) and muddy areas (Zeebrugge, MOW 1). These field studies were also aimed at appreciating the sensitivity of the MBES-measured BS to relatively subtle variations in the nature of the water-sediment interfaces at stake. The backscatter time series were analysed, and the signatures and trends were related to seabed physical properties measured in situ, using several approaches. The potential sources of short-term (half-diel) variability that were investigated relate to: roughness polarization and morphological changes, water-column processes (transmission losses due to seawater and suspended sediment), and surficial substrate changes.

### 4.1. Short-Term Backscatter Tidal Dependence

The MBES-measured BS variability and its causes differed considerably between the three investigated areas. Overall, the effect of water-column absorption variability (i.e., due to seawater only), was ubiquitously negligible to small; this was expected, given the shallow depths surveyed and the good instrumental control of the local seawater characteristics. The effect of suspended sediment on the transmission losses can be expected to cause little uncertainties in the sandy and gravelly areas outside the turbidity maximum zone in Belgian waters; it could, however, become moderate to prohibitive in deeper areas or in case of dense plumes of sediments in the water column related to human activities (dredging, trawling). In general, considering jointly the seasonal and spatial variations of SPMc in the BPNS [70], a maximal water depth of ~50 m over the region, and the preliminary observations from this investigation, it may be surmised that for the gravelly and sandy clear-water areas (offshore and in the SW nearshore areas), the effect of suspended sediment will always be small, since the highest volume concentrations are to be expected in the lowest layer of the water column, thus involving too short a sound travel path to significantly affect the echo level. Previous investigations on the effect of near-bed SPM on BS for the first study area can be found in [33,54] and actually reported negligible effects. On the contrary, in the nearshore zone with soft-material sediments and maximal

turbidity, significantly higher volume concentrations can be met even in the upper part of the water column, evidencing the importance of this SPM-caused attenuation even at very-shallow depths (10 m). Besides these environmental factors, the envelopes of variability were mainly driven by short-term successional changes of the underlying morphology and of the water-sediment interface physical status, thereby relating to actual changes in the targeted seafloor.

#### 4.1.1. Experiment 1—Offshore Gravel Area

Overall, the results pointed at the high stability (<0.5 dB excluding nadir beams in the angular range 0–18°) of the Kwinte gravel area. This was expected, given the known bathymetric and sedimentological spatio-temporal stability of this area [30]. This good stability is explained by year-round, well-stratified and clear water masses [71] and possibly by an overall stochastic re-organization of the substrate (i.e., geometric micro-changes of the sand and bioclastic material) configuration under the effect of currents which limits significant alterations of the interface backscatter. The backscatter AR was here a particularly useful measurement, not only to gain a physical understanding of the backscattering characteristics of the substrate type (the AR curves show three distinct shapes characteristic of each substrate type; see Figure 6A–C), but also to detect the presence of a weak azimuthal-like dependence thanks to the BS values measured in the steep-angle range (see [39]). This would have been impossible using solely backscatter mosaics, which by nature lack the angular component (as the change detection carried out in [72,73]). This shows that a compensation of mosaicked backscatter imagery using an angular interval in the range 30°–60° (as in e.g., *FMGT* standard processing) would omit the azimuthal dependence (which in this gravelly/hillocky terrain extended only up until 18°) while assessing changes of interest (i.e., sediment type at oblique angles) within such seafloor types.

#### 4.1.2. Experiment 2—Nearshore Sandy Area

The sandy area in the nearshore Westdiep swale showed significant variability (>2 dB at 45° and >3 dB over the full angular range) for the time assessed. Water-column processes here also had negligible impact. Here, most BS variability was best explained by azimuthal dependence, similarly to studies in other sandy/siliciclastic areas [28,39]. Ripple features are predominant in such areas [74] and, under the effect of both flood and ebb currents, a geometric reorganization of the morphology at various scales may occur. Wave-induced cross-shore currents, creating micro-ripples, may further contribute to MBES-BS variability; when these ripples are perpendicular to the sonar across-track acoustic line of sight, MBES-measured BS may be altered significantly (e.g., [37,38]). Besides the azimuthal dependence normally limited to steep angles [39], significant variability was also observed at angles beyond 40° (i.e., >2 dB at 45°), suggesting that some degree of sedimentary changes for the period assessed did occur. Similarly as in [75], ground-truth observations were indicative of changes at the interface that likely resulted from cyclicity in deposition/erosion events. The contribution of biological activity (i.e., bioturbation) was not quantified here but is also expected to increase the BS variability. Considerable amounts of biota were observed surrounding this study site, which aligns with previous studies [76,77]. Feeding and burrowing behaviour of certain benthic species can lead to drastic modifications of the sediment in terms of its geotechnical composition (e.g., permeability, porosity, compactness and roughness; [78]) and can therefore have large effects on the backscatter level by altering the average water-sediment impedance contrast. Furthermore, presence of individual species *per se* can act as surface scatterers: e.g., [16,79] related part of the high-reflectivity facies in their acoustic maps to the widespread presence of respectively the tubicolous polychaete *L. conchilega* and the brittle star *A. filiformis* modifying the micro-roughness as a function of their feeding behaviour (rising of tentacles in the water-column/boundary layer). Recently, laboratory tank-based experiments showed that in sandy sediments the effect of microphytobenthos photosynthetic activity can also introduce a variability of the backscattering properties of the inhabited marine sediment by as much as ~2.5 dB at 250 kHz and over a diel cycle [45]. This experiment demonstrates the necessity of jointly

analysing mosaicked and AR BS to avoid misinterpretations of the observed changes, particularly in sandy/siliciclastic areas such as on this Westdiep area. It is worth noting that this polarization effect may raise specific (and usually underestimated) challenges when merging surveys acquired in different orientations and it will have to be considered in the compilation of existing backscatter maps.

#### 4.1.3. Experiment 3—Nearshore Muddy Area

The MBES-BS dataset acquired near the Zeebrugge MOW 1 Pile area was by far the most variable, with a mean variability >4 dB at 45° and beyond for the remaining angular range. The variability was fully unrelated to the azimuthal dependence since the study area ground-truthing showed a levelled and relatively homogeneous terrain, lacking organized morphology. Our interpretation is rather that the variability related to a combination of the intrinsic dynamic nature of the boundary condition (creating a "fuzzy" boundary layer), to granulometric changes at the water-sediment interface (implying fluctuating fractions of sand and mud) and to a highly turbid water column. This very dynamic muddy/sandy substrate site is particularly complex from an acoustic perspective, since the sediment structure exhibits high vertical heterogeneity (i.e., an intricate layering of intercalated sediment matrix of sand and mud on anoxic mud, topped by depositions of up to 30 cm of fluffy material at specific tidal moments). This likely resulted in volumic contributions (i.e., subsurface sediment scattering) opposite to the other two experimental sites, where the impedance contrast of the water-sediment interface was significantly higher due to the presence of coarser substrates (i.e., gravel, shells and sandy-quartz sediments), and hence dominated the backscattering process. Significant acoustic penetration into the soft sandy sediments is expected to be about 2–3 cm at 300 kHz [80], increasing with softer, muddy and unconsolidated sediment as shown in this third experiment. The vertical complexity of the upper sediment layer in this area changes under the influence of the local hydrodynamic forcing that may modify at least the first 3 cm of the interface (observed from analysis of the Reineck box-core data; not shown here), as well as being subject to HCMS dynamics, that can add up to ~30 cm of fluffy material to the seafloor interface [49]. As such, different water-sediment interface configurations progressively occur during different phases of the tide and thus the echo contributions coming either from the upper layer (interface) or from the buried interface (subsurface) will together affect the bottom detection, yielding to shifts in the AR and mosaic values retrieved during the various instances. The accuracy of the bottom detection upon which depth registration relies obviously depends on how "clean" an interface is. To test this observation, the mean Kongsberg Quality Factor (QF) was processed within the ROI to complement the interpretation of the MBES-BS trend. Significant and interrelated associations were found between registered MBES BS, QF and SPMc at 0.3 mab, confirming the MBES-BS sensitivity to the boundary dynamics of this study site, as identified in [48,49]. Lastly, it should be noted that the presence of trawl marks in the ROI (see Figure 5C) may represent a further explanatory candidate of the backscatter variability. These morphological depressions would be prone to accumulation of fine material (e.g., particularly around slack tide), thereby changing the constituency of the sediment interface and influencing the BS response. The same is valid for the erosional elliptic depressions which cooccur with the trawl marks.

### *4.2. Recommendations on Future Experiments on MBES-BS Variability*

When tidal dynamicity and/or environment seasonality are expected to cause seafloor BS variability, field studies are recommended to evaluate the significance. While the instrumentation and set-up used in the present investigation proved highly valuable for targeting this aim, some improvements could be made. Hereafter, good practice is reiterated, and shortcomings flagged. Future solutions could come in from new instrumentation and/or methodological approaches. In any case, it is critical that the surveys are conducted under favourable hydro-meteorological conditions. Table 9 shows the motion sensor-related variables during the data logging. These are used as a form of quality control on the datasets.

**Table 9.** Motion sensor derived variables used as a form of quality control on the datasets. The sea state (using the World Meteorological Organization scale) is also reported Figures in degrees (°).

| | Mean Roll + Range | Mean Pitch + Range | Mean Heave + Range | Mean Heading + Range | Sea State * |
|---|---|---|---|---|---|
| **Exp. 1** | 0.6–0.5 | 0.3–0.24 | 0.006–0.03 | 204–12 | 2–0.1 to 0.5 m (Smooth wavelets) |
| **Exp. 2** | 0.8–1.16 | 2.9–0.12 | 0.3–0.06 | 67.4–4 | 2 to 3–0.1 to 1.25 m (Slight) |
| **Exp.3** | 3.2–0.65 | 1.2–0.22 | 0.007–0.08 | 60.6–12.3 | 1 to 2–0 to 0.5 m (Calm to Smooth wavelets) |

* World Meteorological Organization code and information of the wave height and appearance.

Noticeably, an average difference of 12° in the heading range during the first experiment could explain the slight azimuthal-like dependence observed. A similar heading average range in the third experiment has no effect in terms of azimuth given the very flat (level) seafloor. At all times during the surveys, the wave height was always lower than 1 m. Overall, the mono-directional survey strategy applied here was optimal in preventing (or at least minimizing) the effect of survey azimuth relative to the navigation heading [39]. Deviations from the planned track-line did occur for a range of reasons, but were kept minimal during the experiments. Experience showed that shorter track lines (about 1-km long) were needed to get high-density datasets enhancing the comparability and detectability of trends in the MBES BS and environmental data ($n$ = 44 instances during the 3rd experiment, compared to $n$ = 15 and 19 for the 1st and 2nd experiments, respectively). The use of a benthic lander device proved promising, combining various sensors on a single frame, thus retrieving multiple and relevant oceanographic data at once. However, several limitations were identified. First, there was a difference in retrieval location between the oceanographic data and the MBES data. The time bias between the measurements could in part be overcome by coupling the various data types by a unified mean time stamp (mean surveying time within the ROIs). However, the validity of this approach depends on the data acquisition periodicity by each sensor, which dictates the representativeness of the averages produced for certain tidal moments. For example, the ABS sensor used in the second experiment recorded data in bursts of 30 min, thereby possibly insufficiently capturing the sand transport behaviour at shorter time scale and possibly missing key moments of the tidal cycle (e.g., peak current velocities). Increasing and homogenising (across sensors) the frequency of registration would improve this limitation. For most optimal experiments, it is recommended to anchor the vessel on four points (i.e., port, starboard, bow and stern). This would allow collection of the various data types closer in space, as well as increase the frequency of seabed and water-column sampling by grabs and down-cast frames, thereby improving cost-time effectiveness of the experiment and data inter-comparability.

For the calculation of sound absorption due to suspended sediment in the water column, the modelling reported in [40,65] was simplified due to the limited data availability, and strong assumptions were made when vertically averaging or homogenizing the profiles. For more adequate modelling and correction of this phenomenon (e.g., in deeper clear waters where small turbidity changes may already significantly alter the BS), future experiments should collect more detailed information on concentration, particle size and vertical distribution (i.e., *Rouse* distribution (e.g., [81])). Uncertainty estimates due to this factor obtained by the reconstruction of full vertical sediment profiles showed that, within nearshore areas, transmission losses can vary significantly and have noticeable impact on the interpretation of multi-pass acoustic surveys. An interesting point to consider here is the rapid evolution of capabilities in water-column backscatter (WCB) data collection by modern MBES systems. Similarly to acoustic Doppler current profilers data, WCB can be calibrated against water samples to create spatially explicit profiles of SPMc and particle size, providing detailed information from near the sea-surface, down to the sonar bottom detection [82]. This raises the possibility to use more representative data and robustly implement sound-loss corrections in dynamic and deeper survey areas. Additionally, this would also be cost-effective and more complete compared to the deployment of benthic landers and associated instruments which are time consuming, labour intensive and ultimately impede the retrieval of data for the full water column.

The sonar measurements were interpreted in complement to an array of oceanographic measurements (where applicable) relating to local seafloor and water-column processes. They could be quantified by means of different equipment. Besides deploying multi-sensor benthic landers, downcast of the CTD frame allowed characterizing the water-column profile in detail, thus deriving better estimates of absorption coefficients than solely using sea-surface data. Substrate sampling gears such as the Reineck box-core, retrieving relatively undisturbed samples, proved useful to quantify short-term changes of the substrate composition, and core slicing allowed appreciating the fine-scale layering; such an instrument should be used more systematically in muddy/soft sediment areas to

fully evaluate the relations between acoustic response and sub-bottom complexity. Regarding the collection of SPMc measurements, different instruments were used. Chains of OBS mounted on a benthic lander proved very useful to understand the differences between SPMc at the boundary layer (i.e., 0.3 mab) and the upper-water column (i.e., ~2.5 mab). However, they do not provide estimates of the particle size, for which a LISST and/or ABS system should be used. In any case, it is recommended that further studies are dedicated to understand the differences between optically and acoustically derived estimates and that their sensitivity to varying particle sizes and concentrations are addressed (as in [83]) so that adequacy of the instruments to different environments can be better understood.

### *4.3. Implications for Repeated Backscatter Mapping Using MBES*

The short-term backscatter variability is only one aspect to consider when using MBES for repeated BS mapping. For the ultimate goal of merging datasets in space and time from different systems and vessels (e.g., cross-border datasets), careful consideration of multibeam system accuracy and stability, conditioning data repeatability and scaling, are required [84]. This starts with standardizing operational procedures, in terms of acquisition and processing, ideally inspired from community-driven experiences (e.g., the GeoHab backscatter working group [11]). Accuracy of an MBES system is largely dependent on the calibration process, requiring manufacturer-based operations (i.e., providing users with measurements/calibration tests results) and/or dedicated facilities and instrumentation to carry out in situ calibration (otherwise unfeasible for hull-mounted systems—see [21,29] for detailed considerations regarding calibration). Data repeatability refers to controlling the spatio-temporal consistency of the acoustic data in terms of instrumental and environment-caused drifts. Beyond direct metrological checks using dedicated equipment, instrumental drift can be controlled by repeated surveys over naturally stable areas (e.g., [29,30]) and/or fixed platforms, and regular dry-dock maintenance operations verifying the sensor status (as it is the case for the sonar systems used in this investigation). The focus of this paper was rather on the environmental drift, which refers here to evaluating the variability introduced by factors that do not directly relate to seafloor substrate type, but to water-column or near-bed sediment transport processes, as well as to target-geometry insonification related issues (i.e., azimuthal dependence, micro-scale roughness polarization). Such knowledge is important both for "snapshot in time" and for repeated mapping applications since improving the links between environmental variables and acoustic responses can improve the modelling and replication of field observations in space and time and enhance the interpretability of acoustic measurements.

It is paramount to understand the consequences of short-term environmental variability upon the interpretation of longer-term MBES-BS time series. This requires dedicated and specifically designed field experiments (e.g., this study, or the SAX experiments in [85], and those advocated in [32]).

As shown in this study, tidal periodicity and seasonality call for careful consideration, especially in shallow areas with soft-material seabeds and high sedimentary dynamics. Indeed, successive surveys of the same area may provide different information at various time scales (from day to year). In this regard, it is important that the tidal dependence is analysed per MBES-BS time series. Spotting outliers (i.e., abrupt changes in sediment response) will be relatively straightforward in the clear water and stationary areas (such as the Kwinte swale in the first experiment where tidal dependencies were low), since the magnitude of the short-term variance remains within the envelope of sensor sensitivity (i.e., the manufacturer-set $\pm 1$ dB for EM3002 and EM2040 Kongsberg systems [86]). On the contrary, the intrinsic "noisiness" (i.e., periodical variability) of the nearshore areas results in a potentially masking/blurring effect, introducing uncertainties due to the status of the water column (i.e., turbidity) or to the "mobility" of the water-sediment interface. Within such areas, the stability threshold must be defined contextually in accordance to the underlying sedimentary environment, and a transition in seafloor status can only be detected from a trend analysis on a sufficient number of serial surveys. Direction and consistency of the trend, regardless of the noise envelope, can be a valuable proxy of change and bypass conflicting results from surveys acquired at different tidal and/or seasonal

moments. Interpretation of serial backscatter surveys in such environments should largely benefit both from time series of driving variables (collected via the deployment of benthic landers as in [49,70]) and from regional predictive oceanographic models providing local conditions usable for designing monitoring surveys accordingly.

In the third experiment, the observations showed that regardless of the variability or 'noise' on the AR curves (except for that exerted by the roughness polarization in the second experiment), the main shape of the angular behaviour, indicative of a sediment type, remained the same. While part of this variability was related to transmission losses due to suspended sediment, the observed shifts in backscatter values (a decrease in reflectivity across the full angular range between flood and ebb tide moments) was related to HCMS dynamics, which changed the water-sediment interface, evidencing the BS sensitivity to short-term and relatively subtle granulometric and volume heterogeneity changes known to occur in this area [49]. The sensitivity of the angular response to such differences in sediment composition (within the same main sediment class) was observed in several investigations. For example, in [28], the high sensitivity of AR is particularly clear: AR curves are used as the basis of classification of a large MBES dataset, resulting in an evident within-cluster variability of up to 10 dB at 45°. Further insights can be found in data presented in [87], in which different AR curves are related to varying degrees of percentage cover of coarse clastic material (i.e., shell and gravel scatterers). This suggests that from well-controlled backscatter measurements with sufficient ground truth data allowing detailed interpretation, the derived BS AR curves can capture instantaneous and temporal physical changes in substrate composition. Critical is then to decipher whether the change was naturally or anthropogenically driven, requiring knowledge of the magnitudes of short-term and seasonal variability. A priori knowledge of the magnitude of natural variability would largely assist such interpretations.

## 5. Conclusions and Future Directions

This research focused on the reliability/utility of BS field measurements by ship-borne MBES for the monitoring of the seafloor interface. More specifically, the aim was to study short-term BS fluctuations specifically associated with tidally induced half-diel variations of the environment. Three experiments were conducted during which BS was acquired together with environmental variables. Results showed that the latter are important factors in explaining variations in the shape and values of the BS-AR curves and the associated imagery, with various impact levels depending on the local sedimentary configuration. Consequently, it is recommended that, beyond further investigations of the different sources of MBES data variability, detailed environmental variables are systematically collected together with settings of MBES and associated devices, as well as application of best practice in survey designing. For users and surveyors operating within tidally dominated environments (both for mapping and monitoring purposes), such experiments raise several points of interest. Assuming a stable sonar system with no instrumental drift and a rigorously standardised acquisition and processing routine, the following observations were made: (1) in relatively stable and gravelly offshore areas, characterized by clear seawater, the variability due to external sources is limited and the BS measurement confidently relates to the water-sediment interface. (2) In nearshore sandy areas, roughness polarization may occur at various scales (depending on the hydrodynamic forcing) and a joint investigation of BS mosaics and BS-AR data products are needed to confidently discern between these geometrical effects and actual sediment changes. (3) In nearshore muddy and turbid areas, the influence of suspended sediment is prone to be significant and needs to be corrected for, requiring careful sampling and quantitative estimation of water-column processes. In the absence of sampling, interpretation of MBES BS requires a minima knowledge of the variability of environmental processes, from available time-series data and /or high-resolution sediment transport and current models.

**Author Contributions:** Conceptualisation, G.M.-G., M.R., X.L. and V.V.L.; Formal analysis, G.M.-G., M.R., M.B., N.T. and F.F.; Investigation, G.M.-G., M.R., K.D., X.L., V.V.L., N.T. and F.F.; Methodology, G.M.-G., M.R., K.D., X.L., M.B., N.T. and V.V.L.; Project administration, V.V.L., M.R. and X.L.; Writing—Original Draft, G.M.-G.; Writing—Review and Editing, G.M.-G., N.T., M.R., X.L. and V.V.L.

**Funding:** This paper is a contribution to the project INDI67 (BELSPO, contract BR/143/A2/INDI67) under which Giacomo Montereale Gavazzi's PhD is funded. Ship time *RV Belgica* was provided by BELSPO and RBINS–OD Nature and *RV Simon Stevin* by Flanders Marine Institute.

**Acknowledgments:** We thank the crews, commander and captain of *RV Belgica* and *RV Simon Stevin* respectively for their help during the data collection phase of this investigation.

**Conflicts of Interest:** The authors declare no conflict of interest.

**Data Availability:** Raw multibeam echosounder and associated datasets from the various sensors employed in the investigation are stored at the Royal Belgian Institute of Natural Sciences and are available upon request.

## References

1. Halpern, B.S.; Walbridge, S.; Selkoe, K.A.; Kappel, C.V.; Micheli, F.; D'Agrosa, C.; Bruno, J.F.; Casey, K.S.; Ebert, C.; Fox, H.E.; et al. A Global Map of Human Impact on Marine Ecosystems. *Science* **2008**, *319*, 948–952. [CrossRef] [PubMed]
2. Douvere, F.; Maes, F.; Vanhulle, A.; Schrijvers, J. The role of marine spatial planning in sea use management: The Belgian case. *Mar. Policy* **2007**, *31*, 182–191. [CrossRef]
3. McArthur, M.A.; Brooke, B.P.; Przeslawski, R.; Ryan, D.A.; Lucieer, V.L.; Nichol, S.; McCallum, A.W.; Mellin, C.; Cresswell, I.D.; Radke, L.C. On the use of abiotic surrogates to describe marine benthic biodiversity. *Estuar. Coast. Shelf Sci.* **2010**, *88*, 21–32. [CrossRef]
4. Rice, J.; Arvanitidis, C.; Borja, A.; Frid, C.; Hiddink, J.G.; Krause, J.; Lorance, P.; Ragnarsson, S.Á.; Sköld, M.; Trabucco, B.; et al. Indicators for Sea-floor Integrity under the European Marine Strategy Framework Directive. *Ecol. Indic.* **2012**, *12*, 174–184. [CrossRef]
5. Belgian State. Determination of Good Environmental Status & Establishment of Environmental Targets for the Belgian Marine Waters, Marine Strategy Framework Directive—Art 9 & 10. Available online: https://www.health.belgium.be/sites/default/files/uploads/fields/fpshealth_theme_file/19087665/Goede%20milieutoestand-MSFD%20EN.pdf (accessed on 1 November 2018).
6. De Moustier, C.; Matsumoto, H. Seafloor acoustic remote sensing with multibeam echo-sounders and bathymetric sidescan sonar systems. *Mar. Geophys. Res.* **1993**, *15*, 27–42. [CrossRef]
7. Brown, C.J.; Blondel, P. Developments in the application of multibeam sonar backscatter for seafloor habitat mapping. *Appl. Acoust.* **2009**, *70*, 1242–1247. [CrossRef]
8. Urick, R.J. *Principles of Underwater Sound for Engineers*, 3rd ed.; Tata McGraw-Hill Education: New York, NY, USA, 1967.
9. Hughes Clarke, J.E.; Mayer, L.A.; Wells, D.E. Shallow-water imaging multibeam sonars: A new tool for investigating seafloor processes in the coastal zone and on the continental shelf. *Mar. Geophys. Res.* **1996**, *18*, 607–629. [CrossRef]
10. Ferrini, V.L.; Flood, R.D. The effects of fine-scale surface roughness and grain size on 300 kHz multibeam backscatter intensity in sandy marine sedimentary environments. *Mar. Geol.* **2006**, *228*, 153–172. [CrossRef]
11. Lamarche, G.; Lurton, X. Recommendations for improved and coherent acquisition and processing of backscatter data from seafloor-mapping sonars. *Mar. Geophys. Res.* **2018**, *39*, 5–22. [CrossRef]
12. Lurton, X. *An Introduction to Underwater Acoustics: Principles and Applications*; Springer: Berlin/Heidelberg, Germany, 2002; p. 680. ISBN 978-3-540-78480-7.
13. Strong, J.A.; Elliott, M. The value of remote sensing techniques in supporting effective extrapolation across multiple marine spatial scales. *Mar. Pollut. Bull.* **2017**, *116*, 405–419. [CrossRef]
14. Brown, C.J.; Sameoto, J.A.; Smith, S.J. Multiple methods, maps, and management applications: Purpose made seafloor maps in support of ocean management. *J. Sea Res.* **2012**, *72*, 1–13. [CrossRef]
15. Buhl-Mortensen, L.; Buhl-Mortensen, P.; Dolan, M.F.J.; Holte, B. The MAREANO programme—A full coverage mapping of the Norwegian off-shore benthic environment and fauna. *Mar. Biol. Res.* **2015**, *11*, 4–17. [CrossRef]

16. Holler, P.; Markert, E.; Bartholomä, A.; Capperucci, R.; Hass, H.C.; Kröncke, I.; Mielck, F.; Reimers, H.C. Tools to evaluate seafloor integrity: Comparison of multi-device acoustic seafloor classifications for benthic macrofauna-driven patterns in the German Bight, Southern North Sea. *Geo-Mar. Lett.* **2017**, *37*, 93–109. [CrossRef]
17. Madricardo, F.; Foglini, F.; Kruss, A.; Ferrarin, C.; Pizzeghello, N.M.; Murri, C.; Rossi, M.; Bajo, M.; Bellafiore, D.; Campiani, E.; et al. High resolution multibeam and hydrodynamic datasets of tidal channels and inlets of the Venice Lagoon. *Sci. Data* **2017**, *4*, 170121. [CrossRef] [PubMed]
18. Jackson, D.R.; Baird, A.M.; Crisp, J.J.; Thomson, P.A.G. High-frequency bottom backscatter measurements in shallow water. *J. Acoust. Soc. Am.* **1986**, *80*, 1188–1199. [CrossRef]
19. Hughes Clarke, J.E.; Danforth, B.W.; Valentine, P. Areal Seabed Classification using Backscatter Angular Response at 95 kHz. In Proceedings of the Conference of High Frequency Acoustics in Shallow Water, NATO SACLANT Undersea Research Centre, Lerici, Italy, 30 June–4 July 1997.
20. Che Hasan, R.; Ierodiaconou, D.; Laurenson, L.; Schimel, A. Integrating Multibeam Backscatter Angular Response, Mosaic and Bathymetry Data for Benthic Habitat Mapping. *PLoS ONE* **2014**, *9*, e97339. [CrossRef] [PubMed]
21. Eleftherakis, D.; Berger, L.; Le Bouffant, N.; Pacault, A.; Augustin, J.-M.; Lurton, X. Backscatter calibration of high-frequency multibeam echosounder using a reference single-beam system, on natural seafloor. *Mar. Geophys. Res.* **2018**, *39*, 55–73. [CrossRef]
22. Fonseca, L.; Mayer, L. Remote estimation of surficial seafloor properties through the application Angular Range Analysis to multibeam sonar data. *Mar. Geophys. Res.* **2007**, *28*, 119–126. [CrossRef]
23. Galparsoro, I.; Borja, Á.; Bald, J.; Liria, P.; Chust, G. Predicting suitable habitat for the European lobster (Homarus gammarus), on the Basque continental shelf (Bay of Biscay), using Ecological-Niche Factor Analysis. *Ecol. Model.* **2009**, *220*, 556–567. [CrossRef]
24. Wedding, L.; Lepczyk, C.; Pittman, S.; Friedlander, A.; Jorgensen, S. Quantifying seascape structure: Extending terrestrial spatial pattern metrics to the marine realm. *Mar. Ecol. Prog. Ser.* **2011**, *427*, 219–232. [CrossRef]
25. Ierodiaconou, D.; Schimel, A.C.G.; Kennedy, D.; Monk, J.; Gaylard, G.; Young, M.; Diesing, M.; Rattray, A. Combining pixel and object based image analysis of ultra-high resolution multibeam bathymetry and backscatter for habitat mapping in shallow marine waters. *Mar. Geophys. Res.* **2018**, *39*, 271–288. [CrossRef]
26. Lamarche, G.; Lurton, X.; Verdier, A.-L.; Augustin, J.-M. Quantitative characterisation of seafloor substrate and bedforms using advanced processing of multibeam backscatter—Application to Cook Strait, New Zealand. *Cont. Shelf Res.* **2011**, *31*, S93–S109. [CrossRef]
27. Ladroit, Y.; Lamarche, G.; Pallentin, A. Seafloor multibeam backscatter calibration experiment: Comparing 45°-tilted 38-kHz split-beam echosounder and 30-kHz multibeam data. *Mar. Geophys. Res.* **2018**, *39*, 41–53. [CrossRef]
28. Fezzani, R.; Berger, L. Analysis of calibrated seafloor backscatter for habitat classification methodology and case study of 158 spots in the Bay of Biscay and Celtic Sea. *Mar. Geophys. Res.* **2018**, *39*, 169–181. [CrossRef]
29. Weber, T.C.; Rice, G.; Smith, M. Toward a standard line for use in multibeam echo sounder calibration. *Mar. Geophys. Res.* **2018**, *39*, 75–87. [CrossRef]
30. Roche, M.; Degrendele, K.; Vrignaud, C.; Loyer, S.; Le Bas, T.; Augustin, J.-M.; Lurton, X. Control of the repeatability of high frequency multibeam echosounder backscatter by using natural reference areas. *Mar. Geophys. Res.* **2018**, *39*, 89–104. [CrossRef]
31. Roche, M.; Degrendele, K.; Vandenreyken, H.; Schotte, P. Multi Time and Space scale Monitoring of the Sand Extraction and Its Impact on the Seabed by Coupling EMS Data and MBES Measurements. 33. Belgian Marine Sand: A Scarce Resource? Belgian FPS Economy—Study day 9. June 2017. Available online: http://economie.fgov.be/fr/binaries/Articles-study-day-2017_tcm326-283850.pdf (accessed on 1 November 2018).
32. Lucieer, V.; Roche, M.; Degrendele, K.; Malik, M.; Dolan, M.; Lamarche, G. User expectations for multibeam echo sounders backscatter strength data-looking back into the future. *Mar. Geophys. Res.* **2018**, *39*, 23–40. [CrossRef]
33. Roche, M.; Baeye, M.; Bisschop, J.D.; Degrendele, K.; Papili, S.; Lopera, O.; Lancker, V.V. Backscatter stability and influence of water column conditions: Estimation by multibeam echosounder and repeated oceanographic measurements, Belgian part of the North Sea. *Inst. Acoust.* **2015**, *37*, 8.

34. Singh, A. Review Article Digital change detection techniques using remotely-sensed data. *Int. J. Remote Sens.* **1989**, *10*, 989–1003. [CrossRef]
35. Floricioiu, D.; Rott, H. Seasonal and short-term variability of multifrequency, polarimetric radar backscatter of Alpine terrain from SIR-C/X-SAR and AIRSAR data. *IEEE Trans. Geosci. Remote Sens.* **2001**, *39*, 2634–2648. [CrossRef]
36. Boehme, H.; Chotiros, N.P.; Rolleigh, L.D.; Pitt, S.P.; Garcia, A.L.; Goldsberry, T.G.; Lamb, R.A. Acoustic backscattering at low grazing angles from the ocean bottom. I. Bottom backscattering strength. *J. Acoust. Soc. Am.* **1984**, *75*, S30. [CrossRef]
37. Briggs, K.B.; Williams, K.L.; Richardson, M.D.; Jackson, D.R. Effects of Changing Roughness on Acoustic Scattering: (1) Natural Changes. *Proc. Inst. Acoust.* **2001**, *23*, 375–382.
38. Richardson, M.D.; Briggs, K.B.; Williams, K.L.; Lyons, A.P.; Jackson, D.R. Effects of Changing Roughness on Acoustic Scattering: (2) Anthropogenic Changes. 2001. Available online: http://www.apl.washington.edu/programs/SAX99/IOSpapers/Richardson.pdf (accessed on 4 December 2018).
39. Lurton, X.; Eleftherakis, D.; Augustin, J.-M. Analysis of seafloor backscatter strength dependence on the survey azimuth using multibeam echosounder data. *Mar. Geophys. Res.* **2018**, *39*, 183–203. [CrossRef]
40. Francois, R.E.; Garrison, G.R. Sound absorption based on ocean measurements: Part I: Pure water and magnesium sulfate contributions. *J. Acoust. Soc. Am.* **1982**, *72*, 896–907. [CrossRef]
41. Francois, R.E.; Garrison, G.R. Sound absorption based on ocean measurements. Part II: Boric acid contribution and equation for total absorption. *J. Acoust. Soc. Am.* **1982**, *72*, 1879–1890. [CrossRef]
42. De Campos Carvalho, R.; de Oliveira Junior, A.M.; Clarke, J.E.H. Proper environmental reduction for attenuation in multi-sector sonars. In Proceedings of the 2013 IEEE/OES Acoustics in Underwater Geosciences Symposium, Rio de Janeiro, Brazil, 24–26 July 2013; pp. 1–6.
43. Richards, S.D.; Heathershaw, A.D.; Thorne, P.D. The effect of suspended particulate matter on sound attenuation in seawater. *J. Acoust. Soc. Am.* **1996**, *100*, 1447–1450. [CrossRef]
44. Holliday, D.V.; Pieper, R.E. Volume scattering strengths and zooplankton distributions at acoustic frequencies between 0.5 and 3 MHz. *J. Acoust. Soc. Am.* **1980**, *67*, 135–146. [CrossRef]
45. Gorska, N.; Kowalska-Duda, E.; Pniewski, F.; Latała, A. On diel variability of marine sediment backscattering properties caused by microphytobenthos photosynthesis: Impact of environmental factors. *J. Mar. Syst.* **2018**, *182*, 1–11. [CrossRef]
46. Bellec, V.K.; Lancker, V.V.; Degrendele, K.; Roche, M. Geo-environmental Characterization of the Kwinte Bank. *J. Coast. Res.* **2010**, 63–76.
47. Van Lancker, V. Sediment and Morphodynamics of a Siliciclastic near Coastal Area, in Relation to Hydrodynamical and Meteorological Conditions: Belgian Continental Shelf. Ph.D. Thesis, Gent University, Gent, Belgium, 24 June 1999.
48. Fettweis, M.; Baeye, M. Seasonal variation in concentration, size, and settling velocity of muddy marine flocs in the benthic boundary layer: Seasonality of SPM concentration. *J. Geophys. Res. Oceans* **2015**, *120*, 5648–5667. [CrossRef]
49. Baeye, M.; Fettweis, M.; Legrand, S.; Dupont, Y.; Van Lancker, V. Mine burial in the seabed of high-turbidity area—Findings of a first experiment. *Cont. Shelf Res.* **2012**, *43*, 107–119. [CrossRef]
50. Lanckneus, J.; Van Lancker, V.; Moerkerke, G.; Van Den Eynde, D.; Fettweis, M.; De Batist, M.; Jacobs, P. *Investigation of the Natural Sand Transport on the Belgian Continental Shelf (BUDGET)*; Federal Office for Scientific, Technical and Cultural Affairs (OSTC): Brussel, Belgium, 2001; pp. 104–187. Available online: http://www.vliz.be/imisdocs/publications/ocrd/262275.pdf (accessed on 1 November 2018).
51. Van Lancker, V.; De Batist, M.; Fettweis, M.; Pichot, G.; Monbaliu, J. *Management, Research and Budgeting of Aggregates in Shelf Seas Related to End-Users (MAREBASSE)*; Belgian Scientific Policy Office: Brussel, Belgium, 2007; p. 66. Available online: http://www.vliz.be/imisdocs/publications/139287.pdf (accessed on 5 October 2018).
52. Davies, C.E.; Moss, D.; Hill, M.O. EUNIS Habitat Classification Revised. European Environment Agency European Topic Centre on Nature Protection and Biodiversity, October 2004. Available online: https://www.eea.europa.eu/data-and-maps/data/eunis-habitat-classification (accessed on 1 November 2018).
53. Kongsberg Maritime. *Seafloor Information System Reference Manual—429004/A*, 5th ed.; Kongsberg Maritime: Kongsberg, Norway, April 2018; Available online: https://www.km.kongsberg.com/ks/web/nokbg0397.nsf/AllWeb/A269870356C3A572C1256E19004ECFA9/$file/164878ac_SIS_Product_specification.pdf (accessed on 1 November 2018).

54. De Bisschop, J. Influence of Water Column Properties on Multibeam Backscatter. Master's Thesis, Gent University, Gent, Belgium, September 2016.
55. Fettweis, M.; Baeye, M.; Lee, B.J.; Chen, P.; Yu, J.C.S. Hydro-meteorological influences and multimodal suspended particle size distributions in the Belgian nearshore area (southern North Sea). *Geo-Mar. Lett.* **2012**, *32*, 123–137. [CrossRef]
56. Thorne, P.D.; Hanes, D.M. A review of acoustic measurement of small-scale sediment processes. *Cont. Shelf Res.* **2002**, *22*, 603–632. [CrossRef]
57. Blott, S.J.; Pye, K. GRADISTAT: A grain size distribution and statistics package for the analysis of unconsolidated sediments. *Earth Surf. Process. Landf.* **2001**, *26*, 1237–1248. [CrossRef]
58. Hartigan, J.A.; Wong, M.A. Algorithm AS 136: A K-Means Clustering Algorithm. *Appl. Stat.* **1979**, *28*, 100. [CrossRef]
59. Kongsberg Maritime. *EM Series Multibeam Echo Sounders Datagram Formats—850-160692/W*; Kongsberg Maritime: Kongsberg, Norway, January 2018; Available online: https://www.km.kongsberg.com/ks/web/nokbg0397.nsf/AllWeb/253E4C58DB98DDA4C1256D790048373B/$file/160692_em_datagram_formats.pdf (accessed on 9 September 2018).
60. QPS. Available online: http://www.qps.nl/display/main/home (accessed on 12 October 2018).
61. SonarScope—Ifremer Fleet. Available online: http://flotte.ifremer.fr/fleet/Presentation-of-the-fleet/On-board-software/SonarScope (accessed on 12 October 2018).
62. Qimera. Available online: http://www.qps.nl/display/qimera/Home;jsessionid=DC46DBAC82D50C8F37EAFDF66AD21338 (accessed on 2 November 2018).
63. Ernstsen, V.B.; Noormets, R.; Hebbeln, D.; Bartholomä, A.; Flemming, B.W. Precision of high-resolution multibeam echo sounding coupled with high-accuracy positioning in a shallow water coastal environment. *Geo-Mar. Lett.* **2006**, *26*, 141–149. [CrossRef]
64. International Hydrographic Organisation. Available online: https://www.iho.int/iho_pubs/standard/S-44_5E.pdf (accessed on 2 November 2018).
65. Urick, R.J. The Absorption of Sound in Suspensions of Irregular Particles. *J. Acoust. Soc. Am.* **1948**, *20*, 283–289. [CrossRef]
66. Hoitink, A.J.F.; Hoekstra, P. Observations of suspended sediment from ADCP and OBS measurements in a mud-dominated environment. *Coast. Eng.* **2005**, *52*, 103–118. [CrossRef]
67. Van den Eynde, D.; Giardino, A.; Portilla, J.; Fettweis, M.; Francken, F.; Monbaliu, J. Modelling the effects of sand extraction, on sediment transport due to tides, on the Kwinte Bank. *J. Coast. Res.* **2010**, *51*, 101–116.
68. Soulsby, R. *Dynamics of Marine Sands: A Manual for Practical Applications*, 1st ed.; Thomas Telford Publications: London, UK, 1997.
69. Malik, M.; Lurton, X.; Mayer, L. A framework to quantify uncertainties of seafloor backscatter from swath mapping echosounders. *Mar. Geophys. Res.* **2018**, *39*, 151–168. [CrossRef]
70. Fettweis, M.; Lee, B. Spatial and Seasonal Variation of Biomineral Suspended Particulate Matter Properties in High-Turbid Nearshore and Low-Turbid Offshore Zones. *Water* **2017**, *9*, 694. [CrossRef]
71. Van Leeuwen, S.; Tett, P.; Mills, D.; van der Molen, J. Stratified and nonstratified areas in the North Sea: Long-term variability and biological and policy implications: North sea stratification regimes. *J. Geophys. Res. Oceans* **2015**, *120*, 4670–4686. [CrossRef]
72. Rattray, A.; Ierodiaconou, D.; Monk, J.; Versace, V.; Laurenson, L. Detecting patterns of change in benthic habitats by acoustic remote sensing. *Mar. Ecol. Prog. Ser.* **2013**, *477*, 1–13. [CrossRef]
73. Montereale-Gavazzi, G.; Roche, M.; Lurton, X.; Degrendele, K.; Terseleer, N.; Van Lancker, V. Seafloor change detection using multibeam echosounder backscatter: Case study on the Belgian part of the North Sea. *Mar. Geophys. Res.* **2018**, *39*, 229–247. [CrossRef]
74. Masselink, G.; Austin, M.J.; O'Hare, T.J.; Russell, P.E. Geometry and dynamics of wave ripples in the nearshore zone of a coarse sandy beach. *J. Geophys. Res.* **2007**, *112*. [CrossRef]
75. Ernstsen, V.B.; Noormets, R.; Winter, C.; Hebbeln, D.; Bartholomä, A.; Flemming, B.W.; Bartholdy, J. Quantification of dune dynamics during a tidal cycle in an inlet channel of the Danish Wadden Sea. *Geo-Mar. Lett.* **2006**, *26*, 151–163. [CrossRef]
76. Van Hoey, G.; Degraer, S.; Vincx, M. Macrobenthic community structure of soft-bottom sediments at the Belgian Continental Shelf. *Estuar. Coast. Shelf Sci.* **2004**, *59*, 599–613. [CrossRef]

77. Degraer, S.; Verfaillie, E.; Willems, W.; Adriaens, E.; Vincx, M.; Van Lancker, V. Habitat suitability modelling as a mapping tool for macrobenthic communities: An example from the Belgian part of the North Sea. *Cont. Shelf Res.* **2008**, *28*, 369–379. [CrossRef]
78. Rowden, A.A.; Jago, C.F.; Jones, S.E. Influence of benthic macrofauna on the geotechnical and geophysical properties of surficial sediment, North Sea. *Cont. Shelf Res.* **1998**, *18*, 1347–1363. [CrossRef]
79. Degraer, S.; Moerkerke, G.; Rabaut, M.; Van Hoey, G.; Du Four, I.; Vincx, M.; Henriet, J.-P.; Van Lancker, V. Very-high resolution side-scan sonar mapping of biogenic reefs of the tube-worm Lanice conchilega. *Remote Sens. Environ.* **2008**, *112*, 3323–3328. [CrossRef]
80. Huff, L. Acoustic Remote Sensing as a Tool for Habitat Mapping in Alaska Waters. In *Marine Habitat Mapping Technology for Alaska*; Reynolds, J., Greene, H., Eds.; Alaska Sea Grant, University of Alaska Fairbanks: Fairbanks, AK, USA, 2008; pp. 29–46.
81. Zyserman, J.A.; Fredsøe, J. Data Analysis of Bed Concentration of Suspended Sediment. *J. Hydraul. Eng.* **1994**, *120*, 1021–1042. [CrossRef]
82. Simmons, S.M.; Parsons, D.R.; Best, J.L.; Orfeo, O.; Lane, S.N.; Kostaschuk, R.; Hardy, R.J.; West, G.; Malzone, C.; Marcus, J.; et al. Monitoring Suspended Sediment Dynamics Using MBES. *J. Hydraul. Eng.* **2010**, *136*, 45–49. [CrossRef]
83. Hawley, N. A Comparison of Suspended Sediment Concentrations Measured by Acoustic and Optical Sensors. *J. Gt. Lakes Res.* **2004**, *30*, 301–309. [CrossRef]
84. Anderson, J.T.; Van Holliday, D.; Kloser, R.; Reid, D.G.; Simard, Y. Acoustic seabed classification: Current practice and future directions. *ICES J. Mar. Sci.* **2008**, *65*, 1004–1011. [CrossRef]
85. Williams, K.L.; Jackson, D.R.; Tang, D.; Briggs, K.B.; Thorsos, E.I. Acoustic Backscattering from a Sand and a Sand/Mud Environment: Experiments and Data/Model Comparisons. *IEEE J. Ocean. Eng.* **2009**, *34*, 388–398. [CrossRef]
86. Hammerstad, E. EM technical note: Backscattering and seabed image reflectivity. *Horten Nor. Kongsberg Marit. AS* **2000**, 1–5. Available online: https://www.km.kongsberg.com/ks/web/nokbg0397.nsf/AllWeb/C2AE0703809C1FA5C1257B580044DD83/$file/EM_technical_note_web_BackscatteringSeabedImageReflectivity.pdf (accessed on 12 October 2018).
87. Daniell, J.; Siwabessy, J.; Nichol, S.; Brooke, B. Insights into environmental drivers of acoustic angular response using a self-organising map and hierarchical clustering. *Geo-Mar. Lett.* **2015**, *35*, 387–403. [CrossRef]